Doctoral Thesis

Monitoring lava dome growth and deformation with photogrammetric methods and modelling

by

Edgar Ulrich Zorn

Cumulative dissertation submitted in fulfilment of the requirements
for the degree of “Doctor rerum naturalium” (Dr. rer. nat.)
in the scientific field “Geology”

Institute of Geosciences
Faculty of Science
University of Potsdam

Supervisor: Dr. Thomas Walter

Mentor: Dr. Ulrich Küppers

Defence date:

06.11.2020

Published online on the
Publication Server of the University of Potsdam:
https://doi.org/10.25932/publishup-48360
https://nbn-resolving.org/urn:nbn:de:kobv:517-opus4-483600

Declaration of originality

I hereby declare that this thesis is the product of my own work. All assistance received in preparing this thesis and the sources used have been acknowledged. This thesis has not been submitted at any other university.

Edgar Ulrich Zorn
17.06.2020

Abstract

Lava domes are severely hazardous, mound-shaped extrusions of highly viscous lava and commonly erupt at many active stratovolcanoes around the world. Due to gradual growth and flank oversteepening, such lava domes regularly experience partial or full collapses, resulting in destructive and far-reaching pyroclastic density currents. They are also associated with cyclic explosive activity as the complex interplay of cooling, degassing, and solidification of dome lavas regularly causes gas pressurizations on the dome or the underlying volcano conduit. Lava dome extrusions can last from days to decades, further highlighting the need for accurate and reliable monitoring data.

This thesis aims to improve our understanding of lava dome processes and to contribute to the monitoring and prediction of hazards posed by these domes. The recent rise and sophistication of photogrammetric techniques allows for the extraction of observational data in unprecedented detail and creates ideal tools for accomplishing this purpose. Here, I study natural lava dome extrusions as well as laboratory-based analogue models of lava dome extrusions and employ photogrammetric monitoring by Structure-from-Motion (SfM) and Particle-Image-Velocimetry (PIV) techniques. I primarily use aerial photography data obtained by helicopter, airplanes, Unoccupied Aircraft Systems (UAS) or ground-based timelapse cameras. Firstly, by combining a long time-series of overflight data at Volcán de Colima, México, with seismic and satellite radar data, I construct a detailed timeline of lava dome and crater evolution. Using numerical model, the impact of the extrusion on dome morphology and loading stress is further evaluated and an impact on the growth direction is identified, bearing important implications for the location of collapse hazards. Secondly, sequential overflight surveys at the Santiaguito lava dome, Guatemala, reveal surface motion data in high detail. I quantify the growth of the lava dome and the movement of a lava flow, showing complex motions that occur on different timescales and I provide insight into rock properties relevant for hazard assessment inferred purely by photogrammetric processing of remote sensing data. Lastly, I recreate artificial lava dome and spine growth using analogue modelling under controlled conditions, providing new insights into lava extrusion processes and structures as well as the conditions in which they form.

These findings demonstrate the capabilities of photogrammetric data analyses to successfully monitor lava dome growth and evolution while highlighting the advantages of complementary modelling methods to explain the observed phenomena. The results presented herein further bear important new insights and implications for the hazards posed by lava domes.

Zusammenfassung

Lavadome sind kuppelförmige Aufstauungen aus zähflüssiger Lava und bilden sich häufig bei Eruptionen an aktiven Stratovulkanen. Sie stellen dabei oft eine erhebliche Gefahr für Menschen und Infrastruktur dar, weil Lavadome instabil werden können und bei einem Kollaps pyroklastische Ströme (auch Glutlawinen) erzeugen können. Diese können innerhalb von Minuten weite Flächen verwüsten, daher ist die Überwachung von Lavadomen und deren Wachstum mit genauen und zuverlässigen Daten von großer Bedeutung.

In dieser Arbeit werden das Wachstum und die Bewegungen von Lavadomen mit fotogrammetrischen Methoden (Vermessungen anhand von Fotos) und mit Modellierungen in drei Teilstudien getestet und untersucht. Dazu wurden Daten sowohl an Lavadomen von Vulkanen in Mexiko und Guatemala als auch mittels künstlich erzeugter Dome im Labor erhoben. Hierbei wurden insbesondere das Structure-from-Motion-Verfahren, bei dem mithilfe einer Serie von Luftaufnahmen ein hochauflösendes 3D-Modell des Lavadoms und des Vulkans erstellt wird, und das Particle-Image-Velocimetry-Verfahren, bei dem aus einer Zeitreihe von Fotos kleinste Bewegungen detailliert gemessen werden können, verwendet.

In der ersten Teilstudie wird aus einer Kombination von Überflugsbildern, Radardaten eines Satelliten, und seismischen Daten eine detaillierte Zeitreihe des Lavadom-Wachstums und der Kraterentwickelung am Volcán de Colima, México, erstellt. Anschließend werden die dabei erfassten Richtungen des Domwachstums mit numerischen Modellen auf Basis der fotogrammetrischen 3D-Modelle simuliert, welche zeigen, dass sich lokale Änderungen der Topografie auf die Wachstumsrichtung auswirken können. In der zweiten Teilstudie werden Drohnen in verschiedenen Zeitintervallen über einen Lavadom am Santa Maria Vulkan, Guatemala, geflogen. Die Überflugsdaten zeigen dabei Bewegungen sowohl an einem Lavastrom als auch ein Anschwellen des Doms mit jeweils unterschiedlichen Geschwindigkeiten. Ferner können die Daten genutzt werden um Oberflächentemperatur und die Viskosität (Zähflüssigkeit) der Lava zu vermessen, welche für die Gefahrenanalyse eine wichtige Rolle spielen. In der dritten Teilstudie werden künstliche Dom-Modelle mithilfe von Sand-Gips-Gemischen erzeugt. Diese können sowohl den Aufbau und Morphologie als auch die internen Strukturen von Lavadomen simulieren und anhand von Zeitraffer-Aufnahmen im Detail nachstellen.

Die Ergebnisse zeigen, dass Fotogrammetrie und Modellierungen geeignete Mittel sind um Lavadome sowie deren Entstehungsprozesse und Gefahren zu verfolgen und neue Erkenntnisse zu gewinnen.

Acknowledgements

Becoming a volcanologist was a dream I had since I was about 10 years old, where a volcano movie managed to scare me into memorising volcano-related children's books by heart. I have been fascinated with the topic ever since and strived to experience and learn more about the captivating spectacle of volcanic eruptions. Over the past years I had the privilege to visit and work at many volcanoes in all parts of the world and I am sincerely grateful to all people that supported and accompanied me.

I would further like to acknowledge and thank the following people, which have assisted me during the creation of this thesis:

My supervisors and mentors Thomas Walter and Ulrich Küppers for the guidance and assistance throughout the study as well as the encouragement to pursue, realize and present my own ideas. I greatly appreciate the experiences I gained in during my work.

All my colleagues in our volcanology group and in our section at the GFZ, for a creating a welcoming and respectful work environment, excellent company both in office and during fieldwork as well as many fruitful and helpful discussions.

All family and friends – both in Germany and abroad - for their support, acceptance, and regular moral boosts.

Finally, my parents, Gabriele and Ulrich Zorn, for continued unconditional support throughout my entire academic career.

Table of Contents

List of Figures

List of Tables

Chapter 1:
Introduction

1.1 Background

Active volcanoes pose a fundamental threat to the people and communities living nearby. There are currently ~1,400 volcanoes worldwide that are considered historically active and ~70 erupting volcanoes being recorded every year (Global Volcanism Program, 2013). Between 1600 and 2010, approximately 280,000 people were killed as a result of volcanic activity (Auker et al., 2013) and with the growing human population, the annual number of fatal incidents has been continually increasing as more people live close to volcanoes (Witham, 2005; Auker et al., 2013). Volcanic eruptions have also demonstrated the vulnerability of our increasingly globalising economy, with the 2010 eruption of Eyjafjallajökull volcano, Iceland, and the closure of airports in Europe causing an estimated loss of 1.6 billion dollars to the airline industry alone (Harris et al., 2012), the total economic damage being ~5 billion (Oxford Economics, 2010). Just in recent years there were a number of noteworthy incidents; the 2017 eruption of Agung on Bali Island, Indonesia, closed airports at a major touristic destination due to the movement of its ash plume (Marchese et al., 2018). In 2018, a tsunami caused by a sector collapse at Anak Krakatoa, Indonesia, resulted in 430 fatalities on nearby shores (Walter et al., 2019a). At Fuego volcano, Guatemala, a series of explosions caused pyroclastic flows which buried a village and killed at least 110 people (Global Volcanism Program, 2018), although the real number of fatalities is likely much higher. In 2019, a small explosion on the popular tourist destination Whakaari (White Island), New Zealand, killed 23 tourists and tour guides that were on the Island (Global Volcanism Program, 2019). Finally, in 2020, the eruption of Taal volcano, Phillipines, caused widespread ashfall, airport closures, and the evacuation of ~460.000 people (Global Volcanism Program, 2020). These eruptions demonstrated that the issues and hazards related to volcanic eruptions are still relevant today and can threaten human lives, infrastructures, and economic security in the affected regions.

Many deadly events in volcanological history are associated with lava domes. Between 1500 and today there are over 70,000 fatalities that could be directly linked to the growth of lava domes (Calder et al., 2015). The most famous example is the 1902 eruption of Mt. Pelée, Martinique. Here the collapse of the summit lava dome caused a devastating pyroclastic density current (the main hazard associated with lava domes) which destroyed the town St. Pierre and killed ~28,000 people over the course minutes (Tanguy, 1994). A major contributor to this

catastrophe was the insufficient knowledge of volcanism and its hazards at the time, causing officials to misinterpret or ignore the warning signs (Tanguy, 1994). Since then, awareness for hazards posed by lava domes has increased, however, pyroclastic density currents are still responsible for ~45,000 deaths since the beginning of the 20th century (Witham, 2005). In recent years, the Merapi eruption in 2010, Indonesia, caused 367 fatalities (Surono et al., 2012) and the ongoing dome extrusion since 2013 at Sinabung, Indonesia, has displaced nearly 10,000 people with 16 known fatalities (Andreastuti et al., 2019). These events highlight that the study and assessment of hazards at lava-dome building volcanoes is still highly relevant today and further advancements in our understanding of lava domes may help to mitigate potential future disasters. Due to their hazardous nature, this thesis relies on photogrammetry and remote sensing techniques as well as modelling approaches to monitor and the growth, topography and displacements of lava domes.

1.2 Lava domes and associated hazards

Lava domes are mound-shaped extrusions that form when lava is highly viscous and cannot flow freely from the vent, causing it to pile up instead (Fig. 1.1a). They commonly appear at volcanoes of andesitic and dacitic compositions (mostly stratovolcanoes). Nearly 400 individual episodes of dome growth have been registered worldwide at 223 volcanoes since 1000 AD, some of them lasting several decades (Ogburn et al., 2015). Most lava domes develop a classic "dome" shape with a flat-topped and steep-sided morphology, a distinct blocky surface, and a talus apron (James and Varley, 2012; Hutchison et al., 2013; Zorn et al., 2019; Zorn et al., 2020a), but more complex morphologies include coulées (short lava flows) (Walter et al., 2013a), lobes (Wooster and Kaneko, 1998), and spines (Hornby et al., 2015; Zorn et al., 2020b). Consequently, lava domes are often described using morphological archetypes, namely Peléan (or spiny), platy, lobate, or axisymmetric domes as well as upheaved plugs (Blake, 1990; Fink and Griffiths, 1998; Husain et al., 2019), all associated with distinct growth conditions. Lava dome growth is further classified as endogenous (internal inflation) or exogenous (emplacement of new lava at the surface) (Fig. 1.1c, d) (e.g. Kaneko et al., 2002; Hale and Wadge, 2008). These growth styles and the explosivity of the dome are largely controlled by complex interactions of lava ascent and extrusion, outgassing, as well as cooling and solidification (Sparks, 1997; Melnik and Sparks, 1999; Sparks et al., 2000; Watts et al., 2002; Husain et al., 2014). The magma composition, temperature and viscosity are consequently important factors. Endogenous growth occurs by the gradual intrusion of magma into the dome edifice, causing the dome to inflate comparable to a balloon filling with air. While the inner

dome and the intruding magma are ductile, the outer dome parts exposed to the surface are commonly cooled and solidified, thus no longer ductile, and form a brittle carapace (Nakada et al., 1995). Continued inflation causes the carapace to stretch, resulting in the fracturing of the dome surface. Exogenous growth, on the other hand, simply occurs by lava extruding directly at the surface, which can be in the form of lobes, spines or lava flows (Watts et al., 2002; Shevchenko et al., 2015).

Lava domes pose a number of hazards stemming from their inherent instability with ongoing growth and the volatile nature of the degassing processes. Inefficient degassing and pressurisation may cause intermittent explosive activity as the gas permeability can quickly reduce due to pore and fracture closure from the partially viscous lava (Sparks, 1997; Gaunt et al., 2016) or pore blockage as a result of hydrothermal mineralisation (Horwell et al., 2013). Microlite crystallization due to degassing may also contribute to building fluid pressure in dome and shallow conduit environments (Sparks, 1997). This leads to cyclic explosive activity

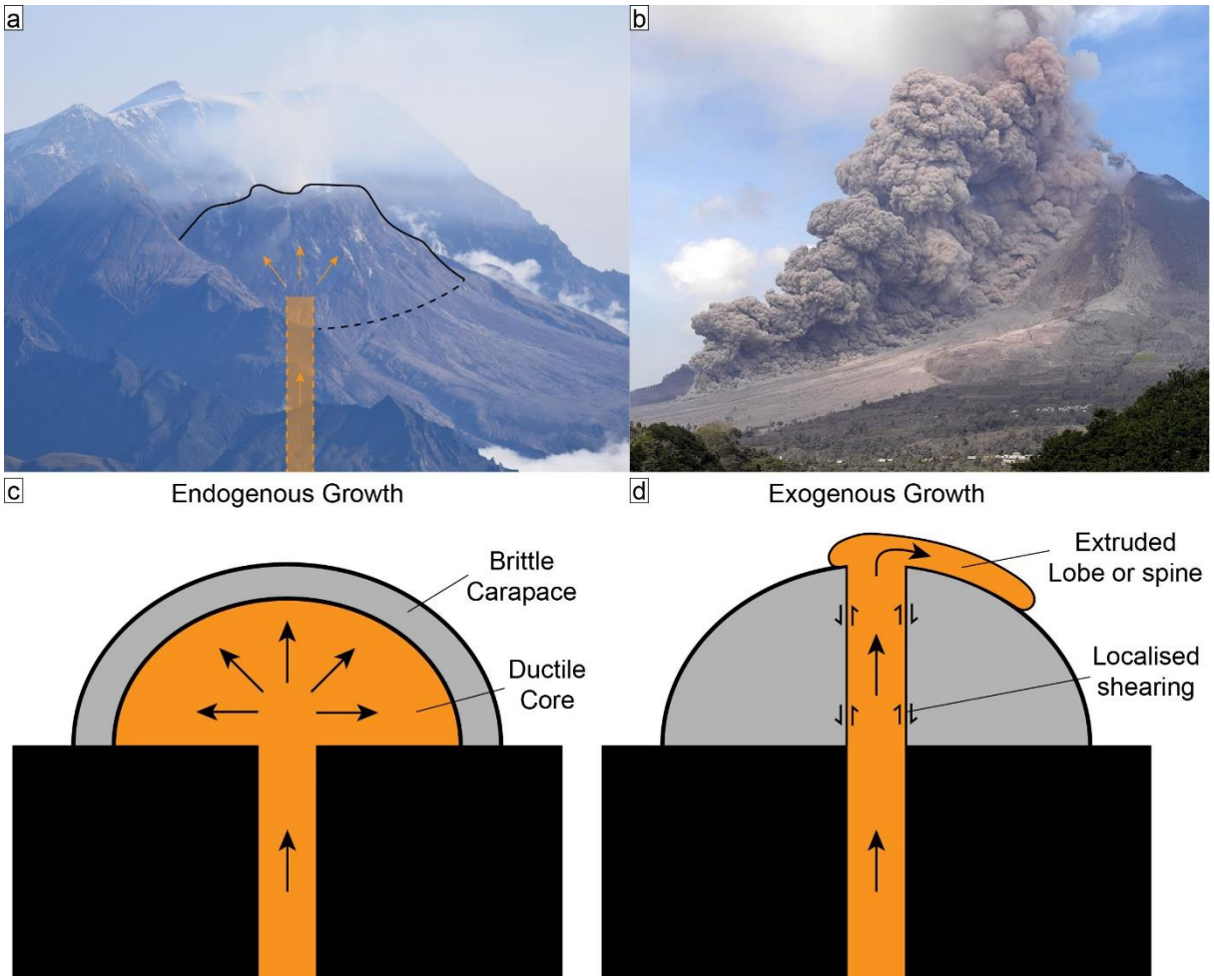

Figure 1.1: (a) Aerial image of the Shiveluch lava dome, Kamtchatka, in 2019 (own photo), (b) Photo of a PDC as a result of a lava dome collapse at Sinabung, Indonesia. The original image was taken by Marc Szlegat and is used with permission. (c) and (d) show a sketch of endogenous and exogenous growth styles. The sketches are modified after Hale and Wadge (2008).

commonly seen at many lava domes (e.g. Matthews et al., 1997; Voight et al., 1999) as gases repeatedly pressurise under the dome surface and eventually break through followed by a resealing of the open degassing pathways. Lava domes may also source pyroclastic density currents (PDCs) (Fig. 1.1b), which are the single deadliest volcanic hazards responsible for ~50% of all fatalities related to volcanic eruptions (Witham, 2005). These are fast-moving avalanches consisting of a chaotic mixture of heated (~800°C) rock fragments, ash, and gases forming from the (partial) collapse of a lava dome (Sato et al., 1992; Calder et al., 2002) – then also sometimes referred to as a block-and-ash flows (BAFs) (Schwarzkopf et al., 2005; Sarocchi et al., 2011) – or the collapse of an eruptive column (Sparks et al., 1978). High volumes and volatile contents make PDCs very mobile and especially hazardous as parts of the flow can escape channel confinements as surges and sweep over topography (Calder et al., 1999; Cronin et al., 2013). At lava domes such PDC-producing collapses are dominantly gravitational as parts of the dome oversteepen during growth, although pore pressurisation through inhibited escape of volcanic gases can facilitate partial dome failure as it decreases the tensile strength of the dome rocks (Sato et al., 1992; Voight and Elsworth, 2000). Large explosions or earthquakes can also trigger the collapse of unstable dome parts (Miller et al., 1998; Voight and Elsworth, 2000) and, in turn, sudden unloading of the conduit magma due a dome collapse can also trigger explosive activity (Druitt et al., 2002).

Analysing and monitoring the growth and instability of lava domes is often challenging and the scientific understanding can be advanced by observation with photogrammetric techniques combined with numerical and/or analogue modelling. This thesis links these methods and provides new insights on the growth processes, structures, and growth directions and what controls these factors.

1.3 Photogrammetric methods

The term photogrammetry generally refers to any measurement that can be done using photographs. Consequently, there are a wide range of methods and techniques suitable for scientific use in geology and volcanology. First studies utilized stereo-photography for efficient topographic mapping (Birdseye, 1940) and further sophistication of the techniques resulted in widespread use, not only limited to aerial surveys, but also ground and UAS-based imaging (Bemis et al., 2014). Some satellite systems are also suitable for photogrammetric processing such as IKONOS (Tao et al., 2004) or Pléiades (Stumpf et al., 2014). Most commonly, photogrammetric measurements are performed to generate topographic and surface models

(Matthews, 2008) as well as to gain geomorphological information (Chandler, 1999; Lane et al., 2000; Grosse et al., 2012).

For the purpose of monitoring dome building eruptions, such photogrammetric techniques have allowed to monitor growth and extrusion rates (Schilling et al., 2008; Diefenbach et al., 2013), perform morphological and structure mapping of the dome surface (James and Varley, 2012; Darmawan et al., 2018a), or assess the thermal structure (Thiele et al., 2017).

In this thesis, I use three main photogrammetric methods to create, visualise, and describe topographic models and DEMs to quantify surface changes and to measure ground motions. An overview is provided in the following paragraphs.

1.3.1 Structure-from-Motion

Currently, the most popular photogrammetric tool in geosciences is the Structure-from-Motion Multi-View-Stereo (SfM-MVS) workflow as many commonly used programs allow for the creation of high-quality topographic models, Digital Elevation Models (DEMs) and Orthophotos (Westoby et al., 2012). The workflow is also very flexible and permits the use and even combination of a wide range of photo and camera types, while also being nearly fully automated.

The basic principle is the detection and triangulation of the same recognisable points in a series of sequential photographs, e.g. an aerial survey of a volcanic crater. With sufficient overlap between images, many ground features such as rocks or cliffs can be detected on several images with different viewing angles. This allows for the triangulation of both camera positions and ground features in a 3D space and an initial selection of features is subsequently saved as key-points, creating an initial "sparse" point model. By systematically going over all detectable features a full "dense" 3D point cloud is created, which can be further processed into a traditional DEM, Orthophotos, textured models, and object files (e.g. for 3D printing).

In order to create a successful 3D model using SfM-MVS in volcanic environments, specifically lava domes, several factors need to be considered. If done correctly, the full topography of the survey area can be recreated with cm-scale accuracy (Fig. 1.2). Ideal are contrast-rich images with 60-90% overlap, which facilitate the automatic detection of ground features (James et al., 2020). On the other hand, contrast-poor surfaces such as snow and water, moving features such as trees and lighting artefacts as well as shadows can hinder detection or produce errors and misplaced points. The image acquisition strategy can also play a significant role; aerial data at volcanoes is commonly obtained either by helicopter or airplane, which commonly fly a circle around the area of interest with the camera looking down at an oblique angle, or by Unoccupied

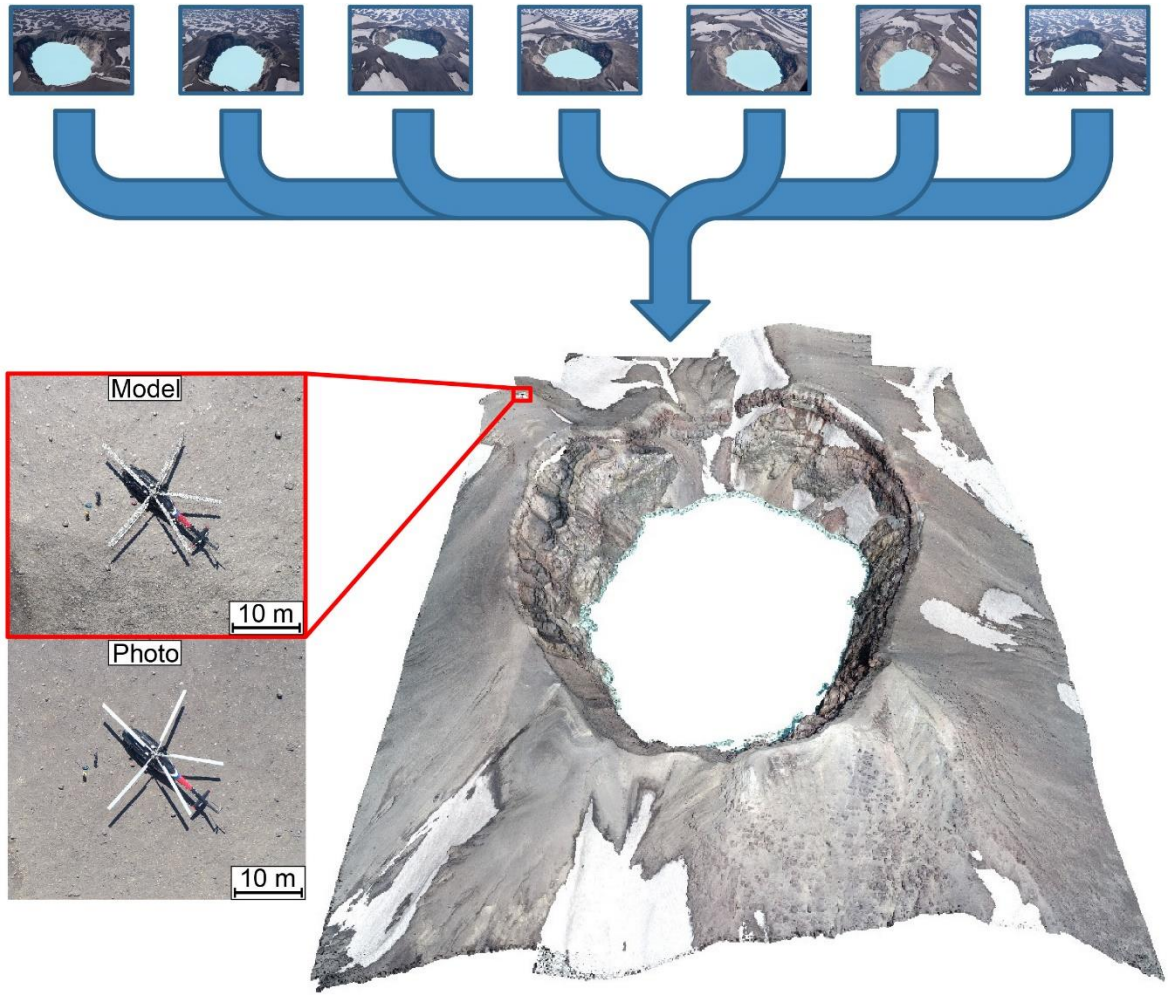

Figure 1.2: Illustration of the SfM-workflow. Aerial images from different angles are used to calculate a full-scale 3D topography model. A comparison of the model and a photo highlights the potential quality and resolution of the method (own data). The contrast-poor surface of the crater lake cannot be reconstructed.

Aircraft Systems (UAS or drone), which can fly a "lawnmower" pattern (Fig. 5.6) with the camera looking straight down (nadir). Nadir acquisitions generally produce better results with less processing time, likely due to excessive overlap of the oblique view because the same features are visible in more individual images. However, processing nadir images in steep terrain can be challenging as vertical features are less easily resolved. Here, the best results are achieved with nadir acquisitions and a few additional oblique images, which can enhance the view perspectives and prevent systematic errors (James and Robson, 2014; Nesbit and Hugenholtz, 2019).

An inherent advantage of this method is that it works regardless of known camera or ground feature positions. However, this results in a model that is initially unscaled and in order to create DEMs or orthophotos they must be georeferenced. Although the GNSS-tagging of photos made by UAS can assist with the initial orientation, their accuracy is usually unsuitable for scientific purposes (with the exception of RTK-GNSS capable models). Instead, georeferencing can be

achieved with ground control points that can be placed on the photos or models, or by connecting the models to existing DEMs.

For this thesis, SfM-data is used to provide highly detailed topography and morphology data and to highlight changes occurring between acquisitions. It further serves as a basis for numerical models incorporating local topography.

1.3.2 Stereo-photogrammetry

Stereo-photogrammetry is considered a more classical photogrammetric approach. It uses the same feature triangulation principles as SfM to reconstruct topography data, but with only few survey images that form individual stereopairs. Typical acquisitions are performed in strips or block patterns to cover the target area with high accuracy. A minimum of two images is required, but multiple pairings can be processed. Consequently, the image quality is typically very high and the exact camera calibration parameters and positions must be known prior to processing. The images also need to have complete overlap for the areas that are modelled. First, the internal image orientations are calibrated using the camera calibration parameters, then the image pairs are orientated relative to each other by picking a large number of recognizable tie points across all image pairs, which can be done automatically but commonly required manual input. The geoposition is either assigned by marking known ground control points or (if the information is available) calibrated from camera metadata. The ground topography is then calculated into stereomodels using automated point triangulation, with multiple stereomodels being merged before a final point-cloud is created.

For measuring volcanoes, this workflow is commonly applied to very high-quality image pairs of survey flights (Schilling et al., 2008; Dvigalo et al., 2013) or satellite images such as Pléiades (Bagnardi et al., 2016), mostly used to asses volume changes, extrusion rates or to assess morphologies. Here, such data is primarily used to contextualize our data with topographic data and to provide georeferencing for the more detailed SfM-data.

1.3.3 Particle-Image-Velocimetry

Particle-Image-Velocimetry (PIV) is a specialised image correlation technique that allows for a vector-based tracking of detectable features (particles). Such methods are commonly used to track changes in fluid systems occurring on a sequence of co-registered images (i.e. timelapse). PIV enables the calculation of the full displacement field between images and extracts particle motion directions and magnitudes (Fig 1.3) as well as relative motion metrics such as strain or

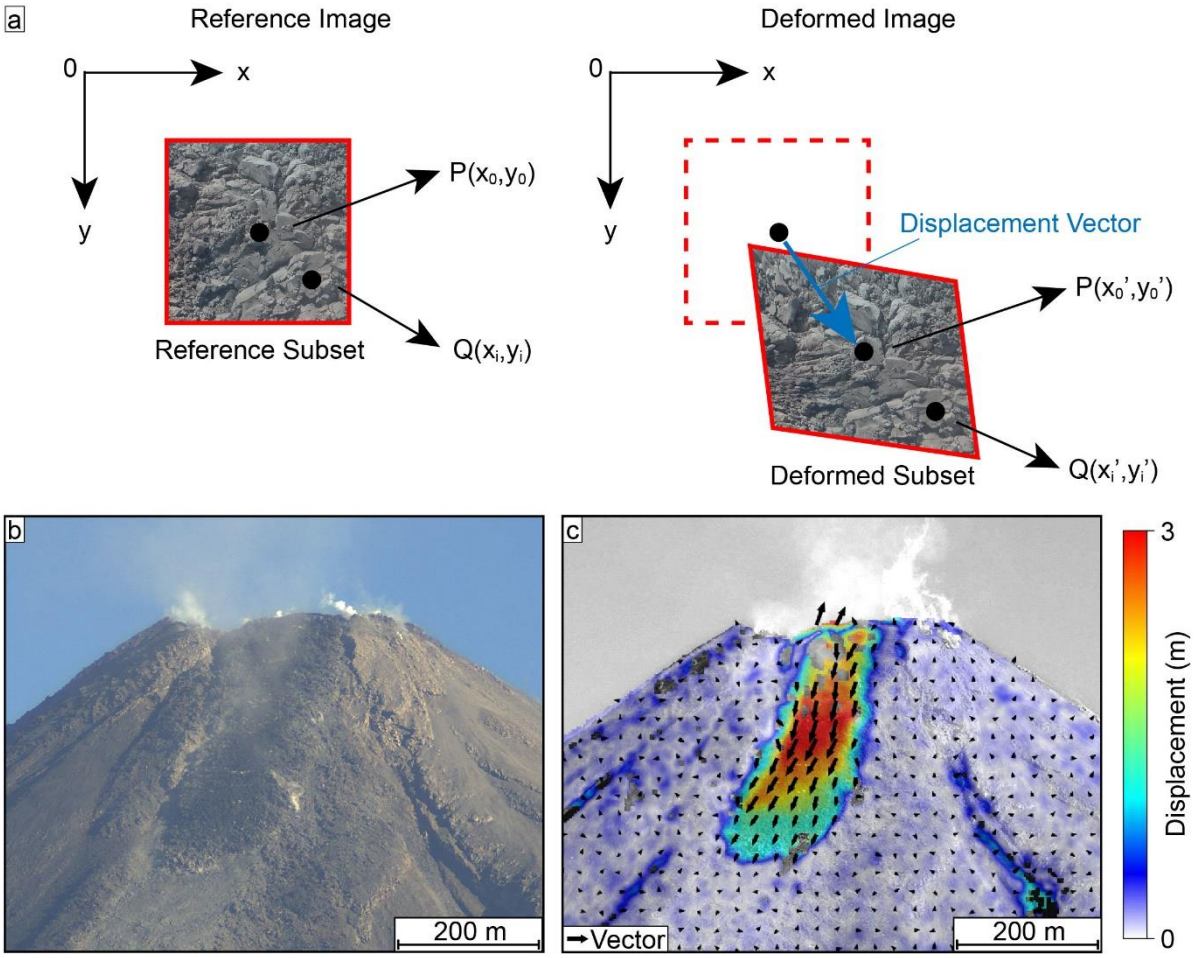

Figure 1.3: Illustration of the PIV workflow. (a) shows the concept of measuring motions in a 2D plane. The sketch is modified after Pan et al. (2009). (b) and (c) show and example from the top of Volcán de Colima with the original view and the calculated displacement field (own data).

particle divergence. It employs square search windows (or sub-regions) that detect features and patterns and incrementally move over a sequence of two images. To increase the detectable amount of moving particles and the robustness of the measurements, these windows are often used multiple times with decreasing sizes (Adrian, 1991).

PIV and the similar Digital Image Correlation (DIC) methods have been used in several studies at lava domes to track their growth speed and direction (Walter et al., 2013b; Walter et al., 2013a; Salzer et al., 2016) to detect short-term inflation and deflation motions associated with explosions (Johnson et al., 2008), and to measure strain metrics (Walter, 2011). In this thesis, PIV is primarily used to track motions and strain on a lava dome surface and visualise the associated structures.

1.4 Modelling approaches

Natural lava dome extrusions are inherently complex and incorporate a large number of unknown and often interacting factors and influences that can prevent a full understanding of the active processes. Due to this, constructing artificial lava dome models can be invaluable to separate such factors as it allows for the observation of the dome growth processes under simplified and controlled conditions, thus enabling researchers to target specific aspects of lava dome growth and to potentially predict their behaviour. Modelling methods are generally separated into two types, with numerical modelling on the one hand, simulating lava dome extrusions with computational algorithms, and analogue modelling on the other hand, investigating dome extrusions using laboratory-based experiments.

The study of numerical lava domes with computer models has seen a broad range of approaches and is typically constrained by mathematical, physical, or chemical laws and processes. Numerical lava dome extrusions can be used to explore the dynamic and quasi-static nature of lava rheology (Iverson, 1990; Hale and Wadge, 2003; Lavallée et al., 2007), the evolution of these domes (Bourgouin et al., 2007), and their relation to cooling, degassing, and pressurisation of the dome (Sparks, 1997). The conditions for seismogenic faulting through stick-slip behaviour and strain localisation of dome lavas have also been constrained (Iverson et al., 2006). Similarly, the effects of dynamically changing lava rheology (Hale and Wadge, 2008; Husain et al., 2019) and extrusion rates (Husain et al., 2014) were modelled to impact the growth style and morphology of the extruding domes, which compares well to real cases of dome growth, further incorporating a viscous core, a brittle carapace, and a clastic talus apron (Hale et al., 2009b; Hale et al., 2009a; Husain et al., 2018). Recent models have also incorporated the impacts of different crater morphologies on the dome extrusion and further assessed the stability of the modelled domes (Harnett et al., 2018). These models are further capable of constraining and visualizing high strain regions within the dome and predict the development of structures such as shear bands (Harnett et al., 2018). External factors such as hydrothermal weakening of lava dome rocks have also been shown to potentially affect the long-term stability after extrusions ceased (Ball et al., 2015).

Analogue lava dome models are artificial recreations of extrusions in the laboratory, creating and/or using conditions and materials that are comparable (analogue) to the natural processes. Naturally, there is a wide variety of approaches that can highlight various aspects of lava dome growth using granular, brittle, or viscous analogue materials. As with the numerical models, dynamic rheology changes through cooling and the impact on the dome extrusion and morphology has been studied in detail (Blake, 1990; Griffiths and Fink, 1993; Fink and

Griffiths, 1998). Evolving dome morphologies for Bingham fluids could further be used to identify and predict yield strengths within domes that were extruded on horizontal (Blake, 1990) and inclined (Lyman et al., 2004) surfaces. The inner motions and structures of lava domes have been investigated by recreating deformation and internal strain patterns using viscous material (Buisson and Merle, 2002) and by simulating repeated intrusions of lobes, building complex dome structures (Závada et al., 2009). Similarly, inner dome structures could be generated in brittle analogue material (Acocella et al., 2001; Brothelande and Merle, 2015), developing discrete fault architectures. Dynamic gas escape and conduit margin shearing could be recreated by artificial conduit fracturing during induced pressure cycles (Lane et al., 2008) and flank instability due to lava intrusion was also studied by intruding viscous fluids into an artificial volcanic edifice (Rincón et al., 2018).

In the studies for this thesis, both numerical modelling (finite element) and analogue modelling are employed to further our understanding of specific controls that impact lava dome growth, including surface loading, lava properties, and structural architecture.

1.5 Aims and organisation of this thesis

The general objective of this thesis is to apply a number of photogrammetric approaches to gain insights on the extrusion of lava domes and improve our understanding of the involved processes with suitable models. More specifically, the following research questions will be addressed here:

- *Which factors control the style and direction of lava dome growth and how can they change the growth behaviour?*
- *On which timescales does deformation occur on lava domes and can these be related to the current activity?*
- *What is the structural architecture of growing lava domes and how does it affect the deformation patterns of the dome?*
- *How can photogrammetric monitoring and/or modelling assist in the identification and study of hazards posed by lava domes?*

To answer these questions, photogrammetric monitoring provides key advantages because dome growth can be measured on various spatial and temporal scales. Especially the unprecedented accuracy and details at which active processes can be captured and understood offer ideal tools for geoscientific analyses. Imaging by UAS, airplane, helicopter, or ground-based cameras further represents a relatively safe method to observe hazardous processes and

can be easily integrated into other observational data or enhance existing datasets, e.g. from satellite or seismic data.

Due to the many-faceted types of activities that lava domes can display, the main research is conducted at distinct and different settings. Dome growth is observed both at natural sites at Volcán de Colima (Mexico), representing a system with drastic morphological changes and repeated instances of dome growth and collapse, and Santiaguito (Guatemala), representing a long-lived extrusion system with persistent and stable dome growth activity. I further consider modelling approaches to focus on specific growth processes, employing both numerical and analogue dome models to assess the growth behaviour under controlled conditions and understand the impact of individual factors on the growing dome.

In accordance with the thesis aims, the work is presented in research chapters based on peer-reviewed publications, some minor modifications were made to account for the different formatting. The first three studies (chapters 2, 3, 4) are my first author publications and represent the main research chapters of this thesis, showcasing different advancements in lava dome research. Chapter 5 then summarizes my contributions to other publications and Chapter 6 provides a summary and contextualization of the outcomes. Further details are outlined here:

Chapter 2: Load Stress Controls on Directional Lava Dome Growth at Volcán de Colima, Mexico

This paper explores the first research question and examines directionalities of lava dome growth. To achieve this, the potential of SfM photogrammetry is used to create a time-series of observational data at Volcán de Colima and to summarize the eruptive sequence in high detail. Lava dome morphologies and growth are described and measured, then integrated with seismic and satellite radar data to create a comprehensive understanding of the growth sequence over three years. Finally, the SfM data is used to create a numerical model to delineate a shift of extrusion directions in response to surface loading due to repeated lava dome emplacements and collapses. The results also address the final research question and showcase how this type of monitoring and analyses can be used to evaluate changing PDC hazards as these are inherently tied to the growth direction of lava domes.

Author contributions:

Edgar Zorn is the leading author of the study and is responsible for the bulk of the work. This includes the conceptualizing, writing, and editing of the manuscript as well as handling the

peer-review and publishing process. This also involves the analyses of all photogrammetric data and the creation of the figures.

The co-authors contributed as follows: Nicolas LeCorvec conceptualized and generated the numerical models with the data input based on the photogrammetric data processed by Edgar Zorn. Jacqueline Salzer processed the radar data and provided some overflight photos for photogrammetric analyses. Nick Varley provided additional thermal and photogrammetric data and added valuable insight into eruptive processed from local observations. Thomas Walter initiated and supervised the study and added relevant scientific input. Carlos Navarro-Ochoa and Rául Arámbula provided nearly all photos from the overflight surveys for photogrammetric analyses and added valuable local information and logistics. Dulce Vargas-Bracamontes provided and processed all seismic data and contributed to the construction of the eruptive timeline. Samuel Thiele contributed with observations from optical and thermal data, providing highly valuable insight into the eruptive processes and morphological and structural features. All authors contributed to the writing and editing of the manuscript.

This chapter and the corresponding supplementary material have been published in *Frontiers in Earth Sciences* and are freely accessible:

Zorn, E.U., Le Corvec, N., Varley, N.R., Salzer, J.T., Walter, T.R., Navarro-Ochoa, C., Vargas-Bracamontes, D.M., Thiele, S.T. and Arámbula Mendoza, R. (2019). Load Stress Controls on Directional Lava Dome Growth at Volcán de Colima, Mexico. Frontiers in Earth Science, 7(84). DOI: 10.3389/feart.2019.00084

Chapter 3: UAS-based tracking of the Santiaguito Lava Dome, Guatemala

In this chapter the second research question is addressed by measuring different timescales of deformation and identifying the correlating type of activity. SfM and PIV photogrammetry are combined to create highly detailed data on the surface motions of the Santiaguito lava dome. Topographic models and orthophotos are used to detect dome growth and structures on the dome surface as well as to measure the flow velocity and channel dimensions of a small lava flow. As with the last paper, this study also contributes to the hazard assessment at lava domes and, thus, the final research question. The deformation data is used to infer the viscosity of the lava, which is (among others) a major factor representing the hazard state of a lava dome. It is also obtained using purely remote sensing data from UAS imaging, presenting a very safe method to gain such important data.

Author contributions:
Edgar Zorn is the leading author of the study and is responsible for the bulk of the work. This includes the conceptualizing, writing, and editing of the manuscript as well as handling the peer-review and publishing process. This also involves the acquisition and processing of all UAS data in the field and the photogrammetric analyses as well as the creation of the figures.
The co-authors contributed as follows: Thomas Walter supervised the study and added relevant scientific input. Jeffrey Johnson provided and processed the ground-based camera data from 2007, 2009, and 2012. René Mania processed the reference DEM from the Pléiades satellite. All authors contributed to the writing and editing of the manuscript.

This chapter and the corresponding supplementary material have been published in *Scientific Reports* and are freely accessible:
Zorn, E.U., Walter, T.R., Johnson, J.B., Mania, R. (2020). UAS-based tracking of the Santiaguito Lava Dome, Guatemala. Scientific Reports 10(1). DOI: 10.1038/s41598-020-65386-2

A data publication containing the processed files used in this chapter is also freely available via the *GFZ Data Services* and is included in Appendix A:
Zorn, E.U., Walter, T.R., Johnson, J.B., Mania, R. (2020). High-resolution photogrammetry data of the Santiaguito lava dome collected by UAS surveys. GFZ Data Services. DOI: 10.5880/GFZ.2.1.2020.001

Chapter 4: Insights into lava dome and spine extrusion using analogue sandbox experiments
This chapter seeks to address the third research question and unravels the structural architecture of lava domes and how they impact deformation of the dome. The study recreates natural lava dome extrusion as analogue models in laboratory experiments. Mixtures of sand and plaster powder are used to create domes with different material properties and morphologies (such as spines) and PIV is employed to monitor dome growth, measure deformation, and visualise structures. The results provide new insights on many features that were previously observed or suggested at natural domes and other models while also adding to the growing body of rock mechanics research at lava domes. Here too, the final research question is addressed as the study

identifies dome areas prone to collapse based on their relative deformation rate, potentially implying similar processes could govern collapse hazards at natural volcanoes.

Author contributions:
Edgar Zorn is the leading author of the study and is responsible for the bulk of the work. This includes the conceptualizing, writing, and editing of the manuscript as well as handling the peer-review and publishing process. This also involves the conducting of all experiments, the acquisition of almost all data and the analyses as well as the creation of the figures.
The co-authors contributed as follows: Thomas Walter initiated the experiments and supervised the study. Michael Heap designed the uniaxial compression experiments, which were performed by Michael Heap and Edgar Zorn. Ulrich Kueppers provided assistance with the data interpretation. All authors contributed to the writing and editing of the manuscript.

This chapter and the corresponding supplementary material have been published in *Earth and Planetary Science Letters*:
Zorn, E. U., Walter, T. R., Heap, M. J., & Kueppers, U. (2020). Insights into lava dome and spine extrusion using analogue sandbox experiments. Earth and Planetary Science Letters, 551, 116571. DOI: 10.1016/j.epsl.2020.116571

Chapter 5: Further contributions
The two excerpts shown in this chapter highlight my contributions to lava dome and photogrammetric research in other papers as a co-author. Here I mainly contributed to the writing and editing of the manuscripts. The first is sourced from Walter et al. (2019b), where I assisted with the interpretation of dome rock and yield strength. The second is sourced from James et al. (2020), a review paper summarizing recent advancements in the use of UAS for volcanological applications. Here I additionally provided data and images that I processed for fig. 5.7. The authors list in this publication is sorted alphabetically and not by the relative amount of work.

The excerpts in this chapter are sourced from individual publications, and only include the parts relevant for this thesis. The full papers have been published in peer-reviewed journals and are freely accessible.

Chapter 5.1:

Walter, T. R., Harnett, C. E., Varley, N., Bracamontes, D. V., Salzer, J., Zorn, E. U., Bretón, M., Arámbula, R., Thomas, M. E. (2019). Imaging the 2013 explosive crater excavation and new dome formation at Volcán de Colima with TerraSAR-X, time-lapse cameras and modelling. Journal of Volcanology and Geothermal Research, 369. 224-237. DOI: 10.1016/j.jvolgeores.2018.11.016

Chapter 5.2:

James, M. R., Carr, B., D'Arcy, F., Diefenbach, A., Dietterich, H., Fornaciai, A., Lev, E., Liu, E., Pieri, D., Rodgers, M., Smets, B., Terada, A., von Aulock, F., Walter, T., Wood, K. and Zorn, E.U. (2020). Volcanological applications of unoccupied aircraft systems (UAS): Developments, strategies, and future challenges, Volcanica, 3(1). 67-114. DOI: 10.30909/vol.03.01.67114

Chapter 2:

Load stress controls on directional lava dome growth at Volcán de Colima, Mexico

Edgar U. Zorn[1,2], Nicolas Le Corvec[1], Jacqueline T. Salzer[1], Nick R. Varley[3], Thomas R. Walter[1], Carlos Navarro-Ochoa[4], Dulce M. Vargas-Bracamontes[5], Samuel T. Thiele[6], Raúl Arámbula Mendoza[4]

[1]German Research Centre for Geosciences GFZ, Potsdam, Germany

[2]Institute of Geosciences, University of Potsdam, Potsdam, Germany

[3]Colima Intercambio e Investigación en Vulcanología, Universidad de Colima, Colima, Mexico

[4]Centro Universitario de Estudios e Investigaciones Vulcanológia, Universidad de Colima, Colima, Mexico

[5]CONACYT-CUEIV, Universidad de Colima, Colima, Mexico

[6]School of Earth, Atmosphere and Environment, Monash University, Clayton, Australia

Abstract

During eruptive activity of andesitic stratovolcanoes, the extrusion of lava domes, their collapse and intermittent explosions are common volcanic hazards. Many lava domes grow in a preferred direction, in turn affecting the direction of lava flows and pyroclastic density currents. Access to active lava domes is difficult and hazardous, so detailed data characterizing lava dome growth are typically limited, keeping the processes controlling the directionality of extrusions unclear. Here, we combine TerraSAR-X satellite radar observations with high-resolution airborne photogrammetry to assess morphological changes, and perform finite element modelling to investigate the impact of loading stress on shallow magma ascent directions associated with lava dome extrusion and crater formation at Volcán de Colima, México. The TerraSAR-X data, acquired in ~1-m resolution spotlight mode, enable us to derive a chronology of the eruptive processes from intensity-based time-lapse observations of the general crater and dome evolution. The satellite images are complemented by close-range airborne photos, processed by the Structure-from-Motion workflow. This allows the derivation of high-resolution digital elevation models, providing insight into detailed loading and unloading features. During the observation period from Jan-2013 to Feb-2016, we identify a dominantly W-directed dome growth and lava flow production until Jan-2015. In Feb-2015, following the

removal of the active summit dome, the surface crater widened and elongated along a NE-SW axis. Later in May-2015, a new dome grew toward the SW of the crater while a separate vent developed in the NE of the crater, reflecting a change in the direction of magma ascent and possible conduit bifurcation. Finite element models show a significant stress change in agreement with the observed magma ascent direction changes in response to the changing surface loads, both for loading (dome growth) and unloading (crater forming excavation) cases. These results allow insight into shallow dome growth dynamics and the migration of magma ascent in response to changing volcano summit morphology. They further highlight the importance of detailed volcano summit morphology surveillance, as changes in direction or location of dome extrusion may have major implications regarding the directions of potential volcanic hazards, such as pyroclastic density currents generated by dome collapse.

2.1 Introduction

The growth of lava domes is a common volcanic phenomenon, being recorded at over 120 volcanoes worldwide (Ogburn et al., 2015), with many varying growth styles. Understanding the growth of lava domes at stratovolcanoes is one of the most important tasks in volcanology as domes can pose a severe threat to human lives and infrastructure. The collapse of a lava dome can produce destructive pyroclastic density currents (PDCs), a hazard responsible for many volcano-related deaths (Witham, 2005). One of the most prominent examples of the destructive potential of a lava dome occurred in 1902 with the sudden collapse of the Mount Pelee, Martinique, lava dome. This resulted in a PDC that destroyed the nearby town St. Pierre, causing ~28,000 deaths within a few minutes (Tanguy, 1994). More recently, during the 2010 eruption of Merapi, Indonesia, PDCs resulting from dome collapse extended for >15 km from the summit, leading to the evacuation of a third of a million of people (Surono et al., 2012; Cronin et al., 2013). Lava domes that are emplaced on slopes or grow by oblique extrusion are especially prone to gravitational collapse due to potential oversteepening (Voight, 2000), so a clear understanding of the dome growth dynamics is highly important.

Inclined or directional dome growth as well as extrusion from multiple vents are commonly observed at many volcanoes producing very viscous lava domes. Dome growth at Soufrière Hills, Montserrat, between 1995 and 1998 produced several oblique spines in different directions (Watts et al., 2002). Similar observations were made during the 2004–2006 dome extrusion of Mount St. Helens, USA, which also produced directional spines likely originating from the same vent (Vallance et al., 2008), episodically extruding, spreading and sliding laterally (Walter, 2011; Salzer et al., 2016). At Chaiten, Chile, such spines eventually collapsed

in 2008 and produced far reaching PDCs (Pallister et al., 2013a). At Merapi, Indonesia, a clear lava dome growth directionality was identified toward the populated southern slopes years before the 2010 eruption (Walter et al., 2013a).

While it is clear that lava domes regularly display directional or oblique growth patterns, the reasons and mechanisms behind the growth asymmetry are still poorly understood. Emplacement on an inclined slope and a complex morphology of the lava dome or crater can result in a preferred growth direction (Harnett et al., 2018). Based on numerical modelling and observations at Soufrière Hills, Montserrat (Husain et al., 2014), another proposed mechanism is the change of dome extrusion direction after plugging of ascent pathways and the pileup of extruded lava. The resulting transition from endogenous to exogenous growth and the establishment of new shear zones causes further spine extrusions to be deflected in other directions (Hale and Wadge, 2008). Similarly, the occurrence of multiple vent extrusions at Volcán de Colima has been attributed to a dense plug which deflects magma ascent around it (Lavallée et al., 2012). Furthermore, the growth of lava domes and their directionality might be largely controlled by shear bands and slip behaviour at the conduit walls (Hale and Wadge, 2008). Pre-existing morphology can also direct dome growth through channelling (Walter et al., 2013a). Therefore, these previous studies suggest that shallow extrusion processes at the conduit and the local morphology play an important role in establishing directional lava dome growth. Here, we contribute to this discussion by providing new and detailed geomorphological data from Volcán de Colima. Our analysis of aerial photogrammetry suggests a relationship between morphology change and the directionality of dome growth. To investigate this observed relationship, we perform numerical modelling on the influence of local stress changes in response to loading and unloading associated with dome growth and crater formation. We further propose stress changes as a principal mechanism to explain the developments of new vents and directional dome extrusion.

2.1.1 Lava dome monitoring

While dome building volcanoes can be well monitored by traditional seismic and geodetic techniques, domes at steep sided volcanoes are often hazardous to approach and are therefore monitored by remote sensing. Studies increasingly utilize Synthetic Aperture Radar (SAR) as a tool independent of cloud cover to assess the topography, structure, and deformation of volcanoes. Most studies analyse either the reflected amplitude or perform interferometric processing of the signal phase values. Interferometric SAR (InSAR) measures the phase difference between satellite radar acquisitions, but resolving the growth of lava domes remains

challenging as the phase images require good correlation between acquisitions (Walter et al., 2015). Thus, most InSAR studies focus on crustal deformation affecting the flanks of dome-growing volcanoes (Salzer et al., 2014; Welch and Schmidt, 2017). Lava dome cooling and subsidence (Salzer et al., 2017) and cracks splitting a lava dome have also been detected (Walter et al., 2015). For monitoring lava domes, the analysis of the SAR amplitude is particularly valuable as it can be used to document and quantify lava dome growth e.g., at Merapi and Sinabung, Indonesia (Pallister et al., 2013b; Pallister et al., 2018) and Mount Cleveland, Alaska (Wang et al., 2015). SAR data also allow the construction of DEMs, which provide a detailed quantification of volume changes at growing lava domes (Kubanek et al., 2015).

In addition to radar monitoring, aerial photogrammetric surface reconstructions have become a widespread tool in geosciences (Bemis et al., 2014), especially as the development of the Structure-from-Motion Multi-View Stereo (SfM-MVS) workflow has allowed the reconstruction of a three dimensional point cloud and digital terrain modelling based on oblique and nadir photogrammetric data (Westoby et al., 2012). At dome building volcanoes, these photogrammetrically built models can be used to identify detailed features of the dome surface (Darmawan et al., 2018a), monitor growth and extrusion rates (Diefenbach et al., 2012; Diefenbach et al., 2013) and characterize interaction of lava domes with snow (Walder et al., 2007). A comparison of sequential models can also allow the estimation of volume changes from ground movement, dome collapse (Herd et al., 2005), lava flow/PDC emplacement (Dai and Howat, 2017; Pedersen et al., 2018), or the study of secondary volcano hazards such as lahars (Gomez et al., 2018; Walter et al., 2018). In this paper, we combine both SAR and SfM-MVS photogrammetry to investigate the oblique dome growth processes at one of the most active volcanoes in Central America.

2.1.2 Regional background

Volcán de Colima (or sometimes referred to as Fuego de Colima) is an andesitic stratovolcano located in western Mexico (Fig. 2.1) as part of the Trans-Mexican Volcanic Belt. The volcano is situated within a 5 km wide collapse scar, which is open to the south and originated from a large flank-collapse, likely older than 23 ka (Roverato et al., 2011). Its recent activity has been dominated by lava dome growth and intermittent Vulcanian explosions originating at the summit crater with several instances of effusion that were recorded between 1998 and 2010 (Varley et al., 2010), and lasted until 2011. Following quiescence from 2011 to 2012, a short inflation heralded a new dome-growing phase in January 2013 (Salzer et al., 2014; Walter et al., 2019b) and transitioned to explosive activity in 2015. The July 2015 eruption marked the

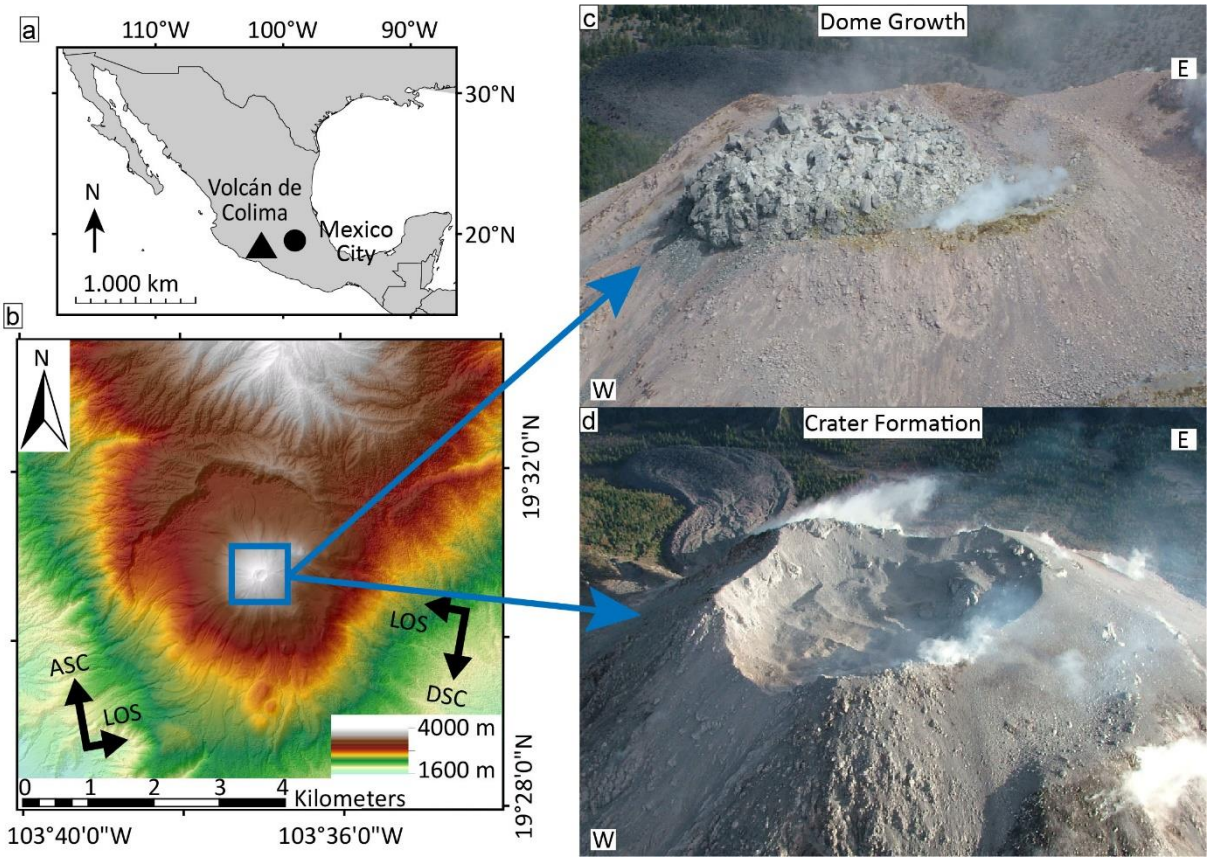

Figure 2.1: The map shows the location (a) and the local topography (b) of Volcán de Colima. The SAR acquisition geometry with Line of Sight (LOS) for the ascending (ASC) and descending (DSC) orbits are also indicated. The two photos highlight the dynamic morphological changes occurring at the summit of andesitic stratovolcanoes. These involve (c) repeated cycles of dome growth (photo from 13.03.2013), and (d) destruction by the collapse of the dome or explosive excavation, forming a crater (photo from 25.03.2015).

most hazardous event in over a century (Reyes-Dávila et al., 2016). It featured two major dome collapses and produced PDCs extending for more than 10 km (Reyes-Dávila et al., 2016; Capra et al., 2018). The eruption caused strong morphologic changes, as it left an amphitheater-shaped scar at the summit, which is breached to the south. Moderate activity, including vulcanian explosions, dome growth, and lava flow effusion continued until February 2017, when the most recent active period terminated. In this work we further elucidate the 2013–2016 activity and quantify the large morphology changes associated with summit growth and destruction.

The activity of Volcán de Colima shows a ~100-year cycle, characterized by lava flow effusion, dome growth and moderate explosions, with an intensification in activity before culminating in a large sub-plinian to plinian eruption (Luhr and Carmichael, 1980; González et al., 2002; Luhr, 2002). The last large eruptions occurred in 1818 (Macías et al., 2017) and 1913 (Saucedo et al., 2010; Massaro et al., 2018), making close monitoring of the volcano an important topic due to the possibility of a plinian eruption in the near future. Therefore, many recent studies are aimed

at monitoring and understanding the dynamics of volcano deformation. Small-scale deformation has been observed with interferometrically processed TerraSAR-X (TSX) data (Salzer et al., 2014; Salzer et al., 2017), identifying shallow pressurization and suggesting the existence of a dense plug and a complex conduit system at shallow depth. At the surface, morphological and volumetric observations of the lava dome at Volcán de Colima have previously been studied based on airborne LiDAR in 5 m resolution (Davila et al., 2007) and TanDEM-X satellites in an approximate 10 m resolution (Kubanek et al., 2014). However, these rather rare datasets could hardly be used for year-long monitoring and were only realized for

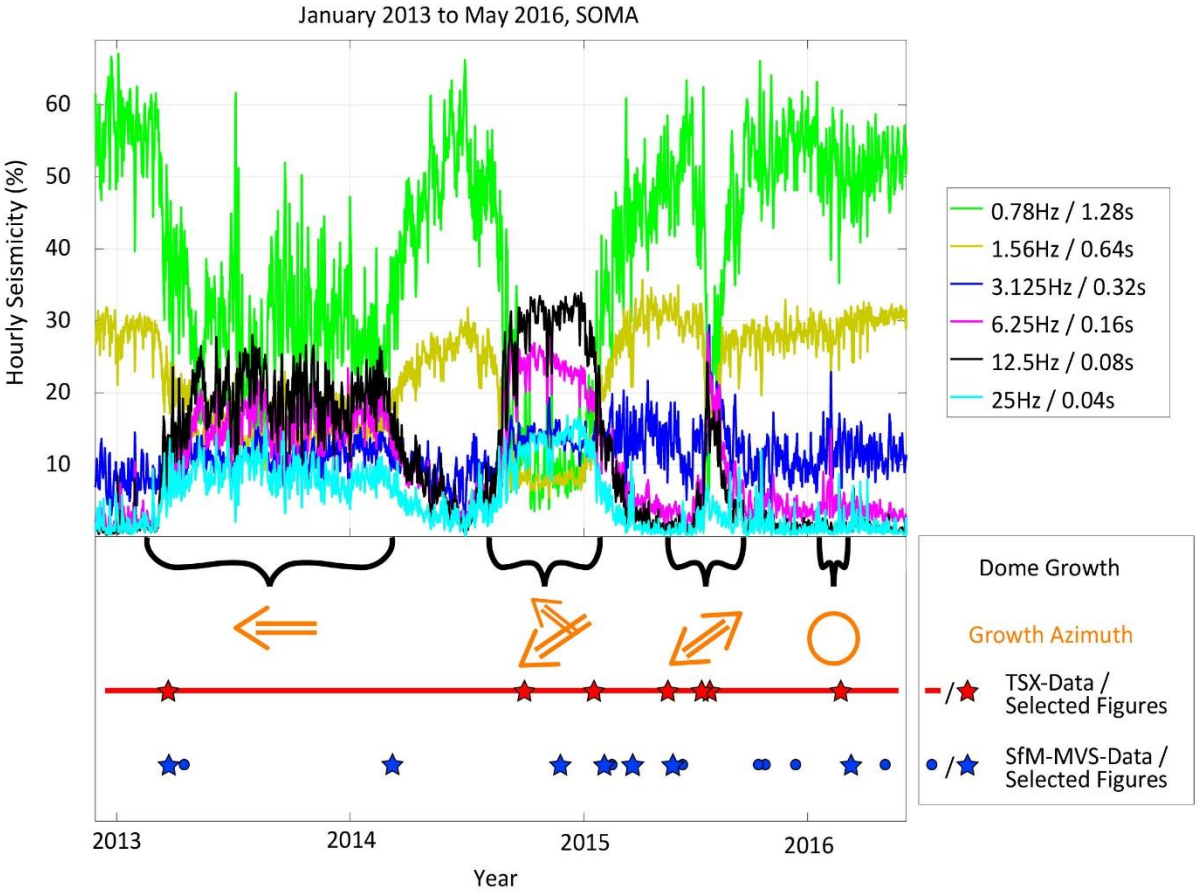

Figure 2.2: Overview of the seismic activity of Volcán de Colima during the study period characterized by the decomposed frequency content of the seismic signal. The seismicity is presented as the rate of normalized seismic energy per hour at scales of 2^j samples (Vargas-Bracamontes et al., 2009), the associated frequencies are indicated at the top-right corner of the figure. While in a dome-growing stage, the seismicity is dominantly characterized by high-frequencies due to regular rockfalls. During an explosive stage, lower frequencies dominate, indicating the explosive activity from a pressurized conduit. The bottom of the plot shows a timeline of the multiple dome growth phases as well as the growth directions. The main azimuth shown is based on the direction of advancing lava flows/lobes originating from the dome. The last growth phase had no clear growth direction and is indicated with a circle. The TSX/SfM data used for the study are also included. Stars indicate that the data are shown in figs. 2.4 and 2.5, respectively.

distinct years and eruptive episodes. The SfM-MVS workflow has also been used to model the summit dome and crater from both optical (James and Varley, 2012) and thermal (Thiele et al., 2017) surveys, allowing morphologic studies each time an overflight is realized.

2.2 Data and methodology

Volcán de Colima has a continuous seismic monitoring network (Arámbula-Mendoza et al., 2018). To obtain an overview of the volcanic activity in the observation period from Jan 2013 to Feb 2016, we employed the records from the seismic station closest to the investigated dome. For this, data from the vertical component of the broadband Guralp CMG-6TD seismic station SOMA, located on the NW flank at 1.7 km from the summit, were decomposed and normalized employing the discrete wavelet transform (DWT). A 0.5 Hz high-pass filter was applied to reduce microseismic noise. This type of signal decomposition has been previously used at Volcán de Colima observatory (Vargas-Bracamontes et al., 2009) and, similar to previous seismic studies at Volcán de Colima (Lamb et al., 2014), allows for the identification of dome growth phases as these are associated with characteristic frequency distributions (Fig. 2.2). Phases of dome growth, collapse, and crater formation were further investigated in remote sensing data as described below.

2.2.1 High-resolution satellite radar observations

We processed amplitude SAR data from the German TerraSAR-X satellite (TSX) acquired between January 2013 and February 2016 at Volcán de Colima. The satellite has a continuous 11 day return orbit and a 12 h time gap between the chosen ascending and descending acquisitions, resulting in constant temporal data acquisition and providing a good overview of the visible changes at Volcán de Colima and, thus, its eruptive activity. Due to the rapid changes and temporal decorrelation of the SAR signal at dome building volcanoes (Walter et al., 2015; Wang et al., 2015; Arnold et al., 2017; Chaussard, 2017), we investigate the amplitude information rather than the phase information.

For this study, we consider a total of 166 SAR-images in both ascending (86 images) and descending geometries (80 images) (Figs. 2.1, 2.3), which we acquired in spotlight mode for high resolution (Roth et al., 2003). The resulting TSX footprint captures an area of ~12 × 10 km around Volcán de Colima, providing a ground resolution of ~1 m, although distortions are common due to the nature of the radar acquisition and the steep terrain. The radar images were geocoded based on coregistration with the simulated backscatter from a digital elevation model

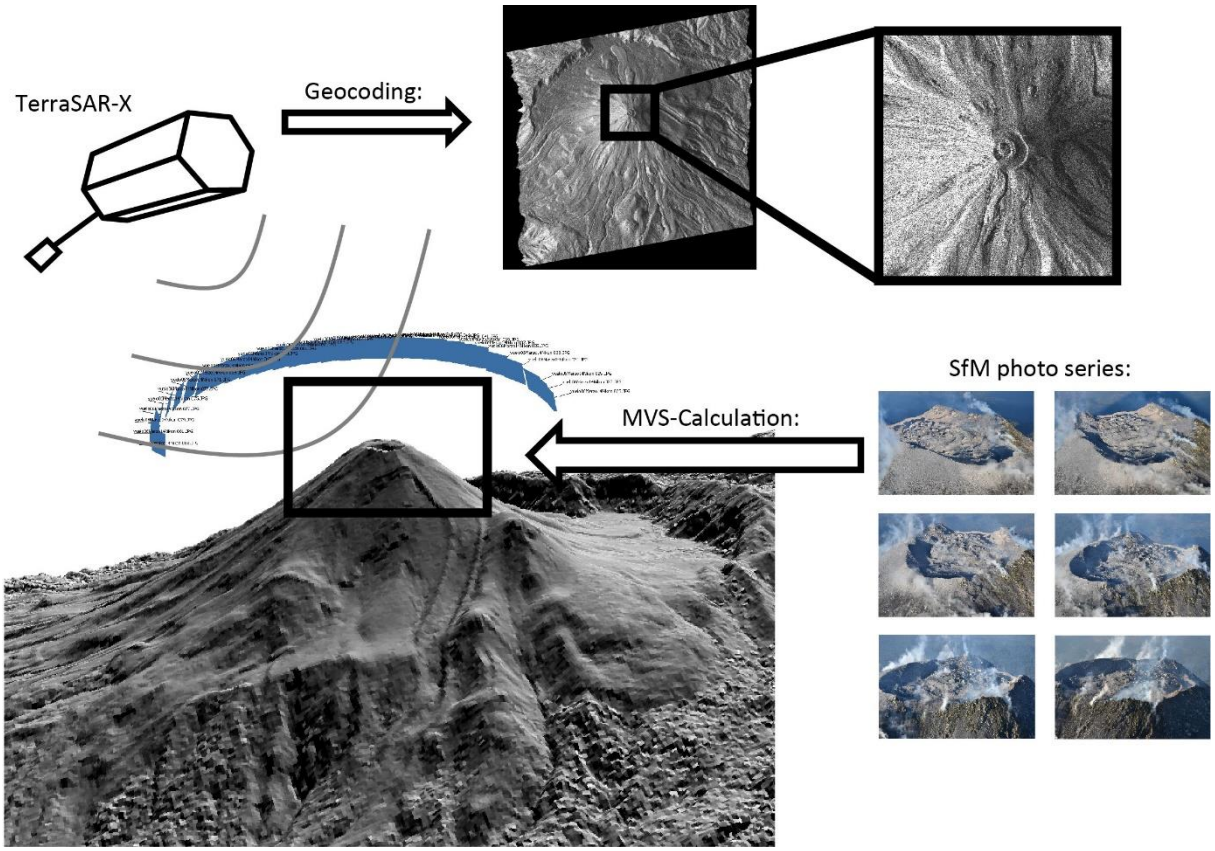

Figure 2.3: Illustrated remote sensing methods including radar amplitude images from the TerraSAR-X satellite, oblique aerial photos and the workflow of the SfM-MVS approach.

(DEM) using the GAMMA software (Werner et al., 2000). Because the DEM has a major influence on the geometric correction of SAR data, we used a DEM based on a tri-stereo photogrammetric dataset (acquired 10.01.2016) processed in ERDAS Imagine. We follow the workflow proposed by Bagnardi et al. (2016), i.e., photogrammetric terrain reconstructed based on three optical high resolution stereo-images. The resulting DEM was resampled at 1 m and allowed accurate geocoding of the TSX data. These were then speckle-filtered to enhance the image quality. We analyse the radar intensity images, yielding the reflectivity measure of the ground. By this, topography can be assessed indirectly, as those slopes facing the satellite appear brighter, while those at the opposite sites are darker.

2.2.2 High-resolution airborne photogrammetry

Flights were conducted by helicopter or plane with flight paths comprised of single or multiple circles around the crater and an oblique viewing geometry (Fig. 2.3). Airborne photogrammetric data were acquired at irregular intervals, depending on weather and flight access, though allowing a high spatial resolution. Our photogrammetric survey data consist of 13 flights between 2013 and 2016, each capturing the crater area with digital single-lens reflex handheld

cameras (DSLR). The image sizes and resolution varied due to the number of different cameras used (Canon, Nikon, Sony, Fujifilm) and are between 1,280 × 960 and 6,000 × 4,000 pixels, while the image to ground distances vary between a few hundred meters to a kilometre. Image input also varied greatly between 61 and 344 photos per survey. This is due to the overflight taking place over several years and the imaging was conducted by several different camera operators with changing equipment.

Photogrammetric reconstruction was performed using Agisoft Photoscan Professional (Version 1.4.1.5925), which uses SfM-MVS to locate and orient each image and produce a dense point cloud of the terrain (Westoby et al., 2012). As the images were acquired by handheld cameras, they have no geotagging, and as no ground control point could be measured in the field due to hazardous crater access, the resulting point clouds were not referenced. Here, georeferencing was achieved using the ~1 m resolution point cloud from the Pleiades tri-stereo DEM. We use this dataset to reference the photogrammetric point cloud closest to the Pleiades acquisition date (here 02.12.2015) by using point pair-picking registration in CloudCompare. As the SfM photogrammetry point clouds have a much higher resolution compared to the Pleiades point cloud, and to ensure internal consistency within our dataset, all other point clouds were referenced directly against this (02.12.2015) high-resolution SfM point cloud using the same manual point-matching method. The georeferencing to the Pleiades dataset could be achieved with an RMS of ±2.4 m plus an additional error between ±0.2 m and ±0.5 m from the subsequent point-matching of the other clouds to the first reference cloud.

Using the referenced SfM point clouds, detailed DEMs could be constructed using ESRI ArcMap (Version 10.5). Here all DEMs were built at 10 cm resolution after performing a statistical outlier subsampling on the point clouds, removing any singular points outside of the standard deviation for the average point distance. This is used to prevent misplaced points from affecting the final DEMs. From the 13 flights realized between 2013 and 2016 we derived 13 DEMs, providing a detailed view of morphology gain and loss at the summit of Volcán de Colima.

2.2.3 Modelling

The stress-field pattern of a volcano is known to influence or even control the path of ascending magmas (Nakamura, 1977; Rivalta et al., 2015; Sulpizio and Massaro, 2017). In addition, recent studies show that loading or unloading of a volcanic edifice (Maccaferri et al., 2017) or a crater excavation and filling (Le Corvec et al., 2018) can reorient magma propagation. Here, we investigate the response of edifice-stresses to load-changes associated with the addition and

removal of the summit dome. We develop a model using DEM changes in the finite-element method implemented with COMSOL Multiphysics®. Sequential topographic profiles derived from our photogrammetric data of different eruptive stages were used to calculate the changes in surface-loading. We further assess the impact of the stress changes on the shallow magma ascent direction by implementing a slip-failure based approach.

The direction of magma propagation is controlled by the least compressive principal stress. Such low viscosity magmas accordingly propagate through tensile mode-I type cracks opening in ascent direction (Rubin, 1995). For this study, however, we model a case revolving around the extrusion of a lava dome fed by a high viscosity or even solid magma. In this case, magma propagates upwards by pushing through a pipe-like conduit, developing shear fault-like features and slip surfaces on the walls of the conduit (Iverson et al., 2006; Pallister et al., 2013c; Kendrick et al., 2014; Ryan et al., 2018a) or, in the case of less viscous magma, form ductile shear bands (Tuffen and Dingwell, 2005). If conduit walls are fault-like, we may apply quasi-static metrics of stress changes such as normal stress, shear stress and, accordingly, Coulomb failure stress. These are concepts that are normally applied in the study of earthquake distributions (Stein et al., 1997; Freed, 2005), but they have been used in numerical modelling of lava dome extrusions before, successfully predicting extrusion volumes and deformation data (Chadwick et al., 1988).

Our model consists of an elastic domain and assumes andesitic composition with a Young's Modulus (E_c) of 10 GPa, a density (ρ_c) of 2,290 kg m^{-3}, and a Poisson's ratio (μ) of 0.33, which are typical values for andesites such as those at Volcán de Colima (Heap et al., 2014a). We consider a 2D axisymmetric domain of linear elastic materials with cylindrical coordinates (r, φ, z), i.e., a 2D profile is revolved on its z axis to construct a 3D environment. The axisymmetric simplifications allow for the simulation of a dense mesh and for the consideration of small topographic changes. To avoid boundary effects, the area of the elastic domain is set to 100 km × 100 km and is subjected to gravitational loads expressed by an initial lithostatic stress (Grosfils, 2007):

$$\sigma_r = \sigma_\varphi = \sigma_z = -g \cdot \rho_c \cdot Z \qquad (1)$$

with σ_r, σ_φ, σ_z being the normal stresses acting in the radial, azimuthal, vertical direction. Z corresponds to the vertical coordinates and is negative downwards, therefore considering the convention that negative stress values indicate compression, and g is the Earth's gravitational acceleration (−9.81 m s^{-2}). The model is further subjected to a volume load equal to

$$g \cdot \rho_c \qquad (2)$$

For our scenario, we infer magma ascent to occur by slip at the conduit walls. To assess the direction of the expected slip, we calculate Mohr-Coulomb slip planes, acting as conduit wall analogues, assuming a rock cohesion of 25 MPa, this being an average value of a medium strength rock that is highly fractured (Hoek and Brown, 1997). The orientation of the slip-planes was calculated using the visualization method developed by Grosfils et al. (2015).

We further consider the conduit position of the ascending magma column inferred from the photogrammetric data and define the observed conduit walls (assumed to be initially vertical) as stress change receiver faults. For consistency with the use of Mohr-Coulomb slip planes, we infer the conduit walls to act as shear faults for the extrusion of magma representing the side of a hypothetical conduit. These are included as two imaginary vertical lines, with the Mohr-Coulomb slip planes acting as continuation paths for the conduit wall slip, thus deflecting magma ascent. The change in CFS was calculated along the two imaginary vertical lines using:

$$\Delta CFS = \Delta\tau + \mu \cdot (\Delta\sigma_n) \qquad (3)$$

where $\Delta\tau$ is the shear stress change, $\Delta\sigma_n$ the normal stress change and μ is the coefficient of internal friction defined by the angle of internal friction (here μ = tan(25) as a common value for dry volcanic rock) (Byerlee, 1978). The change in CFS on the conduit faults can indicate the tendency to encourage (positive ΔCFS) or discourage (negative ΔCFS) fault failure with depth.

We evaluate stress changes based on morphological changes in the "elastic domain/volcano" for two case scenarios: (1) "the dome-building case," and (2) "the crater-forming case." For the dome-building (loading) case, the dome domain is created based on the natural topography (cf. section 2.2.2) to which we added the andesitic physical characteristics and gravitational loads. For the crater-forming (unloading) case, a later profile representing the excavation created by explosive activity in early 2015 is used. Here, for Z < 0 an additional unloading force equal to the negative lithostatic stress is applied at the surface of the crater and pulling it upwards. This is to account for the sudden stress in equilibrium due to the fast unloading.

2.3 Results

Our results allow detailed insight into eruptive activity and dome building processes at Volcán de Colima. A comprehensive timeline of SAR and photogrammetric results presented in this study is shown complementary to the seismic data (Fig. 2.2).

2.3.1 Overview of temporal data from TSX and seismic station

The TSX data allow the identification of changes at the volcano summit in a constant spatial and temporal resolution, whereas the seismic data provide an insight into the type of activity. The 11-day temporal acquisition of the TSX data permits the distinction of four phases of dome growth during the 3-year period between January 2013 and February 2016 (Fig. 2.4). These are also expressed in seismic data, where three phases of extrusion are associated with strong high-frequency seismic signals (Fig. 2.2) indicative of rockfalls (Arámbula-Mendoza et al., 2018), with the last being too minor to be recorded clearly. The pauses between the dome growth phases all lasted roughly 4–5 months, but interestingly, the phase durations seemed to decrease progressively (Fig. 2.2). The complete TSX dataset with the seismic timeline is shown in Appendix B1, with the relevant data being presented here.

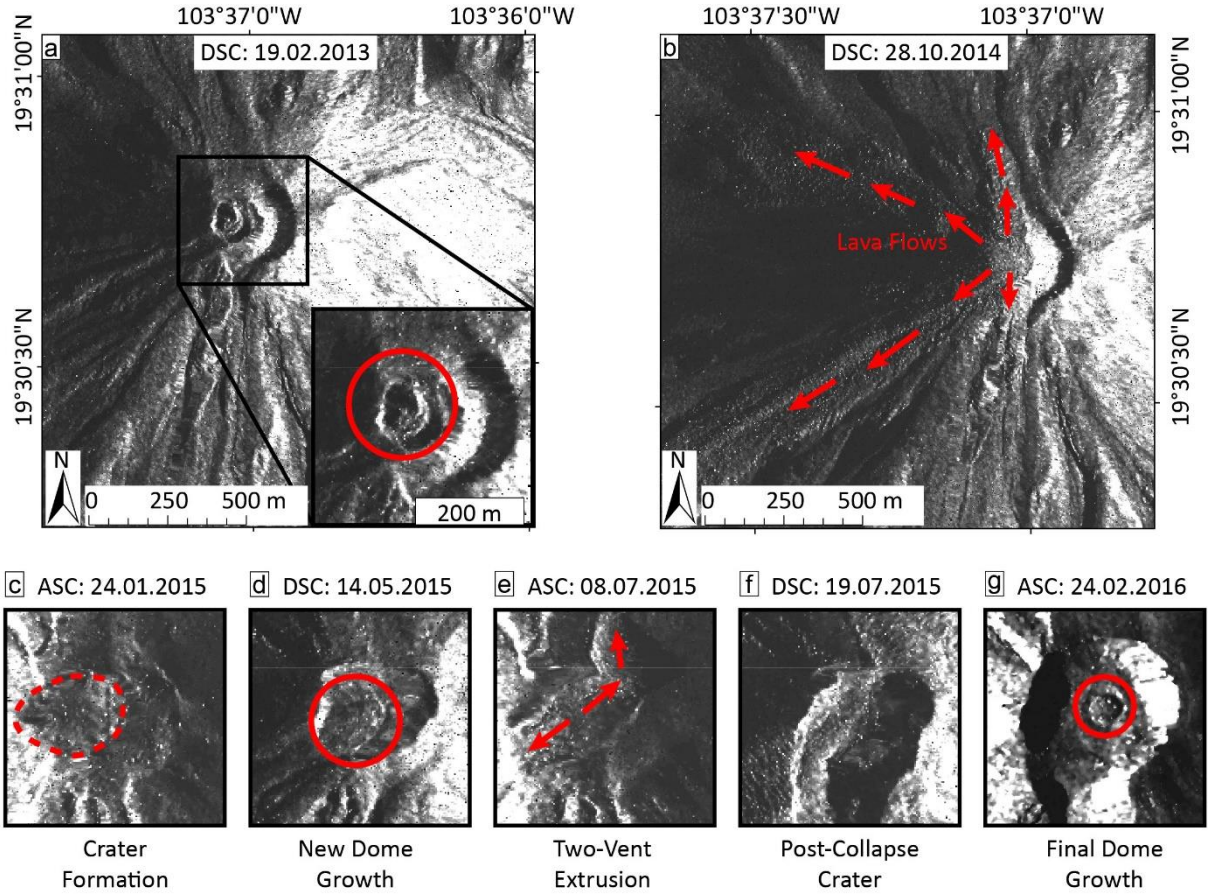

Figure 2.4: SAR amplitude images highlighting important developments at the summit crater at various stages of the observation period, red circles mark lava dome positions. (a) first dome growth phase, (b) the second dome growth phase with the production of lava flows (arrows indicate flow directions), (c) outline of the newly formed crater (the dashed line indicated the extent of the crater), (d) third dome growth phase, (e) continued dome extrusion and lava flow production from two vents (arrows indicate flow directions), (f) large collapse crater after the July 2015 eruption, (g) fourth dome growth phase.

TSX and seismic data both indicate the growth of the first lava dome, representing the start of the renewed eruptive activity at Volcán de Colima, occurred in early 2013. The eruptive activity was dominantly constructive with the addition of lava at the summit and the western volcano flanks and can be observed in the TSX data (Figs. 2.4a, b). According to helicopter observations, the very first extrusion of lava started on 11 January 2013; however, this new dome was destroyed by the ongoing explosive activity. We first identify the lava dome in the TSX image from 19 February 2013 (Fig. 2.4a). The dome grew westward and by March 2013 resulted in the formation of a lava flow that descended the western flank. In early 2014, seismic data indicate either a prolonged pause in extrusion or a significant reduction of the extrusion rate, as seismic events changed to low-frequency dominated events. In simple terms, this indicated that fewer rockfalls associated with dome-growth occurred. The pause in extrusion is supported by the TSX data, as it shows the dome staying stagnant at the summit and no major morphological changes occur during this time (March to July 2014).

Between July and August 2014, activity resumed with a strong extrusion as evidenced by four lava flows appearing in the TSX acquisitions (Fig. 2.4b). This second extrusion produced lava flows to the SW and NW (Fig. 2.4b), which by October extend to 2.3 and 1.3 km from the summit, respectively. Smaller flows to the N and S extend less than 500 m from the summit (Fig. 2.4b). A final lava flow developed in November 2014 toward the SW, also not extending more than a few hundred meters down the flank (Fig. 2.5c), meaning that almost all the extruded material during this phase was deposited on the western half of the volcano. In December 2014, extrusions slowed and the activity became more explosive. The TSX images do not show any further extrusion and the seismic data indicate that 17 to 25 January 2015 was a transition period from extrusive to explosive activity. The transition is characterized by a change from high- to low-frequency dominated seismic signals, representing rockfall and explosion signatures, respectively (Fig. 2.2). More detailed seismic data showing this transition are included and explained in Appendix B2. Explosive activity resulted in the partial collapse of the summit dome, likely within a few days in late January 2015, as a new crater formed in its place (Fig. 2.4c). Over the following months, the crater deepened through further explosive excavation and elongated along a southwest-northeast axis, developing an elliptical shape (Fig. 2.4d).

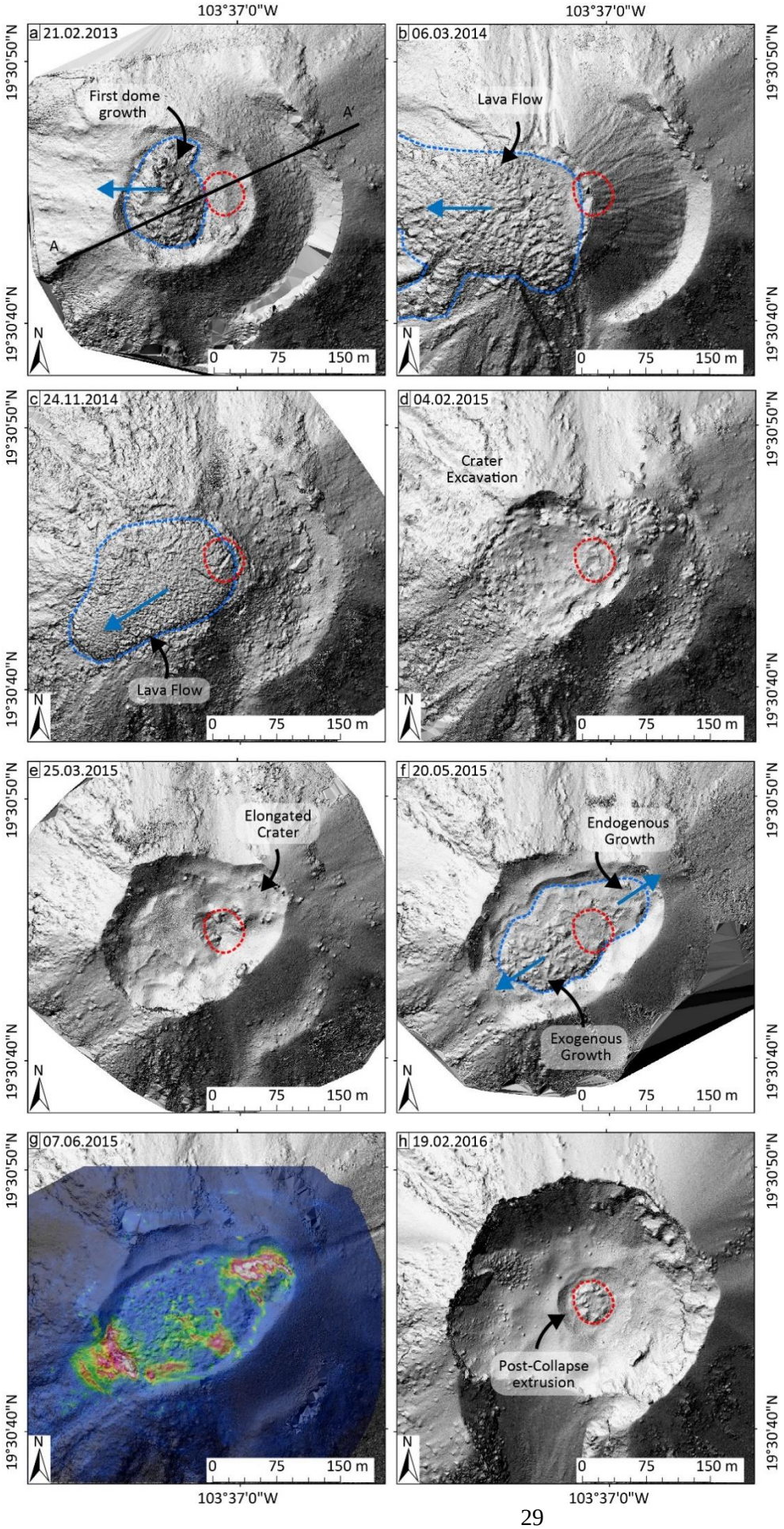

Figure 2.5:
DEMs built from aerial SfM-MVS photogrammetry, showing highly detailed morphological changes within the crater area. (a) The initial dome growth in January 2013; (b) overtopping of lava toward the west; (c) final lava flow emplacement during the constructive activity on the SW side; (d) initial crater after the dome collapse; (e) deepened and elongated crater following ongoing explosive activity; (f) bifurcated dome growth on both the NE and SW side; (g) overlay of thermal data, highlighting the conduit bifurcation reflected by two active dome areas in the NE and SW, respectively; (h) Collapse crater after the July 2015 eruption with the new extrusion at the crater floor. Dashed blue lines mark the extent of the summit lava dome or lava flow and the dashed red line marks the deep vent position inferred from (h). The profile position used in fig. 2.6 is marked with a black line in (a).

A third lava dome began to grow in May 2015 and involved simultaneous explosive activity. While the crater remained elongated on its southwest-northeast axis, a new lava dome grew inside the crater (Fig. 2.4d); however, the growth was initially seen only within the SW half of the crater. On the NE side of the crater, activity was reportedly comprised of small explosions (Reyes-Dávila et al., 2016). By June 2015, the dome filled the entire crater and in July it produced lava flows in both SW and NE directions (Fig. 2.4e). The onset of new rockfalls coinciding with the start of the lava flows is also seen in the seismic data, with a change to high-frequency dominated events (Fig. 2.2). Extrusive activity intensified and culminated in the catastrophic collapse of the summit area from 10 to 11 July. The eruption and collapse produced a large crater which was breached toward the south (Fig. 2.4f). After July 2015, activity at Volcán de Colima declined and displayed only minor to moderate explosive activity.

In February 2016, seismic data indicated that a new dome had started to grow inside the centre of the crater. This dome is visible as a small and roughly circular extrusion in the TSX images (Fig. 2.4g) and did not grow much larger.

2.3.2 Overview of structural data from SfM and thermal images

The SfM reconstructions performed well on the flight data. The summit area of Volcán de Colima was resolved in all 13 datasets that were considered for the 2013–2016 observation period. We obtained a morphologic time-lapse dataset showing the growth and destruction of the summit lava dome(s) and the growth direction. The exceptionally high resolution of 10 cm allows the identification of small features such as individual explosion pits and lava bombs and further allows us to identify the structures associated with the direction of dome growth. The complete SfM dataset is shown as shaded reliefs in Appendix B3.

Our model from the first extrusion in February 2013 shows an elliptical (N-S elongated, aspect ratio AR = 1.37) lava dome with a diameter of ~100 m within a ~160 m wide crater (Fig. 2.5a). With continued dome extrusion until the end of 2014, both the older dome and the surrounding main summit crater were gradually buried (Figs. 2.5a-c). The dome itself is a single extrusion lobe characterized by a flat-topped blocky surface with a surrounding talus. The flat top also shows a slight inclination during the first months of growth (Fig. 2.6a). By March 2014, the dome had filled the crater and overtopped it to the W (Fig. 2.5b). This is consistent with previous observations, showing a clear westwards directionality from the start of the dome growth (Walter et al., 2019b). After a pause in extrusion, activity resumed and another new dome lobe was seen at the summit in November 2014, overtopping the previous extrusions toward the SW and its surface shows the same blocky nature as the previous dome (Fig. 2.5c).

As the flight data did not capture the initial growth stage, it is not clear whether the extrusion occurred with an elongation.

By February 2015, after the start of the destructive activity, the top of the summit dome was removed and a ~165 m wide and round crater had formed in its place (Fig. 2.5d). This crater grew larger within a few weeks, as much of the explosive activity was focused on its NE side, thus gradually elongating it along the southwest-northeast axis by March 2015 (Fig. 2.5e). By the time, the third dome started to grow in May 2015, the crater had formed a ~240 m long and 180 m wide depression (Fig. 2.5f). A new extrusion then formed within that depression, reaching a size of 195 m by 110 m (NE-SW elongated, AR = 1.77) (Fig. 2.5f). This dome, compared to the first dome from February 2013 (Fig. 2.5a), also had a blocky surface, but had a much lower profile. Initial dome growth was also focused to the SW half of the elongated crater and the direction of growth occurred mainly toward the SW, while the northeast side of the crater first showed steaming and explosive activity, then transitioned to lava extrusion. From additional thermal data during this stage, we identified two main anomalies in the NE and the SW, respectively (Fig. 2.5g). As seen from the TSX data, the dome became increasingly elongated across this NE-SW axis (Fig. 2.4e). During the last stage of dome growth, and shortly before the large eruption in July 2015, the dome filled the entire crater, topping over both the NE and SW sides of the crater and generating advancing lava lobes in both directions (Fig.

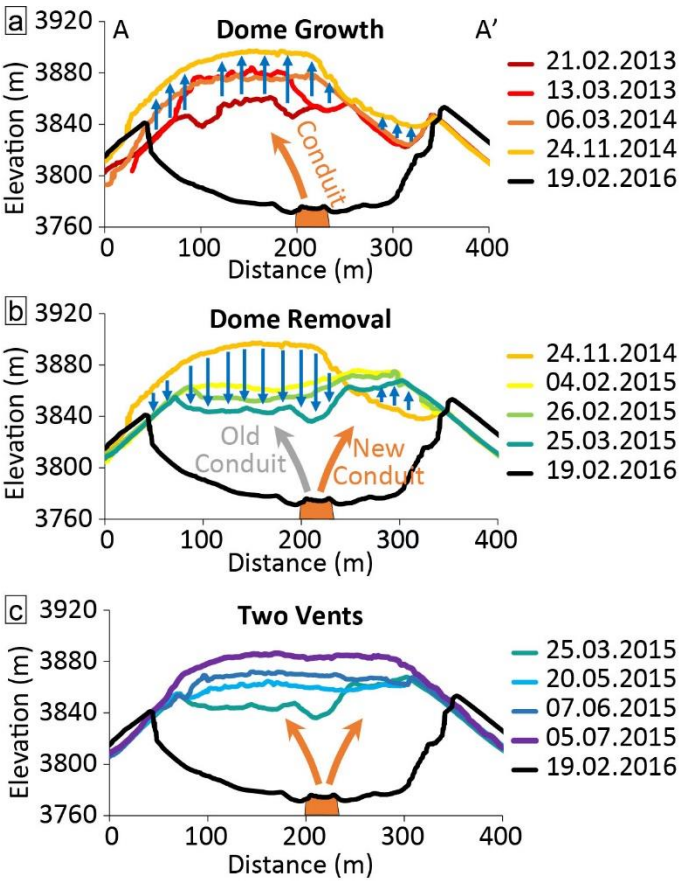

Figure 2.6:
Profile view from A-A' marked in fig. 2.5a of the DEM data showing the changes resulting from the important eruptive phases, (a) the growth of the lava dome, (b) its removal, and (c) the lava dome regrowth and conduit bifurcation. The inferred deep conduit position (see fig. 2.5h) is also shown.

2.4e). At this stage, the dome had bifurcated into two growth directions, to the SW and to the NE.

After the July 2015 dome collapse, the final flight we processed shows a ~300 m wide and ~80 m deep crater open to the south (Fig. 2.5h). The excavation decapitated the previous conduit system and a new and near circular dome extrusion ~45 m across (AR = 1.16) was visible in the bottom of this crater, which marks the new conduit position below the previous level (Fig. 2.5h).

2.3.3 Topographic stress modelling

We use stress-change modelling to better understand why dome growth at Volcán de Colima develops directionality as observed during our study period (W until late 2014 to SW and NE in early 2015). Specifically, we test the effect of changes in the local stress field on the magma ascent directions due to the changing topography in case of dome growth or destruction.

To quantify the changes in the topographic loading due to dome growth, the elevation difference between the 21.02.2013 DEM and the 24.11.2014 DEM was used (Fig. 2.6a). This captures the entire constructive dome growth activity before the dome was removed in early 2015. The models thus reflect the gradual emplacement of the load through the lava dome, which had grown toward the western side of the crater. For the unloading model, the topography difference between the 24.11.2014 and the 25.03.2015 was used (Fig 2.6b). This captures the removal of the summit dome and excavation of the crater in its place during early 2015. It is also at a stage where the elongation of the crater had not yet started or was not yet visible, meaning it is also before the second vent in the NE appeared.

The stress models show a clear response of the Mohr–Coulomb slip-lines to the changed stresses with the addition and removal of the dome loading, respectively (Fig. 2.7). Generally, slip planes are directed toward additional load, thus favouring conduit wall slip into elevated topography, here the newly grown lava dome. On the other hand, the excavation of material from the dome deflects the slip lines away from the removed load and toward the remaining topography on the side of the crater. Here, this promoted fracturing and slip toward the eastern excavation rim after the lava dome was removed.

By loading and unloading of the lava dome, the Coulomb failure stress changed along the conduit walls of the ascending magma column. This can be observed on the modelled imaginary conduit (Fig. 2.7). Depending on the depth the stress difference can be up to 0.25 MPa (ΔCFS)

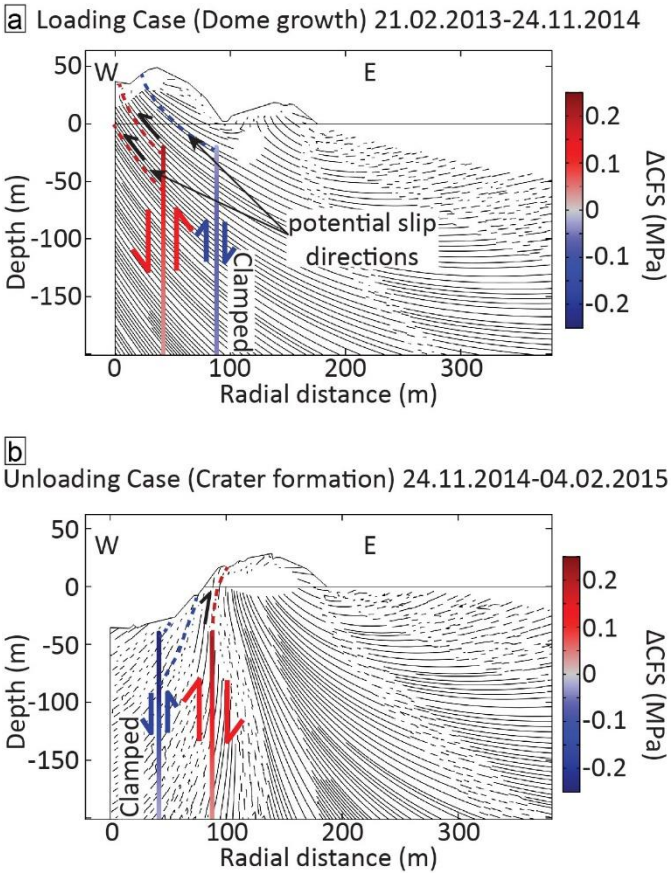

Figure 2.7:
Coulomb Stress Change (ΔCFS) along the walls of a magmatic conduit in the case of (a) loading with dome growth, and (b) unloading with crater formation. The topographic profiles are taken as differences from the SfM-DEMs. The topography change is from 21.02.2013 to 24.11.2014 for (a) and 24.11.2014 to 25. 03. 2015 for (b). The ΔCFS inhibits fault movements when negative (blue colour) and favours fault movements when positive (red colour). Thin black lines show orientations of the Mohr–Coulomb slip planes (Cohesion = 25 MPa, Φ_{frict} = 25°) that have the same orientation as the favoured movement along the conduit. For the dome growth the Mohr–Coulomb slip planes are directed westwards (i.e., toward the additional load). For the crater formation they are eastwards (i.e., away from the unloaded crater). Actual conduit extrusion would follow the imaginary wall faults at ~80 m depth, then deviate from that path following the Mohr–Coulomb slip planes at any point above.

(Fig. 2.7), which may contribute to activating or clamping the conduit. The position of the conduit at a depth of ~80 m could be inferred from the 2016 model (Fig. 2.5h). This assumes a constant position of the deeper magma column as well as magma extrusion by shearing of a conduit fault. In the loading model, the western conduit fault located toward the dip of the dome would be activated preferentially, whereas the eastern side of the conduit would tend to clamp due to the reduction in ΔCFS (Fig. 2.7a). This is reversed in the unloading model, where the eastern side conduit fault will activate preferentially and the western side will clamp (Fig. 2.7b).

2.4 Discussion

Lava domes growing in the summit regions of active volcanoes are a major source of hazards, as parts of a dome may become unstable, fail, and generate PDCs. Lava domes growing in a preferred direction may allow better judgment of the direction of this instability, however, the reasons for the preferred growth direction have not been investigated in detail yet. In this work we propose a model in which the local stress field is controlled by the eruptive sequence, which

could be coupled with other processes and effects, such as pre-existing morphology and slope, rheology, and structural interactions, as further elaborated below.

2.4.1 Magma ascent response to load changes

2.4.1.1 Conduit position

By integrating photogrammetric data, satellite radar images, and numerical modelling methods, we are able to gain insight into the physical processes controlling the lava dome growth at Volcán de Colima, Mexico. Based on deformation studies, the location of the feeding conduit could already be inferred in a 2013 dataset (Salzer et al., 2014), which matches very well with the conduit position in our study (Fig. 2.5h). The July 2015 eruption produced an 80 m deep crater and carved the conduit on the crater floor with the onset of a new extrusion in 2016, indicating that the location has been constant for the period 2013–2016. Therefore, we could infer the conduit location (centre at 103°37'0.75“W and 19°30'44.881”N) (Fig. 2.5h) and identify approximate extrusion paths and growth directions of the lava dome in the 2013–2015 growth phase. This is done under the assumption that the conduit position at depth was constant between 2013 and 2016. We assume this is valid as the dome that grew in 2016 did not show any directionality and is in a central position of the current crater. This is further supported by the ~70 m westward offset of the initial 2013 dome with respect to the observed deeper conduit (Fig. 2.5a) and a noticeable tilt in the flat dome top (Fig. 2.6a), suggesting an inclined extrusion vent and implying a shallow bend in the conduit, likely between the surface and ~80 m depth. Such a bend has also been suggested to occur as a result of conduit bifurcation at a shallow depth in previous works (Lavallée et al., 2012; Salzer et al., 2014) and is thus in good agreement with our interpretation (Fig. 2.8a).

2.4.1.2 Changes in loading stress

We are able to provide an explanation for the extrusion direction of the lava dome and the conduit bifurcation following the collapse of the dome and infer the dynamics of the shallow conduit system based on changes in the local load stress field. The additional load due to the growing dome and the lava flows on the western side emplaced between 2013 and late 2014 aligned conduit slip planes toward the western side (Fig. 2.7a). This likely favoured the activation of conduit slip in this direction, providing Mohr-Coulomb slip surfaces for the magma ascent in this direction, which resulted in further west-directed extrusion. It also likely favoured the formation of cracks and fissures in this direction due to the conduit movement at

shallow depth. The change in CFS suggests that the extrusion mostly moved by the activation of the western conduit fault/margin (Fig. 2.8a), thus piling additional material to the west and creating a self-sustained directionality. Support for this sustained system can be seen in the timespan of purely west-directed lava extrusion as it lasted almost 2 years and through two phases of extrusion.

The west-directed extrusion only stopped when the load, i.e., most of the summit dome, was removed and the crater deepened during the onset of explosive eruptive activity during late January and early February 2015 (Fig. 2.4c). During the removal of the dome and subsequent crater elongation, activity shifted to the northeast on the other side of the deep conduit position (Figs. 2.5e-g). We interpret this as a newly opened vent, which could have been formed from a new or reactivated fissure originating from the same conduit (Figs. 2.6c, 2.8b), which has been previously described at Volcán de Colima (Lavallée et al., 2012). Here our model suggests the new vent formation was caused by the removal of the load, rather than a deflection caused by a dense plug. This deflected the slip planes away from the new-formed crater and toward the remaining load on the crater rim (Fig. 2.7b), which was where the new vent developed. Another factor favouring the fracturing and opening of new fissures may have been the transitional period from effusive to explosive activity (Fig. 2.2 and Appendix B2) as this will have involved repeated conduit pressurization. Under the new load stresses, it is likely that the new fissure branched off the eastern conduit wall coinciding with the activation of the conduit wall fault, thus causing the conduit bifurcation we observed (Figs. 2.8b-d). Since both the NE and the SW vents started extruding in May 2015, we presume that the previously west-directed extrusion vent was likely reactivated by a new pulse of magma. As this would involve multiple shallow conduits our model cannot resolve this behaviour properly, although it is possible that extrusion may still take place on the active conduit wall (here the eastern side) for both vents.

The stress response to loading and unloading can also be used to explain the shift in dome extrusion from an initial E-W axis to the NE-SW axis observed toward the end of the eruption. At the start of the dome extrusion in 2013, the direction of the dome growth and the following lava flow were directed purely to the west (Figs. 2.5b, 2.6a). However, this shifted in 2014 as the accumulated extrusion products were buried and lava flows developed in other directions, most prominently toward the SW with the final pulse in November 2014 (Figs. 2.4b, 2.5c). The highest load was therefore placed on the SW side, explaining why the new vent opened on the other NE side after this load was removed in early 2015.

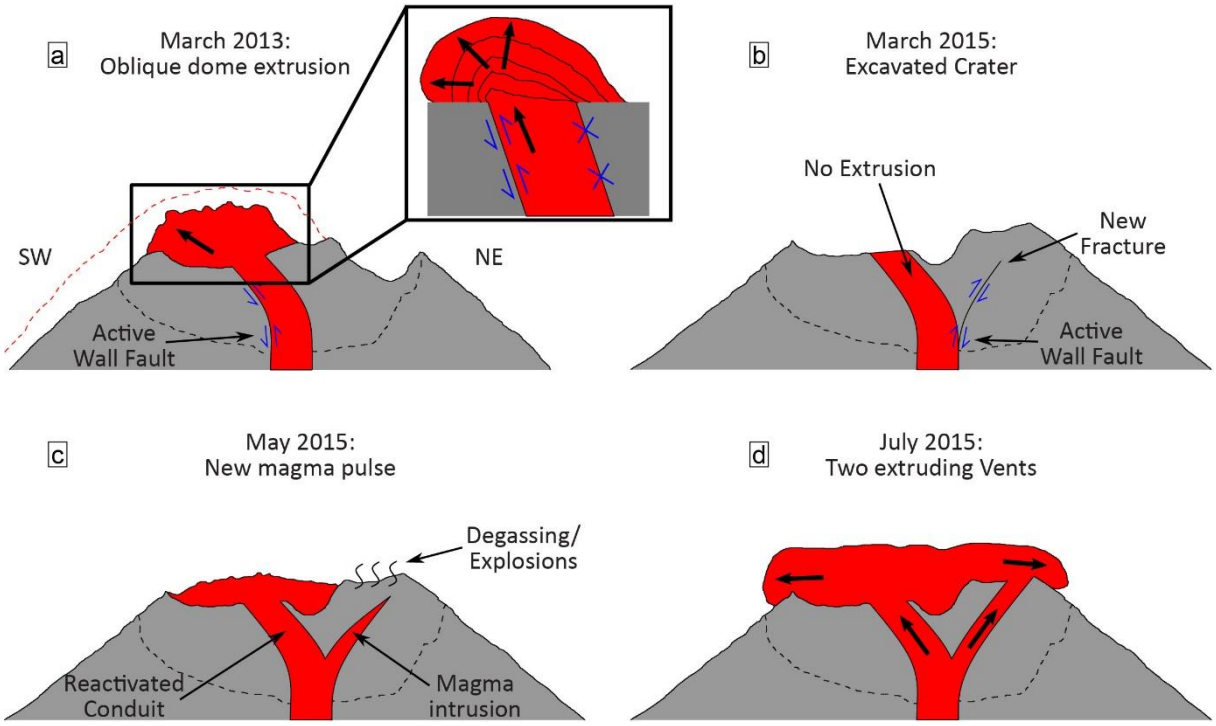

Figure 2.8: Illustration of the proposed processes during the observation period. The sketches are not to scale and orientated based on the A-A' profile view marked in fig. 2.5a and used in fig. 2.6. (a) The initial stages of dome growth, showing the dome extruding westwards by activation of the inner conduit wall fault. (b) The crater after the removal of the summit dome. The load stress field has shifted, causing new fractures to branch of the conduit wall to the NE side. (c) Regrowth of the lava dome and the conduit bifurcation. (d) Final stage of the lava dome before the large collapse in July 2015, the dome is growing in two directions (NE and SW) fed by two separate vents.

These results are in agreement with previous studies investigating the ascent of magma in response to changing surface loads, which were found to occur due to a shift in principal stresses on a local (Le Corvec et al., 2018) and crustal scale (Maccaferri et al., 2017).

2.4.2 Causes of magma deflection and growth directionality

Our observations of directional dome growth, vent offset, and possible conduit bifurcation are consistent with previous investigations into the dynamics of the shallow crater system at Volcán de Colima. Our study further suggests an evolution in growth directionality as the first dome growth is west-directed, then becomes both west and east-directed, and finally bifurcates into a western and an eastern branch. The mechanism causing the directed extrusion proposed here provides a new explanation that differs from other mechanisms discussed in previous studies.

Firstly, the topography around the extrusion of a lava dome has been proposed to play an important role. Emplacement on a sloped surface or within uneven craters can cause directed growth downslope (Harnett et al., 2018). Here, the dome at Volcán de Colima grew inside an

explosion crater, with the western crater wall slightly lower than the eastern wall. Similarly, observational data at other volcanoes showed that the crater shape may significantly affect the direction and speed of dome growth (Walter et al., 2013a). Thus, we cannot rule out an impact of topography after the dome started to overflow the crater. However, as the dome was already growing westwards before overtopping the crater, this is unlikely to be the cause of the directionality.

Secondly, changing extrusion directions have been linked to a structural or mechanical control within older emplaced domes, where an inclined growth lobe develops along a curved shear fault originating at the side of the conduit (Watts et al., 2002). This is also reflected by changes from endogenous to exogenous growth styles, when a lava lobe is pushed through the previously emplaced dome (Watts et al., 2002; Hale and Wadge, 2008; Husain et al., 2014). In our study, we see a change from endogenous to exogenous only for the newly opened NE vent in 2015 and only after the direction of dome growth had already changed. The changes of extrusion directions at Volcán de Colima are thus linked to the removal of dome material occurring previously, not the growth style. However, the movement along shear faults originating from the conduit walls is supported by our study, and the importance of the conduit wall for lava dome emplacement through shear faulting has been emphasized in many earlier studies (Chadwick et al., 1988; Tuffen and Dingwell, 2005; Pallister et al., 2013c; Kendrick et al., 2014; Ryan et al., 2018a).

Thirdly, changes in growth direction at Volcán de Colima were characterized by the activation of new lobes as rockfalls would cause local unloading on the dome (Hutchison et al., 2013). The growth lobes thus advanced in this direction as the rockfall area became unconfined by the talus surrounding the dome (Walter, 2011). A similar change in growth direction and even extrusion rate in response to local unloading due to slumps was also found at Mount St. Helens (Vallance et al., 2008). This mechanism is similar to our interpretation as it is also based on topographic loading and unloading, however, the unloading and redirection of growth occurs only with the already extruded parts of the dome as it becomes unconfined on one side while remaining confined (or buttressed) on the other. Our interpretation adds to this discussion by suggesting a loading-based deflection of extrusion to occur prior to extrusion (and likely at an inclined angle), which is a separate process from the one proposed by Hutchison et al. (2013), and a combination of both is likely.

Lastly, there can be some external factors impacting the direction of magma extrusion. Several studies have suggested the existence of a dense plug in the shallow levels of the Colima conduit, causing a deflection of magma ascent and pressurization at shallow depth (Lavallée et al., 2012;

Salzer et al., 2014). An offset of the dome from the main summit crater centre was already noted in 2010 (James and Varley, 2012; Lavallée et al., 2012). The deeper conduit position (Fig. 2.5h) highlights that active vents between 2013 and 2015 shifted due to shallow conduit deflection; however, our models suggest a reorientation in slip-lines due to changing load stresses as a mechanism. Considering the existence of the dense plug, our models may contribute to the concept of shallow conduit deflections by providing a preferred direction, with which magma will ascend around such obstacles.

With respect to the changing Coulomb stress along the conduit wall faults, our models suggest a differential conduit wall fault activation, with one side being preferentially activated, the other being clamped (Figs. 2.7, 2.8). Aside from an inclined conduit, this may be another factor explaining the strong directionality in the observed dome growth. The existence of conduit wall faults is well known and documented, mainly as slip-surfaces (Pallister et al., 2013c; Kendrick et al., 2014; Ryan et al., 2018a), but also as ductile shear bands (Tuffen and Dingwell, 2005); however a one-sided trap-door style extrusion as illustrated in fig. 2.8a has not been described or observed at growing lava domes before, this is only implied by our model. Normally this style of fault movement is seen in large scale caldera collapses (i.e., Lipman, 1997; Cole et al., 2005), whereas here we would assume a one-sided upwards movement as it occurs with resurgent blocks on a larger scale (Acocella et al., 2001). As our data are static, the extrusion movement cannot be clearly resolved, but considering the continuing extrusions eventually formed viscous lava flows, the fault movement was most likely accomplished by a combination of ductile and stick-slip movement.

Considering the factors discussed above, the directed dome growth at Volcán de Colima was most likely an effect of (1) load stress interaction, (2) shear fault movement originating from the conduit walls and (3) an inclined vent and shallow conduit. Impacts due to sloped emplacement are unlikely and the influence of a potential impermeable plug deflecting magma ascent remains unclear.

2.4.3 Method limitations

The use of satellite radar, photogrammetry, and seismic data to observe volcanic activity combined with numerical modelling introduces some inherent limitations. The most important ones will be briefly discussed here.

2.4.3.1 Remote sensing limitations

Our interpretation of the amplitude SAR-images may be biased by the acquisition geometry. The radar data contain shortening and lengthening at slopes due to the inclined sensor (foreshortening), distorting the image and potentially leading to layover and shadowing effects. Accurate geocoding with a suitable DEM, as done in this study, can correct some of these distortions; however, such geocoding may introduce other artifacts at points where the DEM (here Pleiades 2016) does not reflect the same topography as the SAR image (2013–2016), especially if they were generated at different times and the topography has changed among multiple images. The speckle filter applied here, while smoothing the image and enhancing important features, also lowers the resolution slightly. In this study, these effects impact the corrected SAR-images to a small degree as the crater showed many topographic changes and all SAR-images were geocoded with the same DEM. We used the SAR data to identify prominent brightness changes associated with topographic changes, which are very well resolved and discernible. Therefore, our SAR images are most likely only distorted to minor degrees, i.e., only at small topographic features such as cliffs and ledges. The features, outlines and positions of lava flows, domes and craters can still be recognized very clearly in the images (see e.g., the circular lava dome in fig. 2.4g). The same applies for the directions of dome growth or flows between subsequent images, so our interpretation of the images is not affected by the limitations listed above. The TSX data also agree well with the photogrammetry data and provide a very regular 11-day interval view onto the dome of the active volcano, whereas the photogrammetric data could only be realized when weather and funding allowed for overflights. While the SAR data capture the entire volcanic edifice and permit the tracking of active lava flows down the volcano flank, all high-resolution SfM-MVS generated DEMs used in this study only cover the summit area within a few hundred meters of the vent. Additionally, contrary to SAR data, overflight data are only available on occasion and not all data can be used for photogrammetric processing as steam and gas often limit the visibility. In some cases this effect can be overcome with thermal images (Thiele et al., 2017), but this will result in lower spatial resolution models due to the limitations of such cameras. Here, our observations made outside of the summit area are affected by these limits, therefore we can only use occasional DEMs, acting as high-resolution snapshots to complement the SAR data.

As the SfM point clouds could not be georeferenced directly in Agisoft PhotoScan Professional, the ground sampling distance (GSD), a common indicator for the resolution of photogrammetric surveys, could not be calculated precisely and the imaging distances had to be estimated. Most surveys resulted in GSDs slightly better than 10 cm per pixel as indicated by the point distances

within the cloud, but there may be some variations due to the number of different cameras, focal lengths and viewing distances applied. We omitted these by resolving all DEMs at 10 cm resolution, also providing consistency between the DEMs.

2.4.3.2 Seismic data limitations

The main purpose of the seismic data used (Fig. 2.2) was to provide an overview of the dominant seismic signal during our study period based on frequency content. However, neither this type of analysis nor the location of the seismic station (closest to the crater at 1.7 km) are enough to detect and identify the details of dome extrusion mechanisms and directionality, which take place at a very shallow level in the volcanic system or at the crater's surface. Additional seismometers near to the crater or on the volcanic edifice might allow to pursue such a task, which is beyond the scope of this paper. For example, at Mount St. Helens Moran et al. (2008) used a network of seismic stations inside the crater and suggested that changes in drumbeat-seismicity characteristics (size and spacing) during the dome-building 2005 eruption were a function of the mechanics of extrusion rather than of the extrusion rate.

The seismic data provide a good overview of the current activity and the changing dominant eruptive modes, i.e., dome extrusion and explosions (Fig. 2.2). However, there can be a significant delay in the onset of high-frequencies representing dome extrusion. One such delay occurred around May 2015 with the onset of renewed lava dome growth, when the dominant frequencies only changed to higher frequencies several weeks after the dome growth had started. This is likely due to the time gap between the initial dome growth within the crater and the overtopping the crater to produce rockfalls, which generate the high-frequency seismic signal. The true onset of dome growth can in general still be seen in the characteristics of individual seismic events; however, until rockfalls occur, high frequency signals are not dominant.

2.4.3.3 Model limitations

Using a numerical model to explain real observations always includes a number of assumptions and simplifications. Our models are based on the gravitational loading derived from changing topography, which is not the same as the total stress. For example, the effects of internal magma and fluid pressure as well as material heterogeneities are neglected as they are very complex and difficult to include in such a model. This is unlikely to affect the general finding regarding the deflection of slip planes in response to load stresses. However, it is important to note that

the real stress field within the volcanic edifice may be quite different compared to a simple gravitational model, and factors such as the dense plug discussed above may play an additional important role when addressing magma ascent directionality.

Another limitation of the model is the use of a 2D axisymmetric half-space to create a 3D model from a profile. This is a common simplification used in several similar studies (Chadwick et al., 1988; Corbi et al., 2016; Le Corvec et al., 2018) and is due to the difficult implementation of the large datasets and computing power that are required to use a full 3D surface model. While we manage to capture and include all important features including the conduit and vent positions, it is important to note that our model is derived from a change in topography of a 2D environment and is thus not a complete representation of the real morphology (e.g., variable crater depth or dome heights cannot be included). Here, we picked the rotated profile location (Figs. 2.5a, 2.6) to be the best representation of the summit morphology.

The model relies on the concept that the conduit walls of the ascending magma column act as frictional planes (Costa et al., 2012; Kendrick et al., 2014), which is a reasonable assumption when considering highly viscous or solid magmas. However, these conduit faults are normally associated with spine-type lava domes such as Mount St. Helens, USA (Kendrick et al., 2012; Kennedy and Russell, 2012) or Mount Unzen, Japan (Hornby et al., 2015). At Volcán de Colima the viscosity of the magma is clearly lower, producing mostly lava lobes that transition to lava flows. This is also evidenced by the blocky surfaces of the extruded domes (Figs. 2.5a-c, f-h), suggesting a viscous magma core fracturing a solid dome carapace through inflation. The extent to which a classic fault structure can be applied to the conduit of Volcán de Colima is not clear. However, recent insights into similar episodic activity expressed by seismicity and ground deformation highlight the relevance of conduit shear stresses even for viscous magmas (Neuberg et al., 2018). Previous models successfully predicted extrusion patterns (e.g., ground tilt) using only shear stress (Chadwick et al., 1988). Additionally, movements along the conduit occur by stick-slip motion (Kendrick et al., 2014), indicated by observed episodic extrusion patterns at Volcán de Colima (Walter et al., 2013b), which suggest that partial slip movements occur along discrete fault zones.

The use of Coulomb stress changes (ΔCFS) is restricted to the summit region only, yet the resulting values are high enough to compare to values seen on larger scales. Depending on depth in the conduit, the maximum Coulomb stress change is as large as 0.25 MPa. For context, stress changes of <0.01 MPa can be sufficient to induce failure and earthquakes (Stein, 1999). These values are high, given we only consider very local loads within a few hundred meters of the free surface. As the model used here assumes a purely elastic environment and is very close to

the surface, this may induce an artificial stress-build up. However, the relative changes of increasing or decreasing Coulomb stress with respect to load stress are likely to have a real effect on the conduit faults.

2.4.4 Hazard implications

The potential impact of both local and regional stresses carries some major implications for the hazard potential, especially for dome-building stratovolcanoes. PDCs originating from the collapse of lava domes are among the most deadly and destructive volcanic hazards. In the case of Volcán de Colima, they exceeded 10 km distance during the July 2015 eruption (Reyes-Dávila et al., 2016; Capra et al., 2018). This highlights that accurate assessment of potential scale and flow direction of these hazards is one of the most important tasks in volcanology.

Directed effusion and the development of new vents or their migration in response to load stress changes, as we propose for the 2013–2015 eruption at Volcán de Colima, will affect the direction of dome-related flows, explosions and collapses, and hence the distribution of hazards around the volcano, mainly PDCs, lava flows and possibly ballistic ejecta. The distribution of ashfall is likely only affected to a minor degree as the wind is the primary control on the ashfall direction. The second growth direction that developed at Volcán de Colima caused lava flows and PDCs to flow down the NE side of the volcano, whereas previous flows were directed mostly to the W and SW. Similarly, changes in the inclination of a growing dome will affect the stability of the dome, with collapses and resulting block-and-ash flows occurring more likely with a larger inclination.

The effects of unloading and the removal of large parts of a lava dome or crater wall will not only affect the local stress field and magma ascent direction but will also remove pressure from magma stored in the shallow subsurface. A sudden drop in pressure can release volatiles entrained within an incompletely degassed magma and induce vesiculation and vesicle expansion (Alidibirov and Dingwell, 1996; Watts et al., 2002), leading to a strong increase in extrusion and ascent rate or explosive activity. A similar effect due to unloading at the summit is hypothesized to have been a driver of the 1913 eruption of Volcán de Colima (Massaro et al., 2018). Due to the increased ascent rate this can, in turn, affect the stability and shape of subsequent lava domes, with faster extrusion rates resulting in weaker lava dome rocks (Heap et al., 2016; Zorn et al., 2018) and so increase the risk of collapse.

Finally, regional tectonic stresses may control the orientation of fracturing in summit lava domes, leading to destabilization and partial collapse to form block-and-ash flows, e.g., at the Merapi lava dome (Walter et al., 2015; Darmawan et al., 2018a). While no such observations

have been made at a lava dome from Volcán de Colima, changes in eruption style due to regional stress changes have been observed (e.g., through tectonic earthquakes lowering lithostatic stress, Sulpizio and Massaro, 2017), although their importance for Volcán de Colima remains unclear as there are many other potential explanations for this effect (Massaro et al., 2018).

The effects of directional dome growth on volcanic hazards presented here are described in the context of a simple shift in the direction of the erupting vent and dome growth. In reality, there are several other factors that influence the direction of hazards from a volcano, e.g., local ground morphology such as river valleys or breached calderas, redirecting or channelling PDCs (Major et al., 2013). Similarly, the dome volume, temperature, volatile charge and slope steepness will affect the mobility of such PDCs and thus their travel distance (Bourdier and Abdurachman, 2001; Cronin et al., 2013). The redirection of hazards due to shifting lava dome growth directionality is only one aspect and, for a detailed hazard assessment, all the complexities of the potential hazards have to be considered.

2.5 Conclusions

Between January 2013 and February 2016, we observe four distinct phases of dome extrusion at Volcán de Colima including a prolonged west-directed dome growth followed by a removal of the dome with explosive crater excavation and finally renewed dome growth in two directions to the SW and NE. Modelling suggests that the emplacement and removal of the lava dome affected the local stress field and varied the direction of magma ascent and extrusion as well as the opening of new a vent, likely causing a conduit bifurcation. A growing lava dome will increasingly deflect conduit slip toward the added load, whereas an excavated crater will cause a diversion of slip direction toward the crater rim. The models provide a potential explanation to the observations made at Volcán de Colima and suggest that the dome growth stage in July 2015 reflects combined activity from a pre-established oblique conduit and a new vent formed in response to the earlier dome removal.

These results imply that small scale changes in crater morphology can sufficiently affect the local stress field to influence shallow magma ascent directions. This has implications for volcanic hazards posed by dome building volcanoes, as the position and growth directionality of the lava domes govern the direction of resulting PDCs or lava flows.

2.6 Acknowledgements

This is a contribution to VOLCAPSE, a research project funded by the European Research Council under the European Union's H2020 Programme/ERC consolidator grant ERC-CoG 646858. We thank the DLR for support; the acquisition of the spotmode TerraSAR-X data was realized through proposal GEO1505. DV-B is grateful to CONACYT-PDCAPN project 2579. We would like to thank Jose Manuel Álvarez Nieves for technical assistance during field work. We would also like to acknowledge Rogelio García Flores for providing helpful insight and data on Volcán de Colima photogrammetric surveys. Finally, we thank Sébastien Valade for providing useful scripts for visualization of the results.

Chapter 3:
UAS-based tracking of the Santiaguito Lava Dome, Guatemala

Edgar U. Zorn[1], Thomas R. Walter[1], Jeffrey B. Johnson[2], René Mania[1]

[1]German Research Centre for Geosciences GFZ, Potsdam, Germany
[2]Boise State University, Boise, United States

Abstract

Imaging growing lava domes has remained a great challenge in volcanology due to their inaccessibility and the severe hazard of collapse or explosion. Changes in surface movement, temperature, or lava viscosity are considered crucial data for hazard assessments at active lava domes and thus valuable study targets. Here, we present results from a series of repeated survey flights with both optical and thermal cameras at the Caliente lava dome, part of the Santiaguito complex at Santa Maria volcano, Guatemala, using an Unoccupied Aircraft System (UAS) to create topography data and orthophotos of the lava dome. This enabled us to track pixel-offsets and delineate the 2D displacement field, strain components, extrusion rate, and apparent lava viscosity. We find that the lava dome displays motions on two separate timescales, (i) slow radial expansion and growth of the dome and (ii) a narrow and fast-moving lava extrusion. Both processes also produced distinctive fracture sets detectable with surface motion, and high strain zones associated with thermal anomalies. Our results highlight that motion patterns at lava domes control the structural and thermal architecture, and different timescales should be considered to better characterize surface motions during dome growth to improve the assessment of volcanic hazards.

3.1 Introduction

Lava domes are among the most hazardous and unpredictable volcanic features, making safe observations and studies challenging for researchers. They form when the extruding lava is too viscous to flow far and thus piles up into a mound-shaped dome, typically steep sided with a flat top (Harris et al., 2004; James and Varley, 2012), although more complex morphologies can develop depending on extrusion rates and lava rheology (Watts et al., 2002; Heap et al., 2016) as well as resulting endogenous or exogenous growth styles (Fink et al., 1990). Episodes of lava dome growth have occurred at over 120 volcanoes since 1000 AD, sometimes lasting

several decades (Ogburn et al., 2015; Sheldrake et al., 2016). The many-faceted interactions between extrusion and lava degassing, cooling and crystallization can cause pressurization and gravitational instability in these systems (Sparks, 1997). Therefore, lava domes potentially produce sudden explosions or dome collapses. These are also the origin of destructive pyroclastic density currents, the volcanic hazard responsible for most fatalities during eruptions worldwide, with single events sometimes causing thousands of deaths (Witham, 2005), highlighting the need for accurate hazard assessments at growing lava domes.

To understand the growth processes and hazards associated with lava domes, critical data such as lava viscosity, dome morphology, growth rate, strain and strain rates, or surface temperature are required. Remote sensing observations on the growth patterns, commonly made by optical (Pallister et al., 2018), radar (Wang et al., 2015; Pallister et al., 2018; Mania et al., 2019; Walter et al., 2019b), and thermal (Werner et al., 2017; Krippner et al., 2018; Pallister et al., 2018) satellite sensors as well as ground-based (Johnson et al., 2008; Poland et al., 2008; Walter et al., 2019b) or aerial (James and Varley, 2012; Diefenbach et al., 2013; Zorn et al., 2019) photogrammetry, can reveal the morphology, size and growth rate of lava domes as well as indicate the direction of growth and most likely the hazards (Zorn et al., 2019). Similarly, insight on lava properties, such as viscosity, can provide valuable information on the hazard state, as they can control the explosive behaviour of a lava dome (Sparks, 1997). Lava viscosity data is particularly challenging to acquire because in-situ measurements are normally impossible, due to the high hazard or inaccessibility, and are instead retrospectively inferred point-wise by testing selected samples after eruptive activity has ceased (Cordonnier et al., 2009; Avard and Whittington, 2012). Indirect methods of viscosity assessment are possible (Rose, 1973; Harris et al., 2004; Belousov and Belousova, 2017), but limited to ground-based imaging. Another important aspect in assessing dome hazards are surface temperature measurements. These can be used to detect thermal anomalies on lava domes and reveal structures associated with deformation. A common structural feature is a ring-shaped anomaly observed around the flat top of a lava dome (Sahetapy-Engel and Harris, 2009; Hutchison et al., 2013). Although attempts to link such thermal anomalies to dome deformation have been made previously, the data resolution did not allow for conclusive statements (Salzer et al., 2017). Thermal imaging can also improve surface observations in low visibility due to degassing, cloudy conditions, or bad lighting (Thiele et al., 2017). Surface strain measurements during lava dome growth are rarely considered, but have been previously derived from fixed camera images (Walter, 2011) and can assist in identifying structural features. Despite these advances, detailed insights on the growth styles of lava domes, such as internal growth

(endogenous) and growth by extrusion of lava (exogenous), are limited and our understanding on the timescales involved are incomplete.

To overcome some of these challenges, Unoccupied Aircraft Systems (UASs) have been increasingly used in the observation of volcanic activity (Jordan, 2019; James et al., 2020). This is due to their increased ease of use, refinements in flight technology, capacity to carry large sensors, and improvements in flight durations and distances. This has opened many new possibilities in gathering and interpreting relevant volcanological data. Volcanic areas of varying sizes can be surveyed with relative ease, and Structure-from-Motion (SfM) photogrammetry allows for the creation of detailed 3D models and high resolution digital elevation models (DEMs), which may facilitate the identification of cm-scale features of lava flows and other volcanic surfaces (Favalli et al., 2018), as well as precise eruptive volumes (De Beni et al., 2019). Similarly, UAS surveys have been used to map and measure the topographic changes in active volcanic settings (Nakano et al., 2014). On a few lava domes, the high resolution capabilities of UASs have allowed for highly detailed insights into the structure of the fracture network (Darmawan et al., 2018a). Another UAS study conducted repeated surveys with thermal sensors on board that facilitated the assessment of the thermal inertia of a lava flow (Carr et al., 2019).

In this study, we remotely assess and characterize a lava dome and lava flow at Santa Maria volcano, Guatemala. A series of several adjacent lava domes are known as Santiaguito; the

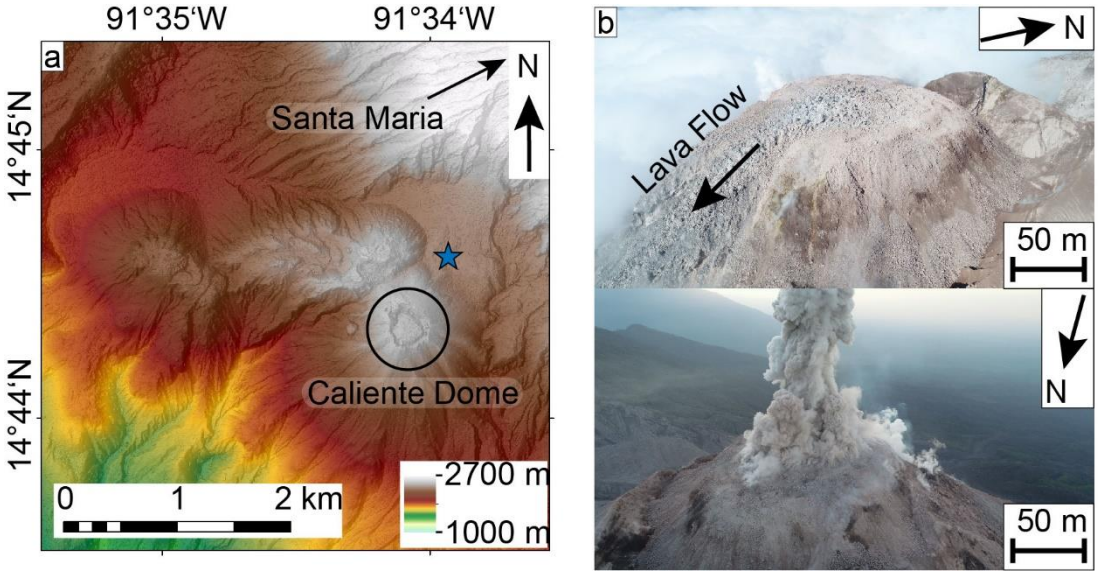

Figure 3.1: (a) Local DEM map of the study area built from Pléiades satellite data, the blue star marks the starting point of our UAS surveys. (b) Aerial photos of the Caliente lava dome showing the lava flow (upper photo, taken 18.02.2019 at 15:17 UTC) and a low intensity explosion (lower photo, taken 15.02.2019 at 15:18 UTC). (a) was plotted in ArcMap (v10.5, https://desktop.arcgis.com/de/arcmap/).

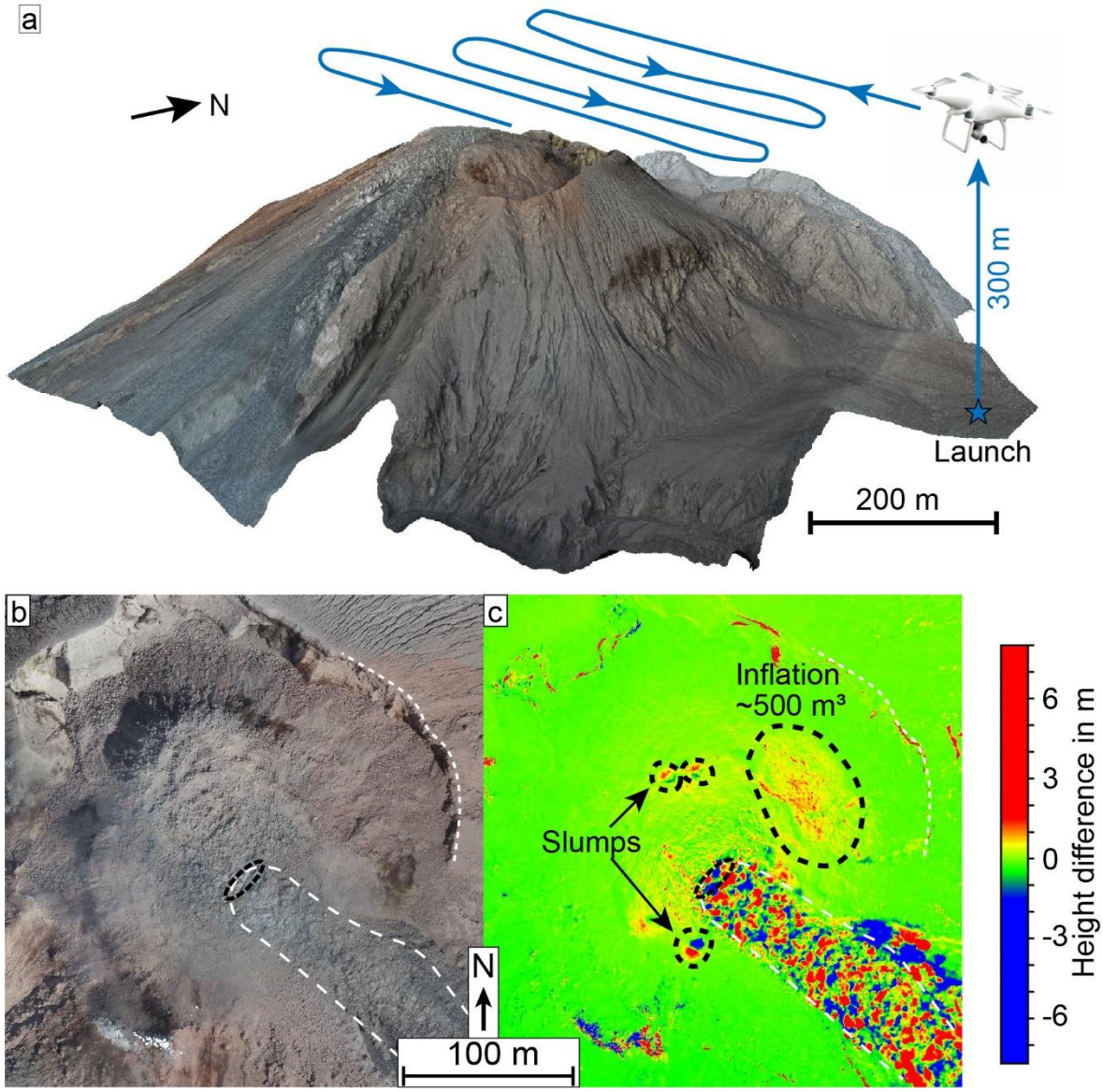

Figure 3.2: (a) A schematic of the UAS acquisition pattern and resulting SfM-model of a survey over the Santiaguito lava dome. The flight height was 300 m above the launch point and approx. 100 m over the top of the dome. (b) is an optical SfM-model of the dome surface and (c) a height difference map from two DEMs spanning a 3-day period (Survey C-D). The height difference map shows detailed surface changes, including an inflation as well as minor slumps on the dome surface. The scale is stretched to visualize the smaller deformation features against the large blocks moving with the lava flow. (a) was plotted in Agisoft Metashape (v1.5.2, www.agisoft.com) and (b, c) in CloudCompare (v.2.11, www.danielgm.net/cc/).

currently active one being called “Caliente” (Fig. 3.1a). The domes formed in the 1902 collapse crater of Santa Maria, one of the largest eruptions of the 20th century (Williams and Self, 1983), with the remnant peak overlooking the domes. Santiaguito has displayed episodic lava dome growth since 1922 (Rose, 1973) and maintained eruptive activity until today, making it ideal to study lava dome processes. Previous studies revealed short term deformation processes associated with gas pressurization during eruptions (Johnson et al., 2008). Here, we used UASs

equipped with optical and thermal infrared cameras to image slow deformations of the lava dome surface (Fig. 3.2a). We construct DEMs and orthophotos, then trace the motions of pixels and use this data to delineate the 2D deformation field and gain insight on flow velocities, extrusion rates, surface strain, lava viscosity, and temperature anomalies over different time periods.

3.2 Results

During fieldwork in February 2019, we performed repeated UAS surveys over the active "Caliente" lava dome, part of the Santiaguito complex at Santa Maria volcano, to assess dome morphology and structure. Topographic models generated with the SfM workflow show a flat-topped lava dome with steep sides and a blocky surface (Fig. 3.2a, b). The dome has a near-circular shape with a diameter of ~200 m and occupies an area of approximately 35,000 m^2. It

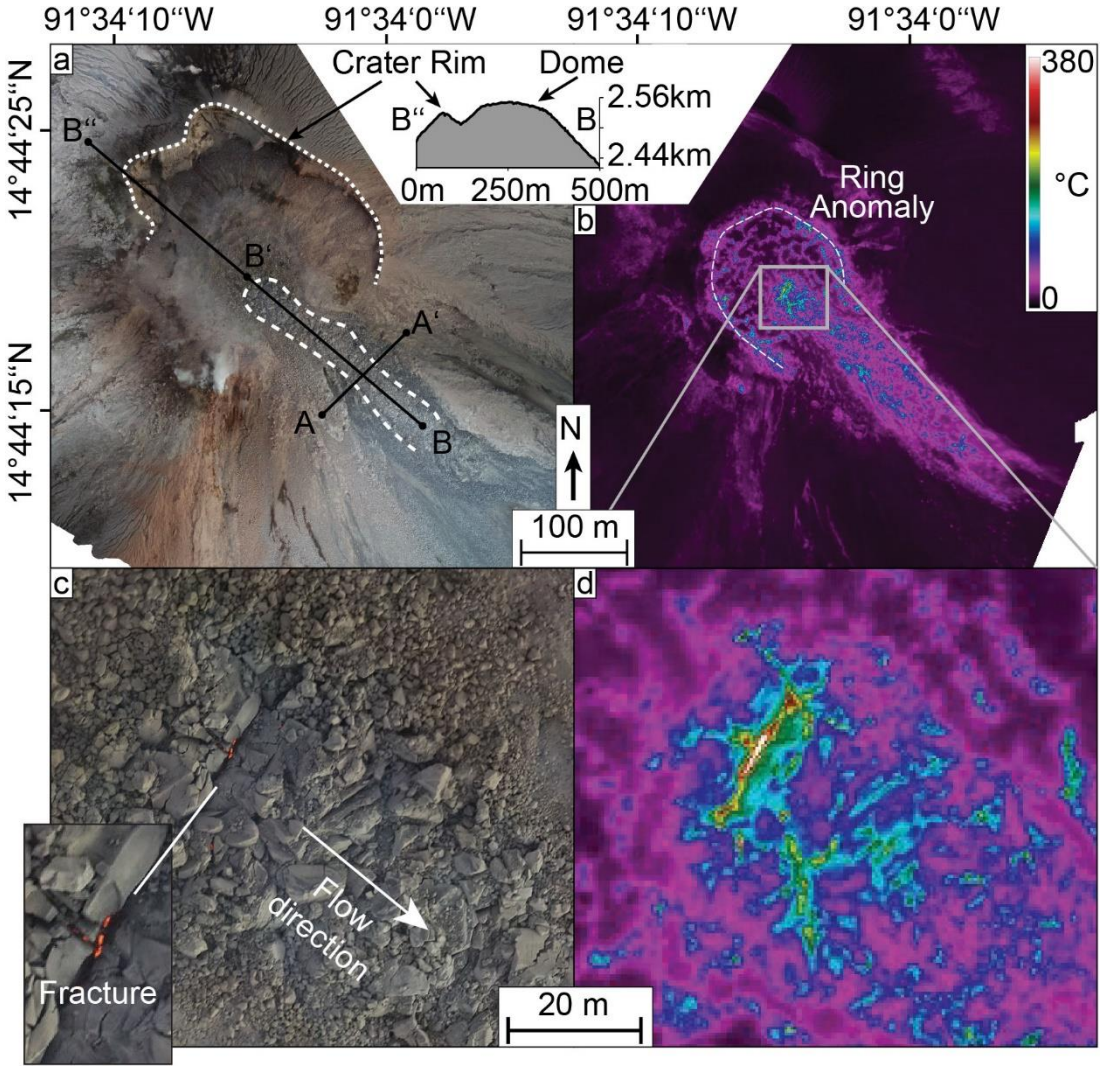

Figure 3.3: Optical (a, c) and thermal (b, d) orthophotos of the active Caliente lava dome and lava flow with a topographic profile. The profiles are further used in fig. 3.6.

is situated within a larger explosion crater created in 2016 (Lamb et al., 2019) and overtops this crater to the southeast, where a ~35 m wide lava flow is advancing down the flank (Figs. 3.1b, 3.3). The lava flow emerges from the summit dome as an embedded feature, moving laterally. It then forms its own channel on top of the outer dome flank. The flow is also rather short as bits of the lower parts repeatedly broke away, resulting in minor rockfalls and very small pyroclastic flows on the north-east side. The thermal model, constructed from UAS-based thermal camera images, reveals high temperature areas on the dome, showing a ring-like temperature anomaly around the outer margins of the flat top (Fig. 3.3b), reminiscent of ring fractures previously observed at Santiaguito (Bluth and Rose, 2004). The lava flow is also distinguishable, having generally higher apparent temperatures compared to the dome surface (Fig. 3.3b). In the centre of the dome, a large fracture marks the start of the lava flow (Fig. 3.3c, d). This fracture is the thermally most active area and incandescence could be observed from it during darkness. It is also located orthogonal to the flow direction, suggesting it to be tension-induced from the lava flow movement.

Calculating height difference maps between the topographic models (spanning a 3-day period) reveals a distinct pattern of volume changes associated with the lava flow due to the movement of the large blocks on the surface (Fig. 3.2c), however, any overall volume gain associated with the lava extrusion could not be determined as the lateral lava extrusion did not cause major surface uplift and the lower parts repeatedly broke away. The flow thus effectively functions as a "conveyor belt" of lava from the dome down the flank and consequently the lava volume at the dome remains nearly constant. Moreover, we detect an inflation volume of ~500 m^3 on the northeast side of the lava dome (Fig. 3.2c in the marked area) and a surface uplift of ~ 1 m. Due to the very low volume and the high signal to noise ratio from the lava flow block (some of which exceed 8 m in size) these values should be seen with caution. Some smaller slumps on the perimeter of the dome are also visible by the removal and addition of material in downslope direction, forming a radial pattern around the dome centre (Fig. 3.2c).

To gain further insight on the lava flow and dome movements and improve on the SfM analyses, we then tracked pixel-offsets in consecutive SfM-generated orthophotos using particle-image-velocimetry (PIV) (see methods) to track the motion of the lava dome surface, and measure surface deformation and flow velocities. This was applied on three pairs of consecutive orthomosaics with varying repeat times between flights (38 minutes, 3 hours, and 3 days), all showing the dome from the same vertical perspective in high resolution. We note that small explosions occurred between surveys (Fig. 3.1b), however, no associated surface changes were observed and they did not noticeably affect our measurements. Results of the PIV show two

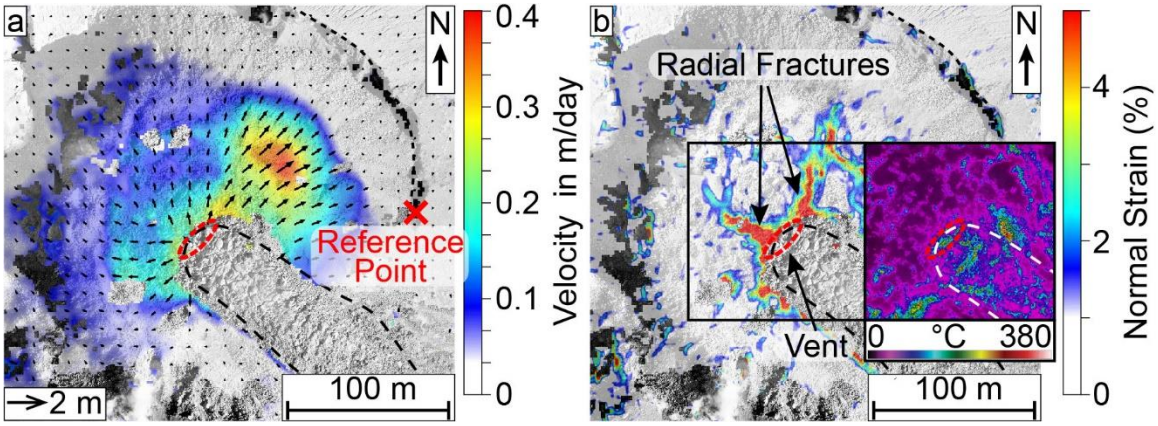

Figure 3.4: (a) deformation and (b) normal strain plot (normal in the image plane) for the lava dome expansion over the course of 3 days (Survey C-D), showing significant movement of the northeast dome side, as well as extending radial fractures near the lava flow vent. The arrow length in (a) shows the measured displacement. Survey C was performed on 15.02.2019 at 15:20-15:33 UTC and survey D on 18.02.2019 at 14:38-14:50 UTC. (b) also includes a thermal view on the vent, also captured on 18.02.2019 at 11:49-12:19 UTC. This shows that active structures of the lava flow produce significant thermal anomalies, however the radial fractures associated with the slower dome growth are not visible. The lava flow and crater rim are marked for orientation, the reference point for the shift and rotation correction is marked in (a). The figures were plotted in LaVision DaVis (v10.0.5.50575, www.lavision.de/de/products/davis-software/).

separate scales of surface deformation; lateral expansion of the dome surface detectable over 3 days (Fig. 3.4a) and a lava flow motion detectable within minutes to hours (Fig. 3.5a, b). The lava flow could not be tracked over the flight interval of 3 days as the surface changes were too significant to allow feature-based pixel tracking, resulting in decorrelation for that area (Fig. 3.4). Instead the tracking highlights a radial expansion of the dome surface moving from the centre outwards, but at much slower rates compared to the active lava flow (Figs. 3.4a, 3.5a, b). The magnitude of the expansion also coincides well with the volume increase detected by the DEM comparison (Fig. 3.2c). Localized expansion of the dome was largest on the north-east side with up to 1.2 m, equalling a velocity of 0.4 m/day (Fig. 3.4a). The expansion affects the dome only, whereas the crater appears stable. Moreover, the expansion establishes discrete zones of normal strain localization that emanate from the dome centre and the lava flow vent (Fig. 3.4b), which are otherwise not visible and do not show up as a thermal anomaly (Fig. 3.4b). The strain localizations are partitioning the dome carapace into 4-5 main blocks. The dome motion resembles a lateral spreading, but with a slight bulging on the north-east, represented by a maximum height increase of ~1 m (c.f. fig. 3.2c).

The shorter survey times of 38 minutes and 3 hours permit the tracking of the lava flow motion. While data is distorted towards the margins of the images (Fig. 3.5; see error discussion in methods), the lava flow is clearly distinguishable by its high displacement field. The flow vectors of the 38 min survey show a maximum displacement of 0.4 m, corresponding to a velocity of approx. 15.2 m/day (Fig. 3.5a). For the 3 h survey (realized later on the same day), the maximum displacement is 2.0 m corresponding to a velocity of 15.4 m/day (Fig. 3.5b). The 3 h survey (Fig. 3.5b) generally shows the lava flow more clearly compared to the shorter 38 min survey, where movement is only detected in the upper flow portion (Fig. 3.5a). This is likely due to the higher absolute displacement over the longer survey time period (2.0 m and 0.4 m, respectively), causing a much more accurate and detailed result against the background errors. The active lava flow is further outlined with the computed shear strain, showing the

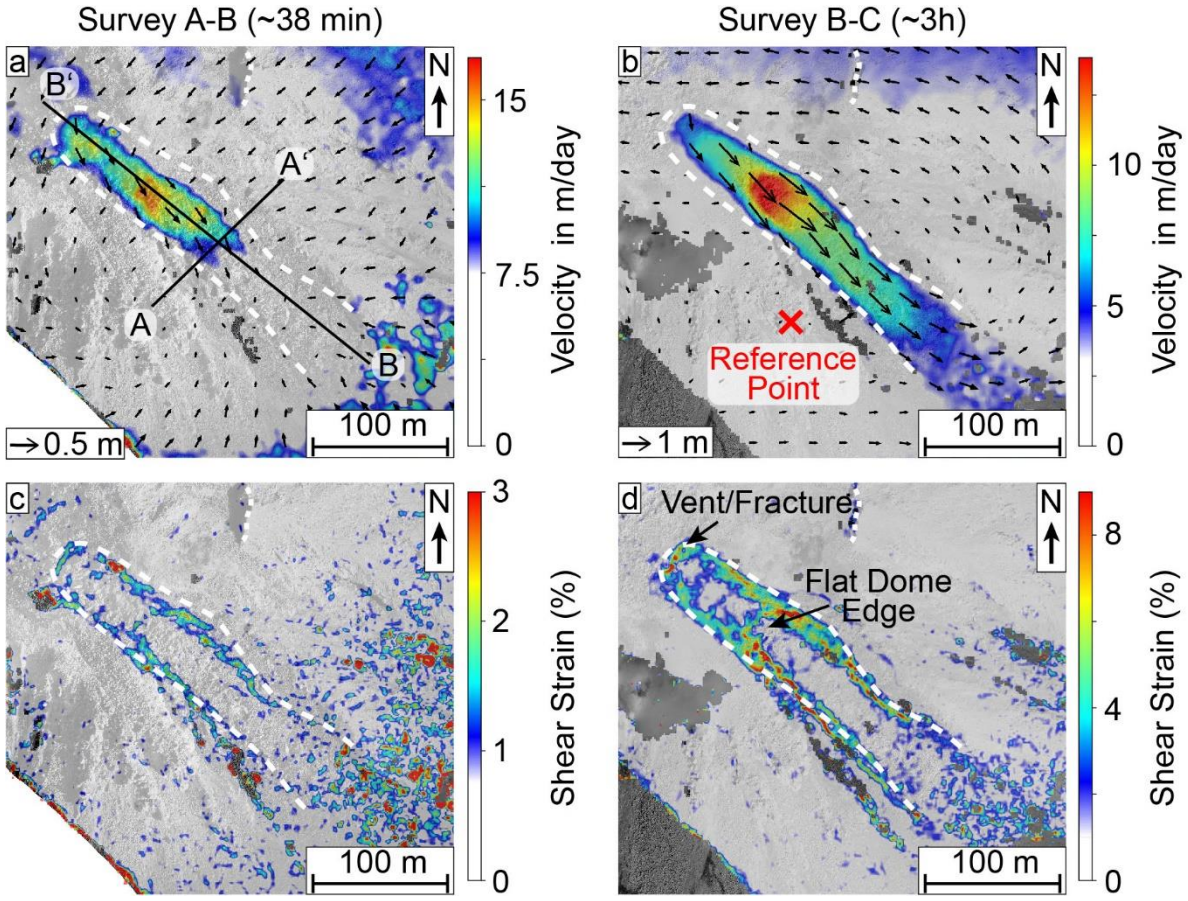

Figure 3.5: (a)-(b) flow velocity and (c)-(d) shear strain plots with 2D vector data for the lava flow. The arrow length in (a, b) shows the measured displacement. The flow is clearly distinguishable in all plots and the scales are adjusted to show the measured values over the background noise. The flights here were conducted on the 15.02.2019, survey A was performed at 11:52-12:18 UTC, survey B on 12:37-12:43 UTC and survey C at 15:20-15:33 UTC. The lava flow and crater rim are marked for orientation, the reference point for the shift and rotation correction is marked in (b). The figures were plotted in LaVision DaVis (v10.0.5.50575, www.lavision.de/de/products/davis-software/).

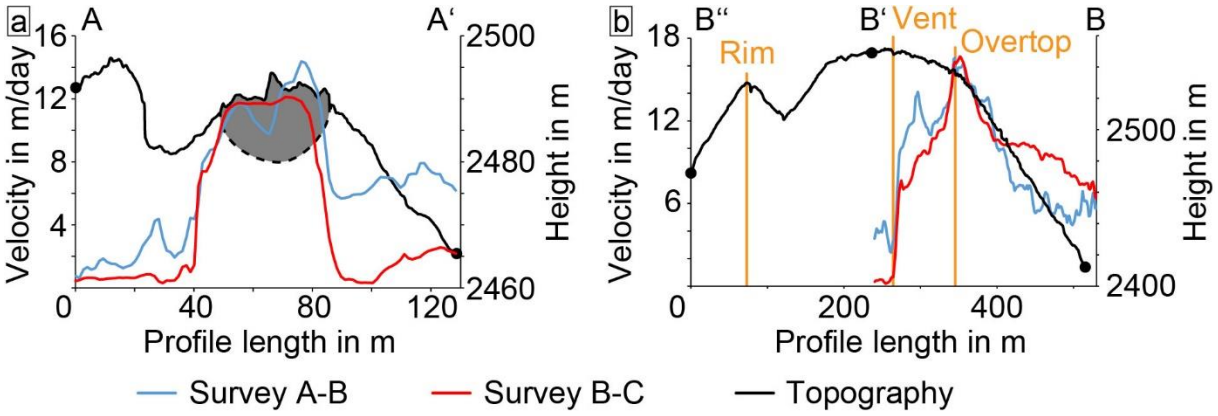

Figure 3.6: Profile for the measurements as marked in figs. 3.3 and 3.5: (a) across the lava flow and (b) lengthwise over the dome and downhill on the flank. The estimated active flow field has been marked in grey. The flow depth is estimated from the flow thickness in the SfM data.

margins of the flow as high strain regions and the flow centre as a low strain region (Fig. 3.5c, d). Moreover, high surface temperature regions correlate well with high shear strain regions at the flow margins as well as the flat dome edge (c.f. figs. 3.3b, 3.5c, d). A profile across the lava flow allows for a clear characterization of the flow dimensions, showing a sharp increase in deformation on the lava flow sides, but a stable value in the flow centre (Fig. 3.6a). The displacement velocity in flow direction shows a gradual increase beginning from the fracture and hitting a spike at the point of overtopping the flat dome surface onto the flank (Figs. 3.5a, b, 3.6b).

We gained further insight into the lava extrusion by selecting three representative points at different flow distances from the vent (Table 1, Appendix C1) from the determined velocity fields (38 min and 3 h surveys) to derive the apparent viscosity of the lava flow. The apparent viscosity of the recent lava flow ranges from $2.6*10^9$ Pa·s to $1.3*10^{10}$ Pa·s and is very consistent between the two survey comparisons, with a notable viscosity increase with distance from the vent. Similarly, we extracted the extrusion rate from the channel dimensions and the lava flow velocity under the assumption that the measured flow rate is equal to the extrusion rate. The resulting values range between 0.04 to 0.06 m^3/s.

Variable	Survey A-B (Flat Top)	Survey B-C (Flat Top)
Time Difference	38 min	3 h
Displacement	0.33 m	1.24 m
ρ	2500 kg/m^3	2500 kg/m^3
g	9.81 m/s^2	9.81 m/s^2
h	~15 m (assumed)	~15 m (assumed)
a	~17 m	~17 m
α	~10°	~10°
V	1.45*10^{-4} m/s	1.15*10^{-4} m/s
η	**2.6*10^9 Pa·s**	**3.3*10^9 Pa·s**
F	**0.06 m^3/s**	**0.05 m^3/s**

Variable	Survey A-B (Overtopping)	Survey B-C (Overtopping)
Time Difference	38 min	3 h
Displacement	0.43 m	1.99 m
ρ	2500 kg/m^3	2500 kg/m^3
g	9.81 m/s^2	9.81 m/s^2
h	~10 m	~10 m
a	~17 m	~17 m
α	~36°	~36° ± 3°
V	1.89*10^{-4} m/s	1.84*10^{-4} m/s
η	**4.5*10^9 Pa·s**	**4.6*10^9 Pa·s**
F	**0.05 m^3/s**	**0.05 m^3/s**

Variable	Survey A-B (Downhill)	Survey B-C (Downhill)
Time Difference	38 min	3 h
Displacement	0.32 m	1.15 m
ρ	2500 kg/m^3	2500 kg/m^3
g	9.81 m/s^2	9.81 m/s^2
h	~15 m	~15 m
a	~17 m	~17 m
α	~39°	~39° °
V	1.40*10^{-4} m/s	1.06*10^{-4} m/s
η	**9.7*10^9 Pa·s**	**1.3*10^{10} Pa·s**
F	**0.06 m^3/s**	**0.04 m^3/s**

Table 3.1: Summary of the viscosity η and flow/extrusion rate F calculation via the flow rate method. The bulk density ρ was inferred from Johnson et al. (2008), the height of the lava flow h, the flow half width a, and the slope α were measured using the SfM-Models. Since we could not measure the channel depth embedded in the flat dome top, we assumed a similar 15 m based on the similar flow speeds and flow width compared to the downhill part. The data for individual Surveys can be found in Appendix C1, C3-8.

3.3 Discussion

The movement of the dome surface was observed in the form of two separate deformation processes with different timescales. Firstly, an expansion of the lava dome on the order of decimetres per day (Fig. 3.4), and secondly a lava flow with flow velocities on the order of several meters per day (Fig. 3.5). Both represent a different style of dome growth; the expansion and low volume increase indicate endogenous growth behaviour while the lava extrusion can be considered exogenous. Although we cannot rule out that these motions occur in sequence (e.g., first dome expansion, then lava extrusion or vice versa), it is more likely that they occur in association or even simultaneously. This is supported by the lava flow surface changing during the time the expansion was observed, and we did not observe any changes in the type of activity during our fieldwork (i.e., slow lava extrusion and low intensity explosions). Here, the expansion motion of the lava dome could be attributed to endogenous growth and lateral spreading supported by the volume increase on the northeast side (Fig. 3.2c), the radial outwards motion of the lava dome flanks (Fig. 3.4a), and the occurrence of radial fractures (Fig. 3.4b). Endogenous growth occurs by gradual intrusion of magma into the dome, which is non-reversible. This contrasts to deformation associated with short term gas-pressure changes described in previous studies (Johnson et al., 2008), which is reversible and represents a third timescale for potential dome deformation and was not observed here.

Interestingly, not all structures are associated with thermal anomalies. The vent fracture, the high shear strain regions, and the edge of the flat dome top show high temperatures, likely due to the opening of fractures as a result of the lava movement (c.f. figs. 3.3b, 3.5). On the other hand, the radial fractures associated with the slower dome growth are not visible in the thermal infrared maps (Fig. 3.4b). This is either due to the slow opening of the fractures and effective cooling, or they do not provide pathways for hot fluids to escape.

Since the lava extrusion at Santiaguito occurred at nearly the same rates in both our measurements, our findings support the idea of very steady magma supply rates, which was hypothesized in earlier studies at this volcano (Harris et al., 2003). The measured extrusion rates of 0.04-0.06 m^3/s are very low, but consistent with previous assessments for Santiaguito in times of low activity (Harris et al., 2003), although during more active cycles values have been observed to exceed 2 m^3/s. Other studies also find generally higher extrusion rates, such as 0.5-1.6 m^3/s between 2001 and 2002 (Harris et al., 2004), 0.2 m^3/s in 2002 (Bluth and Rose, 2004), and a mean of 0.43 m^3/s between 2000 and 2009 (Ebmeier et al., 2012). The extrusion

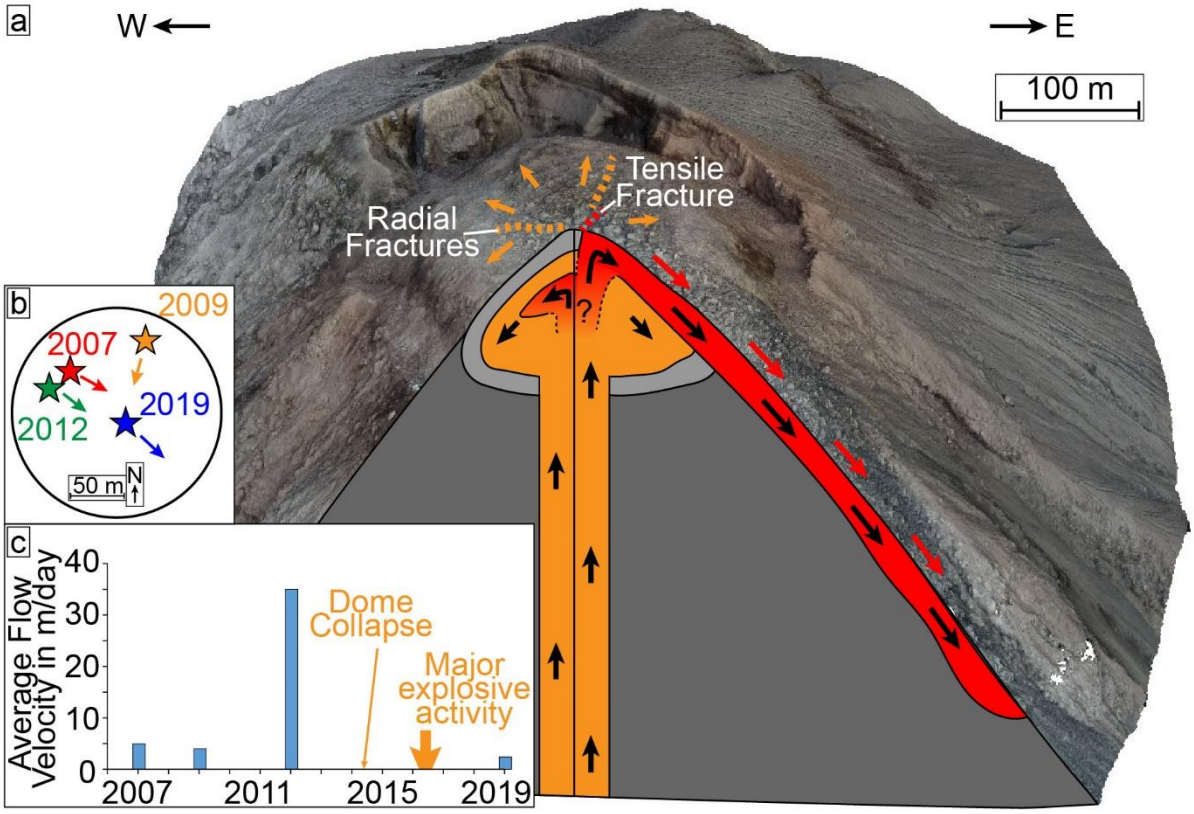

Figure 3.7: (a) Sketch of the inner lava dome structure inferred from our topographic and deformation data. The detected active lava flow extrusion and intrusion of the lava into the dome are marked in red, the current dome and conduit in orange. Fractures associated with both motions are also included. The grey area around the dome represents a brittle dome carapace. (b) Simplistic circle sketch representing the lava dome surface and showing the approximate vent position (star) and dominant flow direction for the different surveys. (c) Timeline plot showing the average dome surface flow velocities at four available data points in 2007, 2009, 2012 and 2019 (see Appendix C2). A major dome collapse event and a phase of increased activity reported by Lamb et al. (2019) are marked. (a) was plotted in Agisoft Metashape (v1.5.2, www.agisoft.com).

rates at Santiaguito have thus slowed very significantly, although activity was still intermittently higher during 2012 (Ebmeier et al., 2012).

With the additional dome expansion, our measured extrusion rate may be slightly underestimating the magma influx into the dome, although judging by the very minor volume increase in the dome this is likely not significant. Part of the magma is extruded to feed the lava flow, whereas another part is intruded into the dome causing it to slowly expand (Fig. 3.7a).

Our calculations resulted in apparent viscosities on the orders of 10^9 and 10^{10} Pa·s for the dome lava, which are similar to viscosity measurements determined for dacite lava flows at Santiaguito being on the same order of 10^9 to 10^{10} Pa·s calculated by both the Jeffreys equation (Harris et al., 2004) and measured in uniaxial compression experiments (Avard and

Whittington, 2012). Studies on older lava flows (1930 and 1960s) further noted that lava viscosities increased with greater distance from the vent, but also measured lower lava viscosities of $5*10^7$ Pa·s in the 1930s (Rose, 1973). In agreement with these studies, we also find a notable increase of the lava viscosity with greater distance from the vent, likely a result of the slow movement as well as gradual cooling and degassing, causing microlite crystallization and solidification, which can increase lava viscosity by up to several orders of magnitude (Sparks, 1997). Here, within less than 200 m flow distance, the viscosity of the 2019 lava flow increased by almost one order of magnitude. Thus, we determine that our data fit very well with previous assessments and are in agreement with these studies within an order of magnitude.

Rheological investigations at other silicic dome building volcanoes indicate that viscosity may vary significantly. At Soufrière St. Vincent volcano, Lesser Antilles, theoretical estimations yielded a viscosity of 2×10^{11} Pa·s based on the rates of lateral spreading of the dome (Huppert et al., 1982). Rheological testing on several dome lavas from Volcán de Colima, México, Bezymianny, Kamchatka, and Unzen, Japan, showed values between approx. 10^9 and 10^{12} Pa·s (Lavallée et al., 2007). A lava flow originating from Volcán de Colima, México, in 1998-1999 measured 10^9 to 10^{10} Pa·s (Navarro-Ochoa et al., 2002), which are closest to the rheology of Santiaguito. However, more well-established models (Giordano et al., 2008) predict viscosities of up to 10^{14} Pa·s, but are difficult to compare to dome lavas as the viscosities will have a broad range strongly depending on the state of cooling, outgassing, and crystallization. These factors also influence the flow regime, with our viscosity calculations assuming the lava to behave as a Newtonian fluid (Chevrel et al., 2013). Since the occurrence of high shear stress is limited to the margins of the flow (Fig. 3.5c, d), the latter assumption is likely valid for the inner parts of the flow, where we made the measurements, with the shearing at the channel margins acting as a conveyor belt. However, a transition to non-Newtonian behaviour must occur on the lower flank since the repeated breaking-off of the lava flow front indicates brittle behaviour under the acting strain rates.

The seemingly rather low apparent viscosity (compared to other silicic lavas) observed at Santiaguito in 2019 generally agrees with the ongoing dome extrusion characteristics with only low intensity explosions. However, changes in lava viscosity resulting from changing extrusion rates, increased cooling or degassing can drastically reduce the free escape of volatiles, resulting in increased explosive activity (Sparks, 1997). Particularly, changes in viscosity will affect the failure mode (brittle-ductile) of the dome magma and control surface strain and, in turn, the development of fractures on the dome surface (Hornby et al., 2019). Changing viscosity may

also impact the mode of extrusion between endogenous and exogenous growth (Hale and Wadge, 2008).

We compared our UAS results to previous ground-based imaging realized from the top of the adjacent Santa Maria summit (see Appendix C2). This position provides an oblique view on the top of the Caliente dome, and allows for an estimation of the flow velocities on the dome surface. From this distance, we could not determine the growth of the dome, but we could measure the ongoing lava extrusion. Here, data is available from 2007, 2009, and 2012 showing that the lava flow had velocities on the order of 2-5 meters per day (Fig. 3.7c). A more active period was observed in 2012 with flow speeds being on the order of 30-40 meters per day (Fig. 3.7c), which is in agreement with observations from other campaigns in that period (Ebmeier et al., 2012; Rhodes et al., 2018). While no flow velocity data is available after 2012, other studies report low activity, aside from a major dome collapse in 2014 (Lamb et al., 2019). The low activity lasted until early 2016, which was characterized by both strong explosions and increased lava extrusion (Lamb et al., 2019). This high activity ceased in late 2016 and by 2019 activity had reduced to similar flow velocities as before 2012 (Fig. 3.7c). Such transitional changes are a common trend at Santiaguito since long periods of low and mostly effusive activity are intermitted by periods of heightened explosive activity (Harris et al., 2003; Rhodes et al., 2018; Lamb et al., 2019). An extrusion rate could not be calculated for the ground-based imaging as no detailed topography data are available to characterize the flow channels. Here, our data only covers short observation intervals, so the lava flow velocities or extrusion rate may vary significantly, but the consistent measurements during low activity further suggest the lava flow to be fed from a rather constant magma supply. More regular survey data could help to identify, characterize, and potentially forecast such changes in activity.

We further observe that the lava flow directions have varied only slightly and are dominantly towards the southeast, only being directed south in 2009 (Fig. 3.7b). This is surprising since similar instances of increased explosive activity at other dome-growing volcanoes such as Volcán de Colima, Mexico, can reshape the edifice morphology and change lava flow directions (Zorn et al., 2019). The persistent morphology and activity at Santiaguito suggest that the shallow structures affecting dome growth and flow direction are also persistent and largely unaffected by more intense eruptive phases. This is likely a result of the relatively low lava viscosity compared to other dacite lavas as well as the open outgassing conditions attributed to Santiaguito (Holland et al., 2011; Johnson et al., 2014; Lamb et al., 2019). Furthermore, it is likely that the magma plumbing system at the Caliente dome has not undergone repeated

changes to magma-pathways as comparable dome-building volcanoes such as Volcán de Colima (Lavallée et al., 2012; Salzer et al., 2014; Zorn et al., 2019), although the entire Santiaguito dome complex has formed due to such changes over the course of the last 100 years. However, changes in the degassing system, e.g., the permeability by strain localisation in the conduit (Farquharson et al., 2016), will affect the explosivity of the volcano and should be monitored closely to predict potential changes.

Explosive activity (Fig. 3.1b) can considerably reshape the surface of a lava dome, or crater, and may introduce potential artifacts into our analysis. We counted the number of explosions during the study period using the cyclic inflation signals from a tiltmeter station deployed near the dome and our UAS-launch site. One explosion occurred during the 38 min survey, 2 during the 3 h survey, and 22 during the 3 days survey. By visual observations we find that the explosions were of low intensity without any ballistics. Here, the explosions occurring during lava extrusion are thus more reminiscent of degassing pulses through a relatively open system and it is unlikely that they significantly impacted the surface morphology of the dome and we observed no changes in our survey data. Hence, we do not think that the explosive activity affected our results.

As this study demonstrates, displacements of the lava dome surface occur on different scales. Campaigns using fixed cameras at the summit of Santa Maria in the past years have documented both very rapid dome uplift (10^0-10^1 s) coinciding with explosions (Johnson et al., 2008) as well as slower processes (10^2 to 10^3 s) associated with localized bulging of the dome surface. For example, in 2012, a ten-minute transient bulging event with uplift of several meters was proposed using a 1-minute time lapse sequence from a fixed summit camera (Johnson et al., 2014). While the repeat survey time and relatively low activity of the Santiaguito lava dome during this study did not allow us to capture such movements, we could discriminate variations in surface motion of extruding lava as well as radial expansion and bulging of the dome by intrusive growth. Considering the potentially severe hazards displayed by growing lava domes, we also note that UASs represent a fast and safe way to gather important data such as dome deformation and lava properties as demonstrated in this study. This makes them an excellent tool to assess the activity and hazard potential of an active lava dome, especially in crisis situations.

3.4 Methods

Fieldwork:

During our fieldwork in February 2019 we performed UAS survey flights over the active Caliente vent at Santiaguito volcano with multiple drones and sensors at a height of approx. 100 m over the lava dome (Figs. 3.1a, 3.2a). The flights were recorded using high-resolution optical photos and an additional thermal camera. The optical images were acquired with the onboard sRGB camera of our UAS (DJI Phantom 4 Pro) with a resolution of 5472 ×3078 px and a sampling rate of 0.5 Hz. The thermal images were acquired with a FLIR TAU 2 (9 mm lens), stored in a TEAX ThermalCapture frame grabber, and processed with the Thermoviewer software (v3.0.4). These provided radiometric temperature data and had a resolution of 640 ×512 px with a sampling rate of 8 Hz. Four flights could successfully be processed into 3D-Models and yielded good results via PIV (named surveys A, B, C and D). These were recorded over different timespans of 38 min (A-B), 180 min (B-C) and ~3 days (C-D).

Tri-stereo photogrammetry using Pléiades satellite data:

To georeference the UAS datasets acquired at Santiaguito volcano, we tasked high-resolution optical Pléiades satellite imagery on 15.01.2017. Its tri-stereo capability with one near-nadir and two off-nadir images enables the construction of a highly detailed topography model of the volcano and its surrounding. We processed the three panchromatic images with the ERDAS IMAGINE Photogrammetry toolbox similar to the working process described by Bagnardi et al. (2016), post-processed the resulting point cloud with CloudCompare, and gained a topographic model with a spatial resolution of 5 m/px.

SfM-Photogrammetry:

We performed Structure-from-Motion (SfM) photogrammetric processing (Westoby et al., 2012) using Agisoft Metashape 1.5.2 on all optical and thermal surveys to reconstruct the 3D environment of the active lava dome (Fig. 3.2a), enabling us to construct both high resolution DEMs from dense point clouds as well as detailed orthophotos. The survey photos were acquired in nadir or near-nadir position, with only some single photos being taken at an oblique angle to improve the model quality (Nesbit and Hugenholtz, 2019). The difficult and hazardous terrain did not allow for sufficient ground control points to create a reliable georeferencing. Instead, we utilised the photogrammetric DEM built from Pléiades data for more accurate and consistent georeferencing by point matching the models. In this process, the SfM-built DEM is attached to the Pléiades one by identifying recognizable features in both datasets. The final

referencing had an RMS-error of 3.3 m, but due to the high resolution of the SfM models, they could be better referenced relative to each other, meaning that all other SfM-DEMs now use the pre-referenced Survey D as a basis. This minimizes the relative errors between the DEMs and allows for high-precision data comparison. Here, all models are within 0.3 m accurate relative to each other (see Appendix C3-8).

In order to allow feature tracking, orthophotos (georeferenced nadir photos) of the study area are generated by projecting the survey photos onto the 3D-surface of the DEMs. While this reduces 3D data to 2D, it has the advantage that the image texture resolution of the resulting photo is increased and thus exceeds the spatial resolution of the DEMs, allowing to resolve more detailed ground features and motions in a single large photo. The orthophotos can be found in the Appendix C3-8 and the DEMs can be seen as hillshade maps in Appendix C9-11.

Particle image velocimetry:

For the pixel-offset tracking we employed a particle-image-velocimetry (PIV) (Pan et al., 2009) method for the four high-resolution orthophotos taken from the SfM workflow using LaVision DaVis 10.0.5 to track and calculate changes on the lava dome and lava flow surface based on the intensity value of the orthophotos. This enabled us to accurately quantify the velocity and direction of deformation and flow on the active dome. The maximum normal and shear strain values were also calculated based on the eigenvalues of the 2D stress tensor (at 45° for the shear strain), allowing insight into the nature of deformation. Similar techniques have previously been applied to characterize landslide (Lucieer et al., 2013) and glacier (Patel et al., 2019) motions using either UAS-based photos or satellite images. Here, we add to this method by measuring very low displacement motions in high detail and over different timescales.

Apparent viscosity calculation:

Combined with the 3D terrain reconstruction from the SfM workflow we are further able to constrain all parameters required to estimate the lava viscosity based on the Jeffreys equation (Jeffreys, 1925). This has been used to characterize lava viscosity in several previous studies (Moore, 1987; Panov et al., 1988; Harris et al., 2004; Belousov and Belousova, 2017). Here we used the formula applied to the surface flow behind the flow front adapted to a semi elliptical channel shape after Moore (1987), which is best suited to account for the unknown channel geometry (Lev and James, 2014):

$$\eta = \rho \cdot g \cdot \sin(\alpha)/(V) \cdot \left\{ \frac{h^2}{2 \cdot \left[\left(\frac{h}{a} \right)^2 + 1 \right]} \right\} \qquad (4)$$

where η is the apparent viscosity of the lava, ρ the bulk density, g the gravity acceleration, h the thickness of the lava flow, a the flow half-width, α the slope of the surface, and V the velocity of the flow. The flow rate F was further calculated as a representative value for the extrusion rate, assuming the two values are equal, by multiplying the semi-elliptical channel cross-section area with the measured flow speed.

$$F = \frac{\pi \cdot h \cdot a}{2} \cdot V \qquad (5)$$

This was applied to the three points of the lava flow representative of the flow movements, one near the vent on the flat top of the dome, one near the overtopping of the breached crater to the southeast, and one down the flank. We used the points where the deformation was largest to avoid influences by channel shear and represent the lava flow parts most unaffected by cooling and solidification.

Errors and data accuracy:

The UAS orthophotos achieved a resolution better than 7 cm, allowing the recognition of single blocks and fractures. The thermal data provided lower resolutions of 41 cm or better but allowed additional insight into the apparent surface temperatures. The measured apparent temperatures can vary depending on a number of factors (Spampinato et al., 2011) including object emissivity, humidity, surface roughness, acquisition angle, object distance, solar radiation, and the presence of ash or gas in the atmosphere. Here we assume similar conditions to previous studies at lava domes and correct the atmospheric attenuation in the Thermoviewer software based on an emissivity of 0.95, a transmissivity of 0.7 as well as environmental and path temperatures of 10 C° (Stevenson and Varley, 2008; Walter et al., 2013b). While the temperature measurements are as accurate as possible, the values should still be seen with caution, as some factors could not be considered for correction. One factor impacting our results is the acquisition angle, the sensor is mounted vertically to the UAS but tilts slightly with the drone during flight. This causes drifts in the measured temperatures on the order of a few degrees. It is also likely that some temperatures are underestimated due to the sub-pixel imaging of features like the tensile fracture on the dome top (Fig. 3.3c, d). Here we kept the apparent temperature measurements as accurate as possible by conducting the thermal surveys before sunrise, thus omitting artifacts from solar heating or reflection.

As a result of the georeferencing errors, a slight shift between compared survey orthophotos is expected. Similar SfM-based studies (Lucieer et al., 2013; Darmawan et al., 2018a; Zorn et al., 2019) commonly achieve accuracies on the order of cm to dm and ours have an error of less than 0.30 m for the optical models. However, the maximum lava flow movement between

Survey A-B was just above that with about 0.43 m. To maximize the distinction between moving and stationary components, we employed an additional shift and rotation correction based on contrast-rich stationary points (here, the crater rim or the volcano flank, see figs. 3.4, 3.5), thus further optimizing the accuracy of the PIV. As a result, the deformation values are very reliable, and an estimate for the systematic shift error can be taken from the background values in the lava flow surrounding (approximately of the order of 0.01-0.10 m). Despite the additional shift and rotation correction, we still note an increasing error towards the margins of our models (Fig. 3.5a, b). We attribute this to limitations in the SfM reconstructions on the borders of a photogrammetric model, where a lower degree of overlap between photos causes a lower accuracy of the reconstructed points. In the case of the shorter survey with 38 minutes, the resulting lower effective displacements make the survey more susceptible to such background errors. However, since we picked our velocity data mostly in the central areas of the models, our measurements should still be reliable are likely not affected to a large degree as is confirmed by the very similar measured flow speeds.

The largest expected errors for the Jeffreys equation are systematic in nature (i.e. the margin effects) and we picked our values either from the SfM-models or the PIV data. We tested the robustness of our calculations by systematically varying the input parameters. We find that with the input parameters being accurate to within ~20% of their value, our calculations are accurate to within an order of magnitude. This makes our approach an excellent tool to gain quick first order data on lava viscosity and it should be suitable to assess the type of activity and potential hazards at erupting volcanoes.

3.5 Data availability

The datasets generated during and/or analysed during the current study are available in the GFZ Data Services under https://doi.org/10.5880/GFZ.2.1.2020.001 (Zorn et al., 2020c). This includes the UAS orthophotos, DEMs and point louds. Alternatively, the datasets are available from the corresponding author on request.

3.6 Acknowledgements

This is a contribution to VOLCAPSE, a research project funded by the European Research Council under the European Union's H2020 Programme/ERC consolidator grant ERC-CoG 646858. This work was supported in part by a National Geographic grant (NGS-358S-18). We would like to thank Armando Pineda for the organization, technical assistance, and experienced

insight in the field. We further thank Stefan Bredemeyer, Jacob Anderson, Zach Voss, Matthew Wordell, Felix von Aulock, Eva Hartung and Tom Florence for further assistance and good company during the field campaign.

Chapter 4:

Insights into lava dome and spine extrusion using analogue sandbox experiments

Edgar U. Zorn[1], Thomas R. Walter[1], Michael J. Heap[2], Ulrich Kueppers[3]

[1]German Research Centre for Geosciences GFZ, Potsdam, Germany

[2]Géophysique Expérimentale, Institut de Physique de Globe de Strasbourg (Université de Strasbourg/EOST), Strasbourg, France

[3]Department of Earth and Environmental Sciences, Ludwig-Maximilians-Universität München, Munich, Germany

Abstract

Lava dome formation is a common process at stratovolcanoes involving the shallow intrusion or extrusion of viscous lava and may lead to the rise of spines. Spines are protrusions observed to extrude episodically during lava dome growth, yet the structural and mechanical factors controlling their formation are only partially understood. Here, we provide new, detailed insight into lava dome growth and the production of spines using a novel set of analogue experiments extruding sand-plaster mixtures from a fixed-diameter conduit under isothermal conditions. We trace displacement and strain with photogrammetric methods for precise and detailed monitoring of the extrusion process. Results show initial dome growth forming a steep-sided and flat-topped shape through extrusion of new material, leading to slumping of oversteepening slopes, forming a talus. Spines are found to protrude at a later stage through the dome surface along discrete circular faults that originate from the conduit walls, starting a cycle of spine growth and collapse. As our spines only appear after prolonged extrusion, we relate their appearance to the compaction and strengthening of material within the conduit. We find that spine diameter, height and volume are positively correlated with increasing cohesion and therefore material strength. The spine diameter was also observed to be smaller or equal to the diameter of the underlying conduit, as shear extrusion occurs along vertical to outward-dipping fault planes. For natural domes, our findings imply that spine growth may be the consequence of compaction and densification via porosity loss, shearing, and/or outgassing of conduit magma during ascent. More efficient compaction will yield wider and taller spines as a result of increasing rock strength. Our study further highlights the relevance of analogue experiments

in the study of lava domes and spines, which remain one of the most hazardous and unpredictable features at dome-forming volcanoes worldwide.

4.1 Introduction

Understanding the processes occurring during the extrusion of lava domes is one of the most important and challenging aspects of volcanology. Lava dome growth has been observed at over 120 volcanoes worldwide and poses a severe hazard for people and communities living in their proximity (Ogburn et al., 2015). Collapse events can produce Pyroclastic Density Currents (PDCs) or trigger explosive eruptions by rapid unloading of conduit-dwelling magma (Druitt et al., 2002). For example, the collapse of the 1902 dome of Mount Pelée, Martinique, destroyed the town of St. Pierre and killed ~28,000 people within minutes (Tanguy, 1994). Lava domes often show a variety of different growth styles and morphologies depending on factors such as magma extrusion and ascent rate, rheology, state of degassing and cooling as well as vent morphology (Watts et al., 2002; Cashman et al., 2008; Harnett et al., 2018; Husain et al., 2018). Lava domes can form complex shapes, but often develop flat tops and steep sides (James and Varley, 2012; Zorn et al., 2020a) with a talus apron stabilizing the flanks (Hutchison et al., 2013). They display endogenous and exogenous growth endmembers, where the former occurs from the internal swelling and carapace expansion due to the intrusion of magma into a dome and the latter by the protrusion of new magma through the dome surface via discrete lava lobes or spines (Fink et al., 1990; Hale and Wadge, 2008).

Spines are monolithic structures (i.e. single protruding columns rising above the surrounding dome surface), forming from highly viscous or solid lava (e.g., Nakada and Motomura, 1999; Watts et al., 2002), that can sometimes reach several hundred meters in height before collapsing (Tanguy, 2004). Domes exhibiting spines are sometimes grouped as “Peléan” type or upheaved plugs (Blake, 1990; Husain et al., 2019). Other studies also describe whaleback spines, characterized by a large inclined extrusion of solid conduit magma with a smooth upper surface (Watts et al., 2002; Iverson et al., 2006; Vallance et al., 2008), or similar megaspines, incorporating both a smooth-sided extrusion as well as a headwall of broken dome blocks (Watts et al., 2002). In order to maintain steep vertical features, spines are thought to require a high rock strength, so they typically consist of magma that has outgassed and/or cooled efficiently (e.g., due to a slow ascent rate), thus spine rocks typically exhibit low porosity and high groundmass crystallinity (Nakada and Motomura, 1999; Cashman et al., 2008; Cordonnier et al., 2009; Heap et al., 2016; Husain et al., 2019). Spines are known to extrude via discrete shear faults (e.g., Wallace et al., 2019), sometimes even showing striations on their carapace

which are thought to be slickensides (Anderson and Fink, 1992; Cashman et al., 2008; Kennedy and Russell, 2012) resulting from fault abrasion. Spines can extrude (sub-) vertically (Tanguy, 2004; Rhodes et al., 2018) or inclined/recumbent (Watts et al., 2002; Vallance et al., 2008), but little is known about the conduit fault structures in the subsurface. Although lava dome growth is commonly observed at silicic volcanoes, the extrusion of spines is less common. Documented cases include spines at Mount Pelée, Martinique (Tanguy, 1994) Mount St. Helens, USA (e.g. Poland et al., 2008), Soufrière Hills, Montserrat (Watts et al., 2002), Mount Unzen, Japan (e.g. Hornby et al., 2015; Wallace et al., 2019), Santiaguito, Guatemala (Rhodes et al., 2018), Chaitén, Chile (Bernstein et al., 2013; Pallister et al., 2013a) and Bezymianny, Kamtchatka (Kirsanov and Studenikin, 1971). However, due to their unstable nature, spines are rarely preserved.

The extrusion of lava domes has been studied by a variety of methods involving analogue models with granular, brittle, or viscous materials. However, the extrusion of spines and associated structures have not yet been experimentally studied in detail. Initial approaches on lava dome experiments using liquid wax mixed with kaolin powder focused on the development of dome morphology in relation to effusion rate, magma rheology and surface cooling (Griffiths and Fink, 1993; Fink and Bridges, 1995; Griffiths and Fink, 1997; Fink and Griffiths, 1998), demonstrating that various natural lava dome morphologies can be recreated and studied in controlled laboratory experiments (Fink and Griffiths, 1998), including spines (Griffiths and Fink, 1997). Although extrusion and cooling rate as well as rock strength are considered to exert a first-order influence, the slope of the underlying volcano surface also impacts the morphology of the extruding dome (Lyman et al., 2004). In particular, spine-like lobes appear at low extrusion rates and/or high cooling and degassing rates, correlating with high rock strengths (Blake, 1990; Griffiths and Fink, 1997; Lyman et al., 2004), a concept supported by later studies (Cashman et al., 2008; Heap et al., 2016). Two-dimensional observations of dome extrusion experiments (without spine formation) using viscous silicone putty characterized the distribution and evolution of internal strain in lava domes (Buisson and Merle, 2002). Internal flow patterns of viscous domes show a series of sequential lava lobes forming the characteristic dome morphology and structures via asymmetric shear zones (Závada et al., 2009). Degassing experiments have successfully simulated tilt cycles during lava dome growth such as at Soufriere Hills, Montserrat, via repeated conduit margin fracturing and resealing (Lane et al., 2008), implying that the conduit margin shear zones are temporarily active. Despite the evidence for their existence, the architecture of these conduit shear zones has remained largely unclear.

In this study, we extend the previously existing sets of analogue experiments on lava dome extrusions by presenting a new approach using granular material with controlled cohesion to simulate dome and spine extrusion and the development of associated structures under isothermal conditions. Our setup presented here can further help to visualize and trace fault structures inside the dome.

4.2 Materials and methods

4.2.1 Analogue experiments

We performed a suite of analogue experiments using sand-plaster mixtures to simulate the extrusion of lava domes and to understand the production of spines. A custom-made apparatus capable of extruding material at a controlled rate has been designed for this purpose (Fig. 4.1). It consists of a 50 cm long cylinder (4 cm diameter), filled with a 15 cm high sand-plaster column. A piston below the sand-plaster column pushed the material upwards onto a flat metal surface, extruding a total volume of ~188.5 cm^3. The ascent/extrusion rate could be changed between experiments but was constant for single experiments. Since we use Mohr-Coulomb material, the extrusion rate does not affect the deformation pattern and growth structures (c.f. section 4.2.4 and 4.2.5), as we show in experiments with arbitrary values of 0.45, 1.75 and 3.52 mm/min (equalling a voluminal 0.57, 2.20 and 4.42 cm^3/min, respectively). Further experiments pausing and restarting experiments also had no effect on the dome growth due to the ascent rate independence, lack of viscous relaxation, and the reactivation of structures such as faults once extrusion restarted (Krantz, 1991). Two digital single-lens reflex (SLR) cameras were employed to monitor horizontal and vertical displacement (Fig. 4.1a). The cameras recorded one image every 30 or 60 s for a fast or slow ascent/extrusion rate, respectively. Images with 4928 by 3264 pixels (16 MPx) were obtained from two viewing directions: map

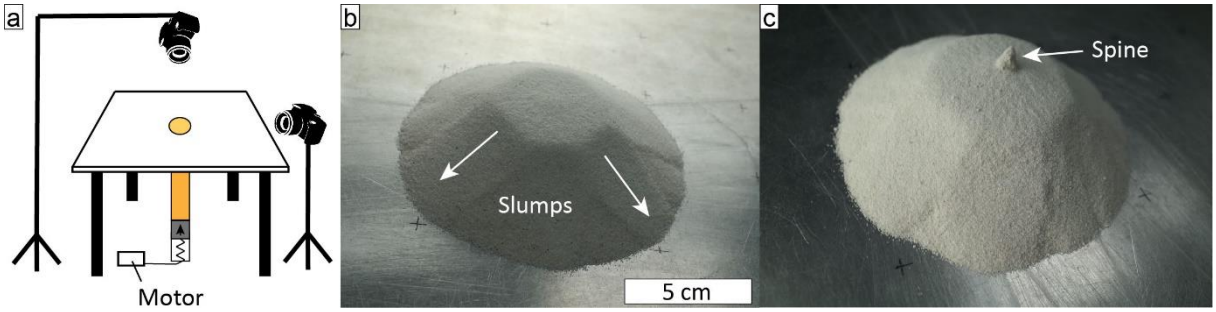

Figure 4.1: (a) Sketch of the experiment setup. The motor pushes the conduit material onto the table at a constant rate. This is recorded by a vertical and a horizontal camera. (b) The dome during sand extrusion (0% plaster). The slumps occurring from the dome top are well visible. (c) Spine growing on top of the dome during an experiment with 10% plaster.

view (vertical camera) from a distance of ~40 cm and a resolution of 14 px/mm at the dome, and profile view (horizontal camera) from a distance of ~50 cm and a resolution of 25 px/mm at the dome.

We used dry sand with well-rounded ~400 µm grain size as an analogue for our domes. Such granular material can be used to reproduce a brittle low-cohesion dome surface (Hale and Wadge, 2008). For spine extrusions, we mixed this sand with plaster powder (grain sizes vary but are sieved to <1 mm), creating a set of homogenous mixtures with 5%, 10%, 15%, 20%, and 30% plaster by volume. Such sand-plaster mixtures are a commonly used analogue for crustal volcanic rocks (Brothelande and Merle, 2015; Brothelande et al., 2016; Rincón et al., 2018) as they are ideal to visualize brittle faulting and structural features (Mathieu, 2018), thus allowing us to monitor the structural evolution of the experimental domes and their spines. We further investigated the internal growth structures in an experiment in which a Plexiglas plate was placed vertically through the dome. The sand on one side was constantly brushed away, allowing us to observe the dome growth as a cross-section from the profile view in real time. Lastly, we conducted experiments using dyed sand to trace the growth sequence, to visualize new material extruding at the surface, and to analyse the distribution of intruded and extruded material with time. Here, 3 cm-thick layers of firstly uncoloured then red-, blue-, green- and black-coloured sand were placed, from top to bottom, inside the cylinder before extrusion. All other experiments are visualized using the PIV method as described below.

4.2.2 Recording and PIV analyses

We employed photogrammetric processing using particle image velocimetry (PIV) (Pan et al., 2009) to track the deformation and growth of our analogue domes. In PIV the pixel appearance of a sub-window is compared on an image-to-image basis. Any systematic shifts of these sub-windows allow pixel displacements to be determined. Similar techniques have been previously used to describe deformation and structures of growing lava domes (Pan et al., 2009; Walter, 2011; Salzer et al., 2016; Walter et al., 2019b; Zorn et al., 2020a) as well as to volcano-sandbox models (Burchardt and Walter, 2010; Le Corvec et al., 2014), and are here applied to analogue sand-plaster domes growing in a controlled environment. Using LaVision DaVis (version 10.0.5), we mapped the 2D displacement field of the dome from a sequence of images as vectors from the map and profile views. Using the 14 px/mm map view and the 25 px/mm profile view images, we employed PIV using the image intensity values via decreasing sub-windows of 256 × 256 px (50% overlap) to 48 × 48 px (75% overlap) for the map view, and 128 × 128 px (50% overlap) to 24 × 24 px (75% overlap) for profile view, respectively. From the mapped

displacement field, we could further calculate and plot the displacement vectors as well as the strain. Here, we choose to plot the vorticity as a representative value for strain, defined as:

$$\omega = \frac{dv}{dx} - \frac{du}{dy} \qquad (6)$$

where x, y are coordinates and v, u are their velocity components. This has the advantage of not only highlighting high strain areas by means of particle rotation, but also the rotation direction and thus shear sense. The final results are displayed as displacement and strain maps in map and profile view.

4.2.3 Ancillary material testing

To gain further insight into the processes during spine growth in our experiments, we quantified the compaction and the concurrent increase in cohesion of our sand-plaster mixtures. For this purpose, we performed ring-shear tests and uniaxial compression experiments. The ring-shear tests are designed for standardized analyses of analogue materials in laboratory experiments (Schulze, 1994; Klinkmüller et al., 2016; Rosenau et al., 2018). The samples are poured into a ring-shaped container cell and a lid with additional vanes protruding into the sample placed on top (Fig. 4.2a). An additional normal load can be placed on the lid using weights. The cell is then rotated while the lid is kept in place by two tie rods that measure the shear-force of the cell against the lid. Here, measurements consist of repeated shear displacement versus shear stress recordings under increasing normal stresses. The normal stress intervals (500, 1000, 2000, 4000, 8000, 16000 Pa) were measured three times each. In each measurement the sample is sheared for approximately 3 minutes at 30 mm/min (equalling a shear distance of ~90 mm). The shear stress is then removed and reapplied by briefly reversing the machine before continuing to shear for another 3 minutes. This provides insight on the initial peak strength of the material, the dynamic strength, and the reactivation strength.

The uniaxial compression experiments were designed to measure the compaction (i.e. porosity loss) of the experimental materials under uniaxial stress conditions (i.e. similar conditions to the extrusion experiments). First, the solid density of each of the mixtures was measured using a helium pycnometer (sample mass measured using an electronic balance). The mixtures were poured into a plastic container with a known internal volume (diameter of 40 mm and length of 100 mm). The plastic container was then placed on a moving platen, which moved upwards at a constant strain rate of 5×10^{-2} s^{-1} such that the sand-plaster mixture was compressed uniaxially by a fixed steel piston (40 mm in diameter) (Fig. 4.2c). The experiments were stopped when the stress reached an arbitrary value of ~3.2 MPa. The displacement of the lower platen,

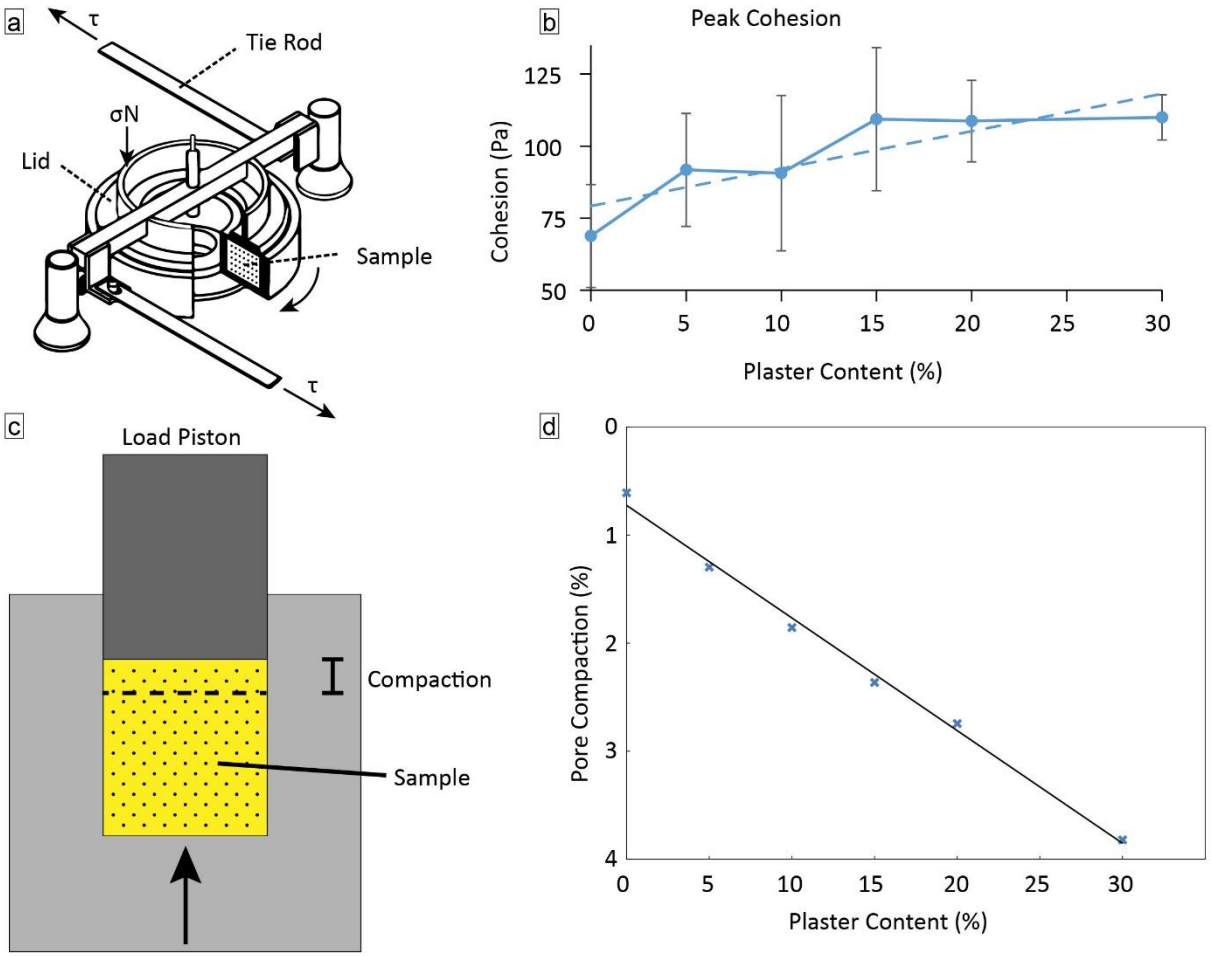

Figure 4.2: (a) Sketch of the ring-shear rig after Schulze (1994) showing the acting shear stress τ and the normal stress σ_N applied to the sample. (b) Ring-shear results showing an increase in cohesion, and therefore material strength, as a function of increasing plaster content. (c) Sketch of the uniaxial compression experiments. The sample is compacted uniaxially by raising the sample assembly onto a fixed steel piston. The displacement of the lower platen corresponds to the change in sample length, allowing us to calculate sample porosity during deformation. The results are summarized in (d), showing a clear linear increase in compactibility as a function of increasing plaster content.

monitored using a linear variable differential transducer, allowed us to determine the porosity loss of the sample during deformation (using the solid density of the mixture and the bulk volume of the sample, calculated using the known sample radius).

4.2.4 Scaling considerations

One of the greatest challenges in all experimental studies is to provide suitable scaling, ideally achieving geometric, kinematic, and dynamic similarity between modelled and natural processes. Here, the use of dry granular material as a lava dome analogue implies that we can only consider purely brittle behaviour, which primarily applies to the solid carapace of a natural

dome (see section 4.2.5 for more details). The granular brittle material behaves according to Mohr-Coulomb law, meaning that the scaling is rate-independent and mainly depends on two parameters: the angle of internal friction and the cohesion (see Merle, 2015 and references therein). If the cohesion is low, this can be reduced to a simple geometric ratio as the angle of internal friction is dimensionless (Brothelande and Merle, 2015).

$$\Phi_{analogue} = \Phi_{nature} \qquad (7)$$

This angle of internal friction Φ is ~30° in our analogue material and ~30° to 40° in nature, meaning that the upper surface of a natural lava dome may produce very similar slopes and geometries compared to our experiments. For our spines (i.e. cases with higher cohesion), we further employ a scale factor using the stress ratio σ^* (Merle, 2015) to scale the cohesion c:

$$c_{analogue} = \sigma^* c_{nature} \qquad (8)$$

$$\sigma^* = \rho^* g^* h^* \qquad (9)$$

where ρ^*, g^* and h^* are the density, gravity, and length ratios, respectively. Since gravity is the same in both experiment and nature, this leaves only the (purely geometric) length ratio and the density ratio:

$$\sigma^* = \rho^* h^* \qquad (10)$$

As a rule of thumb, brittle analogue materials have about half the density of natural lavas (Schellart, 2000; Merle, 2015), although in our experiments, material compaction and the consequent density increase will further affect the final cohesion (see discussion). However, since both material density and the applicable length values (e.g., dome height or conduit width) can vary significantly in nature, we can only provide a rough estimate for scaling values applicable to our experiments. One fixed length value in our experiments is the conduit diameter (measured at the base of the dome, here 4 cm). The 2013 dome at Volcán de Colima (Mexico), for example, had an estimated conduit/vent diameter of ~45 m determined by aerial photogrammetry (Zorn et al., 2019). Therefore, the stress scaling factor σ^* is 2×10^3, meaning the analogue is approximately 2,000-times weaker than the natural rock and the dome geometry (h^*) is approximately 1000 times smaller. However, we note that this value will change quite significantly with varying conduit diameters and with the inherent compaction of our sand-plaster mixtures. Complex conduit geometries also cannot be considered here. To further demonstrate the applicability of our experiments, we compare our experimentally produced features and structures with those formed in nature and establish their similarities (see section 4.4.4).

4.2.5 Experiment limitations

As with any model, analogue or numerical, our experiments have a number of simplifications and assumptions that should be outlined clearly. One of the most significant issues is the exclusion of temperature-dependent viscosity and cooling-induced changes in material properties as it would occur in a natural system. Previous experimental studies have highlighted the importance of cooling and gradual solidification of the dome and carapace lava (Griffiths and Fink, 1993) and their impacts on the resulting dome morphology (Fink and Bridges, 1995; Fink and Griffiths, 1998). In particular, the balance between cooling rate and extrusion rate is listed as a major control for the mode of dome growth (Griffiths and Fink, 1997). Here, gradual changes due to cooling and solidification are neglected, however, the compaction induced changes in material properties during our experiments show similar effects and allow us to successfully recreate certain growth conditions with unconsolidated sand and "solid" compacted sand-plaster mixtures. For this purpose, the use of granular material as a purely brittle analogue can be seen as both an advantage and a disadvantage in modelling lava dome extrusion processes. On the one hand, the brittle conditions provide a dynamic independence from the ascent or extrusion rate (Merle, 2015), which would otherwise be a challenging parameter to dynamically scale correctly. Our experiments show that the ascent/extrusion rate does not affect dome shape, morphology, or deformation pattern, which we explicitly tested and verified (Fig. 4.3a, b). On the other hand, viscous processes commonly associated with lava domes are neglected, so no distinction can be made between a viscous core and a brittle carapace, as is common in many studies (Griffiths and Fink, 1993; Harnett et al., 2018; Husain et al., 2018). However, for the purpose of our spine extrusion experiments, the assumption of purely brittle conditions is likely realistic as spine domes consist of completely solidified, or at least highly viscous, magma that is often highly crystallized (e.g., Watts et al., 2002; Ryan et al., 2018a), making viscous behaviour unlikely or impossible at the strain rates occurring during extrusion. This effective solidification (or at least the transition to brittle failure) is proposed to occur in the conduit at several hundred meters depth as well as along the conduit margins (Cashman et al., 2008; Heap et al., 2015), which is further supported by the brittle faulting occurring at these depths (Tuffen et al., 2008; Kendrick et al., 2012; Kennedy and Russell, 2012).

Another major limitation stems from our setup, which only allows for purely vertical extrusions. The non-vertical extrusion of lava, as it is sometimes reported for lava dome extrusions (e.g. Watts et al., 2002; Vallance et al., 2008; Lavallée et al., 2012; Walter et al., 2013a; Zorn et al., 2019), cannot be reproduced here. Sloped extrusion surfaces or complex crater morphologies

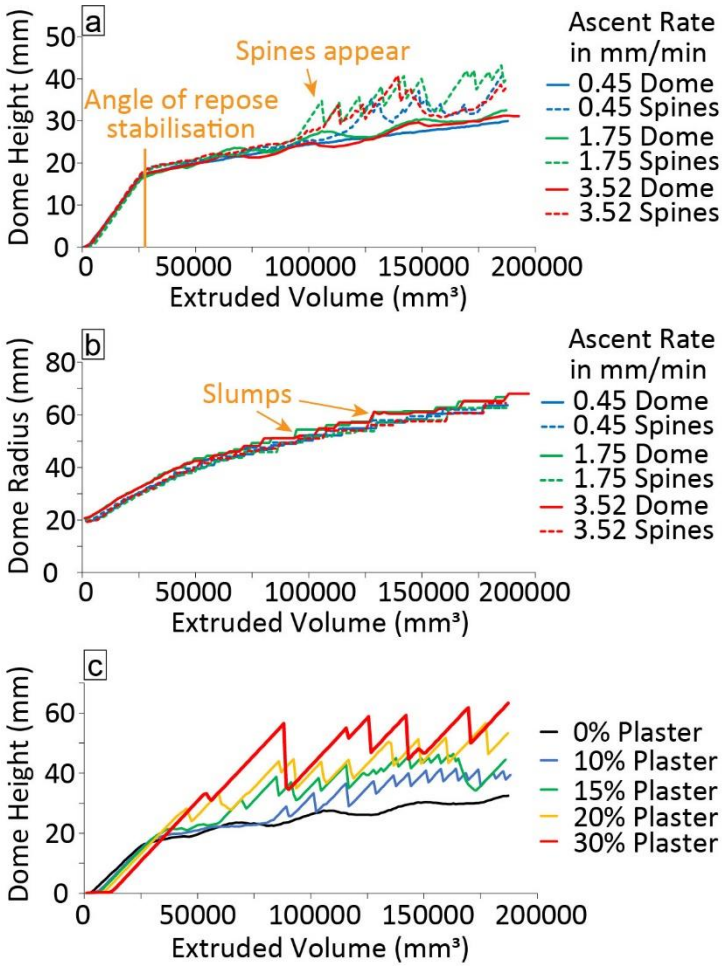

Figure 4.3:
Dome growth metrics recording (a) the dome height and (b) the dome radius at different ascent/extrusion rates. The small steps visible in (b) represent slump events. The spine experiments were performed with 10% plaster content. Results show an independence of all experiments from the ascent/extrusion rate. Spines are the tallest features, however, when they collapse the overall size of the dome is unaffected. (c) The impact of different plaster content on the dome height, with higher contents increasing spine height.

will largely affect the observed structural architecture (Harnett et al., 2018), however, we could not test this here. Rather than one single extrusion, natural domes may also form in clusters, such as the Santiaguito dome complex (Rose, 1972) or as the Mt. St. Helens domes in 2004-2008 (Vallance et al., 2008), and such complex morphologies of multiple overlapping domes could also not be recreated. When extruding domes and spines against a Plexiglas plate, some boundary effects as a result of friction are expected. However, aside from some sand grains adhering to the plate by electrostatic forces, we observed no notable differences to the regular extrusion and therefore do not believe that the Plexiglas influenced the behaviour in any meaningful way. We did not consider conduit widening or test systematic variations of conduit shapes, which in nature are likely more complex than a simple circular opening. Since we used granular material, we expect that different diameters would simply result in the same dome shape and features, only requiring more (for larger diameters) or less (for smaller diameters) material volume to grow. The same applies to using a larger extrusion volume, which would likely produce the same structures, only larger. The spine and dome sizes could hypothetically be used to estimate the conduit diameter as their relative sizes may be similar in our experiments and in nature, however comparable data from known conduit sizes and material strength would be required to train for such a prediction. We include our spine sizes in the Appendix D1.

It is also worth discussing whether a mixture of sand and plaster powder can be considered as a suitable analogue for dome-forming magma. Sand-plaster mixtures can be used as an analogue for brittle volcanic materials, making it possible to visualize faults and structures associated with dome extrusion processes (Brothelande and Merle, 2015; Brothelande et al., 2016). However, the mechanism of compaction inducing the increased cohesion in our experiments is not exactly the same as in natural volcanic settings, albeit the effects are similar. Compaction of our sand-plaster mixtures is achieved by pressing the smaller plaster particles into the void spaces of the sand grains, while the same compaction in natural magmas is achieved by porosity reduction as bubbles migrate and leave the system (see the experiments of Heap et al., 2017). Despite the different nature of compaction, both processes result in a stronger yield/peak strength of the compacted material, which allows these materials to work as suitable analogues to study dome structure and morphology. This allows us to recreate realistically looking spines and their structural features with our analogue experiments, despite all the complexities associated with natural lava dome growth (see section 4.4.4).

4.3 Results

4.3.1 Analogue material properties

The uniaxial compression experiments show an increasing capacity for compaction with increasing plaster content under the same stress. We find a clear linear relationship between plaster concentration and maximum porosity loss (Fig. 4.2d). Repeat experiments at different strain rates resulted in the same porosity change, so varying deformation rates do not impact our results. More detailed results from the uniaxial compression experiments can be found in Appendix D2. In the ring-shear experiments we find a weak, yet notable increase in peak cohesion with higher plaster contents (Fig. 4.2b). Dynamic and reactivation cohesion do not display the same behaviour and are likely not representative of the material strength as they are measured in established shear-zones within the machine (Fig. 4.2b, Appendix D3). Both material tests show that our analogue material has higher compactibility with higher contents of plaster powder, with higher compaction also increasing the cohesion (as is expected for compacting powders, see e.g. Leuenberger (1982). Therefore, the results of the material testing suggest that the material is ideally suited for our simulation purposes.

4.3.2 Dome extrusion (sand only)

Using sand without plaster we are able to simulate symmetric lava dome growth. The first stage of extrusion is dominated by a sharp increase in height and the formation of a rounded dome. We observe constant slumping of sand on the dome margins as the granular material gradually establishes the angle of repose. Once the repose angle was reached, the extrusion of sand produced a steep-sided and flat-topped dome (Fig. 4.1b) as well as a pronounced talus apron. The final dome measured ~30 mm in height and ~130 mm in diameter. During growth, lateral widening of the dome occurs by regular slumps originating from the outer flat top due to the gradual oversteepening of the sides (Fig. 4.1b). The growth metrics are shown in figs. 4.3a, b, highlighting both the stabilization of the repose angle during vertical growth and the slump-driven lateral growth. These results are notably similar to previous numerically modelled and observed natural lava dome growth at Volcán de Colima, Mexico, in Walter et al. (2019b). The PIV from the map view reveals a clear ring-like deformation pattern on the outer margins of

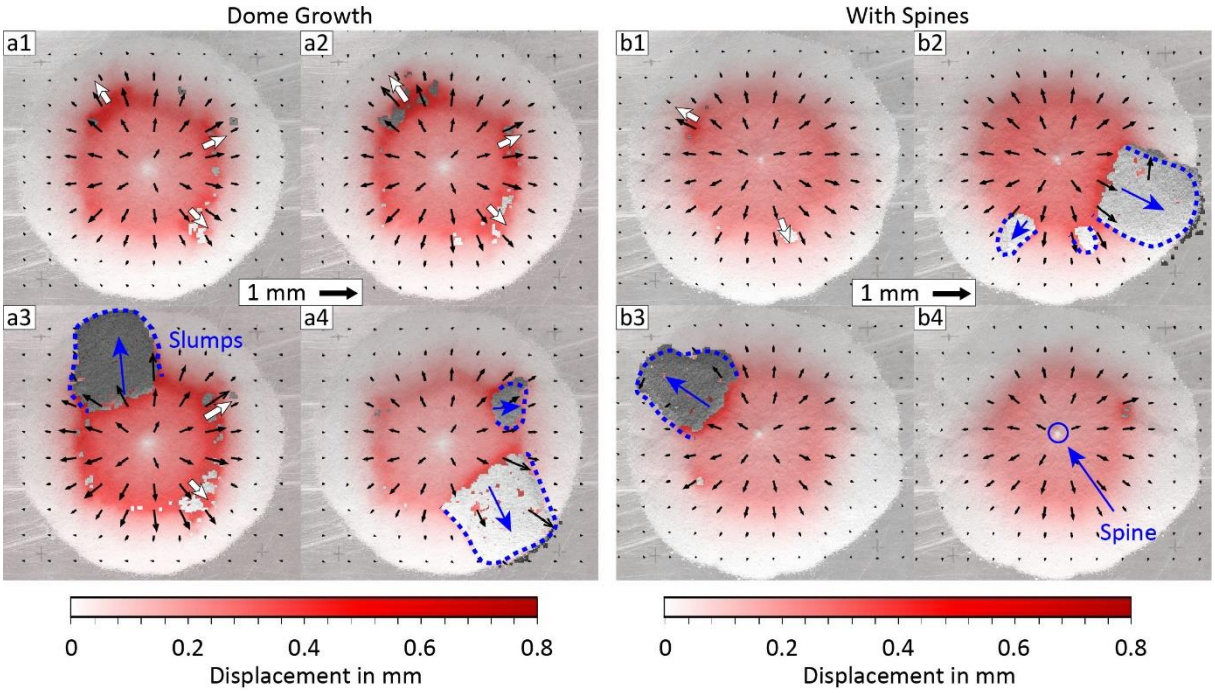

Figure 4.4: (a) Map view of the sequence of dome growth from the vertical camera. The Particle Image Velocimetry (PIV) reveals a ring-like deformation pattern on the dome top as well as increasing deformation, indicated by white arrows, before slumps (blue) occur on those sides. In the centre is a small area with little deformation as particles move dominantly upwards. The experiment material was pure sand (0% plaster). (b) Map view of the sequence of spine dome growth from the vertical camera. The ring-like pattern is less pronounced and the dome top moves more evenly, however the slumping pattern is still the same. The centre area with low lateral movement coincides with the surfacing of the spines. The experiment material in (b) contained 10% plaster. In both experiments the time between photos is 1 minute at an ascent rate of 0.45 mm/min.

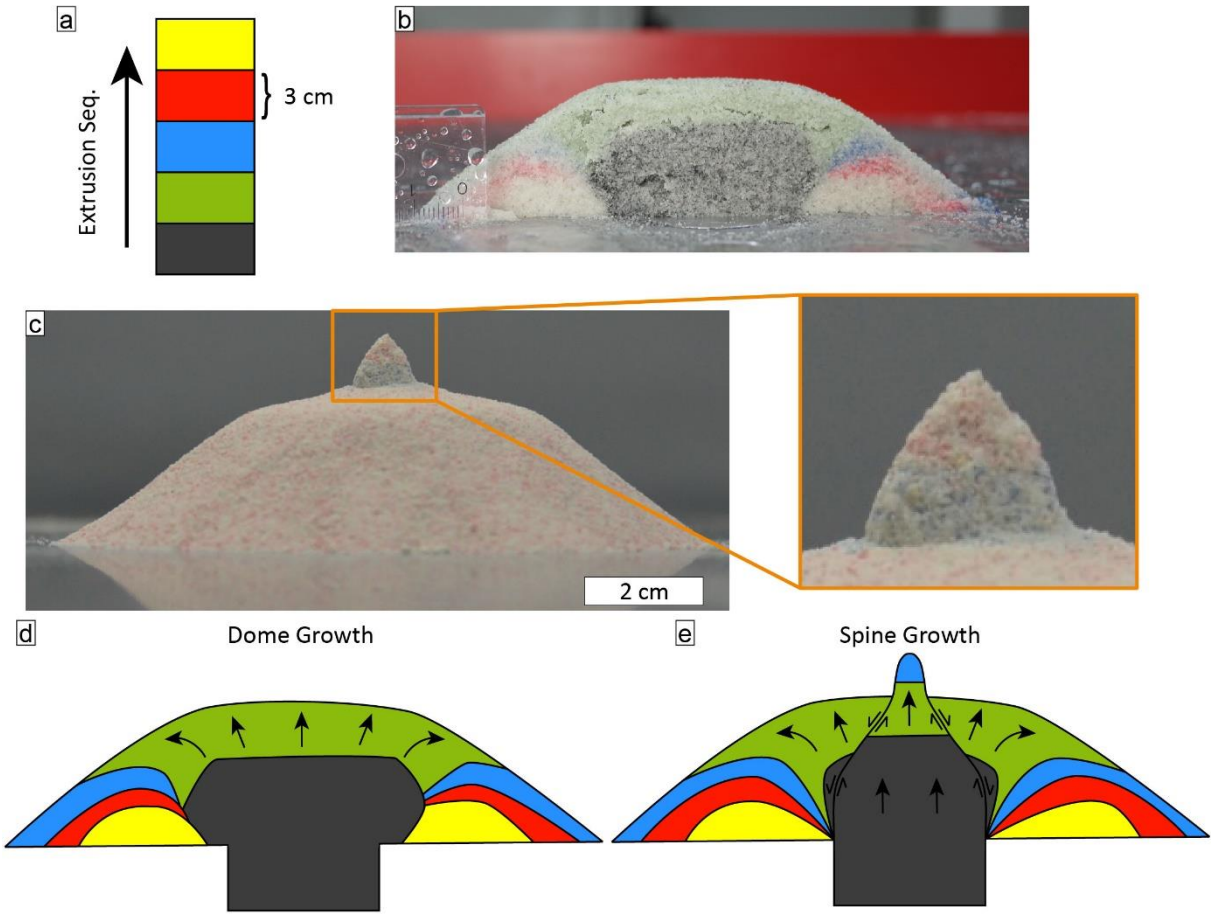

Figure 4.5: (a) Illustration of the experiment using a sequence of dyed sand. (b) is the result of the dome extrusion with 0% plaster cut as a cross section, revealing the inner dome stratigraphy. (c) shows a spine with the lower (blue) layer being lifted above the current (red) layer, highlighting that spines consist of deeper conduit material compared to the rest of the dome surface. Here 10% plaster was used. (d) and (e) are sketches that summarize the resulting domes.

the flat dome top, with the margins moving outwards (Fig. 4.4a). The sequence of images also shows a significant increase in displacement at the headwall area before a slump occurs there (see, for example, the top-left area of fig. 4.4a). In the top centre of the dome a small circular area with little lateral movement is observed at the point of the strongest vertical growth (Fig. 4.4a).

The experiments using dyed sand show that new material surfaces either at the flanks of the dome following slump events or on the top centre of the dome with the ascending material. After the experiments, the talus apron shows an inverse stratigraphy compared to the starting stratigraphy in the conduit. Cutting a cross-section through the grown dome (by spraying the dome with water to temporarily allow structure preservation) reveals the stratigraphy and internal structure of the dome (Figs. 4.5b, d). This profile view shows the material intruding into the dome, which pushes up- and outwards, thus causing the strongest lateral motion on the edges of the flat top as seen in the deformation ring (Fig. 4.4a). The youngest material is thus

intruding in the dome interior, whereas older material is gradually buried beneath the dome talus and forming layers from the slumps.

The experiments using a Plexiglas plate allowed for real time tracking of the dome as a cross-section in profile view (Fig. 4.6a, c, e). The deformation is strongest near the conduit exit in the dome centre and becomes more distributed towards the surface (Fig. 4.6c), which is consistent with the movement pattern implied by the layer outlines (Fig. 4.5d). Plotting the vorticity, an indicator for shear motions, shows a finely distributed pattern of intercrossing motions (Fig. 4.6e) very reminiscent of previously modelled shear bands in the dome centre (Harnett et al., 2018). Areas of increased vorticity on the dome surface are likely artifacts due to particles being tracked on the margin of the measured deformation, introducing artificially high values.

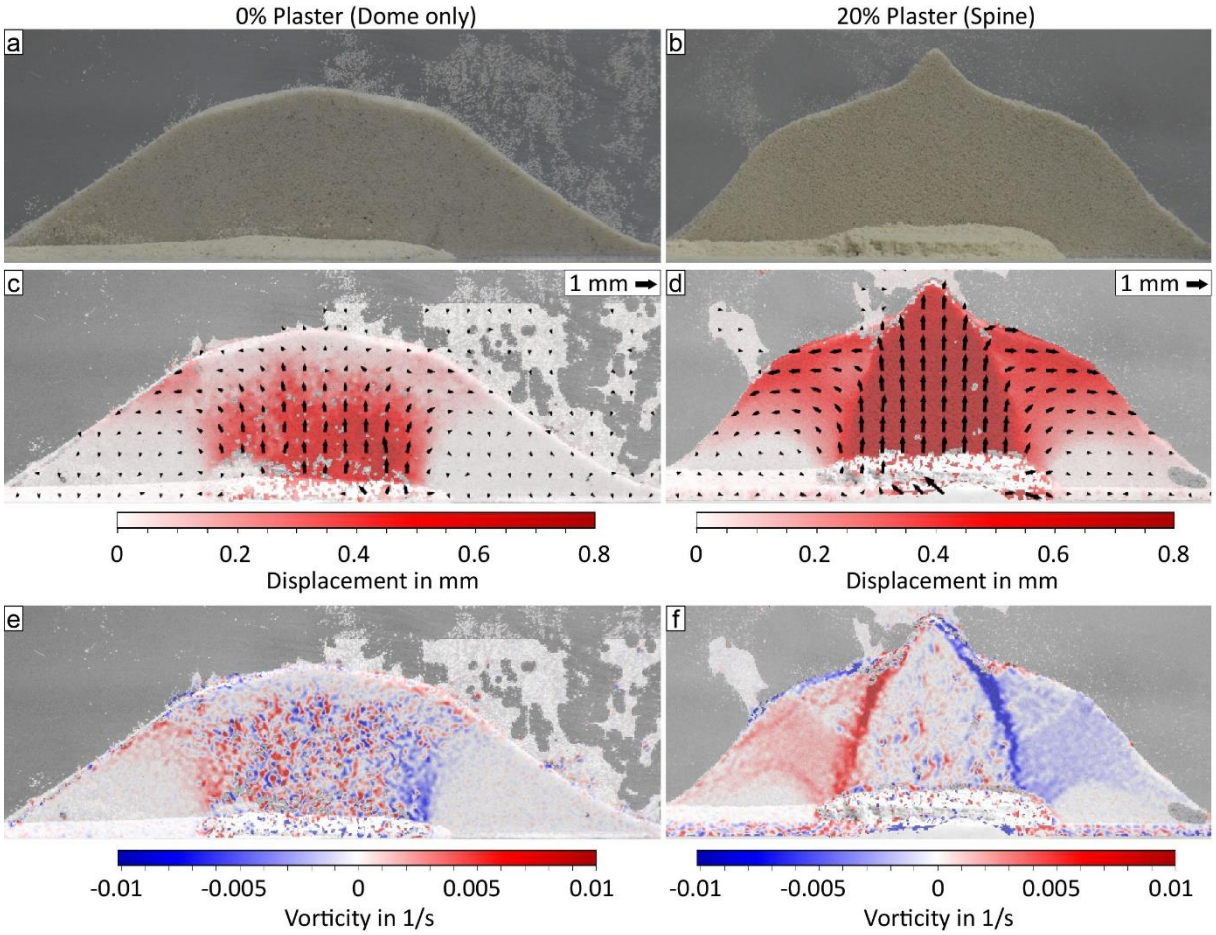

Figure 4.6: Profile view results from the experiments run against a Plexiglas plate, revealing the active structures and deformation patterns in the dome interior during growth over 30s between frames at an ascent rate of 1.75 mm/min. (a) and (b) are RGB images, (c) and (d) show the displacement vectors, and (e) and (f) show the vorticity as a representative of strain localisation. The difference of the more distributed upwelling-type movement in the dome relative to the undeformed wedge pushed up in the spine experiment is clearly visible. The vorticity further highlights shear movement of particles respective to the shear direction as sinistral (red) and dextral (blue). This outlines the shear faults of the spine dome in (f) very clearly and confirms the existence of discrete slip surfaces.

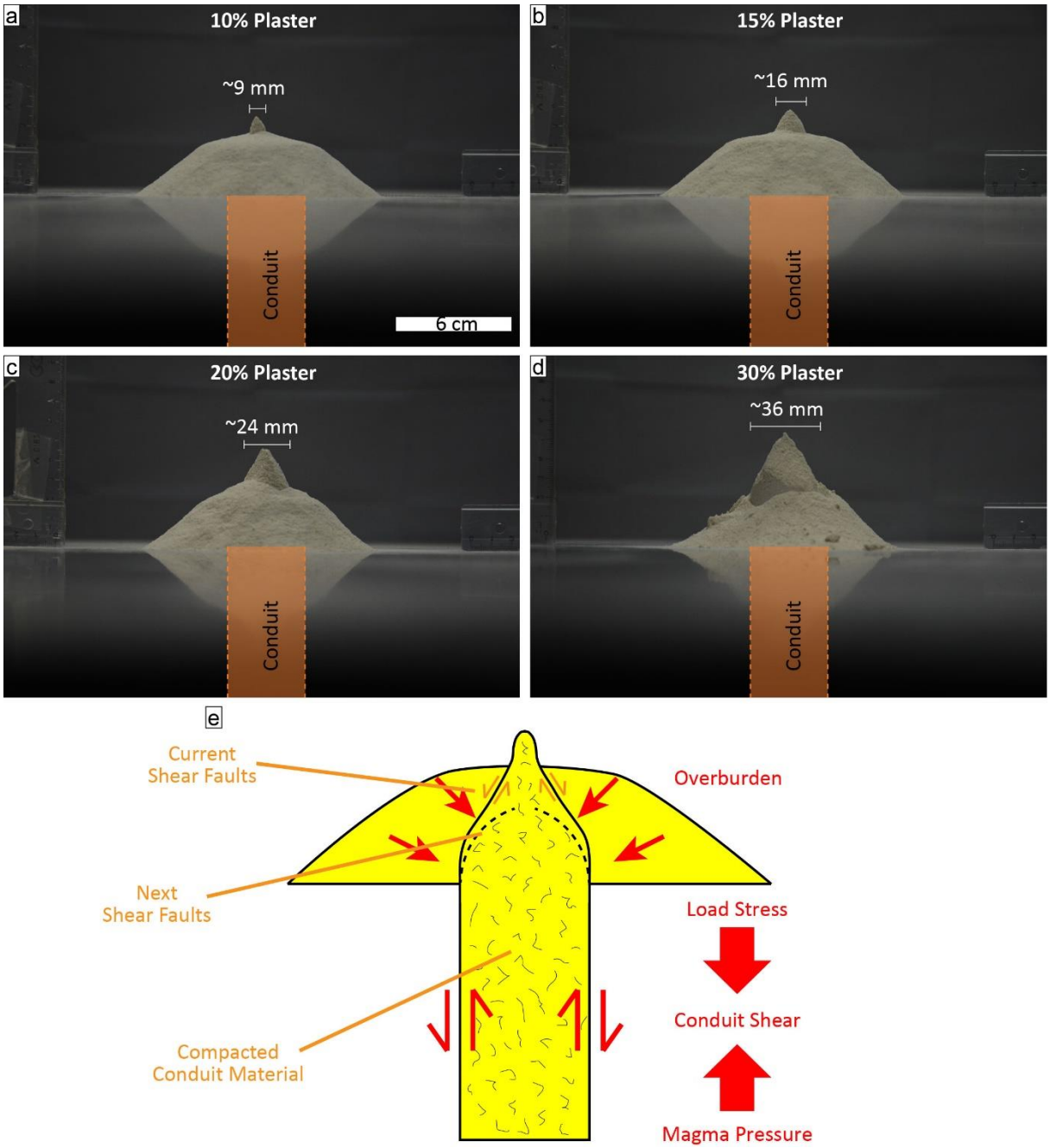

Figure 4.7: Spine size comparison between (a) 10%, (b), 15%, (c) 20%, and (d) 30% plaster content. Both spine height and diameter increase with higher plaster content as a result of compaction induced strengthening. The processes leading to the compaction and the formation of a spine are summarized in (e).

4.3.3 Spine domes (sand-plaster mixtures)

For the mixed sand-plaster material, initial growth occurs in the same fashion as the dome growth using pure sand. We then observe that spines start to extrude from the top of the dome (Figs. 4.1c, 4.3a), with spines appearing earlier using higher plaster concentrations (Fig. 4.3c). The spines form as finger-like features that episodically collapse when they reach a certain height, producing a repeating cycle of spine extrusion and collapse. The spines grow from the

top of the dome, and as the spines are low in volume compared to the underlying dome, they seemingly do not greatly influence the overall shape of the lower dome (Fig. 4.3a, b). However, the profile view shows that the actual spine consists of a subaerial and a subterranean part, totalling approximately 40% of the entire dome volume (Fig. 4.6d). The exceptions are spines with very high cohesion (plaster contents above 20%); for these the dome nearly disappears, leaving only the spine and a talus deposit. Spines grow only vertically at approximately the speed of the conduit extrusion and thus grow significantly faster in height compared to the dome below (Fig. 4.3a, c). Their width and maximum height increase as a function of increasing plaster content and reach nearly the same width as the underlying conduit at 30% plaster content (Fig. 4.3c, 4.7d, Appendix D1). The spine centre position correlates well with the circular area of low lateral movement on the top centre of the dome (Fig. 4.4a, b).

The dyed sand and profile view experiments with the Plexiglas plate show that the internal structure of a dome with a spine on top is revealed to be significantly different compared to the dome without. Firstly, new material arriving at the surface is now pushed out of the dome top as part of the spine, elevating lower parts of the dome interior above the dome surface as part of the spine (Fig. 4.5c, e). This is due to discrete outward-dipping shear faults, as revealed by the cross-section (Fig. 4.6d, f). The faults are circular, originate from the conduit boundaries and border a large and undeforming triangular wedge that is pushed vertically upwards from the conduit, with the spines extruding as the tip of that wedge. This wedge, and by extension the spine, are the fastest moving parts of the dome (Fig. 4.6d).

4.4 Discussion

4.4.1 Phenomenology of dome growth

The strong ring-like deformation pattern of the dome along the margins of its flat top can be attributed to lateral spreading due to lack of lateral confinement. New material first rises vertically, then moves laterally once near the dome surface (Fig. 4.5d, 4.6c), resembling an upwelling-type motion. This causes the formation of the flat top with a diameter larger than the conduit. Some previous classifications of exogenous growth styles state that lava extrudes via discrete lobes or spines (Fink et al., 1990; Kaneko et al., 2002; Hale and Wadge, 2008). Our pure sand experiments exhibit slightly different behaviour that does not fall distinctly under either category. We note that the dome surface swells to some extent, which is indicative of endogenous contributions to the growth, although here this does not occur purely from internal swelling and older material is gradually buried by fresher material in the dome talus. While the dome grows, new material constantly reaches the dome surface by a distributed upwelling-type

motion in the centre. Thus, the observed style of growth in our experiments could be classified as a mixed endogenous-exogenous growth mode.

Our results are in good agreement with many previous studies, which commonly utilize or assume ductile magma extrusion. The gradual displacement and burial of the lava dome front resulting from endogenous swelling was also found in previous experiments, specifically under relatively high extrusion and slow cooling rates (Griffiths and Fink, 1997). However, slower extrusion rates or higher cooling rates would tend to form exogenous lobes and spines instead (Griffiths and Fink, 1997). The movement patterns that can be observed from the profiles (Figs. 4.5d, 4.6c) also show very similar deformation features in the dome interior compared to other experiments (Buisson and Merle, 2002; Buisson and Merle, 2004), with concentric stretching occurring in the centre and upper dome portion, and radial stretching in the lower flanks. However, the internal structure of the domes produced by Závada et al. (2009) are quite different, because the dome here has no overlapping growth lobes. This difference is simply due to the lack of multiple intrusions into the pre-established dome and the brittle nature of our experiments. The overall shape of the dome (flat top and steep sides) is also commonly noted in multiple experimental and numerical studies (Blake, 1990; Buisson and Merle, 2002; Závada et al., 2009; Brothelande et al., 2016; Harnett et al., 2018).

As a result of differential outgassing, cooling, and crystallization, dome lavas are typically not texturally homogenous as flow processes may lead to textural banding with variations in crystal alignment and/or the porosity (e.g. Hornby et al., 2015; Rhodes et al., 2018). Furthermore, natural conduits and lava domes may also show changes in mechanical rock properties with ongoing extrusion (e.g. Nakada and Motomura, 1999), which could be simulated and investigated in future analogue models to consider heterogeneity effects in greater detail.

4.4.2 Phenomenology of spine extrusion

Initially, the dome growth was identical for the sand-plaster mixture and the pure sand experiments. Spines only started after the ongoing extrusion had established a dome edifice (Fig. 4.3a). Accordingly, we suggest that some additional processes are controlling the late formation of spines. The addition of plaster powder increases the compactibility of the mixture as the finer plaster particles can fill the void spaces between the sand-grains when the mixture is pressurized. In turn, this increases the cohesion of the material sufficiently to produce spines. We confirmed this enhanced compaction and the concurrent increase in cohesion as a function of increasing plaster content by testing the analogue material properties (Fig. 4.2). Higher compaction as a function of increasing plaster content correlates well with the increasing height

and width of the growing spines (Fig. 4.7), suggesting a link between reduced porosity, increased strength/cohesion, and the tendency to form spines. These inferences support those forwarded in previously published studies (Heap et al., 2016; Zorn et al., 2018).

In our experiments, compaction (i.e. porosity loss) is achieved through a combination of compressive and shear stress due to the piston moving upwards. Throughout each experiment, material extruded at later stages (from greater column depth) had experienced higher cumulative static load and longer frictional shear along the conduit margins (Fig. 4.7e), explaining the time-dependent variability of compaction and the delay in spine appearance. We suggest that this compaction driven increase of cohesion and rock strength correlates well with natural spine extrusion observed at dome-building volcanoes. Spine formation has been linked to textural changes (decrease in porosity, increase in crystallinity) that are indicative of high degrees of cooling and gas-loss and favour brittle deformation (e.g., Nakada and Motomura, 1999; Cashman et al., 2008; Heap et al., 2016; Coats et al., 2018; Rhodes et al., 2018). Spines are often reported to appear during the late stages of an eruption when extrusion rates have slowed (Nakada and Motomura, 1999; Tanguy, 2004; Rhodes et al., 2018). They thus had more time to degas, further favouring higher degrees of cooling, pore reduction and groundmass crystallization. Similar to our experiments, shear stress will cause bubbles to collapse and thus reduce the porosity (Eichelberger et al., 1986; Heap et al., 2017). The formation of discrete shear zones along the conduit margins facilitates this process by increasing the permeability of the damaged rocks in the direction parallel to the conduit (Rust et al., 2004; Lavallée et al., 2013; Gaunt et al., 2014). Combined with increased microlite crystallization due to cooling or degassing induced undercooling of the magma, the increasing viscosity will cause a tendency for brittle magma behaviour under the relevant strain rates. Efficient outgassing will also produce a rock with a higher rock strength, due to the porosity dependence of rock strength (Al-Harthi et al., 1999; Heap et al., 2014a; Heap et al., 2015; Schaefer et al., 2015; Heap et al., 2017; Coats et al., 2018; Zorn et al., 2018). This means that both cooling and compaction can influence the mechanical behaviour of the lava and govern the conditions required to form spines or other dome morphologies. Analogue to our experiments, increased compressive stress due to static loads as suggested by Zorn et al. (2018) or strong friction at the conduit may facilitate this process and produce sufficiently dense and strong lava to form spines. Furthermore, brittle fracturing is a requirement for the formation of conduit boundary faults and is typically associated with low porosity rocks (Heap et al., 2015; Heap et al., 2016; Ryan et al., 2018a; Zorn et al., 2018). Higher porosity rocks may still form shear zones, but with the

associated ductile failure mode they would likely occur distributed, similar to the dome growth with pure sand in our experiments (Fig. 4.6c).

4.4.3 Structural features associated with spines

Due to the near-solid nature of spine lavas, the extrusion occurs along discrete faults via brittle frictional processes, which are evidenced by brittle fracturing (Lamb et al., 2015) and the formation of discrete shear zones (Wallace et al., 2019). The extrusion produces fault-related seismicity (e.g. Iverson et al., 2006) as well as cataclasite and ash-like gouge (Kennedy and Russell, 2012; Gaunt et al., 2014; Ryan et al., 2018a; Ryan et al., 2018b). Pseudotachylytes are also thought to form due to frictional melting at these faults (Kendrick et al., 2012). While it is clear that such faults are active during spine extrusion, their exact nature and location are rarely observed and often inferred (e.g., from models, see Brothelande et al., 2016) due to their poor preservation potential in natural settings. Our experiments show the formation of circular vertical to outward-dipping shear faults (Fig. 4.8a) in remarkable agreement to the experimental and numerical models in Brothelande et al. (2016) using a rigid indenter. Numerically simulated shear strain patterns also follow a similar pattern to our observed faults (Harnett et al., 2018). Considering the increased material cohesion induced by compaction, the dipping faults here border an undeformed wedge (a feature also noted in Brothelande et al., 2016) that is pushed vertically upwards. Higher material cohesion also results in more vertical fault orientations. Interestingly, the fault position is not constant. For some time following the collapse of a spine, the main shear faults can be observed to rotate to a nearly vertical orientation while the collapsed material moves horizontally towards the flanks (Fig. 4.8b). Subsequently, the main shear fault changes back to an inclined position and the next spine starts to form. The switching (observed in 2D) does not occur symmetrically (i.e. at the same time) (Fig. 4.8c, d), but likely has a rotational component in 3D. The fault switch also occurs quickly (here within three frames equalling 1.5 min), although it does not jump since both faults are active at the same time in one frame per side (Fig. 4.8c, d). The change of fault positions also affects the main dome edifice and briefly produces secondary normal faults in the wedge dipping towards the dome centre (Fig. 4.8b, c), potentially indicating brief surface rifting. These motions likely occur as a result of the removed load on the dome centre, briefly shifting the static stress on the dome edifice. Unfortunately, neither the fault switching, nor the dome surface rifting have been observed in any natural domes and the detection of such features, especially a subsurface fault change, could be challenging to observe. Many previous studies have noted cyclic or episodic extrusion behaviour on domes and spines related to seismicity (Denlinger and Hoblitt, 1999;

Costa et al., 2013; Pallister et al., 2013c) and, although speculative, one-sided conduit activations could hypothetically be linked to such effects.

Some studies infer shear faults during spine growth as upwards extensions of the conduit pushing the near-solid magma out to form a spine (Hale and Wadge, 2008; Husain et al., 2014). Considering the outwards dip of the faults in our experiments, we suggest that the extent of the surface spines may underestimate the real size of the feeding conduit in some cases. A higher strength of the conduit material is more likely to favour spine extrusion closer to the conduit

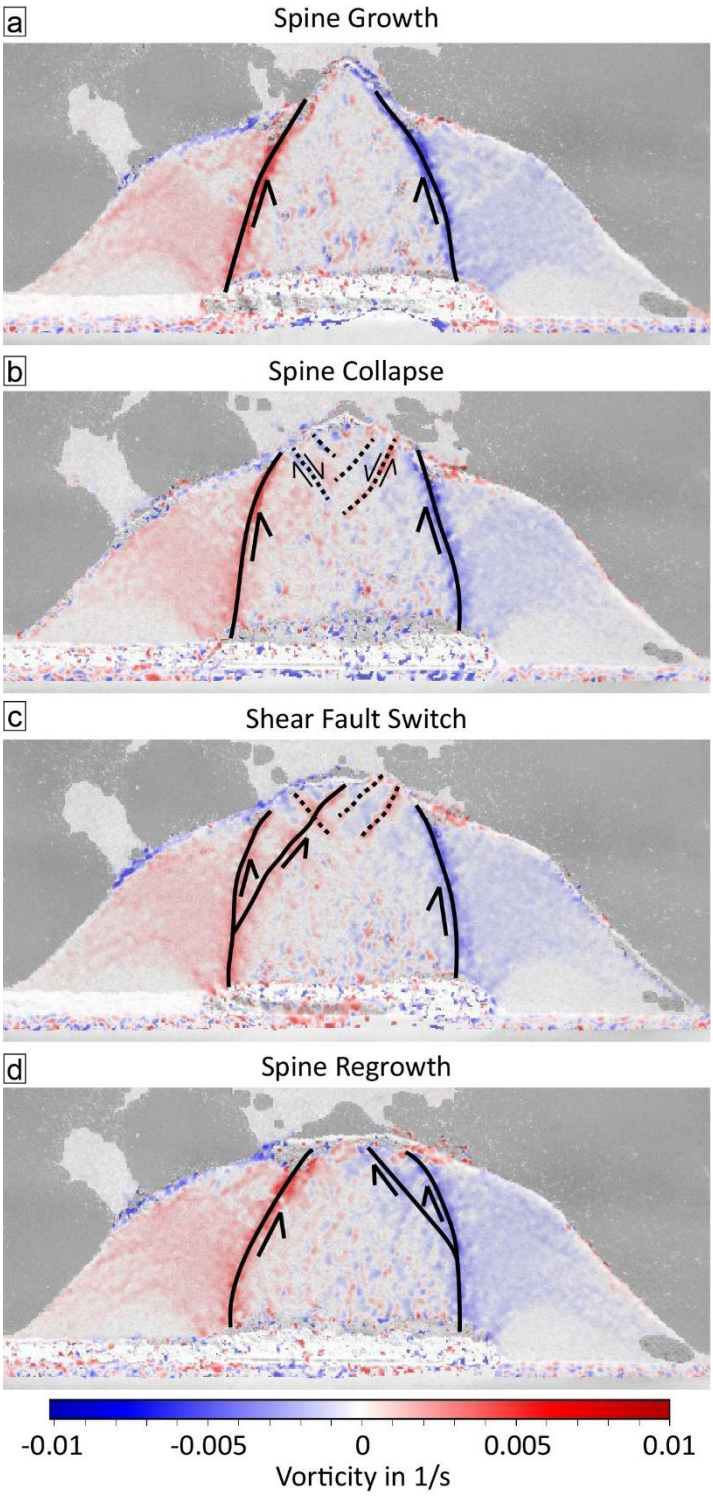

Figure 4.8:
Vorticity plot of a spine growth and collapse sequence (a-d) in profile view. (b) After the spine collapse the main shear faults become more vertical and smaller faults form in the centre. (c, d) As the wedge pushes upwards, the dominant shear faults switch to a more favourable inclined position and re-establish a new spine. Shown here are 30s between frames at an ascent rate of 1.75 mm/min.

diameter, whereas lower strength spines are more likely to have a smaller diameter (Fig. 4.7). This is further supported by the observation of variable spine diameters both in our experiments as well as observations at active volcanoes. At Soufrière Hills, Lesser Antilles, the spine diameter varied from 25-50 m (Watts et al., 2002) and similarly sized domes have been observed at active volcanoes such as Santiaguito, Guatemala, Mt. Pelée, Lesser Antilles, and La Soufrière de Guadeloupe, Lesser Antilles (Fig. 4.9).

4.4.4 Dome and spine extrusion in natural scenarios

The shape of the domes produced in our experiments correlates well with a number of natural examples of recorded lava dome growth such as that at Santiaguito, Guatemala, in 2009 and 2019 (Jones and Johnson, 2011; Zorn et al., 2020a), Merapi, Indonesia, in 2015 (Darmawan et al., 2018a), Volcán de Colima, Mexico, in 2012 and 2013 (Hutchison et al., 2013; Zorn et al., 2019), and Kelut, Indonesia, in 2007 (Jeffery et al., 2013). Likewise, the growth height and width of our growing domes corresponds well to measurements and numerical models made at Volcán de Colima (Walter et al., 2019b). Many reported cases of spine growth also show similar morphologies to our experiments, including a variety of different spine sizes and diameters (Fig. 4.9). Most strikingly, an old study at the Santiaguito dome complex, Guatemala, shows a perfectly vertical and narrow spine situated on top of a flat-topped lava dome (Ospina, 1930) and is shown in fig. 4.9c. The occurrence of spines has repeatedly been reported at Santiaguito (Rose, 1972; Rhodes et al., 2018), so the constant slow extrusion seems to favour their formation. Similarly, we also highlight two small (10-20 m high) spines (Piton Saussure and Piton Dolomieu) that emerge from the larger dome structure at La Soufrière de Guadeloupe, Guadeloupe (Boudon et al., 2008), see fig. 4.9e. Furthermore, the 1902 eruption of Mt. Pelée, Martinique, produced a large vertical spine reported to be more than 300 m high (Gilbert, 1904). The description of the 1902 spine at Mt. Pelée as an extruding cylinder shaped by its collapses (Tanguy, 1994) is very reminiscent of our experimental results (Fig. 4.9f).

4.4.5 Applications for lava dome and hazard monitoring

Our experiments showcase a few features of lava dome growth and deformation that may be insightful for monitoring purposes and to identify potential hazards. A consistent observation is the increase in deformation on the side of the dome prior to a slump. The image sequences shown in fig. 4.4a, b show the strongest deformation on the upper headwall. A local increase in deformation is observed on the headwall before a slump occurs on that side (indicated by the

white arrows). This could be either due to precursory particle movement due to the oversteepening or due to an increase in lateral movement relating to the outer position of the oversteepened margin. While it has been suggested that collapse and slumping on the sides of a lava dome may promote further movement in this direction (Hutchison et al., 2013), this type

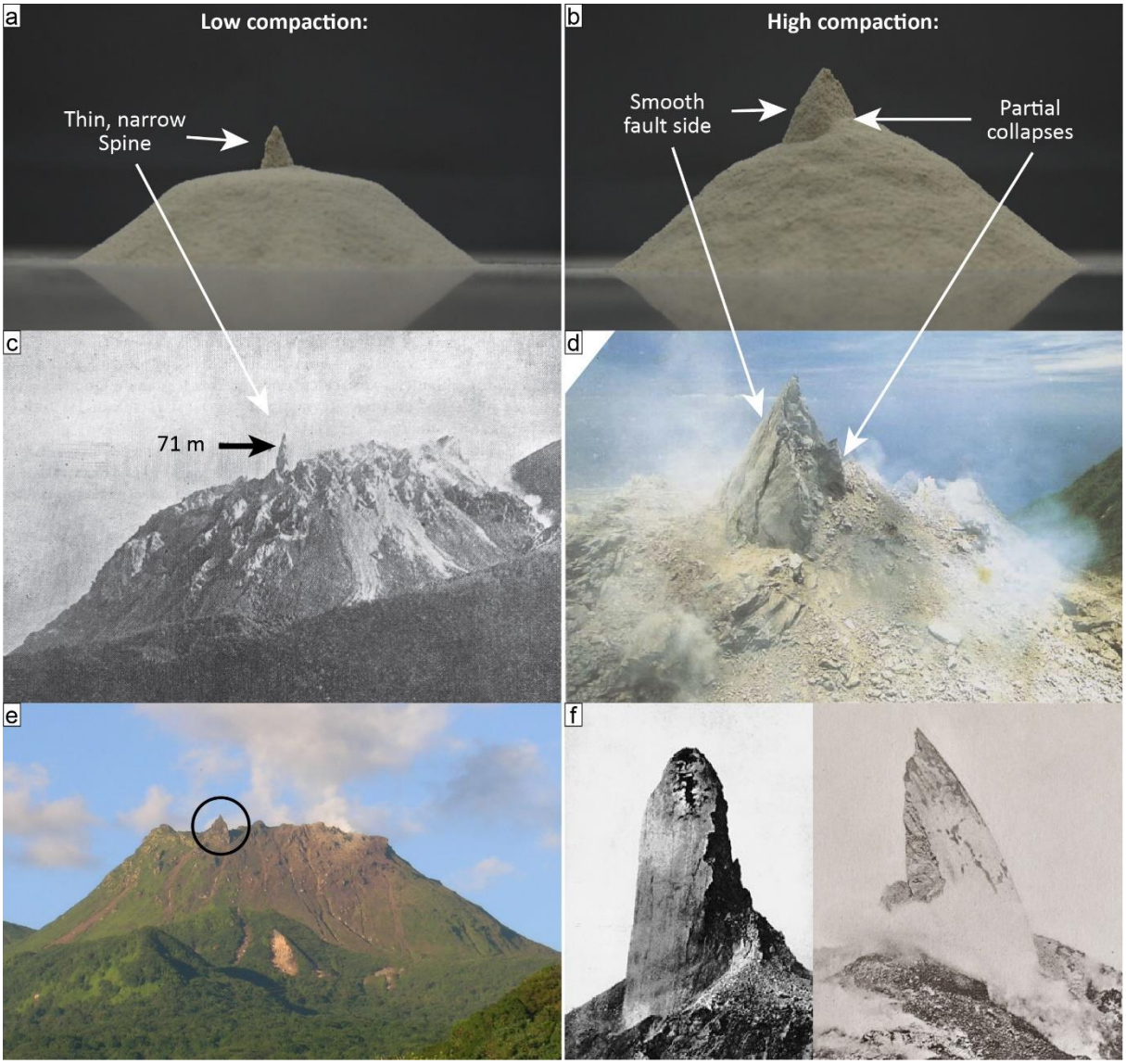

Figure 4.9: Comparison of experimental spine features with natural examples. (a) shows a spine with 10% plaster and (b) a spine with 20% plaster. (c) is a photo of the "La famosa Roca" spine at Santiaguito, which shows a similar narrow spine as our experiment with a low plaster content. Photo modified after Ospina (1930). (d) shows a spine at Soufrière Hills volcano in April 1996, which has a larger base and more complex features. This spine is similar to the experiment spines with higher plaster content. Photo modified after Watts et al. (2002) taken from the Montserrat Volcano Observatory (MVO). (e) is the lava dome at La Soufrière de Guadeloupe volcano with a small spine (Dolomieu Peak, marked by the circle) on the edge of the flat top. The photo was taken by Jean-Christophe Komorowski, see also Boudon et al. (2008). (f) shows the large monolithic spines in 1902 and 1903 at Mount Pelée; the original photos were taken by Alfred Lacroix.

of increased deformation before a collapse has not been described before and may be an important indicator of lava dome flank instability. A link between lava dome extrusion rate and the frequency and volume of rockfalls has been previously established at Volcán de Colima (Mueller et al., 2013). While the timescales in our experiment cannot reliably be translated into reality, such observation on natural domes could allow for a prediction of timing and location of a potential collapse on the dome flank and, consequently, the occurrence and direction of PDCs.

Another potentially useful observation is that the growth rate of vertical spines is nearly the same as the ascent rate of the underlying conduit. The ascent or extrusion rate is considered a critical parameter for the hazard state of silicic volcanoes (Husain et al., 2014; Carr et al., 2016; Zorn et al., 2018) and it could be inferred directly in such situations.

Finally, we found particle tracking via PIV a suitable tool to capture lava dome growth in detail under laboratory conditions. This method has been shown to be effective at natural lava domes and can be used for monitoring purposes (Walter, 2011; Salzer et al., 2016; Walter et al., 2019b) and to assess dome structures and lava viscosity (Zorn et al., 2020a). Provided the pixel resolution remains constant, this method can be applied to any time series images and standardized or automatized use on stationary monitoring cameras may assist in detecting important dome deformation and predict potentially hazardous conditions.

4.5 Conclusion

Our analogue experiments provide insight into a number of features and processes both for dome growth and spine formation. Dome growth occurs by a distributed upwelling-type motion of material within the inner dome, moving from the conduit to the surface, then outwards by slumping on the dome sides. This forms the well-established flat dome morphology, which grows by repeating cycles of internal swelling and slumping on the oversteepening sides at the margins of the flat top. We note that deformation on the dome surface increases significantly before a slump occurs. Spines appear after the dome edifice is established and grow at nearly the same velocity as the ascent rate in the conduit, making them the fastest moving parts of the dome. The spines are constrained by discrete faults that originate from the conduit walls and narrow towards the surface. The size of the spines depends on the compactibility of the magma analogue, with higher compactibility producing higher and wider spines. The spine width is thus smaller than or equal to the conduit diameter.

Many results and features observed on natural lava domes are successfully recreated in our analogue experiments and, in turn, allow for a more detailed understanding of the relevant

factors regarding dome growth and spine formation. Therefore, we highlight the importance and value of analogue experiments in gaining insights into lava dome processes, which are normally impossible or too dangerous to observe directly.

4.6 Acknowledgements

This is a contribution to VOLCAPSE, a research project funded by the European Research Council under the European Union's H2020 Programme/ERC consolidator grant ERC-CoG 646858.

We would like to thank Emma Hadre and Erica DePaolo for assistance with the dome extrusion experiments as well as Jaqueline Salzer for conducting the initial test experiments. We would also like to acknowledge the Natural Environment Research Council (NERC) for the opportunity to participate in the Advanced Training Short Course for Scaling and Design of Laboratory Experiments. We further thank Matthias Rosenau, Michael Rudolf, and Andre Polenz for access and assistance with the ring-shear tests as well as the provision of sieved and dyed sand, our technicians Peter Neuendorf and Stefan Mikulla for assistance with the experiment table setup, Fabian Wadsworth for a helpful discussion in experiment scaling and finally Alexander Belousov, Marina Belousova as well as Alina Shevchenko for sharing and translating spine cases at volcanoes in Kamchatka.

Chapter 5:
Further contributions

5.1: Imaging the 2013 explosive crater excavation and new dome formation at Volcán de Colima with TerraSAR-X, time-lapse cameras and modelling

Thomas R. Walter[1], Claire E. Harnett[2], Nick Varley[3], Dulce Vargas Bracamontes[4,5], Jacqueline Salzer[1], Edgar U. Zorn[1], Mauricio Bretón[3], Raúl Arámbula[4], Mark E. Thomas[2]

[1]German Research Centre for Geosciences GFZ, Potsdam, Germany
[2]Institute of Geophysics and Tectonics, University of Leeds, Leeds, UK
[3]Facultad de Ciencias, Universidad de Colima, Colima, Mexico
[4]Centro Universitario de Estudios e Investigaciones Vulcanológicas (CUEIV), Universidad de Colima, Colima, Mexico
[5]CONACYT-CUEIV, Universidad de Colima, Colima, Mexico

5.1.1 Abstract

The summit region of steep volcanoes hosting lava domes often displays rapid geomorphologic and structural changes, which are important for monitoring the source region of hazards. Explosive crater excavation is often followed by new lava-dome growth, which is one of the most dynamic morphometric changes that may occur at volcanoes. However, details of these crater formations, and the ensuing new dome growth remain poorly studied. A common problem is the lack of observational data due to hazardous field access and the limited resolution of satellite remote sensing techniques. This paper describes the destructive-constructive crater activity at Volcán de Colima, Mexico, which occurred between January and March 2013. The crater geometry and early dome formation were observed through a combination of high-resolution TerraSAR-X spotmode satellite radar images and permanently installed monitoring cameras. This combined time-lapse imagery was used to identify ring-shaped gas emissions prior to the explosion and to distinguish between the sequential explosion and crater excavation stages, which were followed by dome growth. By means of particle image velocimetry, the digital flow field is computed from consecutive camera images, showing that vertical dome growth is dominant at the beginning. The upward growth is found to grade into spreading and a lateral growth domain. After approximately two months of gradually filling the excavated

craters with new magma, the dome overflows the western margin of the crater and develops into a flow that produces block and ash flow hazards. We discuss and compare the observations to discrete element models, allowing us to mimic the vertical and lateral growth history of the dome and to estimate the maximum strength of the bulk rock mass. Moreover, our results allow a discussion on the controls of a critical dome height that may be reached prior to its gravitational spreading.

5.1.2 Methods: Time-lapse camera

Time-lapse terrestrial photographic methods are a very sophisticated and low-cost extension to other volcano monitoring methods (Major, 2005). Digital photogrammetry offers continuous footage at reasonable costs (Walter, 2011; Diefenbach et al., 2012) and, therefore, long-term monitoring perspectives. One of the pioneering time-lapse observations was made at the Showa-Shinzan dome on Hokkaido, Japan, in 1944–45, where the growth history was recorded by daily outline sketches from a fixed observation point (Mimatsu, 1995). This observation has become one of the best documented examples of subaerial dome growth in the world (Minakami et al., 1951; Miyamachi et al., 1987). Digital cameras have now replaced manual drawings; but similar "Mimatsu-diagrams" are still used and investigated at many volcano observatories worldwide (Poland et al., 2008; Wadge et al., 2009; Bretón-González et al., 2013; Ratdomopurbo et al., 2013; Zobin et al., 2015). While these Mimatsu-diagrams allow derivation of first-order parameters, such as investigating the general volume and outline of a dome, capturing the complete movement of the dome requires manual or automatic feature tracking techniques, as applied at lava flows (James et al., 2007) or at domes such as at Redoubt (Bull et al., 2013), Mt. St. Helens (Major et al., 2009; Walter, 2011), and Merapi (Walter et al., 2013a). Sophisticated tracking techniques often rely on mathematical correlation methods, such as the digital image correlation (DIC) or particle image velocimetry (PIV) techniques (Johnson et al., 2008; James et al., 2009; Walter et al., 2013b).

Our camera data were acquired by a 16 MPixel Nikon D5100 camera with an APS-C sensor and a resolution of 4928 × 3264 pixels. The camera is located at Nevado de Colima (N19.564° W103.617°) at a distance of 5790 m from the centre of the Volcán de Colima summit (Fig. 5.1). The camera is placed at a height of 3966 m above sea level, which is slightly higher than the summit height of Volcán de Colima at 3850 m. Due to the large distance between the camera and the target, we used a zoom lens with a focal length of 270 mm, ISO-100, equivalent to a 35-mm focal length of 405 mm. The camera was placed on a stable mount inside the observatory building. We use an external intervalometer for time-lapse control (Harbortronics

Digisnap 2700); the batteries are solar powered, and the internal time is regularly synchronized by GPS. In the period January–April 2013, we set the camera to take one image every hour and recorded 2685 images (11 Nov. 2012 to 14 Mar. 2013); maximum night time exposure was limited to 2 s, to reduce battery power and storage consumption. Pixel brightness (from 0 to 255) allows a first-order image quality estimation. Daylight images and cloudy images have larger mean pixel brightness (from ~125 to 255) than night images (from 0 to 125). Furthermore, the cloudy and night images show a smaller contrast in pixel brightness (difference between minimum and maximum brightness), allowing us to identify clear daylight camera images (black dots in fig. 5.2) and cloud/night camera images (grey dots in fig. 5.2). The threshold value of the pixel brightness difference was arbitrarily defined as b = 125 but was

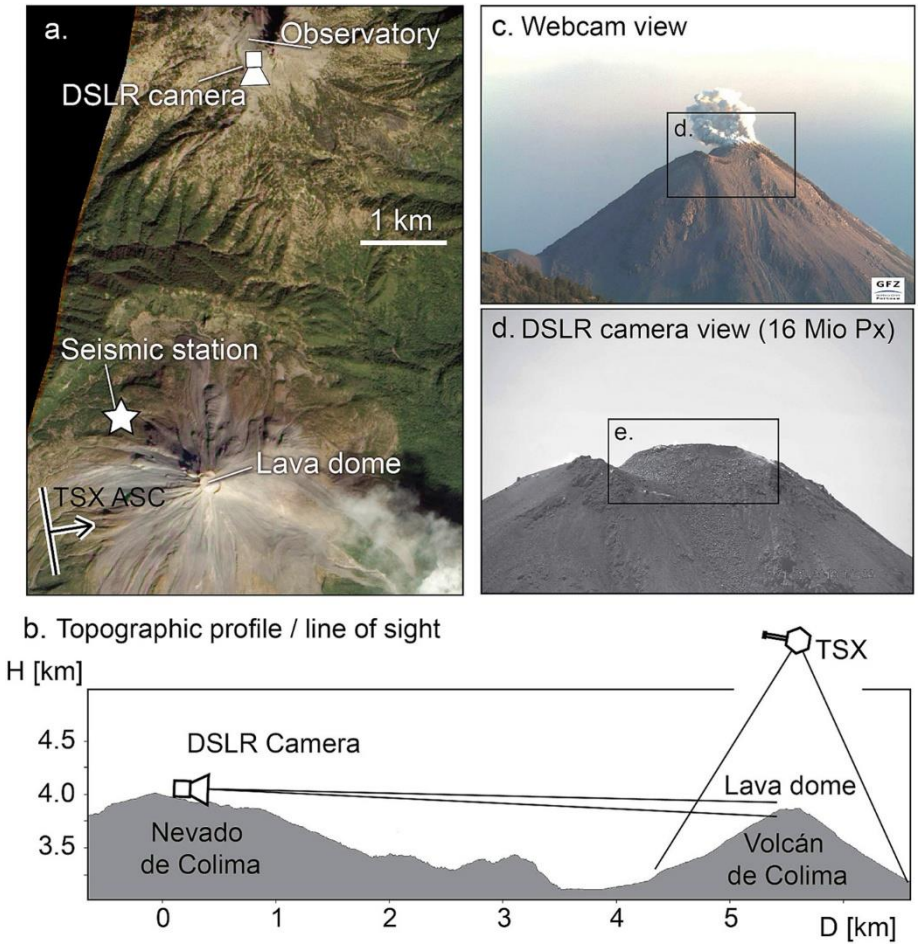

Figure 5.1: Satellite image of Volcán de Colima and the location of the camera and the seismic stations referred to in this work. (a) Volcán de Colima is located 5–6 km south of the observatory post at Nevado de Colima. The closest seismic station is indicated by a star. Camera location (DSLR) and TerraSAR-X viewing geometries (line of sight) are indicated by symbols. (b) Topographic profile from north to south, showing the field-of-view of the camera, and a sketch of the TerraSAR-X (TSX) radar satellite view (not to scale). (c) View from the web camera that is used for monitoring purposes, and (d) close view shown by the high-resolution DSLR time-lapse camera used. (e) Close-up view.

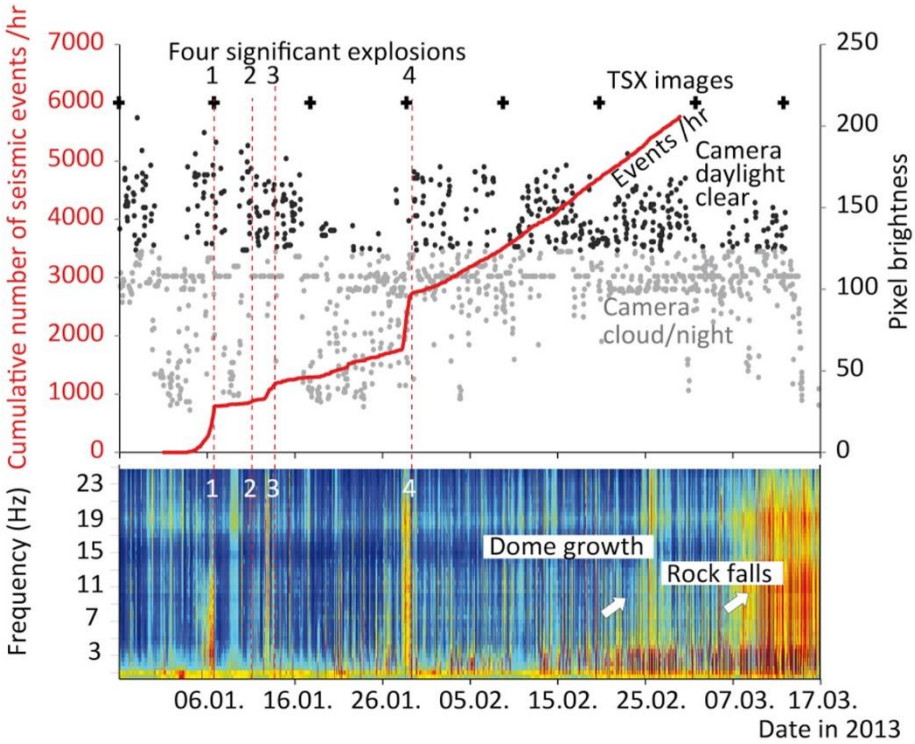

Figure 5.2: Data used in this study as a function of time. (Top) Seismic records show the occurrence of four significant trend changes slightly preceding four explosions in early 2013 due to precursory long-period events (red dashed lines) illustrated by event counts per hour (red trend line, y-axis on left). TerraSAR-X satellite radar images were available every 11 days (black crosses). Available time-lapse camera images are shown as black points (clear daytime images) and grey points (cloudy and night images). (Bottom) Seismic spectral amplitude measurements (SSAM) calculated from averaged power spectral density estimates of overlapped, windowed signal sections (10-min).

found to reduce the number of relevant images considerably (by 71%). From the remaining data we selected daily photos from similar daytimes, which could be used for digital image correlation analysis. The similar daytime image selection is of major benefit since it minimizes the effect of shadowing and insulation changes on the image-to-image comparison.

To translate the pixel scale to meter scale, we used a high-resolution digital elevation model that is based on the combination of aerial photogrammetry and LiDAR data (Salzer et al., 2017). We found that the flat-topped 2007–11 dome summit was 162 m wide in the NE-SW direction (azimuth N50°), and its height was 45 m on the east side as measured to the crater trough. The field-of-view (FOV) was translated through geometric transformations to a metric FOV of 520 m × 344 m, and the pixel dimensions were accordingly approximated to 0.1 m × 0.1 m. The viewing direction was SSE, i.e., the westward lava flow formation was on the right side of the image. We assumed a constant pixel size, although pixels representing areas closer to the camera at the northern flank of the summit are certainly somewhat smaller. Because the camera distance to the summit is very large (5.79 km) and the dome dimension is very small (0.16 km),

we assume that the constant pixel dimension is a reasonable simplification for the geometric problem (Fig. 5.1).

Fixed installed time-lapse cameras have major advantages of stable viewing geometry and constant optical parameters. We observed, however, that the camera images show a systematic and periodic short-term and long-term shift associated with slight movements of the camera, probably due to outdoor temperature changes. For most scenarios, these slight movements are irrelevant. However, as we used a large zoom lens, the effect is clearly visible. Because images we herein use were taken at the same time of day, this effect is reduced, and we further corrected the remaining shaking by simple image cross-correlation and shift translation.

We analysed the time-lapse data on a daily basis. First, we qualitatively describe any changes in morphology and degassing as observed in the images. Second, when growth of the dome occurred, we determine the displacement by applying the digital image correlation (DIC) technique, an image-matching method commonly used in computer vision studies. DIC permits the measurement of the shape, deformation and motion from two-dimensional array imaging data (Sutton et al., 2009). The idea is to first subdivide an image space into subregions and then compare the subregions by applying a correlation function. Using novel approaches of DIC, the accuracy of the subregion matching process can eventually result in position accuracies of 1/100 of a pixel (Schreier et al., 2000). More details on subregion conception, registration and the correlation procedure are provided in earlier reviews (Sutton et al., 2009). In our case, the impact due to variations in insulation is reduced by the selection of images from similar times of a day. Our method is insensitive to variations in the intensity while being sensitive to the offset of intensity variations, where the shifted pixel pattern in the deformed image is estimated (Pan et al., 2009). The correlation criterion then allows the estimation of the degree of similarity between the subregions of the first (master) image and the second (deformed) image of the dome. More details of the so-called zero-normalized sum of the squared differences (ZNSSD) method, already applied for volcano data (Walter, 2011; Walter et al., 2013b), are given in Pan et al. (2009). Subregion windows, with square dimensions, were selected in such a way that they were large enough to contain a distinctive intensity pattern but small enough to achieve a sub-pixel level of accuracy. In our case, the dimensions were 256 × 256 pixels during the first run and then incrementally decreasing to 64 × 64 pixels, with a constant subregion overlap of 75%. Decorrelation was defined to occur when less than three similar intensity peaks could be identified in a subset. Offsets on the order of 0.2 pixels could be detected, representing a displacement of 0.02 m for our camera. The main aim of the DIC analysis at Volcán de Colima is to trace the same physical subregions recorded in multiple images as a function of time. By

applying this method, we quantify the vertical and lateral growth of the dome and, for the first time, are able to identify the occurrence of gravitational spreading of a developing dome. The results are displayed in an image vector format for the selected area, and the full time series is shown for the central, western, and eastern dome in binary plots. These results were then reproduced using numerical models in section 5.1.4.

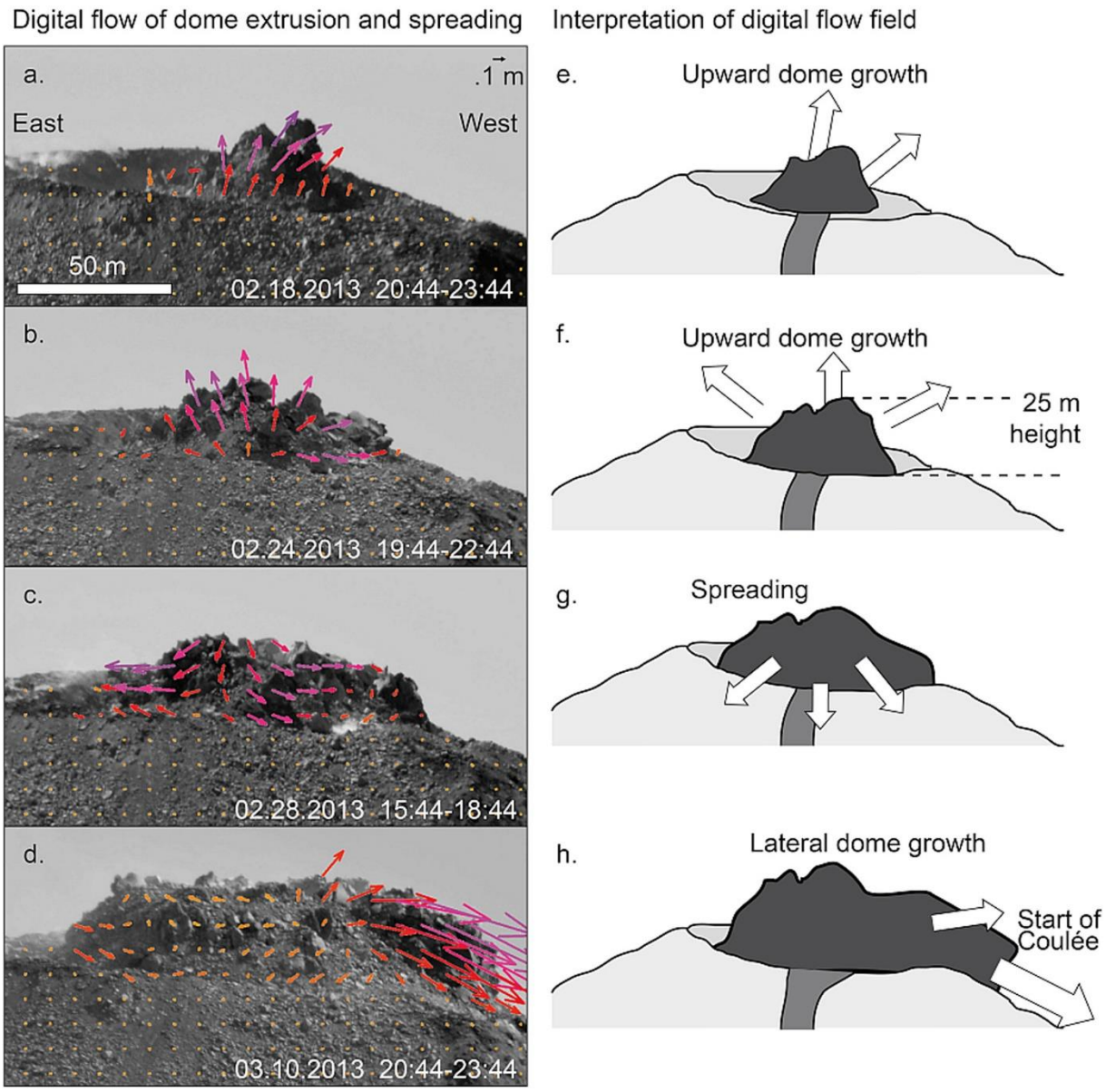

Figure 5.3: Digital image correlation results showing the growth of the dome, initially dominated by vertical growth (a, b). At a height of approximately 25 m, the dominantly vertical growth regime changes into a dominantly lateral growth regime. Occasional short-term subsidence of the dome is observed, possibly associated with block rotation, or spreading (c). Continued growth grades into a lateral direction of magma extrusion forming lava flows (d).

5.1.3 Results: Image correlation

Tracking distinct features in the image dataset means that quantitative information on this dome growth episode can be generated, as seen in the time-lapse camera images (Fig. 5.3). The DIC method allows the tracking of features in the image domain that do not change their optical properties but move by geometric rotation and translation (Walter, 2011). Applied to the dome, we observe first upwardly directed growth (Fig. 5.3a), which is slightly directed westward at its summit on 18 February 2013. This growth is followed by small local subsidence, such as on 23 February, after which the growth resumes again and is clearly identified on 24 February (Fig. 5.3c), directed radially away from the centre of extrusion. A few days later, we again see minor subsidence of the dome and lateral spreading of both the eastern and western flanks. After a short growth pulse to the east, the dome commences to mainly grow westwards, associated with the overflow over the western crater rim (Fig. 5.3d, h). The vertical growth of the dome is minor, if detected at all at this stage.

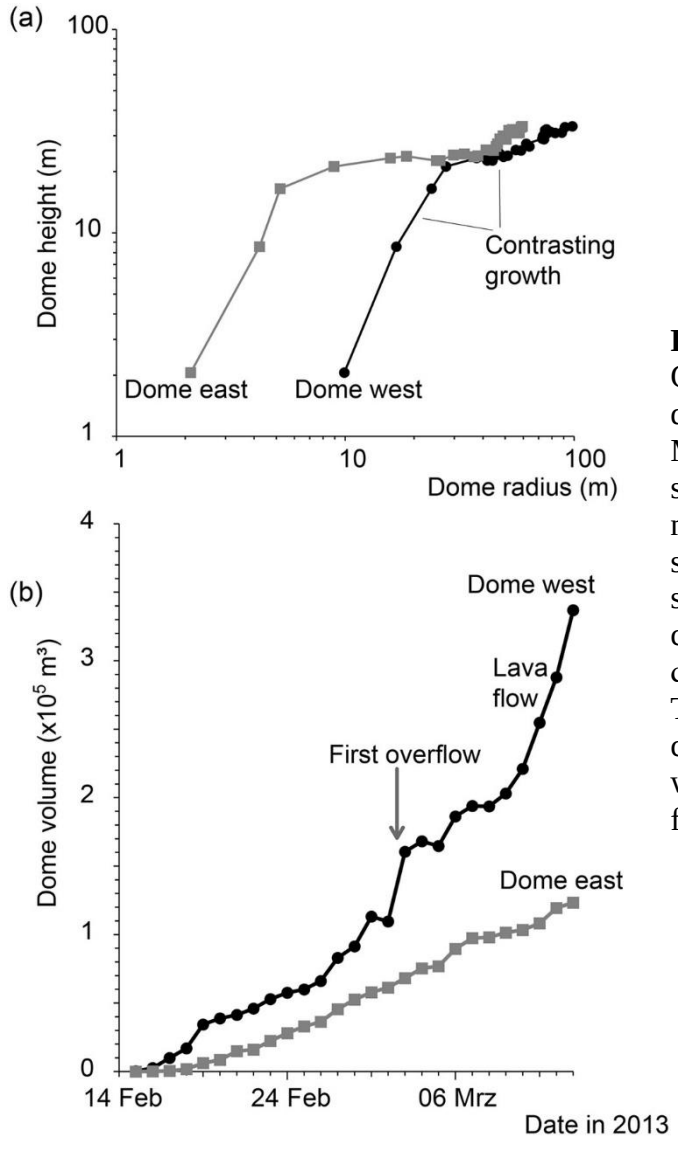

Figure 5.4:
Growth of the dome in the lateral and vertical directions, and volume estimations. Measurements at the east side of the dome are shown as grey symbols (squares), and measurements at the west side of the dome are shown as black symbols (circles). (a) Both sides of the dome show vertical growth changing into a more dominant lateral growth domain after an ~25 m height is reached. (b) The volume of the eastern dome is growing constantly, whereas the volume of the western dome strongly increases the lava flow, and crater overflow develops.

By depicting subregions of 100 × 100 pixels (or 10 × 10 m) in the centre and on the western and eastern flanks of the newly developed dome, we can generate time-growth graphs, as represented in fig. 5.4. The height of the dome is first seen to grow almost linearly, and then, as a critical dome height is reached, we observe a pronounced trend change (on 20 February). From that moment, vertical growth is much slower. As vertical growth decreases, we identify an increase in lateral growth, which is more strongly expressed on the western dome flank than on the eastern flank. This asymmetry evolves, producing overflow of the western crater rim.

Comparing the available datasets, we calculate the half dome volume changes, dividing the dome into western and eastern sections. The volumetric changes are provided in fig. 5.4b, showing that the western dome section first grew slowly in volume. Then it showed a sudden increase when the first crater overflow occurred on 2–3 March, followed by a short decrease before a sharp increase to 3.2×10^5 m^3 was observed. The growth of the eastern dome, in turn, became stable, with a near linear volume increase, reaching 1.2×10^5 m^3 after the same period. Therefore, our results indicate that crater rim overflow was associated with an increase in the eruption rate, directed on the western side, whereas the eastern half of the dome was not affected.

5.1.4 Discussion: Critical dome height and gravitational spreading

We investigate the dome growth scenario as quantified by the camera data. For the modelling we use the two-dimensional discrete element method (DEM) software PFC2D (Itasca Consulting Group, 2017) and follow the method outlined by Harnett et al. (2018). This DEM software creates material out of rigid particles that interact with neighbouring particles via elastic contact laws, where particles carry a force and moment that are updated per model time step. We incorporate different bond styles to model both fluid behaviour for the lava dome core (parallel bonds, Potyondy and Cundall, 2004) and solid behaviour in the outer carapace and talus regions (flat jointed bonds, Potyondy, 2012).

The model is initialized with a "batch" of magma in the conduit, whereby magma viscosity is determined by the bond stiffness of this material (Husain et al., 2014). We use a viscosity of 10^9 Pa·s, following estimates of apparent magma viscosity at Volcán de Colima in the range 10^9 to 10^{11} Pa·s (Lavallée et al., 2007; Lavallée et al., 2008; Kendrick et al., 2012). Constant extrusion is then simulated by adding an upward velocity to material in the conduit, and solidification is tracked throughout the model run. A more viscous dome is likely to be taller and less prone to lateral spreading, whereas a less viscous dome would likely not reach the heights seen from observational data. Similar to previous lava dome emplacement models (Hale

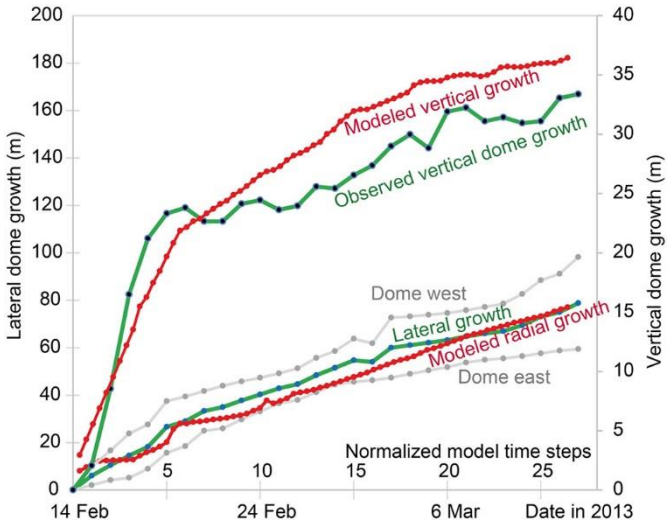

Figure 5.5: Comparison of dome growth camera observations (green curves) and discrete element models (red curves). The lateral (left Y-axis) and vertical dome growth (right Y-axis) are shown separately. The east and west sides of the lateral dome growth are shown in grey, average in green. The initially steep vertical growth and subsequent dominantly lateral growth can be well explained by models. The X-axis shows the date for observations, and normalized time for the models. The change in slope from the graph is explained by the dome reaching a critical strength threshold.

and Wadge, 2008; Hale et al., 2009b; Hale et al., 2009a; Husain et al., 2014), we use the solidus pressure to model the lava solidification process and therefore track the boundary between the fluid core and solid carapace. The mechanical properties of the dome rock are hard to determine at a rock mass scale, despite previous studies on Volcán de Colima andesites at a laboratory scale (Heap et al., 2014a; Heap et al., 2016). We therefore use the morphology of the growing dome to estimate mechanical rock strength by using a calibration procedure process in PFC (e.g., Holt et al., 2005; Holohan et al., 2011; Holohan et al., 2017) and matching the model morphology to the observed morphology (Fig. 5.5). This estimation was achieved through a forward modelling approach (Harnett et al., 2018), and the model results were corrected to account for the 2-dimensional nature of the model.

Matching the model morphology to the observed dome morphology, a peak rock strength of ~3.7 MPa is necessary to yield a critical dome height at which vertical growth abruptly decreases, as observed by the camera data. This strength value is ~20% of the lowest laboratory values and suggests an intense level of fracturing and/or porosity that is present in a cooling and dynamically evolving carapace that has a significant effect on the rock behaviour at a rock mass scale (Zorn et al., 2018). To match the observed dome growth, a reduction in Young's modulus is required from 8.1 GPa in the tested dome rock from Volcán de Colima to 3.5 GPa. This reduction alludes not only to the importance of fracturing, but also the importance of scaling both the strength and elastic parameters of material from the laboratory sample scale to a rock mass scale (Heap et al., 2018).

The modelled dome growth shown in fig. 5.5 shows a morphology similar to the observed dome growth at Volcán de Colima during February/March 2013. Early dome growth is dominated by vertical growth and an initial increase in height; the explicit width of this growth in the early

stage of the model is determined by the initial conditions imposed for the width of the conduit (Fig. 5.5). A height threshold is reached, after which horizontal growth exerts greater control over the lava dome growth (critical height). This means that initially, the dome extrudes and solidifies very quickly to create a near-vertical spine. Once sufficient dome material is extruded, the dome is able to maintain ductile core material within it (and therefore transitions to a more endogenous-style growth). This horizontal growth increase is accordingly interpreted to be due to increased gravitational spreading of the rock mass. As observed in the camera image analysis, oversteepening occurs on the dome flanks, along with the generation of rubbly spine-type features towards the apex of the dome. Although the steep vertical growth observed initially at Volcán de Colima is reproduced well, small differences may suggest an initially stronger material. Possibly, the first magma extrusion could be more degassed and, hence, more viscous; the initial vertical growth domain is therefore likely associated with extrusion of a viscous plug and conduit material before fresh magma reached the surface and spread laterally. Future studies may also be needed to understand the effect of temperature on rock strength.

We note that the models are 2D only and that matching the exact timing of the dome growth phases is challenging, as complete temporal coverage of the extrusion process is not available. The modelled dome starts extruding at time zero, and comparisons are made to the monitored dome until it starts to overflow the crater rim. This model gives a fixed frame of reference and allows comparison against normalized time relative to the dome width. The compared time series of the modelled and observed dome growth can therefore be relatively shifted in the time domain by several days.

5.1.5 Conclusions

At Volcán de Colima, new excavations of several nested summit craters were observed in detail by high-resolution satellite radar data and by a time-lapse monitoring camera. We could identify crater excavation associated with three Vulcanian explosions in January 2013 and the deposition of a major bomb outside of the crater. The craters were carved into the cooled 2007–2011 dome material, with variations observed in the crater geometry and position during successive Vulcanian explosions. Prior to the crater formation, pronounced degassing was observed, partially with a ring-shaped emission pattern, identifying the location of the later explosion crater excavation. Following this destructive crater-forming activity at Volcán de Colima, an early dome formation episode was observed. While the high-resolution TerraSAR-X spotmode satellite radar images allow imaging the early dome deep inside the excavated craters, the permanently installed monitoring cameras allow tracing the details of dome growth

once the dome reached the height of the crater rim. Using PIV, we perform an image-to-image comparison and optical flow field, allowing the identification of initial vertical dome growth. This vertical growth gradually changed to lateral growth caused by gravitational spreading of the dome material. The dome continued to grow laterally, and to a minor degree also vertically, until it overflowed the margin of the crater and developed into a lava flow. We compare these dome growth observations to discrete element models and find that the observed dome morphology can be matched if the lava dome peak rock strength is significantly lower than common laboratory values.

5.2: Volcanological applications of unoccupied aircraft systems (UAS): Developments, strategies, and future challenges

Mike R. James[1,2], Brett B. Carr[3], Fiona D'Arcy[4], Angela K. Diefenbach[5], Hannah R. Dietterich[6], Alessandro Fornaciai[7], Einat Lev[3], Emma J. Liu[8], David C. Pieri[9], Mel Rodgers[10], Benoît Smets[11], Akihiko Terada[12], Felix W. von Aulock[13], Thomas R. Walter[14], Kieran T. Woods[15], Edgar U. Zorn[14]

[1]Lancaster Environment Centre, Lancaster University, Lancaster, UK
[2]UK Lancaster Intelligent Robotic & Autonomous Systems Centre, Lancaster University, Lancaster, UK
[3]Lamont-Doherty Earth Observatory, Columbia University, NY, USA
[4]Department of Earth and Planetary Sciences, McGill University, Montreal, Canada
[5]Volcano Disaster Assistance Program, U.S. Geological Survey, Vancouver, USA
[6]Geological Survey, Alaska Volcano Observatory, Anchorage, USA
[7]Istituto Nazionale di Geofisica e Vulcanologia, Sezione di Pisa, Italy
[8]Earth Sciences, University College London, London, UK
[9]Jet Propulsion Laboratory, California Institute of Technology, Pasadena, USA
[10]School of Geosciences, University of South Florida, Tampa, USA
[11]Natural Hazards Service, Royal Museum for Central Africa, Tervuren, Belgium
[12]Volcanic Fluid Research Centre, School of Science, Tokyo Institute of Technology, Tokyo, Japan
[13]School of Environmental Sciences, University of Liverpool, Liverpool, UK
[14]German Research Centre for Geosciences GFZ, Potsdam, Germany
[15]Department of Aerospace Engineering, University of Bristol, Bristol, UK

5.2.1 Abstract

Unoccupied aircraft systems (UAS) are developing into fundamental tools for tackling the grand challenges in volcanology; here, we review the systems used and their diverse applications. UAS can typically provide image and topographic data at two orders of magnitude better spatial resolution than space-based remote sensing, and close-range observations at temporal resolutions down to those of video frame rates. Responsive deployments facilitate dense time-series measurements, unique opportunities for geophysical surveys, sample

collection from hostile environments such as volcanic plumes and crater lakes, and emergency deployment of ground-based sensors (and robots) into hazardous regions. UAS have already been used to support hazard management and decisionmakers during eruptive crises. As technologies advance, increased system capabilities, autonomy, and availability - supported by more diverse and lighter-weight sensors - will offer unparalleled potential for hazard monitoring. UAS are expected to provide opportunities for pivotal advances in our understanding of complex physical and chemical volcanic processes.

5.2.2 Non-technical summary

Unoccupied aircraft systems (UAS) are developing into essential tools for understanding and monitoring volcanoes. UAS can typically provide much more detailed imagery and 3-D maps of the Earth's surface, and more frequently, than satellites are able to. They can also make measurements and collect samples for geochemical analysis from hazardous regions such as volcanic plumes and near active vents. Through being quick to deploy, they offer key advantages during initial stages of volcano unrest as well as throughout eruptions. Data from UAS have already been used to support hazard management and decision-makers during crises. In the future, UAS will become increasingly capable of flying longer and more complex missions, more autonomously and with more sophisticated sensors, and are likely to become key components of broader sensor networks for monitoring and research.

5.2.3 Imaging and photogrammetric surveys

For topographic imaging (either to generate 2-D products such as orthomosaics, or to derive 3-D and 2.5-D products such as digital elevation models), the survey component of the flight can be designed based on established photogrammetric principles developed for conventional nadir-viewing aerial surveys (e.g. Abdullah et al., 2013). Due to imaging surveys being a common use of UAS, mission planning software usually includes specific design support for photogrammetric data collection. Survey design starts from a definition of the measurement requirements, for example, identifying the survey area, the ground sampling distance (GSD) required, and the planimetric (or 3-D) measurement precision and accuracy to be achieved. The GSD depends on the imaging sensor characteristics (e.g. camera focal length and pixel pitch) and the flight height (e.g. see O'Connor et al., 2017 for a readable summary). Based on these relations, flight planning software can estimate the image capture positions once the required survey area is defined and other parameters such as image overlap are provided. For areas of

steep topography, flying at a fixed altitude can result in significant changes in GSD between high- and low-elevation areas and, in some instances, may result in a failure to obtain sufficient overlap. For these areas, a terrain-following flight plan may be best, where the UAS follows a 'draped' survey at a constant height above the ground.

Surveys designed for 2-D products (e.g. orthomosaics), usually collect images in conventional parallel strips (in a 'lawnmower' pattern), with overlaps between adjacent images of 60–90% (Fig. 5.6a). Where 3-D data are required, the photogrammetric network is strengthened by adding cross-strips and by having image overlaps at the upper end of the range. Carrying out such surveys from tens to hundreds of metres above ground usually enables efficient automatic execution (image acquisition and navigating the flight path) under full autopilot control. In

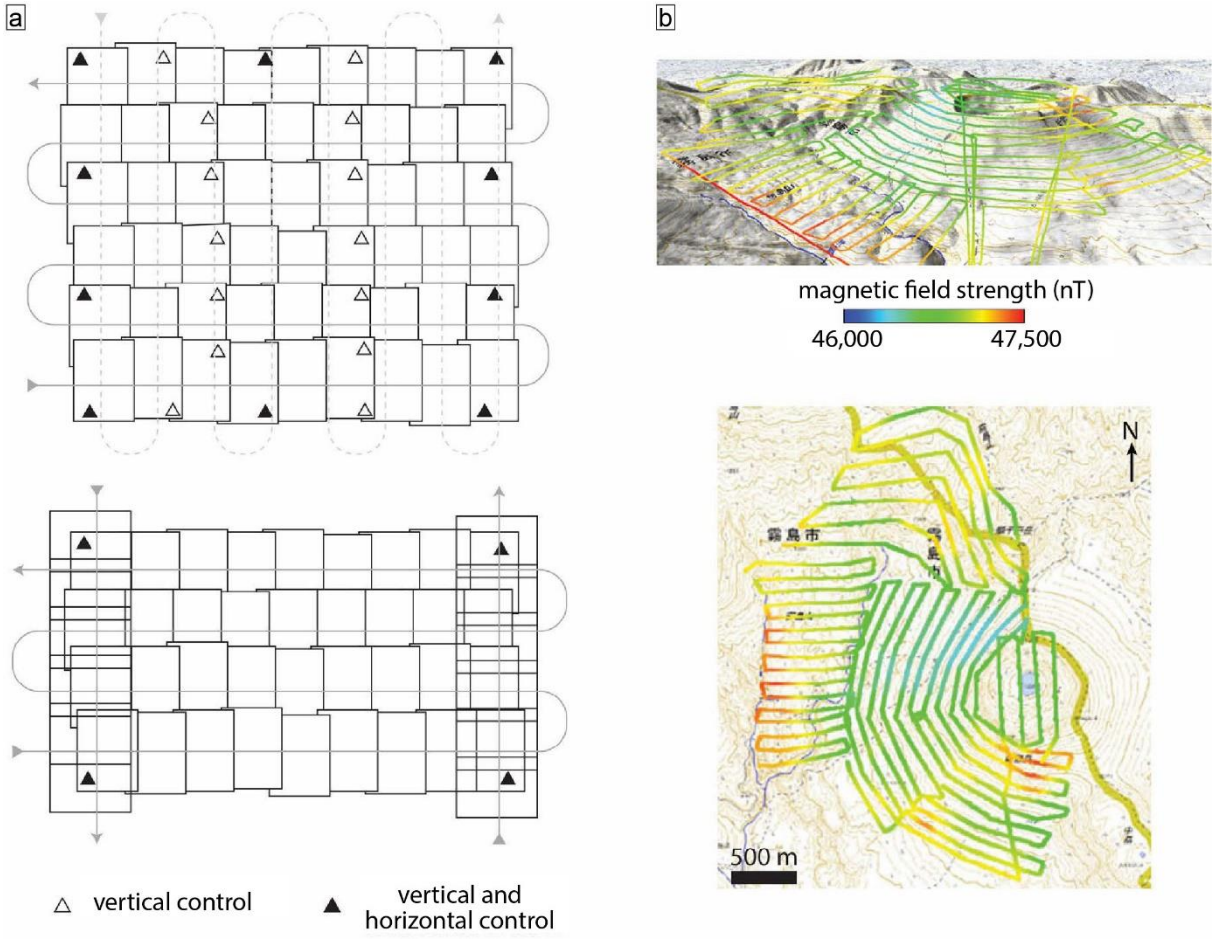

Figure 5.6: Survey flight paths. (a) Schematic of conventional flight paths (grey) for aerial photogrammetric surveys. Surveys comprise two orthogonal grids of parallel flight lines, shown (top) for only ground points (triangle symbols) used as control measurements, or for (bottom) when suitably accurate camera position data are also available. Only a selection of image outlines is shown for the horizontal lines; along-strip image overlap for UAS surveys are often 70–90 %. Adapted from James et al. (2017a). (b) Visualisation of flight lines from a draped total magnetic field survey over Shinmoe-dake, Japan (2011), coloured by measured magnetic field intensity and viewed (top) obliquely or (bottom) in plan (Koyama et al., 2013).

systems where the camera control is not integrated with the autopilot system, image acquisition can be set at a specific time interval, with any excess images not forwarded for processing.

High quality results generally require crisp, well-focused images of highly textured stationary scenes, making colourful weathered bare rock surfaces good survey targets. Motion blur, featureless areas (e.g. fresh snow) or highly complex or moving targets (e.g. vegetation, water) reduce the quality of the image matching, resulting in increased systematic error and noise in modelled surfaces. Since areas of strong shadow can present difficulties during processing, diffuse illumination from overcast weather is the preferred condition for imaging or photogrammetric surveys. Photogrammetric considerations such as overall imaging geometry (including image overlap) and the internal stability of the camera (i.e. how well all photographs can be represented using one camera model) also affect topographic measurement precision.

Processing photogrammetric survey data typically involves an automated camera calibration procedure (Luhmann et al., 2016) that aims to minimise systematic error in the resulting topographic model. Although camera calibration can be carried out separately from the survey (e.g. Harwin et al., 2015) the most reliable results are usually obtained if surveys are designed to facilitate the calibration process by acquiring some images over different ranges and angles (James and Robson, 2014; Harwin et al., 2015; Nesbit and Hugenholtz, 2019), and this is particularly important if there are limited or no external 'control' measurements to include in the processing. Inclusion of such convergent imagery in survey designs strengthens the photogrammetric image network by enabling surface points to be observed from multiple and highly varied viewing directions. This facilitates unique and accurate estimates of camera model parameters during processing (Fraser, 2013) and helps avoid systematic error propagating into topographic results. Consequently, for nadir surveys, including some off-nadir images (~30° oblique) can strongly reduce systematic error in DEMs (James and Robson, 2014; Nesbit and Hugenholtz, 2019). For topographic targets that are strongly 3-D with respect to the mean flight height above ground (e.g. domes or crater walls), using systems with a gimballed camera capable of being reoriented during flight enables better coverage and stronger image networks than conventional nadir survey styles. In some cases, circular flight paths can be adopted, in which the camera is constantly oriented at a central 'point of interest'.

For thermal and multispectral surveys, sensor and lens characteristics usually result in imagery with a lower spatial resolution than from visible-wavelength cameras flown at the same altitude. Thus, for comparable GSDs, thermal and multispectral surveys usually need to be flown at lower elevations above ground. Typically, such imagery are used only for orthomosaic products but, sometimes, thermal imagery can also provide useful 3-D data for areas occluded by

condensing gases, where results from visible-wavelength data have been compromised (e.g. fig. 5.7; Thiele et al., 2017).

When compared with visible-wavelength surveys, thermal and multispectral surveys usually have more stringent radiometric requirements. For calibrated, quantitative analyses of multispectral data, repeat acquisitions of flight segments over a calibration surface of known reflective properties (or temperature) are required to account for changing light conditions. As for visible-light surveys, multispectral surveys are degraded by strong or moving shadows, so best practice is to fly on an overcast day during consistent illumination conditions. For thermal

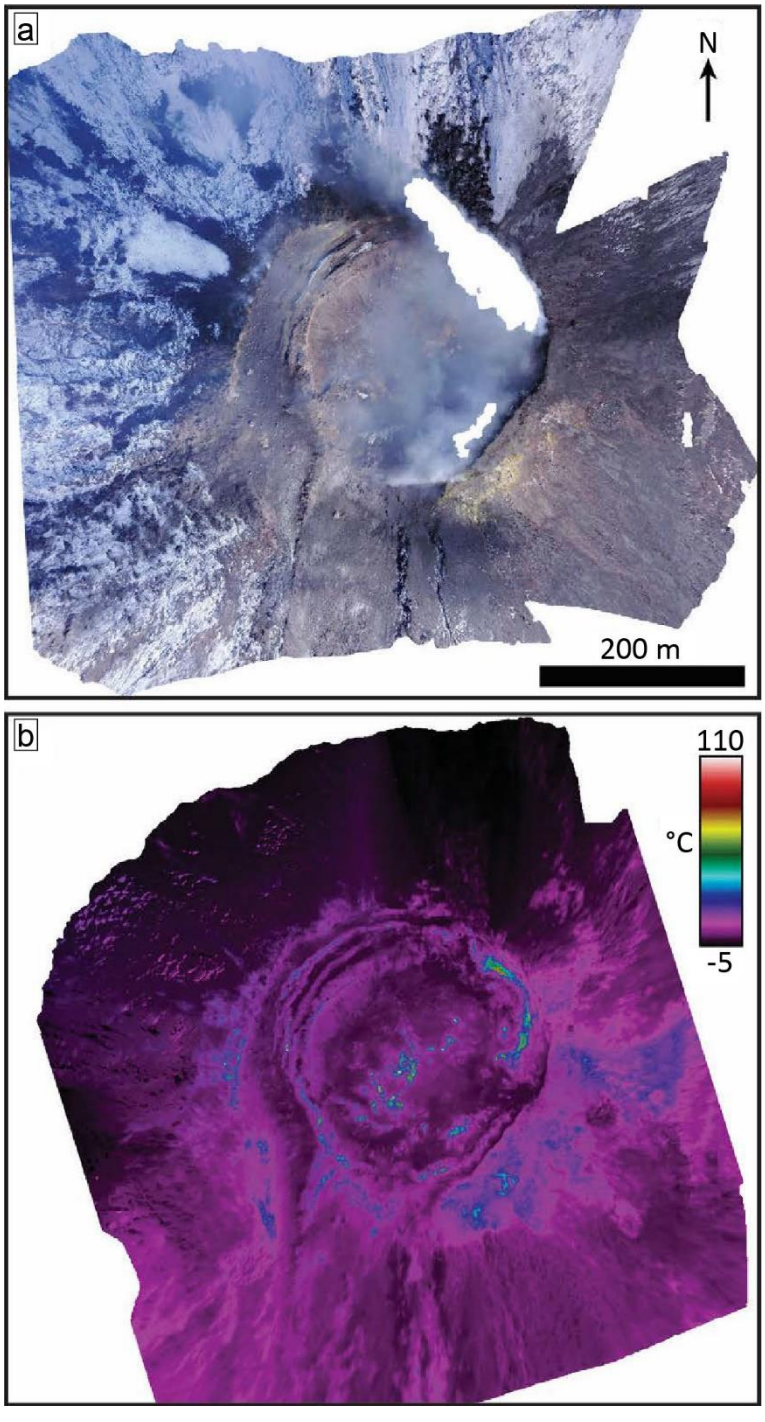

Figure 5.7:
Vertical views of 3-D models of the summit lava dome at Volcán de Colima, Mexico, constructed from quadcopter surveys (2018). (a) A visible-wavelength survey using 58 photographs acquired using a Mavic Pro and (b) 195 thermal images acquired with a FLIR TAU2 thermal camera on a Phantom 4 Pro. Both surveys were carried out at ~120 m above ground, with the higher-resolution visible data resulting in a model resolution of ~7.3 cm, compared to ~40 cm for the lower-resolution thermal data. Note that the visible data did not enable successful modelling of some areas which were obscured by degassing plumes (e.g. the NW-oriented white area of the NE crater wall area), whereas the thermal data provided full topographic coverage.

surveys, to avoid contamination from solar heating or reflection, pre-dawn missions are optimal.

Survey design should also consider georeferencing requirements and be linked to the deployment of ground control (if it is used). For detailed topographic work, considering photogrammetric and georeferencing contributions to measurement precision is important (James et al., 2017a; James et al., 2017b), for example, an image network capable of giving a strong focal length estimate during camera calibration is particularly important if ground control is weak or unavailable, and georeferencing is carried out by using measured camera positions instead. Recourse to the extensive photogrammetric literature will facilitate achieving the best survey accuracies if required (e.g. Kraus, 1993; Mikhail et al., 2001; Kraus, 2007; McGlone and Lee, 2013; Luhmann et al., 2014).

5.2.4 Lava flows, fissures, and domes

Mapping and characterising eruptive fissures, lava flows, and lava domes is becoming increasingly common. The working environments involved are particularly challenging for ground-based data collection, with access on foot often not possible during activity, and being potentially dangerous for years afterwards due to lose and unstable surfaces. Only aerial approaches may be feasible to acquire detailed observations, but crewed helicopters, planes, or microlight aircraft may not be available at remote locations or during disasters and, with personnel on board, may have restricted access due to hazards such as airborne ash. Moreover, use of crewed aircraft requires reasonable advance planning and suitable meteorological conditions over the survey area and the approach route. During changeable weather conditions, UAS have the distinct advantage of requiring much shorter weather windows over much smaller areas within which to offer measurement opportunities.

5.2.4.1 Crisis response

One of the first uses of UAS during an effusive eruptive crisis was during the 2014–2015 Pāhoa eruption of Kīlauea volcano in Hawai‘i. A team from the University of Hawai‘i Hilo, located very close to the communities threatened by the flows, deployed UAS in coordination with the emergency response forces and supplied rapid information to civil defence. Post-analysis suggested that, for accurately forecasting pāhoehoe flow paths through such lowland tropical forest environments, optimal UAS imagery should enable DEMs with a resolution between 1 and 3 m (Turner et al., 2017).

During the 2018 lower East Rift Zone eruption and summit collapse of Kīlauea volcano, UAS were routinely deployed for emergency response and scientific data collection tasks. The UAS provided continuous on-demand flight capability for situational awareness, tracking active lava flow fronts, overflows and caldera growth, gas monitoring with multi-GAS and DOAS, and assisting civil defence in identifying structures and people at risk (Diefenbach et al., 2018). Real-time livestreaming video, rapidly uploaded field images, coordinates, and SfM-derived map products from the field were provided to emergency responders. During one incident, the UAS team identified a new outbreak of lava that was moving rapidly toward a residential area and notified emergency response of the immediate need for evacuation. UAS live-streaming video helped guide evacuation efforts and search teams to a stranded individual who was threatened by advancing lava flows. The individual was instructed to "follow the drone to safety" and was tracked as they moved through the jungle to meet the search teams (for reports and video, see: https://www.usgs.gov/media/videos/k-lauea-volcano-uas-mission-aid-rescue, and https://www.doi.gov/aviation/uas/doi-uas-teams-supportingvolcano-monitoring-emergency-response-rescue). DEMs and orthoimagery derived from daytime optical and night-time thermal surveys were particularly valuable for use during eruption response, especially for flow mapping and to update models of the changing topography for lava flow forecasting. Datasets collected at intervals of <1 hr to a week, at resolutions of 0.05–1 m over areas of 2–10 km^2 each, provided an unprecedented 4-D record of lava flow emplacement and caldera collapse over the three months of the eruption (Fig. 5.8a). Rapid, low-quality processing using

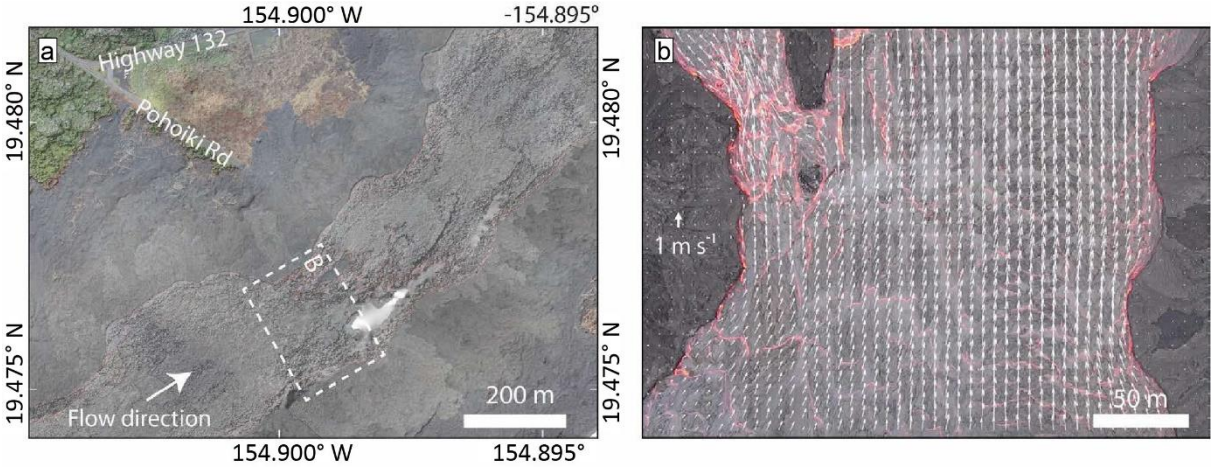

Figure 5.8: UAS imaging of active lava flows at Kīlauea volcano, Hawai'i. (a) Orthomosaic draped over a digital elevation model (DEM) of a section of the Fissure 8 channel of the 2018 Lower East Rift Zone eruption. UAS crew vehicles are visible on the road. Dashed rectangle outlines the location of (b), a segment of the Fissure 8 channel, overlaid by arrows indicating flow velocity magnitude and direction, computed using particle image velocimetry analysis on video acquired during UAS hover.

onboard RTK GNSS for georeferencing during the eruption provided products as quickly as possible, sacrificing higher resolution and accuracy for speed.

The UAS also provided an important tool for monitoring effusion rate changes. UAS acquired gimbal stabilised overhead nadir videos along a defined set of channel site locations from the vent region to the zone of dispersed flow (10 km from vent) at intervals of hours to weeks. Particle velocimetry (PIVlab; Thielicke and Stamhuis, 2014) analyses of short (2–15 min) video segments provided timely measured flow rates within hours (Fig. 5.8b). Results were then integrated with depth estimates to evaluate bulk flux through the channel at the vent, and within different flow branches (Dietterich et al., 2018). These data enabled quantification of changing effusion rates (50–200 m^3s^{-1}) over the course of the eruption (Neal et al., 2019), an improved understanding of the driving forces of effusion rate fluctuation (Patrick et al., 2019), and provided a record of the down-flow evolution in channel dynamics. Such results were important for flow forecasting and assessing changes in activity for eruption response, in addition to representing a substantial dataset on lava flow emplacement.

UAS similarly enabled maps and lava volume estimates for supporting monitoring efforts during the 2017 eruption of Mt. Etna, Italy (De Beni et al., 2019). Given the crisis, timely delivery of results (of order a day) covering >1 km^2 was prioritised over achieving high precision, so extensive ground control was not deployed. The issues encountered highlighted the importance of having sufficiently high-quality pre-eruption baseline topographic data to enable surface-to-surface survey georeferencing when it was not feasible to distribute dedicated GCPs.

5.2.4.2 Dome monitoring

With lava domes usually forming in inaccessible summit regions and being associated with explosion or collapse hazards, UAS have proved advantageous for providing both timely and sufficiently high-resolution imagery to identify structural details such as fractures (Darmawan et al., 2018b) or rapid growth and collapse (De Angelis et al., 2016a; Watson et al., 2017). For example, UAS-based visual images of the active lava dome at Mount Sinabung, Indonesia, resulted in SfM-based point cloud models (with data densities two orders of magnitude greater than those from an earlier ground-based survey; Carr and Lev, 2018). These data permitted estimates of the collapse volume removed from the dome and thus the corresponding volume, morphology, and grain size distribution of the resulting pyroclastic flow deposits (Carr et al., 2019). At Mount Merapi, Indonesia, following the start of the current eruptive phase with an explosion in May 2018, a UAS enabled the first detection of dome growth in the summit crater

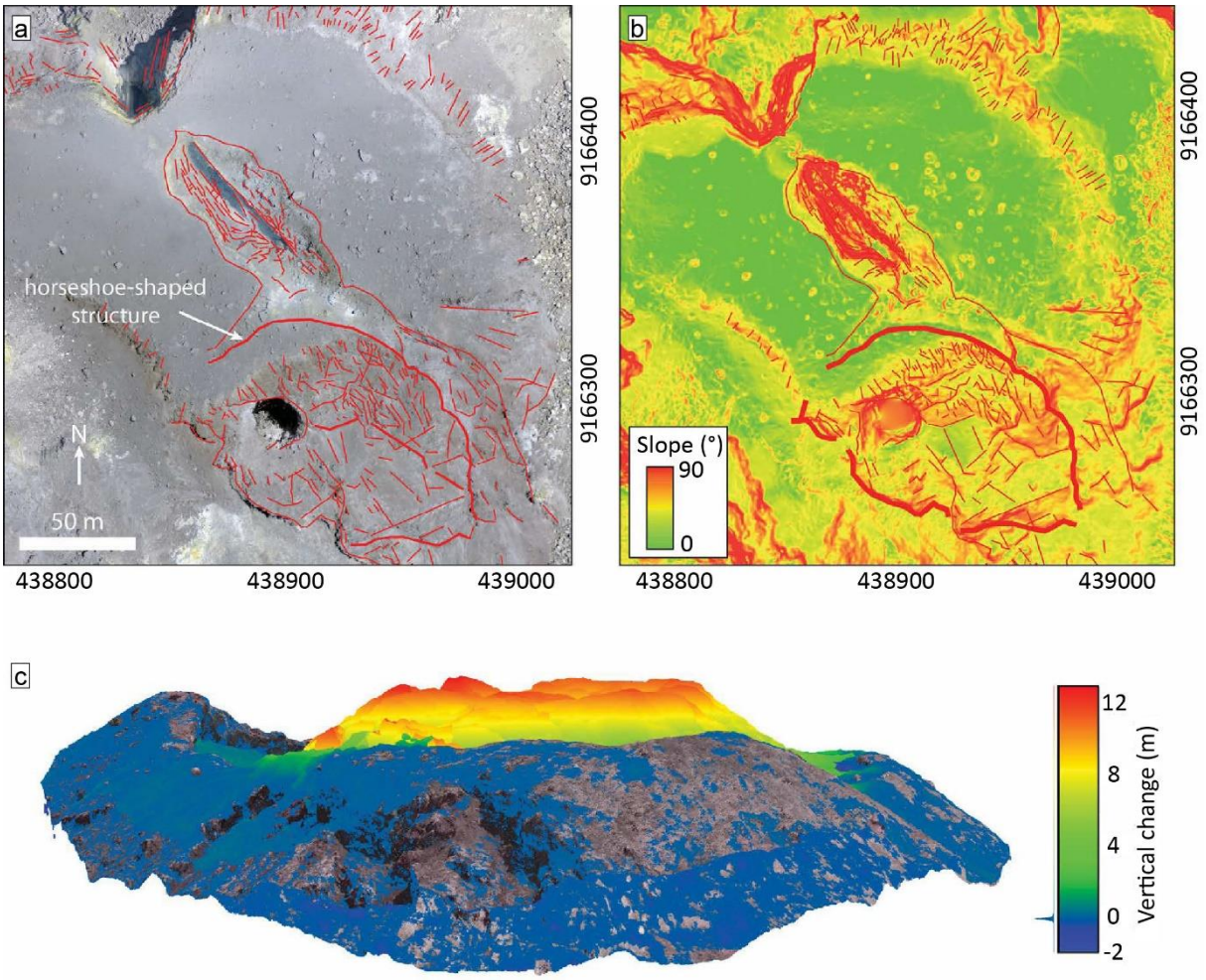

Figure 5.9: Lava domes surveyed by UAS. (a) and (b) The lava dome at Merapi, as mapped by combined UAS and TLS surveys (October 2015), showing a flat summit region, with highly a fractured central fissure area, dome margins, and southern flank. Red lines denote fractures and visible lineaments, and coordinates are in UTM. (a) Photomosaic of imagery collected by a DJI Phantom quadrotor from a height of 140 m above the ground. (b) Slope map from a 0.5-m-resolution DEM. The horseshoe-shaped structure bounds a fractured, southern-sloping region (descending >80 m at the map boundary) for which repeat UAS imaging in 2017 identified mechanical weakening, due to hydrothermal alteration at its northern boundary. Adapted from Darmawan et al. (2018b). (c) Dome growth of Volcán de Fuego captured by repeat flights of a DJI Phantom 3 Pro quadrotor in 2017 (Watson et al., 2017). The oblique view shows two SfM-photogrammetry point clouds of the growing dome in the summit crater derived from imagery acquired on 19 (in true colour) and 23 (coloured by vertical change) February; the flat dome surface is approximately 40 m across. With GCP deployment not possible, the surveys were georeferenced using GNSS information embedded in the image metadata and their relative registration then refined using regions of unchanged surface on the flanks.

(August 2018). Repeat UAS surveys have identified the growth of fracture networks and the excavated volume associated with phreatic explosions during 2012–2015 (Darmawan et al., 2018a). The surveys enabled identification of areas of hydrothermal alteration and structural weakening along the dome structures, that may contribute to future instability and collapse (Fig. 5.9a, b; Darmawan et al., 2018b).

At consistently active domes, regular UAS survey results can be used to provide proximal observations of eruptions, assess dynamics, and integrate with other monitoring datasets. For example, visual and thermal UAS imagery have augmented seismic and geochemical data on Santiaguito volcano, Guatemala (Lamb et al., 2016). Changes in the explosive and effusive activity at the dome and crater have been assessed using video and DEM construction to quantify eruptive behaviour, structural features, lava flow metrics, and ballistics distribution (De Angelis et al., 2016a; von Aulock et al., 2016). At Santiaguito, UAS video footage of an explosion showed 20-30 m long fractures, from which venting occurred during small outgassing events. These observations constrained inversions of acoustic infrasound signals and thus estimates of mass eruption rates during explosions (De Angelis et al., 2016b). At Volcán de Fuego, Guatemala, rapid extrusion rates on the order of 10^4 m^3 per day were measured in the days prior to a paroxysmal eruption on 1 March 2017, based on repeated photogrammetric UAS surveys of the growing dome (Fig. 5.9c; Watson et al., 2017).

5.2.5 Discussion

Applications of UAS within volcanology have already advanced from the limited use of a few, relatively large aircraft prior to circa 2010, to a diverse range of systems being regularly deployed globally, to support a broad range of volcanological work. Their advantages in providing cost effective and responsive data acquisition, along with increased access to difficult and hazardous environments have led to:

- *Decimetric-resolution DEMs of lava flows and domes from high resolution (centimetre-scale) visible-wavelength imaging.* Such products can be more than two orders of magnitude better resolution than widely available space-based products and have enabled the analysis of surface morphology (reflecting emplacement dynamics) and structural assessment, with implications for hazard assessment.
- *High resolution fully 3-D models of vertical or overhanging surfaces (e.g. caldera cliffs).* Rotor-based UAS can collect close-range oblique imagery that is not possible from space-based platforms or regularly available from conventional aerial systems

(e.g. crewed helicopters) and provides unique access for modelling vertical faces for mapping or quantifying mass movements.

- *Centimetric-resolution thermal imagery for detailed analysis of heat loss and thermal structure.* In line with advantages for visible-imaging operations, UAS-compatible thermal cameras provide a two orders of magnitude step change in the resolution of airborne thermal imaging data, enhancing feature identification and change detection at sites such as geothermal fields.
- *Remote measurement and sampling of hazardous environments* such as plumes and surface hydrothermal regions. With personnel able to remain at safe locations, the use of UAS have provided measurement and sampling opportunities in otherwise inaccessible areas. These are often proximal to activity, and hence, the data acquired (e.g. gas geochemistry, particle size distributions, surface temperatures) are particularly valuable for initialising (e.g. plume dispersal) or validating (e.g. cooling) models.
- *Instrument deployment into difficult to access or hazardous environments.* Enabling the installation of seismic stations in near-vent regions within exclusion zones has provided insight into evolving magmatic processes and provided valuable data that have contributed to crisis-response decision-making.
- *Rapid, responsive, and regular mission capabilities* (for all points above). Short deployment timescales and efficient data processing enables UAS use not only for scientific research, but also for generating sufficiently timely data products to support crisis management (e.g. video footage and high-resolution georectified orthomosaics disseminated within minutes to hours). Thus, importantly, UAS demonstrate strong value for both scientific investigation and for monitoring applications, for which requirements in terms of data

5.2.6 Conclusion

The hazardous environments and spatial scales associated with volcanic processes mean that technologies providing remote and automated measurements will always be highly valued. Consequently, the broad (and rapidly increasing) capabilities of UAS are seeing their application and development within volcanological research, monitoring and crisis response. Critically, the use of UAS enables the addressing of existing gaps in temporal and spatial data resolution, both through facilitating physical access and by offering practical and affordable alternatives to expensive crewed systems. Increasing automation and sensor development will

continue to enhance UAS capabilities, and seamless integration with existing systems and data streams is likely to be one of the main challenges ahead. Legislation is a critical contributor to ongoing safety, but inefficiencies can also lead it to be a limiting factor for rapid deployments. Harmonising regulations and streaming flight permission procedures represent key areas for maximising future UAS utility, particularly for international crisis response. UAS have already provided unique insight into volcanic processes and are set to represent an invaluable tool for volcanologists and associated hazard managers.

Chapter 6:
Summary, discussion, and outlook

6.1 Thesis summary

In this thesis, I tested and applied suitable photogrammetric methods to monitor lava dome growth and to advance our understanding of lava dome growth processes. Data was obtained from natural lava domes at Volcán de Colima, Mexico, and Santiaguito, Guatemala, as well as analogue dome models using laboratory experiments, all carrying information on the dome morphology, growth structures, and timing and magnitude of deformation. The results also have important implications for the hazards posed by growing lava domes.

For chapter 2 (Zorn et al., 2019), I created a detailed timeline of the eruptive activity of Volcán de Colima spanning multiple years from 2013 to 2016, using a combination SfM-photogrammetry from aircraft and helicopter surveys, TerraSAR-X satellite radar amplitude images, and seismic data. Tri-stereo photogrammetric data from the Pléiades satellite was also used to build a DEM for referencing purposes. The results show the drastic changes that occurred in the summit region of Volcán de Colima during the study period, experiencing prolonged lava extrusion interspersed with large lava dome collapses. A shift in the directionality of the extrusion is also observed in response to changing loads of the summit lava dome, which is supported by finite element modelling based on the SfM-topography data. This implies that static loading by continuous dome growth in one direction will facilitate further intrusions towards that load by redirecting conduit slip planes. On the other hand, unloading by collapse of the dome will have the opposite effect and promote slip away from the collapse site.

In chapter 3 (Zorn et al., 2020a), I used a combination of UAS-based SfM-photogrammetry and PIV to detail the surface motions of the Santiaguito lava dome with high detail. This data is used to identify both the growth of the lava dome and the extrusion of a short lava flow, which occur on different timescales (dm/day for surface expansion during dome growth and m/day for the lava flow speed). The detailed particle tracking allowed for the detection of active fractures by calculating surface strain. Thermal data also assisted in delineating local structures and features on the dome. With a direct comparison of the SfM-build DEMs, the localisation and volume of growth could also be quantified. Finally, the combined data from the lava flow, incorporating the flow velocity, thickness, and diameter as well as slope angle and density allowed for estimation of the lava viscosity.

Chapter 4 (Zorn et al., 2020b) describes the experimental extrusion of lava domes and spines using granular sand-plaster mixtures as analogue material. The extrusions under controlled conditions allow for deliberate and detailed monitoring of the growth processes both on the outside as well as in the interior of the domes and spines. Using PIV, I showed the developing morphologies, stratigraphy, and structures during dome growth and produced strikingly similar analogue domes compared to natural examples. Results show dome growth to occur by gradual intrusion from the conduit and repeated slumping, gradually forming a typical flat-topped and steep sided dome with a distinct talus apron. Insights into spine growth suggests a compaction driven strengthening of the lava analogue, promoting brittle failure via discrete shear faults, which could be detected and visualised using vorticity plots from the PIV. Spine sizes are also found to increase with material strength following higher degrees of compaction.

Chapter 5 incorporates text excerpts relevant for my contributions to studies made as a co-author. Walter et al. (2019b) explore the initial phase of lava dome growth at Volcán de Colima, Mexico, in early 2013. Through a combination of TerraSAR-X satellite radar and timelapse camera observations the study investigates both constructive and destructive activity at the volcano. The appearance of precursory ring-shaped degassing structures is linked to subsequent explosions occurring before dome growth starts. The initial vertical dome growth was then observed to change into lateral spreading after reaching a maximum height, likely as a result of gravitational instability due to the lava viscosity and low rock strength. Finally, the observed data was compared to numerical simulations of lava dome growth by discrete element modelling, enabling an estimation of the critical dome height the dome may reach before spreading laterally.

James et al. (2020) present an extensive review of UAS applied in volcanological research. It summarizes relevant studies in the scientific community, with specific sections on photogrammetric methods and the observation of lava domes. New data is also presented that is mainly used to illustrate and support the concepts presented in previous studies.

6.2 Outcomes in the context of current lava dome research

This thesis provides several geoscientific advancements related to lava dome research based on the main research questions (see section 1.5). These advancements and the lessons learned from these studies are synthesized here.

Which factors control the style and direction of lava dome growth and how can they change the growth behaviour?

There are several proposed mechanisms that may cause lava domes to grow in a preferred direction, including vent or crater geometry (Harnett et al., 2018), the pile-up of extruded material, plugging of previous extrusion pathways (Husain et al., 2014), localised channelling (Walter et al., 2013a), or deflection by non-homogenous conduit materials such as dense plugs (Lavallée et al., 2012). In Zorn et al. (2019), an additional impact as a result of localised loading and unloading at the surface is identified to affect the direction of lava dome growth. Most of these mechanisms are tied to a specific case or an observed period of dome growth, making a direct comparison of these influences challenging. It is likely that these mechanisms all interact depending on the current activity, so a general statement on what causes growth directionality and deflections cannot be made. Rather, it highlights the very complex and situational observations and interpretations that need to be made in order to successfully explain or predict such features.

On which timescales does deformation occur on lava domes and can these be related to the current activity?

Lava dome growth can be observed on a wide range of timescales, encompassing growth phases on the scale of years to decades (Swanson, 1990; Watts et al., 2002; Harris et al., 2003; Zorn et al., 2019), while individual growth spurts or cycles occur on the scale of days to years (Lamb et al., 2014; Rhodes et al., 2018). Deformation and structure activation is typically measured on the scale of hours to days (Walter, 2011; Diefenbach et al., 2013; Salzer et al., 2016; Zorn et al., 2020a) and even short term motions related to gas driven explosions and pulsations, lasting a few seconds only (Johnson et al., 2008), can be detected. Compiling and contextualising observations from different timescales will provide a much more complete understanding of the active processes at lava domes rather than just one view at any given time. This is demonstrated in Zorn et al. (2020a), where the lava flow is detectable when investigating on the timescale of hours (Fig. 3.5) , but this would have missed the endogenous dome growth and radial fracture formation occurring over the course of days (Fig. 3.4). These motions occurred simultaneously, highlighting the need to adjust the monitoring tools to the adequate deformation rates depending on the type of activity that is observed.

What is the structural architecture of growing lava domes and how does it affect the deformation patterns of the dome?

Gaining insight into structural features at lava domes is a challenging task as they are commonly short-lived and inaccessible while the dome is active. Consequently, features such as faults are typically inferred indirectly from seismic data (e.g. Kendrick et al., 2014; Hornby et al., 2015), lithological indicators such as fault gauge or pseudotachylytes (Hornby et al., 2015; Ryan et al., 2018a) or degassing and fracture patterns stemming from conduit faults found at the surface (Bluth and Rose, 2004; Holland et al., 2011). Here, the use analogue modelling has proven to greatly facilitate the detection and measurement of such structures, which can now be observed directly. Discrete faults enveloping exogenous spines consisting of compacted conduit material were further found to control the appearance of spines. Strain calculations were shown to be particularly insightful to visualize active structures depending on the type of deformation these structures are associated with. Here, these are applied both in the analogue experiments and at the Santiaguito dome. Specifically, this refers to the opening fractures on a lava dome surface through endogenous swelling detected by normal strain, which is sensitive to ground features moving apart (like opening fractures) or together (Zorn et al., 2020a), or the active faults during the exogenous extrusion of spines detected by vorticity, which is sensitive to shearing motions (Zorn et al., 2020b). For the latter, plotting vorticity over regular shear strain also has the advantage of indicating the shear sense of the moving faults (i.e. right-lateral or left-lateral).

How can photogrammetric monitoring and/or modelling assist in the identification and study of hazards posed by lava domes?

All three main chapters contribute to the assessment of various aspects of dome hazards. Zorn et al. (2019) characterize a loading-based control on the direction of lava extrusion, thus directly affecting the direction and pathways of collapse PDCs. While this loading control is likely one of several factors impacting the growth directionality (e.g. Watts et al., 2002; Lavallée et al., 2012; Husain et al., 2014), incorporating these impacts into hazard predictions could benefit future predictions. Zorn et al. (2020a) manage to detect different dome deformations in relation to the type of activity and gathers insight on some vital parameters for assessing the hazard state of the lava dome, including extrusion rates, surface temperature, lava viscosity, and deformation structures (i.e. fractures). Finally, Zorn et al. (2020b) observe an increase in the deformation rate on unstable dome flanks prior to a collapse. This provides insight into both the timing and location of potential hazards, making this a potentially very important phenomenon to consider in future hazard studies.

Using the 2014–2015 Pāhoa eruption of Kīlauea volcano, Hawai'I, as an example, James et al. (2020) further make a point to highlight the advantages of photogrammetric monitoring via UAS for both hazard assessment and prediction as well as direct crisis response. This showcases the value of photogrammetric information and data that can be collected quickly and suggests that UAS may become critical tool in similar future scenarios.

This thesis further contributes to other ongoing research problems at lava domes:

(1) Many studies make a point to highlight that studying lava domes can be a particularly dangerous task due to the many-faceted hazards that they pose or due to difficult field access (e.g. Walter, 2011; Ogburn et al., 2015; Darmawan et al., 2018a) and the studies presented in this thesis are no different (Zorn et al., 2019; Zorn et al., 2020a). However, they present an opportunity to reflect on a few methods suitable to overcome this central problem. The demonstrated use of remote sensing methods is one major point, e.g. fixed timelapse cameras recording activity, growth and deformation of lava domes from a safe distance (Walter et al., 2019b). Similarly, aerial overflight data, satellite photography and radar or a combination of the two can create very detailed insight into the development of lava dome growth without being exposed to high risk (Zorn et al., 2019), and further data such as seismic or tilt recordings may further enhance the results. While aerial flight by helicopter and plane or access to satellite data can be expensive, the advent of UASs as flying platforms that are able to equip a variety of sensors present an opportunity to gain detailed remote sensing data on a cheaper budget and with more flexibility (James et al., 2020; Zorn et al., 2020a). Another method to overcome the typical challenges of studying active lava domes is numerical or analogue modelling, where the conditions of dome growth can be controlled. Numerical models can also be built and based on data acquired at the active sites (Zorn et al., 2019), allowing for a comparison of real and simulated data. Analogue models can simulate lava dome growth in the laboratory and offer insights into various specific aspects of the growth processes (Zorn et al., 2020b).

(2) Lava dome growth can occur with several distinct styles resulting in different morphologies. Most commonly, domes are sorted into endogenous and exogenous growth categories (e.g. Kaneko et al., 2002; Hale and Wadge, 2008), where the former is characterized by internal swelling and intrusion of magma into the dome, and the latter is characterized by active extrusion of lava at the surface on top of the dome. While these growth styles are typically kept separate for simplicity, both Zorn et al. (2020a) and Zorn et al. (2020b) show that these two styles are not always suitable for describing the activity. At Santiaguito, both an extrusion of lava on top of the dome while endogenous swelling and internal growth were found to occur at

the same time, albeit with different growth speeds (Zorn et al., 2020a). The analogue dome produced from pure sand also displayed hybrid characteristics, where the dome would swell internally from material intruding from the conduit below, but through material "upwelling" it reaches the surface of the dome (Zorn et al., 2020b). In spine experiments, this "upwelling" also occurs simultaneously to spine growth, which fits the exogenous criteria rather clearly. In both cases, activity cannot simply be described as definitively one or the other growth style. While endogenous and exogenous growth as descriptors certainly provide a quick and easy to understand impression of the ongoing activity at a growing lava dome, more care and detail needs to be shown when the actual growth may not be appropriately captured using these terms.
(3) Recent studies in rock mechanics have highlighted the importance of the lava dome rock characteristics for the behaviour of the dome. The state of cooling, degassing, and crystallisation of the lava exerts a significant control on the strength of the rocks and is greatly influenced by factors such as the magma ascent rate or the state of the degassing pathways (Nakada and Motomura, 1999; Heap et al., 2016; Zorn et al., 2018). In turn, this may affect the lava dome growth style as suggested by Heap et al. (2016) and is supported by Zorn et al. (2020b). Porosity exerts a first order control on the rock strength (Al-Harthi et al., 1999; Heap et al., 2014b; Zorn et al., 2018), so a reduction in porosity by compaction can induce a change in growth behaviour by strengthening the rocks and enabling brittle failure, forming spines (Zorn et al., 2020b). Another potentially relevant aspect of dome rock strength is showcased by Walter et al. (2019b), where the maximum height of a lava dome directly corresponds to the rock strength as the dome rocks fail under their own weight. This may allow for a prediction of dome heights and shape in future eruptions if the rock strength is known.

6.3 Future perspectives

The work conducted in this thesis has shown the potential of high-resolution imaging and photogrammetric processing to monitor lava dome growth and to investigate extrusion processes. As a final outlook for potential work following this thesis, I list a few outstanding issues and considerations that future studies could, in my opinion, benefit from.

The work presented in this thesis provides new hypotheses that warrant further testing. For example, a significant loading-based control on the directionality of lava dome growth is suggested in Chapter 2 (Zorn et al., 2019) und supported by numerical modelling, however, considering other potential factors (such as crater morphology) it is not clear to what extent this control actually impacts real lava dome growth directions. Further studies observing changes in growth directionality at lava domes on other volcanoes may assist in clarifying the

importance of loading stress in this context. Analogue modelling, as presented in Chapter 4 (Zorn et al., 2020b), may also be valuable for this purpose as it provides a controlled environment, making it easier to separate such loading controls from other factors. This also applies to other features observed e.g. with radar data, where analogue experiments can potentially recreate morphologies, structures, or deformation patterns of active volcanoes and lava domes. In a similar manner, the analogue models have further shown great potential to investigate many other aspects of lava dome growth in more detail, possible examples being topography controls on the extrusion, dome subsidence, surface fracture patterns, stratified conduits (i.e. varying material properties with ongoing extrusions), varying conduit positions, or the testing of other analogue materials (e.g. kinetic sand, silicone oil).

In many cases, the use of aerial photogrammetry at active volcanoes is limited by changing weather and visibility. While the use of UAS has increased strongly within the last years, it is still a relatively young research field and many technical aspects of SfM terrain reconstruction can still be refined (e.g. Kalacska et al., 2020). Using other data sources such as seismic or satellite radar data has the potential to close gaps in photogrammetric acquisitions or add key information as shown in Chapter 2 (Zorn et al., 2019) and should be considered more regularly for future studies. Similarly, thermal infrared cameras were found to penetrate minor amounts of steam and gas that would otherwise obscure the survey target and small thermal cameras can even be mounted on UASs to record alongside regular imaging, see Chapter 5 (James et al., 2020). Provided the spatial resolution of such thermal cameras can be improved, they may be suitable to replace regular RGB cameras in some situations.

Recent years have seen a strong push towards more automated gathering and analyses of monitoring data. For example, the use of artificial intelligence and machine learning tools are capable of processing large amounts of data unsupervised and they could automatically flag unusual deformation measurements that are indicative of a change in volcanic activity. Input data as it is used in this thesis would be ideally suited for the integration into machine learning algorithms or neural networks (e.g. Piscini and Lombardo, 2014; Anantrasirichai et al., 2018) as dome deformation rates, growth volumes, and structure development could be logged automatically. Taking this concept a step further, large parts of the photogrammetric data gathering process could be further automatized as UAS are capable of performing autonomous flights with planning software (see e.g. Koyama et al., 2013; Hashimoto et al., 2014), potentially providing a complete data processing chain from the acquisition to the final product. However, for practical use in future project, several issues will have to be addressed, namely the strong susceptibility of small UAS to unfavourable weather conditions, the short UAS battery power,

legal issues regarding unsupervised flights, and the adequate training of the machine learning algorithms as well as its processing capabilities for large amounts of data.

In terms of rock mechanics and their connection to lava dome collapse hazards, recent studies have suggested a strong influence of hydrothermal alteration rapidly changing rock properties in volcanic settings (Pola et al., 2012; Wyering et al., 2014; Farquharson et al., 2019), which may cause instability of the dome edifice or even entire volcano flanks and sectors. Similarly, the deposition of alteration minerals could potentially induce gas pressurization and explosions due the reduction of permeability (Ball et al., 2015; Heap et al., 2019). This is particularly important as the hazardous events may occur sometime after the eruptive activity ceased and the volcano is not seen as a threat anymore. For example, the partial collapse of the Taranaki lava dome, New Zealand, occurred several decades after its emplacement (Platz et al., 2012), highlighting the need to improve our understanding of post-eruptive weakening of lava domes and their stability.

In conclusion, progress in research at volcanoes and lava domes is made by testing and combining promising methods and workflows. Photogrammetry, and particularly the SfM and PIV workflows, together with modelled simulations proved their potential to advance geoscience research in this thesis and a number of other studies. With the main methodologies established, future research can further test and verify the robustness and practical applicability of these approaches and establish them as potentially regular means of volcano monitoring at observatories worldwide.

Bibliography

Abdullah, Q., Bethel, J., Hussain, M. and Munjy, R. (2013). Photogrammetric project and mission planning. American Society for Photogrammetry and Remote Sensing, 1187-1220 pp.

Acocella, V., Cifelli, F. and Funiciello, R. (2001). The control of overburden thickness on resurgent domes: insights from analogue models. Journal of Volcanology and Geothermal Research, 111(1): 137-153. DOI: 10.1016/S0377-0273(01)00224-4

Adrian, R.J. (1991). Particle-Imaging Techniques for Experimental Fluid Mechanics. Annual Review of Fluid Mechanics, 23(1): 261-304. DOI: 10.1146/annurev.fl.23.010191.001401

Al-Harthi, A.A., Al-Amri, R.M. and Shehata, W.M. (1999). The porosity and engineering properties of vesicular basalt in Saudi Arabia. Engineering Geology, 54(3): 313-320. DOI: 10.1016/S0013-7952(99)00050-2

Alidibirov, M. and Dingwell, D.B. (1996). Magma fragmentation by rapid decompression. Nature, 380(6570): 146-148. DOI: 10.1038/380146a0

Anantrasirichai, N., Biggs, J., Albino, F., Hill, P. and Bull, D. (2018). Application of Machine Learning to Classification of Volcanic Deformation in Routinely Generated InSAR Data. Journal of Geophysical Research: Solid Earth, 123(8): 6592-6606. DOI: 10.1029/2018jb015911

Anderson, S.W. and Fink, J.H. (1992). Crease structures: Indicators of emplacement rates and surface stress regimes of lava flows. GSA Bulletin, 104(5): 615-625. DOI: 10.1130/0016-7606(1992)104<0615:Csioer>2.3.Co;2

Andreastuti, S., Paripurno, E., Gunawan, H., Budianto, A., Syahbana, D. and Pallister, J. (2019). Character of community response to volcanic crises at Sinabung and Kelud volcanoes. Journal of Volcanology and Geothermal Research, 382: 298-310. DOI: 10.1016/j.jvolgeores.2017.01.022

Arámbula-Mendoza, R., Reyes-Dávila, G., Vargas-Bracamontes Dulce, M., González-Amezcua, M., Navarro-Ochoa, C., Martínez-Fierros, A. and Ramírez-Vázquez, A. (2018). Seismic monitoring of effusive-explosive activity and large lava dome collapses during 2013–2015 at Volcán de Colima, Mexico. Journal of Volcanology and Geothermal Research, 351: 75-88. DOI: 10.1016/j.jvolgeores.2017.12.017

Arnold, D.W.D., Biggs, J., Anderson, K., Vallejo Vargas, S., Wadge, G., Ebmeier, S.K., Naranjo, M.F. and Mothes, P. (2017). Decaying Lava Extrusion Rate at El Reventador Volcano, Ecuador, Measured Using High-Resolution Satellite Radar. Journal of Geophysical Research: Solid Earth, 122(12): 9966-9988. DOI: 10.1002/2017JB014580

Auker, M.R., Sparks, R.S.J., Siebert, L., Crosweller, H.S. and Ewert, J. (2013). A statistical analysis of the global historical volcanic fatalities record. Journal of Applied Volcanology, 2(1): 2. DOI: 10.1186/2191-5040-2-2

Avard, G. and Whittington, A.G. (2012). Rheology of arc dacite lavas: experimental determination at low strain rates. Bulletin of Volcanology, 74(5): 1039-1056. DOI: 10.1007/s00445-012-0584-2

Bagnardi, M., González, P.J. and Hooper, A. (2016). High-resolution digital elevation model from tri-stereo Pleiades-1 satellite imagery for lava flow volume estimates at Fogo

Volcano. Geophysical Research Letters, 43(12): 6267-6275. DOI: 10.1002/2016GL069457

Ball, J.L., Stauffer, P.H., Calder, E.S. and Valentine, G.A. (2015). The hydrothermal alteration of cooling lava domes. Bulletin of Volcanology, 77(12): 102. DOI: 10.1007/s00445-015-0986-z

Belousov, A. and Belousova, M. (2017). Dynamics and viscosity of 'a'a and pahoehoe lava flows of the 2012–2013 eruption of Tolbachik volcano, Kamchatka (Russia). Bulletin of Volcanology, 80(6): 1-23. DOI: 10.1007/s00445-017-1180-2

Bemis, S.P., Micklethwaite, S., Turner, D., James, M.R., Akciz, S., T. Thiele, S. and Bangash, H.A. (2014). Ground-based and UAV-Based photogrammetry: A multi-scale, high-resolution mapping tool for structural geology and paleoseismology. Journal of Structural Geology, 69(PA): 163-178. DOI: 10.1016/j.jsg.2014.10.007

Bernstein, M., Pavez, A., Varley, N., Whelley, P. and Calder, E.S. (2013). Rhyolite lava dome growth styles at Chaitén Volcano, Chile (2008-2009): Interpretation of thermal imagery. Andean Geology, 40(2): 295-309. DOI: 10.5027/andgeoV40n2-a07

Birdseye, C.H. (1940). Stereoscopic Phototopographic Mapping. Annals of the Association of American Geographers, 30(1): 1-24. DOI: 10.2307/2561128

Blake, S. (1990). Viscoplastic Models of Lava Domes. In: J.H. Fink (Editor), Lava Flows and Domes: Emplacement Mechanisms and Hazard Implications. Springer Berlin Heidelberg, Berlin, Heidelberg, pp. 88-126. DOI: 10.1007/978-3-642-74379-5_5

Bluth, G.J.S. and Rose, W.I. (2004). Observations of eruptive activity at Santiaguito volcano, Guatemala. Journal of Volcanology and Geothermal Research, 136(3): 297-302. DOI: 10.1016/j.jvolgeores.2004.06.001

Boudon, G., Komorowski, J.C., Villemant, B. and Semet, M.P. (2008). A new scenario for the last magmatic eruption of La Soufrière of Guadeloupe (Lesser Antilles) in 1530 A.D. Evidence from stratigraphy radiocarbon dating and magmatic evolution of erupted products. Journal of Volcanology and Geothermal Research, 178(3): 474-490. DOI: 10.1016/j.jvolgeores.2008.03.006

Bourdier, J.L. and Abdurachman, E. (2001). Decoupling of small-volume pyroclastic flows and related hazards at Merapi volcano, Indonesia. Bulletin of Volcanology, 63(5): 309-325. DOI: 10.1007/s004450100133

Bourgouin, L., Mühlhaus, H.B., Jane Hale, A. and Arsac, A. (2007). Studying the influence of a solid shell on lava dome growth and evolution using the level set method. Geophysical Journal International, 170(3): 1431-1438. DOI: 10.1111/j.1365-246X.2007.03471.x

Bretón-González, M., Campos, A., León, Z., Plascencia, I. and Ramírez, J.J. (2013). The 2007-2012 lava dome growth in the crater of Volcán de Colima, México, derived from video monitoring system, Complex Monitoring of Volcanic Activity: Methods and Results. Nova Science Publishers, pp. 153-169.

Brothelande, E. and Merle, O. (2015). Estimation of magma depth for resurgent domes: An experimental approach. Earth and Planetary Science Letters, 412: 143-151. DOI: 10.1016/j.epsl.2014.12.011

Brothelande, E., Lénat, J.F., Normier, A., Bacri, C., Peltier, A., Paris, R., Kelfoun, K., Merle, O., Finizola, A. and Garaebiti, E. (2016). Insights into the evolution of the Yenkahe resurgent dome (Siwi caldera, Tanna Island, Vanuatu) inferred from aerial high-

resolution photogrammetry. Journal of Volcanology and Geothermal Research, 322: 212-224. DOI: 10.1016/j.jvolgeores.2015.07.001

Buisson, C. and Merle, O. (2002). Experiments on internal strain in lava dome cross sections. Bulletin of Volcanology, 64(6): 363-371. DOI: 10.1007/s00445-002-0213-6

Buisson, C. and Merle, O. (2004). Numerical simulation of strain within lava domes. Journal of Structural Geology, 26(5): 847-853. DOI: 10.1016/j.jsg.2003.11.017

Bull, K.F., Anderson, S.W., Diefenbach, A.K., Wessels, R.L. and Henton, S.M. (2013). Emplacement of the final lava dome of the 2009 eruption of Redoubt Volcano, Alaska. Journal of Volcanology and Geothermal Research, 259: 334-348. DOI: 10.1016/j.jvolgeores.2012.06.014

Burchardt, S. and Walter, T.R. (2010). Propagation, linkage, and interaction of caldera ring-faults: comparison between analogue experiments and caldera collapse at Miyakejima, Japan, in 2000. Bulletin of Volcanology, 72(3): 297-308. DOI: 10.1007/s00445-009-0321-7

Byerlee, J. (1978). Friction of Rocks. In: J.D. Byerlee and M. Wyss (Editors), Rock Friction and Earthquake Prediction. Birkhäuser Basel, Basel, pp. 615-626. DOI: 10.1007/978-3-0348-7182-2_4

Calder, E.S., Cole, P.D., Dade, W.B., Druitt, T.H., Hoblitt, R.P., Huppert, H.E., Ritchie, L., Sparks, R.S.J. and Young, S.R. (1999). Mobility of pyroclastic flows and surges at the Soufriere Hills Volcano, Montserrat. Geophysical Research Letters, 26(5): 537-540. DOI: 10.1029/1999gl900051

Calder, E.S., Luckett, R., Sparks, R.S.J. and Voight, B. (2002). Mechanisms of lava dome instability and generation of rockfalls and pyroclastic flows at Soufrière Hills Volcano, Montserrat. Geological Society, London, Memoirs, 21(1): 173-190. DOI: 10.1144/gsl.Mem.2002.021.01.08

Calder, E.S., Lavallée, Y., Kendrick, J.E. and Bernstein, M. (2015). Lava Dome Eruptions. In: H. Sigurdsson (Editor), The Encyclopedia of Volcanoes (Second Edition). Academic Press, Amsterdam, pp. 343-362. DOI: 10.1016/B978-0-12-385938-9.00018-3

Capra, L., Sulpizio, R., Márquez-Ramirez, V.H., Coviello, V., Doronzo, D.M., Arambula-Mendoza, R. and Cruz, S. (2018). The anatomy of a pyroclastic density current: the 10 July 2015 event at Volcán de Colima (Mexico). Bulletin of Volcanology, 80(4): 34. DOI: 10.1007/s00445-018-1206-4

Carr, B. and Lev, E. (2018). Activity and hazards of the ongoing eruption of Sinabung Volcano, Indonesia, evaluated using UAS-derived datasets. AGU Fall Meeting Abstracts 2018. V23D–0108.

Carr, B., Bennett, K., Lev, E. and Edwards, C. (2019). Utilization of an sUAS-Based Thermal Camera to Determine Relative Thermal Inertia of Volcanic Deposits, Lunar and Planetary Science Conference.

Carr, B.B., Clarke, A.B. and Vanderkluysen, L. (2016). The 2006 lava dome eruption of Merapi Volcano (Indonesia): Detailed analysis using MODIS TIR. Journal of Volcanology and Geothermal Research, 311: 60-71. DOI: 10.1016/j.jvolgeores.2015.12.004

Cashman, K.V., Thornber, C.R. and Pallister, J.S. (2008). From dome to dust: shallow crystallization and fragmentation of conduit magma during the 2004-2006 dome extrusion of Mount St. Helens, Washington. In: D.R. Sherrod, W.E. Scott and P.H. Stauffer (Editors), A volcano rekindled: the renewed eruption of Mount St. Helens,

2004-2006. U.S. Geological Survey Professional Paper, Reston, VA, pp. 387-413. DOI: 10.3133/pp175019

Chadwick, W.W., Archuleta, R.J. and Swanson, D.A. (1988). The mechanics of ground deformation precursory to dome-building extrusions at Mount St. Helens 1981-1982. Journal of Geophysical Research, 93(B5): 4351-4366.

Chandler, J. (1999). Effective application of automated digital photogrammetry for geomorphological research. Earth Surface Processes and Landforms, 24(1): 51-63. DOI: 10.1002/(sici)1096-9837(199901)24:1<51::Aid-esp948>3.0.Co;2-h

Chaussard, E. (2017). A low-cost method applicable worldwide for remotely mapping lava dome growth. Journal of Volcanology and Geothermal Research, 341: 33-41. DOI: 10.1016/j.jvolgeores.2017.05.017

Chevrel, M.O., Platz, T., Hauber, E., Baratoux, D., Lavallée, Y. and Dingwell, D.B. (2013). Lava flow rheology: A comparison of morphological and petrological methods. Earth and Planetary Science Letters, 384: 109-120. DOI: 10.1016/j.epsl.2013.09.022

Coats, R., Kendrick, J.E., Wallace, P.A., Miwa, T., Hornby, A.J., Ashworth, J.D., Matsushima, T. and Lavallée, Y. (2018). Failure criteria for porous dome rocks and lavas: a study of Mt. Unzen, Japan. Solid Earth, 9(6): 1299-1328. DOI: 10.5194/se-9-1299-2018

Cole, J.W., Milner, D.M. and Spinks, K.D. (2005). Calderas and caldera structures: a review. Earth-Science Reviews, 69(1): 1-26. DOI: 10.1016/j.earscirev.2004.06.004

Corbi, F., Rivalta, E., Pinel, V., Maccaferri, F. and Acocella, V. (2016). Understanding the link between circumferential dikes and eruptive fissures around calderas based on numerical and analog models. Geophysical Research Letters, 43(12): 6212-6219. DOI: 10.1002/2016GL068721

Cordonnier, B., Hess, K.U., Lavallee, Y. and Dingwell, D.B. (2009). Rheological properties of dome lavas: Case study of Unzen volcano. Earth and Planetary Science Letters, 279(3): 263-272. DOI: 10.1016/j.epsl.2009.01.014

Costa, A., Wadge, G. and Melnik, O. (2012). Cyclic extrusion of a lava dome based on a stick-slip mechanism. Earth and Planetary Science Letters, 337-338: 39-46. DOI: 10.1016/j.epsl.2012.05.011

Costa, A., Wadge, G., Stewart, R. and Odbert, H. (2013). Coupled subdaily and multiweek cycles during the lava dome eruption of Soufrière Hills Volcano, Montserrat. Journal of Geophysical Research: Solid Earth, 118(5): 1895-1903. DOI: 10.1002/jgrb.50095

Cronin, S.J., Lube, G., Dayudi, D.S., Sumarti, S., Subrandiyo, S. and Surono (2013). Insights into the October–November 2010 Gunung Merapi eruption (Central Java, Indonesia) from the stratigraphy, volume and characteristics of its pyroclastic deposits. Journal of Volcanology and Geothermal Research, 261: 244-259. DOI: 10.1016/j.jvolgeores.2013.01.005

Dai, C. and Howat, I.M. (2017). Measuring Lava Flows With ArcticDEM: Application to the 2012–2013 Eruption of Tolbachik, Kamchatka. Geophysical Research Letters, 44(24): 12133-12140. DOI: 10.1002/2017GL075920

Darmawan, H., Walter, T.R., Brotopuspito, K.S., Subandriyo and Nandaka, I.G.M.A. (2018a). Morphological and structural changes at the Merapi lava dome monitored in 2012–15 using unmanned aerial vehicles (UAVs). Journal of Volcanology and Geothermal Research, 349: 256-267. DOI: 10.1016/j.jvolgeores.2017.11.006

Darmawan, H., Walter, T.R., Troll, V.R. and Budi-Santoso, A. (2018b). Structural weakening of the Merapi dome identified by drone photogrammetry after the 2010 eruption. Nat. Hazards Earth Syst. Sci., 18(12): 3267-3281. DOI: 10.5194/nhess-18-3267-2018

Davila, N., Capra, L., Gavilanes-Ruiz, J.C., Varley, N., Norini, G. and Vazquez, A.G. (2007). Recent lahars at Volcán de Colima (Mexico): Drainage variation and spectral classification. Journal of Volcanology and Geothermal Research, 165(3): 127-141. DOI: 10.1016/j.jvolgeores.2007.05.016

De Angelis, S., von Aulock, F., Lavallée, Y., Hornby, A., Kennedy, B., Lamb, O. and Kendrick, J. (2016a). Observing changes at Santiaguito Volcano, Guatemala with an Unmanned Aerial Vehicle (UAV). AGU Fall Meeting Abstracts 2016. V43A–3130.

De Angelis, S., Lamb, O.D., Lamur, A., Hornby, A.J., von Aulock, F.W., Chigna, G., Lavallée, Y. and Rietbrock, A. (2016b). Characterization of moderate ash-and-gas explosions at Santiaguito volcano, Guatemala, from infrasound waveform inversion and thermal infrared measurements. Geophysical Research Letters, 43(12): 6220-6227. DOI: 10.1002/2016gl069098

De Beni, E., Cantarero, M. and Messina, A. (2019). UAVs for volcano monitoring: A new approach applied on an active lava flow on Mt. Etna (Italy), during the 27 February–02 March 2017 eruption. Journal of Volcanology and Geothermal Research, 369: 250-262. DOI: 10.1016/j.jvolgeores.2018.12.001

Denlinger, R.P. and Hoblitt, R.P. (1999). Cyclic eruptive behavior of silicic volcanoes. Geology, 27(5): 459-462. DOI: 10.1130/0091-7613(1999)027<0459:Cebosv>2.3.Co;2

Diefenbach, A.K., Crider, J.G., Schilling, S.P. and Dzurisin, D. (2012). Rapid, low-cost photogrammetry to monitor volcanic eruptions: an example from Mount St. Helens, Washington, USA. Bulletin of Volcanology, 74(2): 579-587. DOI: 10.1007/s00445-011-0548-y

Diefenbach, A.K., Bull, K.F., Wessels, R.L. and McGimsey, R.G. (2013). Photogrammetric monitoring of lava dome growth during the 2009 eruption of Redoubt Volcano. Journal of Volcanology and Geothermal Research, 259: 308-316. DOI: 10.1016/j.jvolgeores.2011.12.009

Diefenbach, A.K., Adams, J., Burton, T., Koeckeritz, B., Sloan, J. and Stroud, S. (2018). The 2018 US Geological Survey-Department of Interior UAS Kīlauea Eruption Response. AGU Fall Meeting Abstracts 2018. V23D-0107.

Dietterich, H.R., Patrick, M.R., Diefenbach, A.K., Parcheta, C., Lev, E. and Foks, N.L. (2018). Lava flow hazard modeling and the assessment of effusion rates and topographic change with UAS and lidar during the 2018 Kilauea lower East Rift Zone eruption. AGU Fall Meeting Abstracts 2018. V21B-03.

Druitt, T.H., Young, S.R., Baptie, B., Bonadonna, C., Calder, E.S., Clarke, A.B., Cole, P.D., Harford, C.L., Herd, R.A., Luckett, R., Ryan, G. and Voight, B. (2002). Episodes of cyclic Vulcanian explosive activity with fountain collapse at Soufrière Hills Volcano, Montserrat. Geological Society, London, Memoirs, 21(1): 281-306. DOI: 10.1144/GSL.MEM.2002.021.01.13

Dvigalo, V.N., Svirid, I.Y. and Shevchenko, A.V. (2013). The first quantitative estimates of parameters for the Tolbachik Fissure Eruption of 2012–2013 from aerophotogrammetric observations. Journal of Volcanology and Seismology, 8(5): 261-268. DOI: 10.1134/S0742046314050029

Ebmeier, S.K., Biggs, J., Mather, T.A., Elliott, J.R., Wadge, G. and Amelung, F. (2012). Measuring large topographic change with InSAR: Lava thicknesses, extrusion rate and subsidence rate at Santiaguito volcano, Guatemala. Earth and Planetary Science Letters, 335-336: 216-225. DOI: 10.1016/j.epsl.2012.04.027

Eichelberger, J.C., Carrigan, C.R., Westrich, H.R. and Price, R.H. (1986). Non-explosive silicic volcanism. Nature, 323(6089): 598-602. DOI: 10.1038/323598a0

Farquharson, J.I., Heap, M.J., Lavallée, Y., Varley, N.R. and Baud, P. (2016). Evidence for the development of permeability anisotropy in lava domes and volcanic conduits. Journal of Volcanology and Geothermal Research, 323: 163-185. DOI: 10.1016/j.jvolgeores.2016.05.007

Farquharson, J.I., Wild, B., Kushnir, A.R.L., Heap, M.J., Baud, P. and Kennedy, B. (2019). Acid-Induced Dissolution of Andesite: Evolution of Permeability and Strength. Journal of Geophysical Research: Solid Earth, 124(1): 257-273. DOI: 10.1029/2018jb016130

Favalli, M., Fornaciai, A., Nannipieri, L., Harris, A., Calvari, S. and Lormand, C. (2018). UAV-based remote sensing surveys of lava flow fields: a case study from Etna's 1974 channel-fed lava flows. Bulletin of Volcanology, 80(29): 1-18. DOI: 10.1007/s00445-018-1192-6

Fink, J.H., Malin, M.C. and Anderson, S.W. (1990). Intrusive and extrusive growth of the Mount St Helens lava dome. Nature, 348(6300): 435-437. DOI: 10.1038/348435a0

Fink, J.H. and Bridges, N.T. (1995). Effects of eruption history and cooling rate on lava dome growth. Bulletin of Volcanology, 57(4): 229-239. DOI: 10.1007/bf00265423

Fink, J.H. and Griffiths, R.W. (1998). Morphology, eruption rates, and rheology of lava domes: Insights from laboratory models. Journal of Geophysical Research: Solid Earth, 103(B1): 527-545. DOI: 10.1029/97JB02838

Fraser, C.S. (2013). Automatic camera calibration in close range photogrammetry. Photogrammetric Engineering & Remote Sensing, 79(4): 381-388. DOI: 10.14358/PERS.79.4.381

Freed, A.M. (2005). Earthquake triggering by static, dynamic, and postseismic stress transfer. Annual Review of Earth and Planetary Sciences, 33: 335-367. DOI: 10.1146/annurev.earth.33.092203.122505

Gaunt, H.E., Sammonds, P.R., Meredith, P.G., Smith, R. and Pallister, J.S. (2014). Pathways for degassing during the lava dome eruption of Mount St. Helens 2004–2008. Geology, 42(11): 947-950. DOI: 10.1130/g35940.1

Gaunt, H.E., Sammonds, P.R., Meredith, P.G. and Chadderton, A. (2016). Effect of temperature on the permeability of lava dome rocks from the 2004–2008 eruption of Mount St. Helens. Bulletin of Volcanology, 78(4): 30. DOI: 10.1007/s00445-016-1024-5

Gilbert, G.K. (1904). The mechanism of the Mont Pelée spine. Science, 19(494): 927-928. DOI: 10.1126/science.19.494.927

Giordano, D., Russell, J.K. and Dingwell, D.B. (2008). Viscosity of magmatic liquids: A model. Earth and Planetary Science Letters, 271(1): 123-134. DOI: 10.1016/j.epsl.2008.03.038

Global Volcanism Program (2013). Volcanoes of the World, v. 4.9.0 (04 Jun 2020). Venzke, E. Smithsonian Institution. DOI: 10.5479/si.GVP.VOTW4-2013

Global Volcanism Program (2018). Report on Fuego (Guatemala) (Crafford, A.E., and Venzke, E., eds.). Bulletin of the Global Volcanism Network. Smithsonian Institution, 43(8). DOI: 10.5479/si.GVP.BGVN201808-342090

Global Volcanism Program (2019). Report on Whakaari/White Island (New Zealand). In: S.K. Sennert (Editor), Weekly Volcanic Activity Report, 4 December-10 December 2019. Smithsonian Institution and US Geological Survey.

Global Volcanism Program (2020). Report on Taal (Philippines). In: S.K. Sennert (Editor), Weekly Volcanic Activity Report, 8 January-14 January 2020. Smithsonian Institution and US Geological Survey.

Gomez, C., Lavigne, F., Sri Hadmoko, D. and Wassmer, P. (2018). Insights into lahar deposition processes in the Curah Lengkong (Semeru Volcano, Indonesia) using photogrammetry-based geospatial analysis, near-surface geophysics and CFD modelling. Journal of Volcanology and Geothermal Research, 353: 102-113. DOI: 10.1016/j.jvolgeores.2018.01.021

González, M.B., J Ramírez, J. and Navarro, C. (2002). Summary of the historical eruptive activity of Volcán De Colima, Mexico 1519–2000. Journal of Volcanology and Geothermal Research, 117(1-2): 21-46. DOI: 10.1016/S0377-0273(02)00233-0

Griffiths, R.W. and Fink, J.H. (1993). Effects of surface cooling on the spreading of lava flows and domes. Journal of Fluid Mechanics, 252: 667-702. DOI: 10.1017/S0022112093003933

Griffiths, R.W. and Fink, J.H. (1997). Solidifying Bingham extrusions: a model for the growth of silicic lava domes. Journal of Fluid Mechanics, 347: 13-36. DOI: 10.1017/S0022112097006344

Grosfils, E.B. (2007). Magma reservoir failure on the terrestrial planets: Assessing the importance of gravitational loading in simple elastic models. Journal of Volcanology and Geothermal Research, 166(2): 47-75. DOI: 10.1016/j.jvolgeores.2007.06.007

Grosfils, E.B., McGovern, P.J., Gregg, P.M., Galgana, G.A., Hurwitz, D.M., Long, S.M. and Chestler, S.R. (2015). Elastic models of magma reservoir mechanics: A key tool for investigating planetary volcanism. Geological Society, London, Special Publications, 401: 239-267. DOI: 10.1144/SP401.2

Grosse, P., van Wyk de Vries, B., Euillades, P.A., Kervyn, M. and Petrinovic, I.A. (2012). Systematic morphometric characterization of volcanic edifices using digital elevation models. Geomorphology, 136(1): 114-131. DOI: 10.1016/j.geomorph.2011.06.001

Hale, A.J. and Wadge, G. (2003). Numerical modelling of the growth dynamics of a simple silicic lava dome. Geophysical Research Letters, 30(19). DOI: 10.1029/2003gl018182

Hale, A.J. and Wadge, G. (2008). The transition from endogenous to exogenous growth of lava domes with the development of shear bands. Journal of Volcanology and Geothermal Research, 171(3): 237-257. DOI: 10.1016/j.jvolgeores.2007.12.016

Hale, A.J., Calder, E.S., Wadge, G., Loughlin, S.C. and Ryan, G.A. (2009a). Modelling the lava dome extruded at Soufrière Hills Volcano, Montserrat, August 2005–May 2006: Part I: Dome shape and internal structure. Journal of Volcanology and Geothermal Research, 187(1): 53-68. DOI: 10.1016/j.jvolgeores.2009.08.023

Hale, A.J., Calder, E.S., Loughlin, S.C., Wadge, G. and Ryan, G.A. (2009b). Modelling the lava dome extruded at Soufrière Hills Volcano, Montserrat, August 2005–May 2006:

Part II: Rockfall activity and talus deformation. Journal of Volcanology and Geothermal Research, 187(1): 69-84. DOI: 10.1016/j.jvolgeores.2009.08.014

Harnett, C.E., Thomas, M.E., Purvance, M.D. and Neuberg, J. (2018). Using a discrete element approach to model lava dome emplacement and collapse. Journal of Volcanology and Geothermal Research, 359: 68-77. DOI: 10.1016/j.jvolgeores.2018.06.017

Harris, A.J., Rose, W.I. and Flynn, L.P. (2003). Temporal trends in lava dome extrusion at Santiaguito 1922–2000. Bulletin of Volcanology, 65(2): 77-89. DOI: 10.1007/s00445-002-0243-0

Harris, A.J.L., Flynn, L.P., Matias, O., Rose, W.I. and Cornejo, J. (2004). The evolution of an active silicic lava flow field: an ETM+ perspective. Journal of Volcanology and Geothermal Research, 135(1): 147-168. DOI: 10.1016/j.jvolgeores.2003.12.011

Harris, A.J.L., Gurioli, L., Hughes, E.E. and Lagreulet, S. (2012). Impact of the Eyjafjallajökull ash cloud: A newspaper perspective. Journal of Geophysical Research: Solid Earth, 117(B9). DOI: 10.1029/2011jb008735

Harwin, S., Lucieer, A. and Osborn, J. (2015). The impact of the calibration method on the accuracy of point clouds derived using unmanned aerial vehicle multi-view stereopsis. Remote Sensing, 7(9): 11933-11953. DOI: 10.3390/rs70911933

Hashimoto, T., Koyama, T., Kaneko, T., Ohminato, T., Yanagisawa, T., Yoshimoto, M. and Suzuki, E. (2014). Aeromagnetic survey using an unmanned autonomous helicopter over Tarumae Volcano, northern Japan. Exploration Geophysics, 45(1): 37-42. DOI: 10.1071/EG12087

Heap, M.J., Lavallée, Y., Petrakova, L., Baud, P., Reuschlé, T., Varley, N.R. and Dingwell, D.B. (2014a). Microstructural controls on the physical and mechanical properties of edifice-forming andesites at Volcán de Colima, Mexico. Journal of Geophysical Research: Solid Earth, 119(4): 2925-2963. DOI: 10.1002/2013jb010521

Heap, M.J., Xu, T. and Chen, C.F. (2014b). The influence of porosity and vesicle size on the brittle strength of volcanic rocks and magma. Bulletin of Volcanology, 76(9): 856. DOI: 10.1007/s00445-014-0856-0

Heap, M.J., Farquharson, J.I., Baud, P., Lavallée, Y. and Reuschlé, T. (2015). Fracture and compaction of andesite in a volcanic edifice. Bulletin of Volcanology, 77(6): 55. DOI: 10.1007/s00445-015-0938-7

Heap, M.J., Russell, J.K. and Kennedy, L.A. (2016). Mechanical behaviour of dacite from Mount St. Helens (USA): A link between porosity and lava dome extrusion mechanism (dome or spine)? Journal of Volcanology and Geothermal Research, 328: 159-177. DOI: 10.1016/j.jvolgeores.2016.10.015

Heap, M.J., Violay, M., Wadsworth, F.B. and Vasseur, J. (2017). From rock to magma and back again: The evolution of temperature and deformation mechanism in conduit margin zones. Earth and Planetary Science Letters, 463: 92-100. DOI: 10.1016/j.epsl.2017.01.021

Heap, M.J., Villeneuve, M., Farquharson, J.I., Albino, F., Brothelande, E., Amelung, F. and Got, J.L. (2018). Towards more realistic values of elastic moduli for volcano modelling. EGU General Assembly Vienna Geophysical Research Abstracts: EGU2018-3909.

Heap, M.J., Troll, V.R., Kushnir, A.R.L., Gilg, H.A., Collinson, A.S.D., Deegan, F.M., Darmawan, H., Seraphine, N., Neuberg, J. and Walter, T.R. (2019). Hydrothermal

alteration of andesitic lava domes can lead to explosive volcanic behaviour. Nature Communications, 10(1): 5063. DOI: 10.1038/s41467-019-13102-8

Herd, R.A., Edmonds, M. and Bass, V.A. (2005). Catastrophic lava dome failure at Soufrière Hills Volcano, Montserrat, 12–13 July 2003. Journal of Volcanology and Geothermal Research, 148(3): 234-252. DOI: 10.1016/j.jvolgeores.2005.05.003

Hoek, E. and Brown, E.T. (1997). Practical estimates of rock mass strength. International Journal of Rock Mechanics and Mining Sciences, 34(8): 1165-1186. DOI: 10.1016/S1365-1609(97)80069-X

Holland, A.S.P., Watson, I.M., Phillips, J.C., Caricchi, L. and Dalton, M.P. (2011). Degassing processes during lava dome growth: Insights from Santiaguito lava dome, Guatemala. Journal of Volcanology and Geothermal Research, 202(1): 153-166. DOI: 10.1016/j.jvolgeores.2011.02.004

Holohan, E.P., Schöpfer, M.P.J. and Walsh, J.J. (2011). Mechanical and geometric controls on the structural evolution of pit crater and caldera subsidence. Journal of Geophysical Research: Solid Earth, 116(B7). DOI: 10.1029/2010jb008032

Holohan, E.P., Sudhaus, H., Walter, T.R., Schöpfer, M.P.J. and Walsh, J.J. (2017). Effects of Host-rock Fracturing on Elastic-deformation Source Models of Volcano Deflation. Scientific Reports, 7(1): 10970. DOI: 10.1038/s41598-017-10009-6

Holt, R.M., Kjølaas, J., Larsen, I., Li, L., Gotusso Pillitteri, A. and Sønstebø, E.F. (2005). Comparison between controlled laboratory experiments and discrete particle simulations of the mechanical behaviour of rock. International Journal of Rock Mechanics and Mining Sciences, 42(7): 985-995. DOI: 10.1016/j.ijrmms.2005.05.006

Hornby, A.J., Kendrick, J.E., Lamb, O.D., Hirose, T., De Angelis, S., Aulock, F.W., Umakoshi, K., Miwa, T., De Angelis, S.H., Wadsworth, F.B., Hess, K.U., Dingwell, D.B. and Lavallée, Y. (2015). Spine growth and seismogenic faulting at Mt. Unzen, Japan. Journal of Geophysical Research: Solid Earth, 120(6): 4034-4054. DOI: 10.1002/2014JB011660

Hornby, A.J., Lavallée, Y., Kendrick, J.E., De Angelis, S., Lamur, A., Lamb, O.D., Rietbrock, A. and Chigna, G. (2019). Brittle-Ductile Deformation and Tensile Rupture of Dome Lava During Inflation at Santiaguito, Guatemala. Journal of Geophysical Research: Solid Earth, 124(10): 10107-10131. DOI: 10.1029/2018jb017253

Horwell, C.J., Williamson, B.J., Llewellin, E.W., Damby, D.E. and Le Blond, J.S. (2013). The nature and formation of cristobalite at the Soufrière Hills volcano, Montserrat: implications for the petrology and stability of silicic lava domes. Bulletin of Volcanology, 75(3): 696. DOI: 10.1007/s00445-013-0696-3

Huppert, H.E., Shepherd, J.B., Sigurdsson, H.R. and Sparks, S.J. (1982). On lava dome growth, with application to the 1979 lava extrusion of the soufrière of St. Vincent. Journal of Volcanology and Geothermal Research, 14(3): 199-222. DOI: 10.1016/0377-0273(82)90062-2

Husain, T., Elsworth, D., Voight, B., Mattioli, G. and Jansma, P. (2014). Influence of extrusion rate and magma rheology on the growth of lava domes: Insights from particle-dynamics modeling. Journal of Volcanology and Geothermal Research, 285: 100-117. DOI: 10.1016/j.jvolgeores.2014.08.013

Husain, T., Elsworth, D., Voight, B., Mattioli, G. and Jansma, P. (2018). Influence of conduit flow mechanics on magma rheology and the growth style of lava domes. Geophysical Journal International, 213(3): 1768-1784. DOI: 10.1093/gji/ggy073

Husain, T., Elsworth, D., Voight, B., Mattioli, G. and Jansma, P. (2019). Morphologic variation of an evolving dome controlled by the extrusion of finite yield strength magma. Journal of Volcanology and Geothermal Research, 370: 51-64. DOI: 10.1016/j.jvolgeores.2019.01.010

Hutchison, W., Varley, N., Pyle, D.M., Mather, T.A. and Stevenson, J.A. (2013). Airborne thermal remote sensing of the Volcán de Colima (Mexico) lava dome from 2007 to 2010. Geological Society, London, Special Publications, 380(1): 203-228. DOI: 10.1144/sp380.8

Itasca Consulting Group (2017). PFC2D (Particle Flow Code in 2 Dimensions).

Iverson, R.M. (1990). Lava Domes Modeled as Brittle Shells that Enclose Pressurized Magma, with Application to Mount St. Helens. In: J.H. Fink (Editor), Lava Flows and Domes: Emplacement Mechanisms and Hazard Implications. Springer Berlin Heidelberg, Berlin, Heidelberg, pp. 47-69. DOI: 10.1007/978-3-642-74379-5_3

Iverson, R.M., Dzurisin, D., Gardner, C.A., Gerlach, T.M., LaHusen, R.G., Lisowski, M., Major, J.J., Malone, S.D., Messerich, J.A., Moran, S.C., Pallister, J.S., Qamar, A.I., Schilling, S.P. and Vallance, J.W. (2006). Dynamics of seismogenic volcanic extrusion at Mount St Helens in 2004–05. Nature, 444: 439. DOI: 10.1038/nature05322

James, M.R., Pinkerton, H. and Robson, S. (2007). Image-based measurement of flux variation in distal regions of active lava flows. Geochemistry, Geophysics, Geosystems, 8(3): 1-16. DOI: 10.1029/2006gc001448

James, M.R., Pinkerton, H. and Applegarth, L.J. (2009). Detecting the development of active lava flow fields with a very-long-range terrestrial laser scanner and thermal imagery. Geophysical Research Letters, 36(22): 1-5. DOI: 10.1029/2009gl040701

James, M.R. and Varley, N. (2012). Identification of structural controls in an active lava dome with high resolution DEMs: Volcán de Colima, Mexico. Geophysical Research Letters, 39(22): 1-5. DOI: 10.1029/2012GL054245

James, M.R. and Robson, S. (2014). Mitigating systematic error in topographic models derived from UAV and ground-based image networks. Earth Surface Processes and Landforms, 39(10): 1413-1420. DOI: 10.1002/esp.3609

James, M.R., Robson, S., d'Oleire-Oltmanns, S. and Niethammer, U. (2017a). Optimising UAV topographic surveys processed with structure-from-motion: Ground control quality, quantity and bundle adjustment. Geomorphology, 280: 51-66. DOI: 10.1016/j.geomorph.2016.11.021

James, M.R., Robson, S. and Smith, M.W. (2017b). 3-D uncertainty-based topographic change detection with structure-from-motion photogrammetry: precision maps for ground control and directly georeferenced surveys. Earth Surface Processes and Landforms, 42(12): 1769-1788. DOI: 10.1002/esp.4125

James, M.R., Carr, B.B., D'Arcy, F., Diefenbach, A.K., Dietterich, H.R., Fornaciai, A., Lev, E., Liu, E.J., Pieri, D.C., Rodgers, M., Smets, B., Terada, A., von Aulock, F.W., Walter, T.R., Wood, K.T. and Zorn, E.U. (2020). Volcanological applications of unoccupied aircraft systems (UAS): Developments, strategies, and future challenges. Volcanica, 3(1): 67-114. DOI: 10.30909/vol.03.01.67114

Jeffery, A.J., Gertisser, R., Troll, V.R., Jolis, E.M., Dahren, B., Harris, C., Tindle, A.G., Preece, K., O'Driscoll, B., Humaida, H. and Chadwick, J.P. (2013). The pre-eruptive magma plumbing system of the 2007–2008 dome-forming eruption of Kelut volcano, East Java,

Indonesia. Contributions to Mineralogy and Petrology, 166(1): 275-308. DOI: 10.1007/s00410-013-0875-4

Jeffreys, H. (1925). LXXXIV. The flow of water in an inclined channel of rectangular section. The London, Edinburgh, and Dublin Philosophical Magazine and Journal of Science, 49(293): 793-807. DOI: 10.1080/14786442508634662

Johnson, J.B., Lees, J.M., Gerst, A., Sahagian, D. and Varley, N. (2008). Long-period earthquakes and co-eruptive dome inflation seen with particle image velocimetry. Nature, 456: 377-381. DOI: 10.1038/nature07429

Johnson, J.B., Lyons, J.J., Andrews, B.J. and Lees, J.M. (2014). Explosive dome eruptions modulated by periodic gas-driven inflation. Geophysical Research Letters, 41(19): 6689-6697. DOI: 10.1002/2014gl061310

Jones, K.R. and Johnson, J.B. (2011). Mapping complex vent eruptive activity at Santiaguito, Guatemala using network infrasound semblance. Journal of Volcanology and Geothermal Research, 199(1): 15-24. DOI: 10.1016/j.jvolgeores.2010.08.006

Jordan, B.R. (2019). Collecting field data in volcanic landscapes using small UAS (sUAS)/drones. Journal of Volcanology and Geothermal Research, 385: 231-241. DOI: 10.1016/j.jvolgeores.2019.07.006

Kalacska, M., Lucanus, O., Arroyo-Mora, J.P., Laliberté, É., Elmer, K., Leblanc, G. and Groves, A. (2020). Accuracy of 3D Landscape Reconstruction without Ground Control Points Using Different UAS Platforms. Drones, 4(2): 13. DOI: 10.3390/drones4020013

Kaneko, T., Wooster, M.J. and Nakada, S. (2002). Exogenous and endogenous growth of the Unzen lava dome examined by satellite infrared image analysis. Journal of Volcanology and Geothermal Research, 116(1): 151-160. DOI: 10.1016/S0377-0273(02)00216-0

Kendrick, J.E., Lavallée, Y., Ferk, A., Perugini, D., Leonhardt, R. and Dingwell, D.B. (2012). Extreme frictional processes in the volcanic conduit of Mount St. Helens (USA) during the 2004–2008 eruption. Journal of Structural Geology, 38: 61-76. DOI: 10.1016/j.jsg.2011.10.003

Kendrick, J.E., Lavallée, Y., Hirose, T., Di Toro, G., Hornby, A.J., De Angelis, S. and Dingwell, D.B. (2014). Volcanic drumbeat seismicity caused by stick-slip motion and magmatic frictional melting. Nature Geoscience, 7: 438-442. DOI: 10.1038/ngeo2146

Kennedy, L.A. and Russell, J.K. (2012). Cataclastic production of volcanic ash at Mount Saint Helens. Physics and Chemistry of the Earth, Parts A/B/C, 45-46: 40-49. DOI: 10.1016/j.pce.2011.07.052

Kirsanov, I.T. and Studenikin, B.Y. (1971). Dynamics of the extrusive eruption of Bezymianny volcano in 1965–1968 гг. Bulletin of volcanological stations(47): 15-22. (In Russian).

Klinkmüller, M., Schreurs, G., Rosenau, M. and Kemnitz, H. (2016). Properties of granular analogue model materials: A community wide survey. Tectonophysics, 684: 23-38. DOI: 10.1016/j.tecto.2016.01.017

Koyama, T., Kaneko, T., Ohminato, T., Yanagisawa, T., Watanabe, A. and Takeo, M. (2013). An aeromagnetic survey of Shinmoe-dake volcano, Kirishima, Japan, after the 2011 eruption using an unmanned autonomous helicopter. Earth, Planets and Space, 65(6): 16. DOI: 10.5047/eps.2013.03.005

Krantz, R.W. (1991). Measurements of friction coefficients and cohesion for faulting and fault reactivation in laboratory models using sand and sand mixtures. Tectonophysics, 188(1): 203-207. DOI: 10.1016/0040-1951(91)90323-K

Kraus, K. (1993). Photogrammetry, vol. 1. Fundamentals and Standard Processes. Ferdinand Dümmels, Bonn.

Kraus, K. (2007). Photogrammetry. Walter de Gruyter, Berlin, Boston. DOI: 10.1515/9783110892871

Krippner, J.B., Belousov, A.B., Belousova, M.G. and Ramsey, M.S. (2018). Parametric analysis of lava dome-collapse events and pyroclastic deposits at Shiveluch volcano, Kamchatka, using visible and infrared satellite data. Journal of Volcanology and Geothermal Research, 354: 115-129. DOI: 10.1016/j.jvolgeores.2018.01.027

Kubanek, J., Westerhaus, M., Varley, N., James, M.R. and Heck, B. (2014). On using bistatic TanDEM-X data for volcano monitoring, EUSAR 2014; 10th European Conference on Synthetic Aperture Radar, pp. 862-865.

Kubanek, J., Westerhaus, M., Schenk, A., Aisyah, N., Brotopuspito, K.S. and Heck, B. (2015). Volumetric change quantification of the 2010 Merapi eruption using TanDEM-X InSAR. Remote Sensing of Environment, 164: 16-25. DOI: 10.1016/j.rse.2015.02.027

Lamb, O., Lavallée, Y., De Angelis, S., Lamur, A., Hornby, A., von Aulock, F., Kendrick, J., Chigna, G. and Rietbrock, A. (2016). Changes in long-term eruption dynamics at Santiaguito, Guatemala: Observations from seismic data. AGU Fall Meeting Abstracts 2016. V43A-3127.

Lamb, O.D., Varley, N.R., Mather, T.A., Pyle, D.M., Smith, P.J. and Liu, E.J. (2014). Multiple timescales of cyclical behaviour observed at two dome-forming eruptions. Journal of Volcanology and Geothermal Research, 284: 106-121. DOI: 10.1016/j.jvolgeores.2014.07.013

Lamb, O.D., De Angelis, S., Umakoshi, K., Hornby, A.J., Kendrick, J.E. and Lavallée, Y. (2015). Repetitive fracturing during spine extrusion at Unzen volcano, Japan. Solid Earth, 6(4): 1277-1293. DOI: 10.5194/se-6-1277-2015

Lamb, O.D., Lamur, A., Díaz-Moreno, A., De Angelis, S., Hornby, A.J., von Aulock, F.W., Kendrick, J.E., Wallace, P.A., Gottschämmer, E., Rietbrock, A., Alvarez, I., Chigna, G. and Lavallée, Y. (2019). Disruption of Long-Term Effusive-Explosive Activity at Santiaguito, Guatemala. Frontiers in Earth Science, 6(253): 1-14. DOI: 10.3389/feart.2018.00253

Lane, S.J., Phillips, J.C. and Ryan, G.A. (2008). Dome-building eruptions: insights from analogue experiments. Geological Society, London, Special Publications, 307(1): 207. DOI: 10.1144/SP307.12

Lane, S.N., James, T.D. and Crowell, M.D. (2000). Application of Digital Photogrammetry to Complex Topography for Geomorphological Research. The Photogrammetric Record, 16(95): 793-821. DOI: 10.1111/0031-868x.00152

Lavallée, Y., Meredith, P.G., Dingwell, D.B., Hess, K.U., Wassermann, J., Cordonnier, B., Gerik, A. and Kruhl, J.H. (2008). Seismogenic lavas and explosive eruption forecasting. Nature, 453(7194): 507-510. DOI: 10.1038/nature06980

Lavallée, Y., Varley, N.R., Alatorre-Ibargüengoitia, M.A., Hess, K.U., Kueppers, U., Mueller, S., Richard, D., Scheu, B., Spieler, O. and Dingwell, D.B. (2012). Magmatic architecture of dome-building eruptions at Volcán de Colima, Mexico. Bulletin of Volcanology, 74(1): 249-260. DOI: 10.1007/s00445-011-0518-4

Lavallée, Y., Benson, P.M., Heap, M.J., Hess, K.U., Flaws, A., Schillinger, B., Meredith, P.G. and Dingwell, D.B. (2013). Reconstructing magma failure and the degassing network of domebuilding eruptions. Geology, 41(4): 515-518. DOI: 10.1130/G33948.1

Lavallée, Y., Hess, K.U., Cordonnier, B. and Bruce Dingwell, D. (2007). Non-Newtonian rheological law for highly crystalline dome lavas. Geology, 35(9): 843-846. DOI: 10.1130/g23594a.1

Le Corvec, N., Walter, T.R., Ruch, J., Bonforte, A. and Puglisi, G. (2014). Experimental study of the interplay between magmatic rift intrusion and flank instability with application to the 2001 Mount Etna eruption. Journal of Geophysical Research: Solid Earth, 119(7): 5356-5368. DOI: 10.1002/2014jb011224

Le Corvec, N., Muirhead, J.D. and White, J.D.L. (2018). Shallow magma diversions during explosive diatreme-forming eruptions. Nature Communications, 9(1): 1459. DOI: 10.1038/s41467-018-03865-x

Leuenberger, H. (1982). The compressibility and compactibility of powder systems. International Journal of Pharmaceutics, 12(1): 41-55. DOI: 10.1016/0378-5173(82)90132-6

Lev, E. and James, M.R. (2014). The influence of cross-sectional channel geometry on rheology and flux estimates for active lava flows. Bulletin of Volcanology, 76(7): 1-15. DOI: 10.1007/s00445-014-0829-3

Lipman, P.W. (1997). Subsidence of ash-flow calderas: relation to caldera size and magma-chamber geometry. Bulletin of Volcanology, 59(3): 198-218. DOI: 10.1007/s004450050186

Lucieer, A., Jong, S.M.d. and Turner, D. (2013). Mapping landslide displacements using Structure from Motion (SfM) and image correlation of multi-temporal UAV photography. Progress in Physical Geography: Earth and Environment, 38(1): 97-116. DOI: 10.1177/0309133313515293

Luhmann, T., Robson, S., Kyle, S. and Boehm, J. (2014). Close-range photogrammetry and 3D imaging. Walter de Gruyter, Berlin, Boston. DOI: 10.1515/9783110302783

Luhmann, T., Fraser, C. and Maas, H.G. (2016). Sensor modelling and camera calibration for close-range photogrammetry. ISPRS Journal of Photogrammetry and Remote Sensing, 115: 37-46. DOI: 10.1016/j.isprsjprs.2015.10.006

Luhr, J.F. and Carmichael, I.S.E. (1980). The Colima Volcanic complex, Mexico - I. Post-caldera andesites from Volcán Colima. Contributions to Mineralogy and Petrology, 71(4): 343-372. DOI: 10.1007/BF00374707

Luhr, J.F. (2002). Petrology and geochemistry of the 1991 and 1998-1999 lava flows from Volcán de Colima, México: Implications for the end of the current eruptive cycle. Journal of Volcanology and Geothermal Research, 117(1-2): 169-194. DOI: 10.1016/S0377-0273(02)00243-3

Lyman, A.W., Koenig, E. and Fink, J.H. (2004). Predicting yield strengths and effusion rates of lava domes from morphology and underlying topography. Journal of Volcanology and Geothermal Research, 129(1-3): 125-138. DOI: 10.1016/S0377-0273(03)00236-1

Maccaferri, F., Richter, N. and Walter, T.R. (2017). The effect of giant lateral collapses on magma pathways and the location of volcanism. Nature Communications, 8(1): 1-11. DOI: 10.1038/s41467-017-01256-2

Macías, J.L., Sosa-Ceballos, G., Arce, J.L., Gardner, J.E., Saucedo, R. and Valdez-Moreno, G. (2017). Storage conditions and magma processes triggering the 1818CE Plinian eruption of Volcán de Colima. Journal of Volcanology and Geothermal Research, 340: 117-129. DOI: 10.1016/j.jvolgeores.2017.02.025

Major, J.J., Dzurisin, D., Schilling, S.P. and Poland, M.P. (2009). Monitoring lava-dome growth during the 2004–2008 Mount St. Helens, Washington, eruption using oblique terrestrial photography. Earth and Planetary Science Letters, 286(1): 243-254. DOI: 10.1016/j.epsl.2009.06.034

Major, J.J., Pierson, T.C., Hoblitt, R.P. and Moreno, H. (2013). Pyroclastic density currents associated with the 2008-2009 eruption of Chaitén Volcano (Chile): Forest disturbances, deposits, and dynamics. Andean Geology, 40(2): 324-358. DOI: 10.5027/andgeoV40n2-a09

Major, J.J., Poland, M.P., Kingsbury, C.G., Dzurisin, D., LaHusen, R.G., Anonymous (2005). Quantifying spatial and temporal variance in apparent growth rate of the 2004–05 Mount St. Helens lava dome from single-camera images. Abstr. Prog. Geol. Soc. Am., 37(7): 531.

Mania, R., Walter, T.R., Belousova, M., Belousov, A. and Senyukov, S.L. (2019). Deformations and Morphology Changes Associated with the 2016–2017 Eruption Sequence at Bezymianny Volcano, Kamchatka. Remote Sensing, 11(11): 1278. DOI: 10.3390/rs11111278

Marchese, F., Falconieri, A., Pergola, N. and Tramutoli, V. (2018). Monitoring the Agung (Indonesia) Ash Plume of November 2017 by Means of Infrared Himawari 8 Data. Remote Sensing, 10(6): 919. DOI: 10.3390/rs10060919

Massaro, S., Sulpizio, R., Costa, A., Capra, L. and Lucchi, F. (2018). Understanding eruptive style variations at calc-alkaline volcanoes: the 1913 eruption of Fuego de Colima volcano (Mexico). Bulletin of Volcanology, 80(7): 62. DOI: 10.1007/s00445-018-1235-z

Mathieu, L. (2018). The structure of composite volcanoes unravelled by analogue modelling: A review. Journal of Structural Geology, 114: 320-328. DOI: 10.1016/j.jsg.2018.01.009

Matthews, N.A. (2008). Aerial and close-range photogrammetric technology: providing resource documentation, interpretation, and preservation. US Department of the Interior, Bureau of Land Management, National Operations Center, Denver, Colorado.

Matthews, S.J., Gardeweg, M.C. and Sparks, R.S.J. (1997). The 1984 to 1996 cyclic activity of Lascar Volcano, northern Chile: cycles of dome growth, dome subsidence, degassing and explosive eruptions. Bulletin of Volcanology, 59(1): 72-82. DOI: 10.1007/s004450050176

McGlone, J. and Lee, G. (2013). Manual of Photogrammetry, Sixth Edition. The American Society for Photogrammetry and Remote Sensing.

Melnik, O. and Sparks, R.S.J. (1999). Nonlinear dynamics of lava dome extrusion. Nature, 402(6757): 37-41. DOI: 10.1038/46950

Merle, O. (2015). The scaling of experiments on volcanic systems. Frontiers in Earth Science, 3(26): 1-14. DOI: 10.3389/feart.2015.00026

Mikhail, E.M., Bethel, J.S. and McGlone, J.C. (2001). Introduction to Modern Photogrammetry. John Wiley&Sons, New York.

Miller, A.D., Stewart, R.C., White, R.A., Luckett, R., Baptie, B.J., Aspinall, W.P., Latchman, J.L., Lynch, L.L. and Voight, B. (1998). Seismicity associated with dome growth and collapse at the Soufriere Hills Volcano, Montserrat. Geophysical Research Letters, 25(18): 3401-3404. DOI: 10.1029/98gl01778

Mimatsu, M. (1995). Showa-Shinzan Diary. Sobetsu Town Office, Usu, Hokkaido.

Minakami, T., Ishikawa, T. and Yagi, K. (1951). The 1944 Eruption of Volcano Usu in Hokkaido, Japan. Bulletin Volcanologique, 11(1): 45-157. DOI: 10.1007/BF02596029

Miyamachi, H., Watanabe, H., Moriya, T. and Okada, H. (1987). Seismic experiments on Showa-Shinzan lava dome using firework shots. Pure and Applied Geophysics, 125: 1025. DOI: 10.1007/BF00879366

Moore, H.J. (1987). Preliminary estimates of the rheological properties of 1984 Mauna Loa lava (Hawaii). US Geological Survey Professional Paper, 1350(2): 1569-1588.

Moran, S.C., Malone, S.D., Qamar, A.I., Thelen, W.A., Wright, A.K. and Caplan-Auerbach, J. (2008). Seismicity associated with renewed dome building at Mount St. Helens, 2004-2005. In: D.R. Sherrod, W.E. Scott and P.H. Stauffer (Editors), A volcano rekindled: the renewed eruption of Mount St. Helens, 2004-2006. U.S. Geological Survey Professional Paper, Reston, VA, pp. 27-60. DOI: 10.3133/pp17502

Mueller, S.B., Varley, N.R., Kueppers, U., Lesage, P., Reyes Davila, G.Á. and Dingwell, D.B. (2013). Quantification of magma ascent rate through rockfall monitoring at the growing/collapsing lava dome of Volcán de Colima, Mexico. Solid Earth, 4(2): 201-213. DOI: 10.5194/se-4-201-2013

Nakada, S., Miyake, Y., Sato, H., Oshima, O. and Fujinawa, A. (1995). Endogenous growth of dacite dome at Unzen volcano (Japan), 1993–1994. Geology, 23(2): 157-160. DOI: 10.1130/0091-7613(1995)023<0157:Egodda>2.3.Co;2

Nakada, S. and Motomura, Y. (1999). Petrology of the 1991–1995 eruption at Unzen: effusion pulsation and groundmass crystallization. Journal of Volcanology and Geothermal Research, 89(1): 173-196. DOI: 10.1016/S0377-0273(98)00131-0

Nakamura, K. (1977). Volcanoes as possible indicators of tectonic stress orientation — principle and proposal. Journal of Volcanology and Geothermal Research, 2(1): 1-16. DOI: 10.1016/0377-0273(77)90012-9

Nakano, T., Kamiya, I., Tobita, M., Iwahashi, J. and Nakajima, H. (2014). Landform monitoring in active volcano by UAV and SfM-MVS technique. Int. Arch. Photogramm. Remote Sens. Spatial Inf. Sci., XL-8: 71-75. DOI: 10.5194/isprsarchives-XL-8-71-2014

Navarro-Ochoa, C., Gavilanes-Ruíz, J.C. and Cortés-Cortés, A. (2002). Movement and emplacement of lava flows at Volcán de Colima, México: November 1998–February 1999. Journal of Volcanology and Geothermal Research, 117(1): 155-167. DOI: 10.1016/S0377-0273(02)00242-1

Neal, C.A., Brantley, S.R., Antolik, L., Babb, J.L., Burgess, M., Calles, K., Cappos, M., Chang, J.C., Conway, S., Desmither, L., Dotray, P., Elias, T., Fukunaga, P., Fuke, S., Johanson, I.A., Kamibayashi, K., Kauahikaua, J., Lee, R.L., Pekalib, S., Miklius, A., Million, W., Moniz, C.J., Nadeau, P.A., Okubo, P., Parcheta, C., Patrick, M.R., Shiro, B., Swanson, D.A., Tollett, W., Trusdell, F., Younger, E.F., Zoeller, M.H., Montgomery-Brown, E.K., Anderson, K.R., Poland, M.P., Ball, J.L., Bard, J., Coombs, M., Dietterich, H.R., Kern, C., Thelen, W.A., Cervelli, P.F., Orr, T., Houghton, B.F., Gansecki, C., Hazlett, R., Lundgren, P., Diefenbach, A.K., Lerner, A.H., Waite, G., Kelly, P., Clor, L., Werner,

C., Mulliken, K., Fisher, G. and Damby, D. (2019). The 2018 rift eruption and summit collapse of Kīlauea Volcano. Science, 363(6425): 367-374. DOI: 10.1126/science.aav7046

Nesbit, P.R. and Hugenholtz, C.H. (2019). Enhancing UAV–SfM 3D Model Accuracy in High-Relief Landscapes by Incorporating Oblique Images. Remote Sensing, 11(3): 1-24. DOI: 10.3390/rs11030239

Neuberg, J.W., Collinson, A.S.D., Mothes, P.A., C. Ruiz, M. and Aguaiza, S. (2018). Understanding cyclic seismicity and ground deformation patterns at volcanoes: Intriguing lessons from Tungurahua volcano, Ecuador. Earth and Planetary Science Letters, 482: 193-200. DOI: 10.1016/j.epsl.2017.10.050

O'Connor, J., Smith, M.J. and James, M.R. (2017). Cameras and settings for aerial surveys in the geosciences: Optimising image data. Progress in Physical Geography: Earth and Environment, 41(3): 325-344. DOI: 10.1177/0309133317703092

Ogburn, S.E., Loughlin, S.C. and Calder, E.S. (2015). The association of lava dome growth with major explosive activity (VEI ≥ 4): DomeHaz, a global dataset. Bulletin of Volcanology, 77(40): 1-17. DOI: 10.1007/s00445-015-0919-x

Ospina, C.W. (1930). Cuatro horas de marcha por el desierto de arena a corta distancia del crater del Santa Maria: Guatemala. Anales de la Sociedad de Geografia e Historia, 7(1): 68-85. (In Spanish).

Oxford Economics (2010). The economic impacts of air travel restrictions due to volcanic ash. Report. Abbey House, Oxford.

Pallister, J., Wessels, R., Griswold, J., McCausland, W., Kartadinata, N., Gunawan, H., Budianto, A. and Primulyana, S. (2018). Monitoring, forecasting collapse events, and mapping pyroclastic deposits at Sinabung volcano with satellite imagery. Journal of Volcanology and Geothermal Research, 382: 149-163. DOI: 10.1016/j.jvolgeores.2018.05.012

Pallister, J.S., Diefenbach, A.K., Burton, W.C., Muñoz, J., Griswold, J.P., Lara, L.E., Lowenstern, J.B. and Valenzuela, C.E. (2013a). The chaitén Rhyolite lava dome: Eruption sequence, lava dome volumes, rapid effusion rates and source of the Rhyolite magma. Andean Geology, 40(2): 277-294. DOI: 10.5027/andgeoV40n2-a06

Pallister, J.S., Schneider, D.J., Griswold, J.P., Keeler, R.H., Burton, W.C., Noyles, C., Newhall, C.G. and Ratdomopurbo, A. (2013b). Merapi 2010 eruption—Chronology and extrusion rates monitored with satellite radar and used in eruption forecasting. Journal of Volcanology and Geothermal Research, 261: 144-152. DOI: 10.1016/j.jvolgeores.2012.07.012

Pallister, J.S., Cashman, K.V., Hagstrum, J.T., Beeler, N.M., Moran, S.C. and Denlinger, R.P. (2013c). Faulting within the Mount St. Helens conduit and implications for volcanic earthquakes. Bulletin of the Geological Society of America, 125(3-4): 359-376. DOI: 10.1130/B30716.1

Pan, B., Qian, K., Xie, H. and Asundi, A. (2009). Two-dimensional digital image correlation for in-plane displacement and strain measurement: a review. Measurement Science and Technology, 20(6): 1-17. DOI: 10.1088/0957-0233/20/6/062001

Panov, V., Slezin, Y.B. and Storcheus, A. (1988). Mechanical properties of lava extruded in the 1983 Predskazanny eruption (Klyuchevskoi volcano). Volcanology and Seismology, 7: 25-37.

Patel, A., Dharpure, J.K., Snehmani and Ganju, A. (2019). Estimating surface ice velocity on Chhota Shigri glacier from satellite data using Particle Image Velocimetry (PIV) technique. Geocarto International, 34(4): 335-347. DOI: 10.1080/10106049.2017.1404142

Patrick, M.R., Dietterich, H.R., Lyons, J.J., Diefenbach, A.K., Parcheta, C., Anderson, K.R., Namiki, A., Sumita, I., Shiro, B. and Kauahikaua, J.P. (2019). Cyclic lava effusion during the 2018 eruption of Kīlauea Volcano. Science, 366(6470): eaay9070. DOI: 10.1126/science.aay9070

Pedersen, G.B.M., Belart, J.M.C., Magnússon, E., Vilmundardóttir, O.K., Kizel, F., Sigurmundsson, F.S., Gísladóttir, G. and Benediktsson, J.A. (2018). Hekla Volcano, Iceland, in the 20th Century: Lava Volumes, Production Rates, and Effusion Rates. Geophysical Research Letters, 45(4): 1805-1813. DOI: 10.1002/2017GL076887

Piscini, A. and Lombardo, V. (2014). Volcanic hot spot detection from optical multispectral remote sensing data using artificial neural networks. Geophysical Journal International, 196(3): 1525-1535. DOI: 10.1093/gji/ggt506

Platz, T., Cronin, S.J., Procter, J.N., Neall, V.E. and Foley, S.F. (2012). Non-explosive, dome-forming eruptions at Mt. Taranaki, New Zealand. Geomorphology, 136(1): 15-30. DOI: 10.1016/j.geomorph.2011.06.016

Pola, A., Crosta, G., Fusi, N., Barberini, V. and Norini, G. (2012). Influence of alteration on physical properties of volcanic rocks. Tectonophysics, 566-567: 67-86. DOI: 10.1016/j.tecto.2012.07.017

Poland, M.P., Dzurisin, D., LaHusen, R.G., Major, J.J., Lapcewich, D., Endo, E.T., Gooding, D.J., Schilling, S.P. and Janda, C.G. (2008). Remote camera observations of lava dome growth at Mount St. Helens, Washington, October 2004 to February 2006. In: D.R. Sherrod, W.E. Scott and P.H. Stauffer (Editors), A volcano rekindled: the renewed eruption of Mount St. Helens, 2004-2006. U. S. Geological Survey Professional Paper, Reston, VA, pp. 225-236.

Potyondy, D.O. and Cundall, P.A. (2004). A bonded-particle model for rock. International Journal of Rock Mechanics and Mining Sciences, 41(8): 1329-1364. DOI: 10.1016/j.ijrmms.2004.09.011

Potyondy, D.O. (2012). A Flat-Jointed Bonded-Particle Material For Hard Rock, 46th U.S. Rock Mechanics/Geomechanics Symposium. American Rock Mechanics Association, Chicago, Illinois, pp. 10.

Ratdomopurbo, A., Beauducel, F., Subandriyo, J., Agung Nandaka, I.G.M., Newhall, C.G., Suharna, Sayudi, D.S., Suparwaka, H. and Sunarta (2013). Overview of the 2006 eruption of Mt. Merapi. Journal of Volcanology and Geothermal Research, 261: 87-97. DOI: 10.1016/j.jvolgeores.2013.03.019

Reyes-Dávila, G.A., Arámbula-Mendoza, R., Espinasa-Pereña, R., Pankhurst, M.J., Navarro-Ochoa, C., Savov, I., Vargas-Bracamontes, D.M., Cortés-Cortés, A., Gutiérrez-Martínez, C., Valdés-González, C., Domínguez-Reyes, T., González-Amezcua, M., Martínez-Fierros, A., Ramírez-Vázquez, C.A., Cárdenas-González, L., Castañeda-Bastida, E., Vázquez Espinoza de los Monteros, D.M., Nieto-Torres, A., Campion, R., Courtois, L. and Lee, P.D. (2016). Volcán de Colima dome collapse of July, 2015 and associated pyroclastic density currents. Journal of Volcanology and Geothermal Research, 320: 100-106. DOI: 10.1016/j.jvolgeores.2016.04.015

Rhodes, E., Kennedy, B.M., Lavallée, Y., Hornby, A., Edwards, M. and Chigna, G. (2018). Textural Insights Into the Evolving Lava Dome Cycles at Santiaguito Lava Dome, Guatemala. Frontiers in Earth Science, 6(30): 1-18. DOI: 10.3389/feart.2018.00030

Rincón, M., Márquez, A., Herrera, R., Alonso-Torres, A., Granja-Bruña, J.L. and van Wyk de Vries, B. (2018). Contrasting catastrophic eruptions predicted by different intrusion and collapse scenarios. Scientific Reports, 8(1): 6178. DOI: 10.1038/s41598-018-24623-5

Rivalta, E., Taisne, B., Bunger, A.P. and Katz, R.F. (2015). A review of mechanical models of dike propagation: Schools of thought, results and future directions. Tectonophysics, 638: 1-42. DOI: 10.1016/j.tecto.2014.10.003

Rodgers, M., Roman, D.C., Geirsson, H., LaFemina, P., McNutt, S.R., Muñoz, A. and Tenorio, V. (2015). Stable and unstable phases of elevated seismic activity at the persistently restless Telica Volcano, Nicaragua. Journal of Volcanology and Geothermal Research, 290: 63-74. DOI: 10.1016/j.jvolgeores.2014.11.012

Rose, W.I. (1973). Pattern and mechanism of volcanic activity at the Santiaguito Volcanic Dome, Guatemala. Bulletin Volcanologique, 37(1): 73-94. DOI: 10.1007/bf02596881

Rose, W.I., JR. (1972). Santiaguito Volcanic Dome, Guatemala. GSA Bulletin, 83(5): 1413-1434. DOI: 10.1130/0016-7606(1972)83[1413:Svdg]2.0.Co;2

Rosenau, M., Pohlenz, A., Kemnitz, H. and Warsitzka, M. (2018). Ring-shear test data of quartz sand G12 used for analogue experiments in the Helmholtz Laboratory for Tectonic Modelling (HelTec) at the GFZ German Research Centre for Geosciences in Potsdam. GFZ Data Services. DOI: 10.5880/GFZ.4.1.2019.003

Roth, A., Eineder, M. and Schättler, B. (2003). TerraSAR-X: A new perspective for applications requiring high resolution spaceborne SAR data, Proceedings of the Joint ISPRS, EarSel Workshop on High Resolution Mapping from Space 2003, pp. 1-4.

Roverato, M., Capra, L., Sulpizio, R. and Norini, G. (2011). Stratigraphic reconstruction of two debris avalanche deposits at Colima Volcano (Mexico): Insights into pre-failure conditions and climate influence. Journal of Volcanology and Geothermal Research, 207(1): 33-46. DOI: 10.1016/j.jvolgeores.2011.07.003

Rubin, A.M. (1995). Propagation of Magma-Filled Cracks. Annual Review of Earth and Planetary Sciences, 23(1): 287-336. DOI: 10.1146/annurev.ea.23.050195.001443

Rust, A.C., Cashman, K.V. and Wallace, P.J. (2004). Magma degassing buffered by vapor flow through brecciated conduit margins. Geology, 32(4): 349-352. DOI: 10.1130/G20388.2

Ryan, A.G., Friedlander, E.A., Russell, J.K., Heap, M.J. and Kennedy, L.A. (2018a). Hot pressing in conduit faults during lava dome extrusion: Insights from Mount St. Helens 2004–2008. Earth and Planetary Science Letters, 482: 171-180. DOI: 10.1016/j.epsl.2017.11.010

Ryan, A.G., Russell, J.K. and Heap, M.J. (2018b). Rapid solid-state sintering in volcanic systems. American Mineralogist, 103(12): 2028-2031. DOI: 10.2138/am-2018-6714

Sahetapy-Engel, S.T. and Harris, A.J.L. (2009). Thermal structure and heat loss at the summit crater of an active lava dome. Bulletin of Volcanology, 71(1): 15-28. DOI: 10.1007/s00445-008-0204-3

Salzer, J.T., Nikkhoo, M., Walter, T.R., Sudhaus, H., Reyes-Dávila, G., Bretón, M. and Arámbula, R. (2014). Satellite radar data reveal short-term pre-explosive displacements and a complex conduit system at Volcán de Colima, Mexico. Frontiers in Earth Science, 2(12): 1-11. DOI: 10.3389/feart.2014.00012

Salzer, J.T., Thelen, W.A., James, M.R., Walter, T.R., Moran, S. and Denlinger, R. (2016). Volcano dome dynamics at Mount St. Helens: Deformation and intermittent subsidence monitored by seismicity and camera imagery pixel offsets. Journal of Geophysical Research: Solid Earth, 121(11): 7882-7902. DOI: 10.1002/2016JB013045

Salzer, J.T., Milillo, P., Varley, N., Perissin, D., Pantaleo, M. and Walter, T.R. (2017). Evaluating links between deformation, topography and surface temperature at volcanic domes: Results from a multi-sensor study at Volcán de Colima, Mexico. Earth and Planetary Science Letters, 479: 354-365. DOI: 10.1016/j.epsl.2017.09.027

Sarocchi, D., Sulpizio, R., Macías, J.L. and Saucedo, R. (2011). The 17 July 1999 block-and-ash flow (BAF) at Colima Volcano: New insights on volcanic granular flows from textural analysis. Journal of Volcanology and Geothermal Research, 204(1): 40-56. DOI: 10.1016/j.jvolgeores.2011.04.013

Sato, H., Fujii, T. and Nakada, S. (1992). Crumbling of dacite dome lava and generation of pyroclastic flows at Unzen volcano. Nature, 360(6405): 664-666. DOI: 10.1038/360664a0

Saucedo, R., Macías, J.L., Gavilanes, J.C., Arce, J.L., Komorowski, J.C., Gardner, J.E. and Valdez-Moreno, G. (2010). Eyewitness, stratigraphy, chemistry, and eruptive dynamics of the 1913 Plinian eruption of Volcán de Colima, México. Journal of Volcanology and Geothermal Research, 191(3): 149-166. DOI: 10.1016/j.jvolgeores.2010.01.011

Schaefer, L.N., Kendrick, J.E., Oommen, T., Lavallée, Y. and Chigna, G. (2015). Geomechanical rock properties of a basaltic volcano. Frontiers in Earth Science, 3(29): 1-15. DOI: 10.3389/feart.2015.00029

Schellart, W.P. (2000). Shear test results for cohesion and friction coefficients for different granular materials: scaling implications for their usage in analogue modelling. Tectonophysics, 324(1): 1-16. DOI: 10.1016/S0040-1951(00)00111-6

Schilling, S.P., Thompson, R.A., Messerich, J.A. and Iwatsubo, E.Y. (2008). Use of digital aerophotogrammetry to determine rates of lava dome growth, Mount St. Helens, Washington, 2004-2005. In: D.R. Sherrod, W.E. Scott and P.H. Stauffer (Editors), A volcano rekindled: the renewed eruption of Mount St. Helens, 2004-2006. U.S. Geological Survey Professional Paper, Reston, VA, pp. 145-167.

Schreier, H., Braasch, J. and Sutton, M. (2000). Systematic errors in digital image correlation caused by intensity interpolation. Optical Engineering, 39(11). DOI: 10.1117/1.1314593

Schulze, D. (1994). Entwicklung und Anwendung eines neuartigen Ringschergerätes. Aufbereitungs-Technik, 35(10): 524-535. (In German).

Schwarzkopf, L.M., Schmincke, H.U. and Cronin, S.J. (2005). A conceptual model for block-and-ash flow basal avalanche transport and deposition, based on deposit architecture of 1998 and 1994 Merapi flows. Journal of Volcanology and Geothermal Research, 139(1): 117-134. DOI: 10.1016/j.jvolgeores.2004.06.012

Sheldrake, T.E., Sparks, R.S.J., Cashman, K.V., Wadge, G. and Aspinall, W.P. (2016). Similarities and differences in the historical records of lava dome-building volcanoes: Implications for understanding magmatic processes and eruption forecasting. Earth-Science Reviews, 160: 240-263. DOI: 10.1016/j.earscirev.2016.07.013

Shevchenko, A.V., Dvigalo, V.N. and Svirid, I.Y. (2015). Airborne photogrammetry and geomorphological analysis of the 2001–2012 exogenous dome growth at Molodoy

Shiveluch Volcano, Kamchatka. Journal of Volcanology and Geothermal Research, 304: 94-107. DOI: 10.1016/j.jvolgeores.2015.08.013

Spampinato, L., Calvari, S., Oppenheimer, C. and Boschi, E. (2011). Volcano surveillance using infrared cameras. Earth-Science Reviews, 106(1): 63-91. DOI: 10.1016/j.earscirev.2011.01.003

Sparks, R.S.J., Wilson, L. and Hulme, G. (1978). Theoretical modeling of the generation, movement, and emplacement of pyroclastic flows by column collapse. Journal of Geophysical Research: Solid Earth, 83(B4): 1727-1739. DOI: 10.1029/JB083iB04p01727

Sparks, R.S.J. (1997). Causes and consequences of pressurisation in lava dome eruptions. Earth and Planetary Science Letters, 150(3): 177-189. DOI: 10.1016/S0012-821X(97)00109-X

Sparks, R.S.J., Murphy, M.D., Lejeune, A.M., Watts, R.B., Barclay, J. and Young, S.R. (2000). Control on the emplacement of the andesite lava dome of the Soufriere Hills volcano, Montserrat by degassing-induced crystallization. Terra Nova, 12(1): 14-20. DOI: 10.1046/j.1365-3121.2000.00267.x

Stein, R.S., Barka, A.A. and Dieterich, J.H. (1997). Progressive failure on the North Anatolian fault since 1939 by earthquake stress triggering. Geophysical Journal International, 128(3): 594-604. DOI: 10.1111/j.1365-246X.1997.tb05321.x

Stein, R.S. (1999). The role of stress transfer in earthquake occurrence. Nature, 402: 605. DOI: 10.1038/45144

Stevenson, J.A. and Varley, N. (2008). Fumarole monitoring with a handheld infrared camera: Volcán de Colima, Mexico, 2006–2007. Journal of Volcanology and Geothermal Research, 177(4): 911-924. DOI: 10.1016/j.jvolgeores.2008.07.003

Stumpf, A., Malet, J.P., Allemand, P. and Ulrich, P. (2014). Surface reconstruction and landslide displacement measurements with Pléiades satellite images. ISPRS Journal of Photogrammetry and Remote Sensing, 95: 1-12. DOI: 10.1016/j.isprsjprs.2014.05.008

Sulpizio, R. and Massaro, S. (2017). Influence of Stress Field Changes on Eruption Initiation and Dynamics: A Review. Frontiers in Earth Science, 5(18): 1-11. DOI: 10.3389/feart.2017.00018

Surono, Jousset, P., Pallister, J., Boichu, M., Buongiorno, M.F., Budisantoso, A., Costa, F., Andreastuti, S., Prata, F., Schneider, D., Clarisse, L., Humaida, H., Sumarti, S., Bignami, C., Griswold, J., Carn, S., Oppenheimer, C. and Lavigne, F. (2012). The 2010 explosive eruption of Java's Merapi volcano—A '100-year' event. Journal of Volcanology and Geothermal Research, 241-242: 121-135. DOI: 10.1016/j.jvolgeores.2012.06.018

Sutton, M.A., Orteu, J.J. and Schreier, H. (2009). Image correlation for shape, motion and deformation measurements: Basic concepts, theory and applications. Springer, New York.

Swanson, D.A. (1990). A decade of dome growth at Mount St. Helens, 1980-90. Geoscience Canada, 17(3): 154-157.

Tanguy, J.C. (1994). The 1902–1905 eruptions of Montagne Pelée, Martinique: anatomy and retrospection. Journal of Volcanology and Geothermal Research, 60(2): 87-107. DOI: 10.1016/0377-0273(94)90064-7

Tanguy, J.C. (2004). Rapid dome growth at Montagne Pelée during the early stages of the 1902–1905 eruption: a reconstruction from Lacroix's data. Bulletin of Volcanology, 66(7): 615-621. DOI: 10.1007/s00445-004-0344-z

Tao, C.V., Hu, Y. and Jiang, W. (2004). Photogrammetric exploitation of IKONOS imagery for mapping applications. International Journal of Remote Sensing, 25(14): 2833-2853. DOI: 10.1080/01431160310001618392

Thiele, S.T., Varley, N. and James, M.R. (2017). Thermal photogrammetric imaging: A new technique for monitoring dome eruptions. Journal of Volcanology and Geothermal Research, 337: 140-145. DOI: 10.1016/j.jvolgeores.2017.03.022

Thielicke, W. and Stamhuis, E. (2014). PIVlab–towards user-friendly, affordable and accurate digital particle image velocimetry in MATLAB. Journal of Open Research Software, 2(1): 1-10. DOI: 10.5334/jors.bl

Tuffen, H. and Dingwell, D. (2005). Fault textures in volcanic conduits: evidence for seismic trigger mechanisms during silicic eruptions. Bulletin of Volcanology, 67(4): 370-387. DOI: 10.1007/s00445-004-0383-5

Tuffen, H., Smith, R. and Sammonds, P.R. (2008). Evidence for seismogenic fracture of silicic magma. Nature, 453(7194): 511-514. DOI: 10.1038/nature06989

Turner, N.R., Perroy, R.L. and Hon, K. (2017). Lava flow hazard prediction and monitoring with UAS: a case study from the 2014–2015 Pāhoa lava flow crisis, Hawai'i. Journal of Applied Volcanology, 6(1): 17. DOI: 10.1186/s13617-017-0068-3

Vallance, J.W., Schneider, D.J. and Schilling, S.P. (2008). Growth of the 2004-2006 lava-dome complex at Mount St. Helens, Washington. In: D.R. Sherrod, W.E. Scott and P.H. Stauffer (Editors), A volcano rekindled: the renewed eruption of Mount St. Helens, 2004-2006. U.S. Geological Survey Professional Paper, Reston, VA, pp. 169-208. DOI: 10.3133/pp17509

Vargas-Bracamontes, D.M., Nava, F.A. and Reyes-Dávila, G.A. (2009). Time-scale wavelet patterns related to the 1998-1999 eruptions of the Colima volcano, and their possible implications for eruption forecasting. Journal of Volcanology and Geothermal Research, 184(3-4): 271-284. DOI: 10.1016/j.jvolgeores.2009.01.025

Varley, N.R., Arámbula-Mendoza, R., Reyes-Dávila, G., Stevenson, J. and Harwood, R. (2010). Long-period seismicity during magma movement at Volcán de Colima. Bulletin of Volcanology, 72(9): 1093-1107. DOI: 10.1007/s00445-010-0390-7

Voight, B., Sparks, R.S.J., Miller, A.D., Stewart, R.C., Hoblitt, R.P., Clarke, A., Ewart, J., Aspinall, W.P., Baptie, B., Calder, E.S., Cole, P., Druitt, T.H., Hartford, C., Herd, R.A., Jackson, P., Lejeune, A.M., Lockhart, A.B., Loughlin, S.C., Luckett, R., Lynch, L., Norton, G.E., Robertson, R., Watson, I.M., Watts, R. and Young, S.R. (1999). Magma Flow Instability and Cyclic Activity at Soufriere Hills Volcano, Montserrat, British West Indies. Science, 283(5405): 1138-1142. DOI: 10.1126/science.283.5405.1138

Voight, B. and Elsworth, D. (2000). Instability and collapse of hazardous gas-pressurized lava domes. Geophysical Research Letters, 27(1): 1-4. DOI: 10.1029/1999gl008389

Voight, B. (2000). Structural stability of andesite volcanoes and lava domes. Philosophical Transactions of the Royal Society of London A: Mathematical, Physical and Engineering Sciences, 358(1770): 1663-1703. DOI: 10.1098/rsta.2000.0609

von Aulock, F.W., Lavallée, Y., Hornby, A.J., Lamb, O.D., Andrews, B.J. and Kendrick, J.E. (2016). Observing changes at Santiaguito Volcano, Guatemala with an Unmanned

Aerial Vehicle (UAV). EGU General Assembly Conference Abstracts 2016. EPSC2016–11080.

Wadge, G., Ryan, G. and Calder, E.S. (2009). Clastic and core lava components of a silicic lava dome. Geology, 37(6): 551-554. DOI: 10.1130/g25747a.1

Walder, J.S., LaHusen, R.G., Vallance, J.W. and Schilling, S.P. (2007). Emplacement of a silicic lava dome through a crater glacier: Mount St Helens, 2004–06. Annals of Glaciology, 45: 14-20. DOI: 10.3189/172756407782282426

Wallace, P.A., Kendrick, J.E., Miwa, T., Ashworth, J.D., Coats, R., Utley, J.E.P., Henton De Angelis, S., Mariani, E., Biggin, A., Kendrick, R., Nakada, S., Matsushima, T. and Lavallée, Y. (2019). Petrological Architecture of a Magmatic Shear Zone: A Multidisciplinary Investigation of Strain Localisation During Magma Ascent at Unzen Volcano, Japan. Journal of Petrology, 60(4): 791-826. DOI: 10.1093/petrology/egz016

Walter, T.R. (2011). Low cost volcano deformation monitoring: optical strain measurement and application to Mount St. Helens data. Geophysical Journal International, 186(2): 699-705. DOI: 10.1111/j.1365-246X.2011.05051.x

Walter, T.R., Ratdomopurbo, A., Subandriyo, Aisyah, N., Brotopuspito, K.S., Salzer, J. and Lühr, B. (2013a). Dome growth and coulée spreading controlled by surface morphology, as determined by pixel offsets in photographs of the 2006 Merapi eruption. Journal of Volcanology and Geothermal Research, 261: 121-129. DOI: 10.1016/j.jvolgeores.2013.02.004

Walter, T.R., Legrand, D., Granados, H.D., Reyes, G. and Arámbula, R. (2013b). Volcanic eruption monitoring by thermal image correlation: Pixel offsets show episodic dome growth of the Colima volcano. Journal of Geophysical Research: Solid Earth, 118(4): 1408-1419. DOI: 10.1002/jgrb.50066

Walter, T.R., Subandriyo, J., Kirbani, S., Bathke, H., Suryanto, W., Aisyah, N., Darmawan, H., Jousset, P., Luehr, B.G. and Dahm, T. (2015). Volcano-tectonic control of Merapi's lava dome splitting: The November 2013 fracture observed from high resolution TerraSAR-X data. Tectonophysics, 639: 23-33. DOI: 10.1016/j.tecto.2014.11.007

Walter, T.R., Salzer, J., Varley, N., Navarro, C., Arámbula-Mendoza, R. and Vargas-Bracamontes, D. (2018). Localized and distributed erosion triggered by the 2015 Hurricane Patricia investigated by repeated drone surveys and time lapse cameras at Volcán de Colima, Mexico. Geomorphology, 319: 186-198. DOI: 10.1016/j.geomorph.2018.07.020

Walter, T.R., Haghshenas Haghighi, M., Schneider, F.M., Coppola, D., Motagh, M., Saul, J., Babeyko, A., Dahm, T., Troll, V.R., Tilmann, F., Heimann, S., Valade, S., Triyono, R., Khomarudin, R., Kartadinata, N., Laiolo, M., Massimetti, F. and Gaebler, P. (2019a). Complex hazard cascade culminating in the Anak Krakatau sector collapse. Nature Communications, 10(1): 4339. DOI: 10.1038/s41467-019-12284-5

Walter, T.R., Harnett, C.E., Varley, N., Bracamontes, D.V., Salzer, J., Zorn, E.U., Bretón, M., Arámbula, R. and Thomas, M.E. (2019b). Imaging the 2013 explosive crater excavation and new dome formation at Volcán de Colima with TerraSAR-X, time-lapse cameras and modelling. Journal of Volcanology and Geothermal Research, 369: 224-237. DOI: 10.1016/j.jvolgeores.2018.11.016

Wang, T., Poland, M.P. and Lu, Z. (2015). Dome growth at Mount Cleveland, Aleutian Arc, quantified by time series TerraSAR-X imagery. Geophysical Research Letters, 42(24): 10614-10621. DOI: 10.1002/2015GL066784

Watson, M., Chigna, G., Wood, K., Richardson, T., Liu, E., Schellenberg, B., Thomas, H. and Naismith, A. (2017). On the use of UAVs at active volcanoes: a case study from Volcan de Fuego, Guatemala. AGU Fall Meeting Abstracts 2017. NH31C–03.

Watts, R.B., Herd, R.A., Sparks, R.S.J. and Young, S.R. (2002). Growth patterns and emplacement of the andesitic lava dome at Soufrière Hills Volcano, Montserrat. Geological Society, London, Memoirs, 21(1): 115-152. DOI: 10.1144/GSL.MEM.2002.021.01.06

Welch, M.D. and Schmidt, D.A. (2017). Separating volcanic deformation and atmospheric signals at Mount St. Helens using Persistent Scatterer InSAR. Journal of Volcanology and Geothermal Research, 344: 52-64. DOI: 10.1016/j.jvolgeores.2017.05.015

Werner, C., Wegmüller, U., Strozzi, T. and Wiesmann, A. (2000). Gamma SAR and interferometric processing software, Proceedings of the ers-envisat symposium, Gothenburg, Sweden, pp. 1-9.

Werner, C., Kern, C., Coppola, D., Lyons, J.J., Kelly, P.J., Wallace, K.L., Schneider, D.J. and Wessels, R.L. (2017). Magmatic degassing, lava dome extrusion, and explosions from Mount Cleveland volcano, Alaska, 2011–2015: Insight into the continuous nature of volcanic activity over multi-year timescales. Journal of Volcanology and Geothermal Research, 337: 98-110. DOI: 10.1016/j.jvolgeores.2017.03.001

Westoby, M.J., Brasington, J., Glasser, N.F., Hambrey, M.J. and Reynolds, J.M. (2012). 'Structure-from-Motion' photogrammetry: A low-cost, effective tool for geoscience applications. Geomorphology, 179: 300-314. DOI: 10.1016/j.geomorph.2012.08.021

Williams, S.N. and Self, S. (1983). The October 1902 plinian eruption of Santa Maria volcano, Guatemala. Journal of Volcanology and Geothermal Research, 16(1): 33-56. DOI: 10.1016/0377-0273(83)90083-5

Witham, C.S. (2005). Volcanic disasters and incidents: A new database. Journal of Volcanology and Geothermal Research, 148(3): 191-233. DOI: 10.1016/j.jvolgeores.2005.04.017

Wooster, M.J. and Kaneko, T. (1998). Satellite thermal analyses of lava dome effusion rates at Unzen Volcano, Japan. Journal of Geophysical Research: Solid Earth, 103(B9): 20935-20947. DOI: 10.1029/97jb03392

Wyering, L.D., Villeneuve, M.C., Wallis, I.C., Siratovich, P.A., Kennedy, B.M., Gravley, D.M. and Cant, J.L. (2014). Mechanical and physical properties of hydrothermally altered rocks, Taupo Volcanic Zone, New Zealand. Journal of Volcanology and Geothermal Research, 288: 76-93. DOI: 10.1016/j.jvolgeores.2014.10.008

Závada, P., Kratinová, Z., Kusbach, V. and Schulmann, K. (2009). Internal fabric development in complex lava domes. Tectonophysics, 466(1): 101-113. DOI: 10.1016/j.tecto.2008.07.005

Zobin, V.M., Arámbula, R., Bretón, M., Reyes, G., Plascencia, I., Navarro, C., Téllez, A., Campos, A., González, M., León, Z., Martínez, A. and Ramírez, C. (2015). Dynamics of the January 2013–June 2014 explosive-effusive episode in the eruption of Volcán de Colima, México: insights from seismic and video monitoring. Bulletin of Volcanology, 77(4): 31. DOI: 10.1007/s00445-015-0917-z

Zorn, E.U., Rowe, M.C., Cronin, S.J., Ryan, A.G., Kennedy, L.A. and Russell, J.K. (2018). Influence of porosity and groundmass crystallinity on dome rock strength: a case study from Mt. Taranaki, New Zealand. Bulletin of Volcanology, 80(4): 35. DOI: 10.1007/s00445-018-1210-8

Zorn, E.U., Le Corvec, N., Varley, N.R., Salzer, J.T., Walter, T.R., Navarro-Ochoa, C., Vargas-Bracamontes, D.M., Thiele, S.T. and Arámbula Mendoza, R. (2019). Load Stress Controls on Directional Lava Dome Growth at Volcán de Colima, Mexico. Frontiers in Earth Science, 7(84): 1-18. DOI: 10.3389/feart.2019.00084

Zorn, E.U., Walter, T.R., Johnson, J.B. and Mania, R. (2020a). UAS-based tracking of the Santiaguito Lava Dome, Guatemala. Scientific Reports, 10(1): 8644. DOI: 10.1038/s41598-020-65386-2

Zorn, E.U., Walter, T.R., Heap, M.J. and Kueppers, U. (2020b). Insights into lava dome and spine extrusion using analogue sandbox experiments. Earth and Planetary Science Letters, 551: 116571. DOI: 10.1016/j.epsl.2020.116571

Zorn, E.U., Walter, T.R., Johnson, J.B. and Mania, R. (2020c). High-resolution photogrammetry data of the Santiaguito lava dome collected by UAS surveys. GFZ Data Services. DOI: 10.5880/GFZ.2.1.2020.001

Appendix A:

Data publication - High-resolution photogrammetry data of the Santiaguito lava dome collected by UAS surveys

Edgar U. Zorn[1], Thomas R. Walter[1], Jeffrey B. Johnson[2], René Mania[1]

[1]German Research Center for Geosciences GFZ, Potsdam, Germany
[2]Boise State University, Boise, United States

Abstract

Imaging growing lava domes has remained a great challenge in volcanology due to their inaccessibility and the severe hazard of collapse or explosion. Here, we present orthophotos and topography data derived from a series of repeated survey flights with both optical and thermal cameras at the Caliente lava dome, part of the Santiaguito complex at Santa Maria volcano, Guatemala, using an Unoccupied Aircraft System (UAS). The data archived here supplements the material detailed in Zorn et al. (2020a, https://doi.org/10.1038/s41598-020-65386-2).

Note, all files are saved in WGS 84 / UTM Zone 15N format. The data are provided in the following .zip folders via the link below:
ftp://datapub.gfz-potsdam.de/download/10.5880.GFZ.2.1.2020.001btsh

- 2020-001_Zorn-et-al_DEM-Geotiffs-zip: DEMs of surveys A-D in geotiff format (.tif)
- 2020-001_Zorn-et-al_Orthophotos.zip: Orthophotos of surveys A-D and 2 thermal surveys as Tiff-images (.tif). A .jpg of the color scale for the thermal data is also included
- 2020-001_Zorn-et-al_Point_Cloud_Models.zip: Point clouds of surveys A-D, 2 thermal surveys (.las)

Methods

During fieldwork in February 2019 we performed UAS survey flights over the active Caliente vent at Santiaguito volcano with multiple drones and sensors at a height of approx. 100 m over the lava dome (Fig. 3.1a, 3.2a). The flights were recorded using high-resolution optical photos and an additional thermal camera. The optical images were acquired with the onboard sRGB

camera of our UAS (DJI Phantom 4 Pro) with a resolution of 5472 x 3078 px and a sampling rate of 0.5 Hz. The thermal images were acquired with a FLIR TAU 2 (9 mm lens), stored in a TEAX ThermalCapture frame grabber, and processed with the Thermoviewer software (v3.0.4). These provided radiometric temperature data and had a resolution of 640 x 512 px with a sampling rate of 8 Hz. In total, we processed four flights with optical photos (named surveys A, B, C, and D) and two thermal flights.

We performed Structure-from-Motion (SfM) photogrammetric processing using Agisoft Metashape 1.5.2 on all optical and thermal surveys to reconstruct the 3D environment of the active lava dome, enabling us to construct both high resolution DEMs from dense point clouds as well as detailed orthophotos. The survey photos were acquired in nadir or near-nadir position, with only some single photos being taken at an oblique angle to improve the model quality. The difficult and hazardous terrain did not allow for sufficient ground control points to create a reliable georeferencing. To georeference the UAS datasets acquired at Santiaguito volcano, we used a photogrammetric model built from high-resolution optical Pléiades satellite imagery on 15.01.2017. In this process, the SfM-built DEM is attached to the Pléiades one by identifying recognizable features in both datasets. The final referencing had an RMS-error of 3.3 m, but due to the high resolution of the SfM models, they could be better referenced relative to each other, meaning that all other SfM-DEMs now use the pre-referenced Survey D as a basis. This minimizes the relative errors between the DEMs and allows for high-precision data comparison. Here, all models are within 0.3 m accurate relative to each other.

Appendix B:

Load stress controls on directional lava dome growth at Volcán de Colima, Mexico

Edgar U. Zorn[1,2], Nicolas Le Corvec[2], Jacqueline T. Salzer[1], Nick R. Varley[3], Thomas R. Walter[1], Carlos Navarro-Ochoa[4], Dulce M. Vargas-Bracamontes[5], Samuel T. Thiele[6], Raúl Arámbula Mendoza[4]

[1]German Research Centre for Geosciences GFZ, Potsdam, Germany
[2]Institute of Geosciences, University of Potsdam, Potsdam, Germany
[3]Colima Intercambio e Investigación en Vulcanología, Universidad de Colima, Colima, Mexico
[4]Centro Universitario de Estudios e Investigaciones Vulcanológia, Universidad de Colima, Colima, Mexico
[5]CONACYT-CUEIV, Universidad de Colima, Colima, Mexico
[6]School of Earth, Atmosphere and Environment, Monash University, Clayton, Australia

B1: Video summary of the TerraSAR-X radar data during the study period in ascending geometry (ASC) and descending geometry (DSC). The videos also contain the seismic data from fig. 2.2 with the grey bars highlighting active extrusion.
The Supplementary Material for this article can be found online at:
https://www.frontiersin.org/articles/10.3389/feart.2019.00084/full#supplementary-material

B2: Detailed seismic activity from December 15th, 2014, to March 31st, 2015, documenting the transition period from lava effusion to explosive activity, capturing the removal of the summit dome and the proposed opening of a second vent. The normalized decomposition of the seismicity (e) shows that in early January 2015, the transition to an explosive phase had begun, whereas the dominance of the explosions can clearly be seen by the marked changes in (b-d) around the 16th of January. From top to bottom each subfigure corresponds to the following:
(a) RSAM (Real-time Seismic-Amplitude Measurement) per hour; (b) SSAM (Seismic Spectral-Amplitude Measurement); (c) daily mean and mode of the dominant frequency calculated every 10 minutes in the range between 1 to 15 Hz, warm colours inside the circles of the estimated means indicate higher amplitude values of the power spectral density; (d) 10 minutes ratio of high (mean 5-12 Hz) to low (mean 1-5 Hz) spectral energy in log base 2 scale (Rodgers et al., 2015), the red curve represents the daily moving average of the frequency ratio;

(e) rate of normalized seismic energy per hour (see fig. 2.2 for a broader description) at scales with 2^j samples, where j corresponds to the numbers next to the colours in the figures inset.

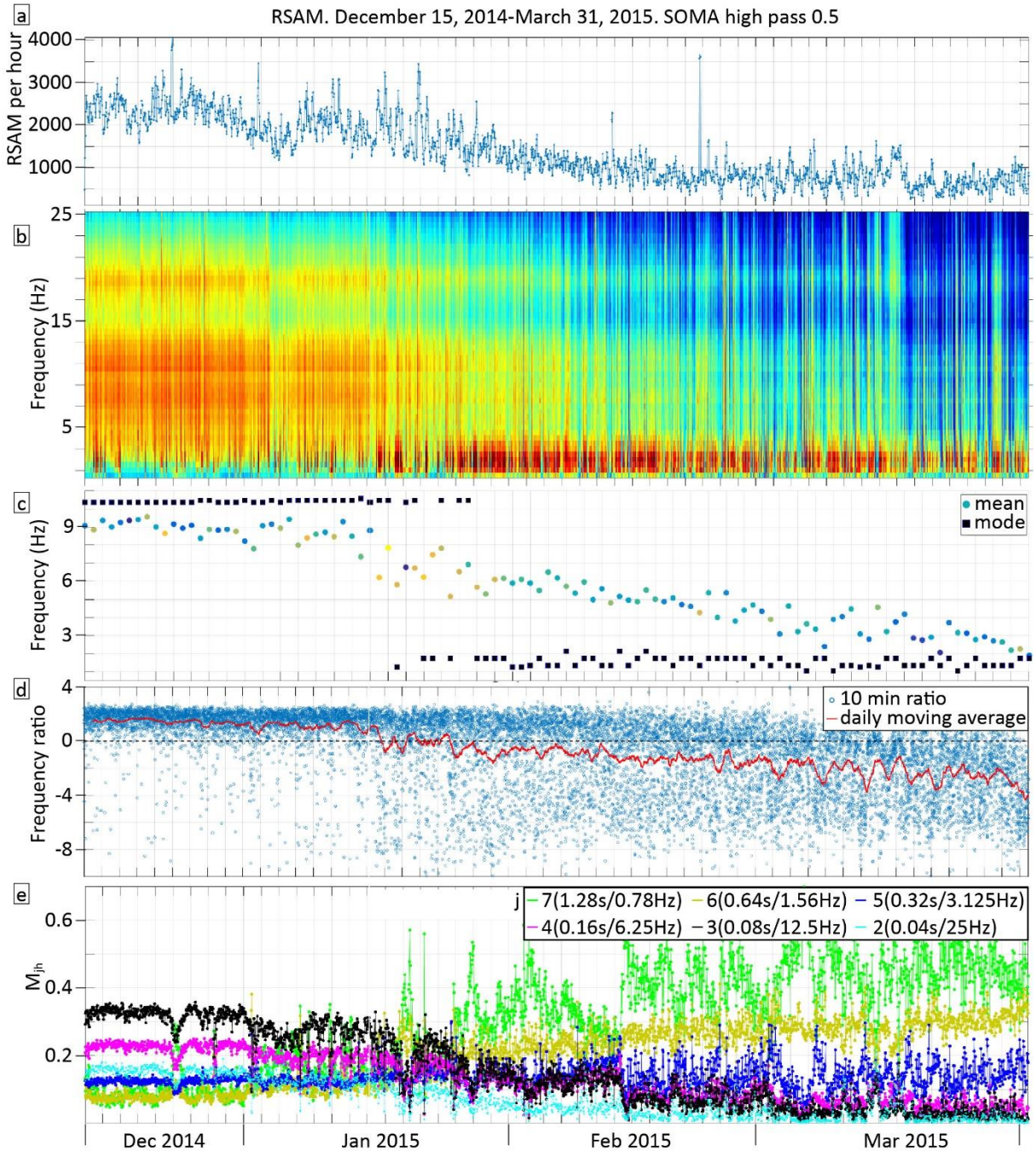

B3: The following pages contain images of all DEMs generated from the aerial overflights over Volcán de Colima. They were processed using the SfM-MVS workflow and resolved at 10 cm.

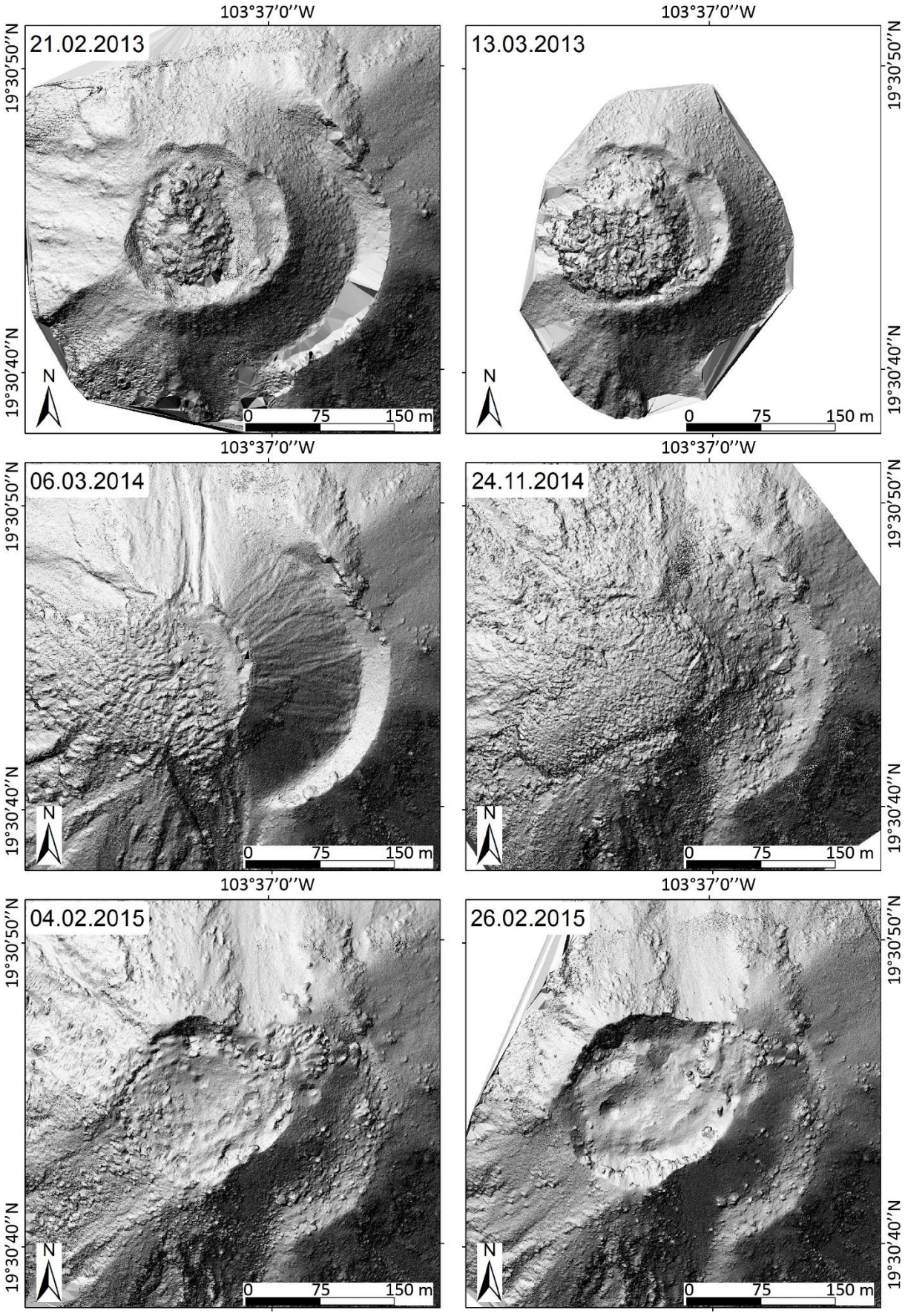

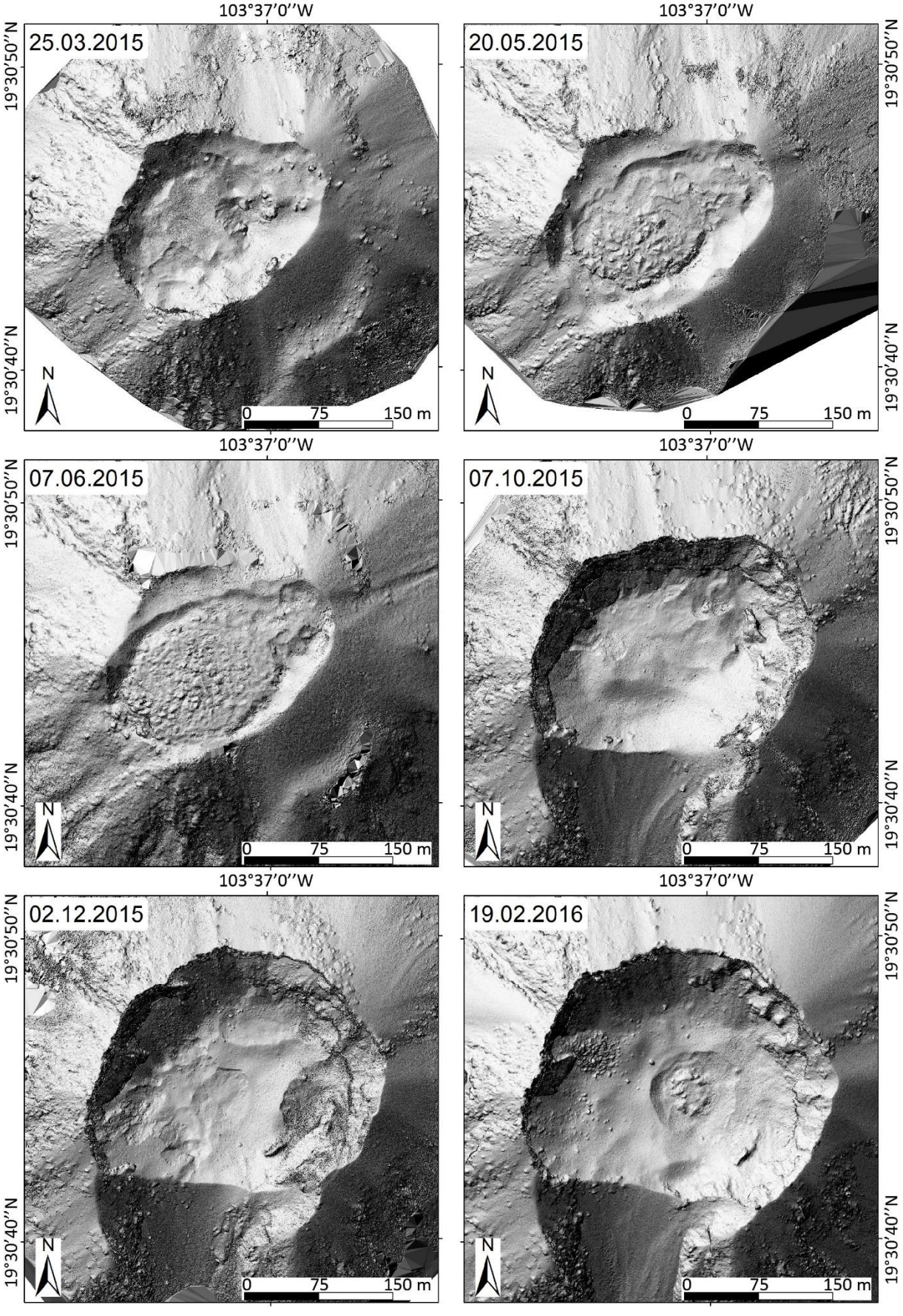
103°37′0′′W
19°30′50′′N
19°30′40′′N
25.03.2015
20.05.2015
07.06.2015
07.10.2015
02.12.2015
19.02.2016
N
0
75
150 m

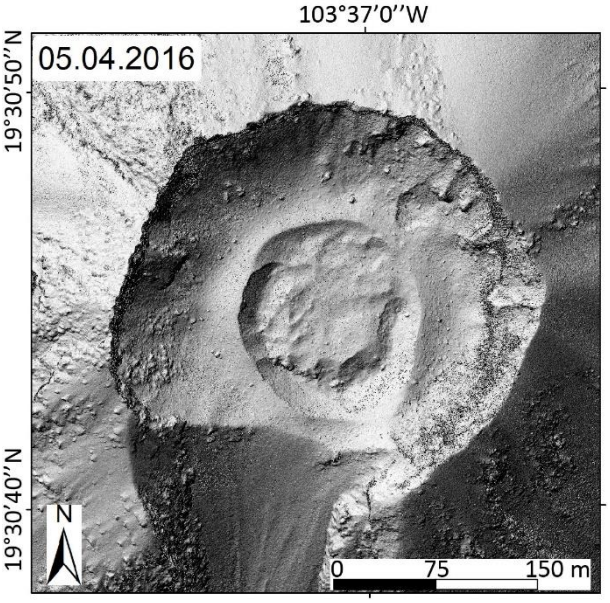
103°37′0′′W
19°30′50′′N
19°30′40′′N
05.04.2016
N
0
75
150 m

Appendix C:

UAS-based tracking of the Santiaguito Lava Dome, Guatemala

Edgar U. Zorn[1], Thomas R. Walter[1], Jeffrey B. Johnson[2], René Mania[1]

[1]German Research Centre for Geosciences GFZ, Potsdam, Germany

[2]Boise State University, Boise, United States

C1: The Figure shows (a) the measurement points (red dots) for the apparent viscosity calculations and profiles across the flow channel at these points. Particle divergence plotting (b) also shows the relative lava flow motion, assisting in picking appropriate points representative of different flow regions. It shows stretching near the large fracture at the dome centre and on the edge of the flat top near the overtopping onto flank, where the flow bends downwards as it transitions to the flank, minor compression follows below. The corresponding profiles are shown in (c-e). (b) was plotted with LaVision DaVis (v8.4.0, www.lavision.de/de/products/davis-software/).

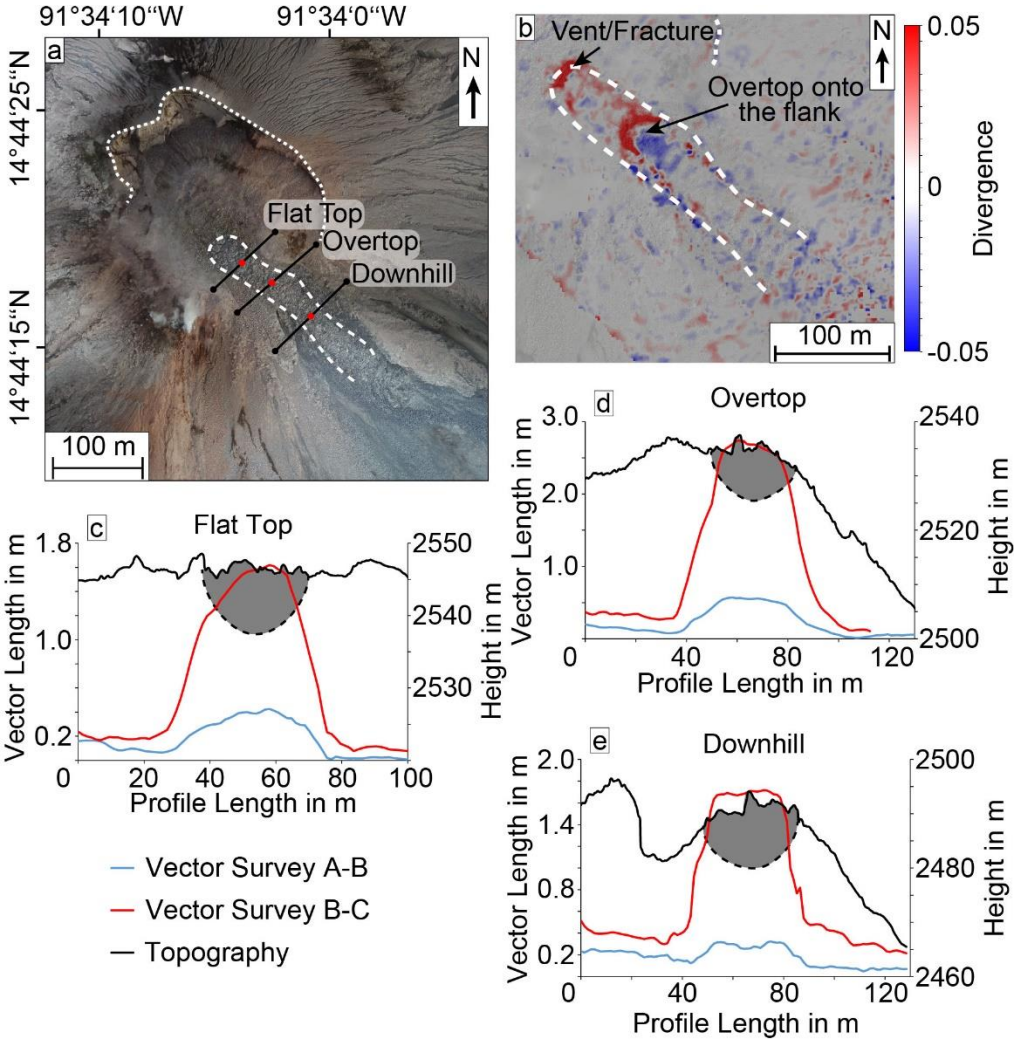

C2:

Time lapse PIV in (a) 2007, (c) 2009, and (e) 2012 recorded from the Santa Maria summit was used to measure surface movements on the flat top of the lava dome over 4-hour time spans. A look angle of 30 degrees (relative to horizontal) was assumed and used to estimate vector amplitudes projected on to a horizontal plane. Lava flow motions were calculated from 2-D image cross correlation in the spatial frequency domain. Vector fields were then interpolated and smoothed. Yellow dash-dot line annotations indicate approximate boundaries of active and stagnant lava. Solid yellow lines indicate fracture zones and surface lava rifting. Yellow stars correspond to approximate locations of vertical upwelling. Histograms (b), (d), (f) are shown for vector fields within the yellow dash-dot lines and are scaled to 1-day (24-hour) motions. The same histogram (h) is calculated based on the current vectors measured by UAV in this study (g). The area was masked to only include the flat dome top for this purpose to keep the data comparable and to avoid unmoving areas in the measurements.

The data shows that the type of activity at the Caliente lava dome has stayed very consistent throughout the last decade as the dome and lava flow show the same features as in 2019, these being the flat-topped dome inside the main crater and a constant lava flow down one side. The velocity of the lava flows since 2007 is on the order of several meters per day (b, d, f), which is very consistent with our new data from 2019 (g-h). A more active period is observed in 2012 with flow speeds being on the order of tens of meters per day (e-f). Another notable observation is the distribution of flow movement. In 2007 and 2009 large portion of the dome surface moved evenly and resulted in a rather uniform distribution of velocity vectors (b, d). This changed in 2012, where high velocity areas became more localized and resulted in few high velocity vectors and many low velocity ones as the flow area narrowed (e, f). In 2019, this is even more apparent as the lava flow moves in a single narrow channel, with the rest of the dome surface only moving slowly instead (g, h). We thus conclude that the UAV-based data is suitable to be compared with and improve upon previously captured image data.

(a, c, e) were plotted in MATLAB R2018b (v9.5.0, de.mathworks.com/products/matlab.html) and (g) was plotted in LaVision DaVis (v10.0.5.50575, www.lavision.de/de/products/davis-software/).

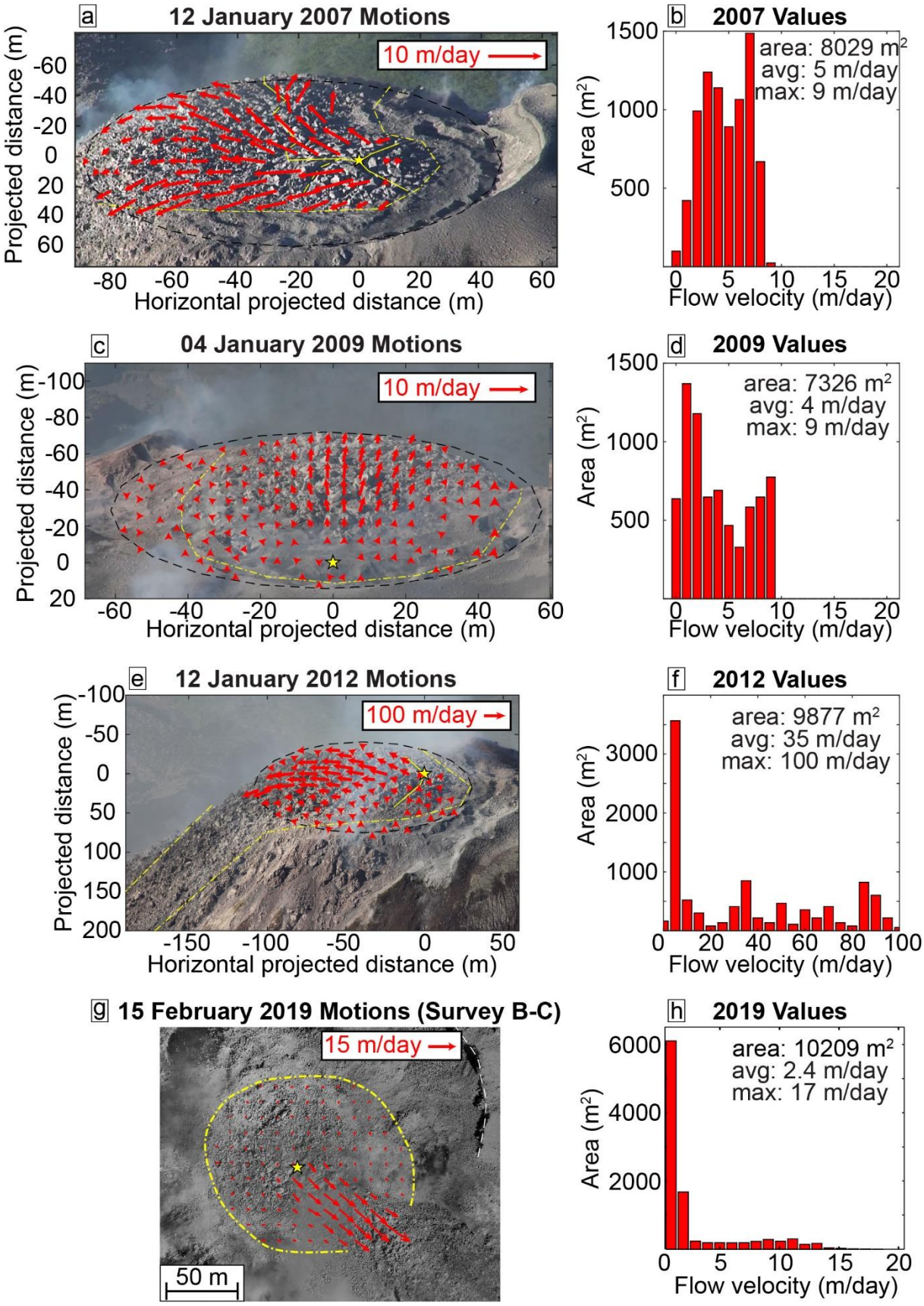
a
12 January 2007 Motions
10 m/day
Projected distance (m)
Horizontal projected distance (m)
b
2007 Values
area: 8029 m²
avg: 5 m/day
max: 9 m/day
Area (m²)
Flow velocity (m/day)
c
04 January 2009 Motions
10 m/day
Projected distance (m)
Horizontal projected distance (m)
d
2009 Values
area: 7326 m²
avg: 4 m/day
max: 9 m/day
Area (m²)
Flow velocity (m/day)
e
12 January 2012 Motions
100 m/day
Projected distance (m)
Horizontal projected distance (m)
f
2012 Values
area: 9877 m²
avg: 35 m/day
max: 100 m/day
Area (m²)
Flow velocity (m/day)
g
15 February 2019 Motions (Survey B-C)
15 m/day
50 m
h
2019 Values
area: 10209 m²
avg: 2.4 m/day
max: 17 m/day
Area (m²)
Flow velocity (m/day)

The survey orthophotos can be found on the following pages. The provided georeferencing RMS represents the relative referencing errors between the point clouds (relative to Survey D). All clouds have an additional error of 2.93 m to their absolute geolocation indicated by the point matching to the Pléiades satellite data (see methods).
The data was generated with Agisoft Metashape (v1.5.2, www.agisoft.com).

C3 (Survey A):

15.02.2019 at 11:52-12:18 UTC with DJI Phantom 4 Pro

SfM spatial Resolution: 13.3 cm

Orthophoto texture resolution: 18330 by 18816 px, 6.65 cm/px

Relative georeferencing RMS: 0.28 m

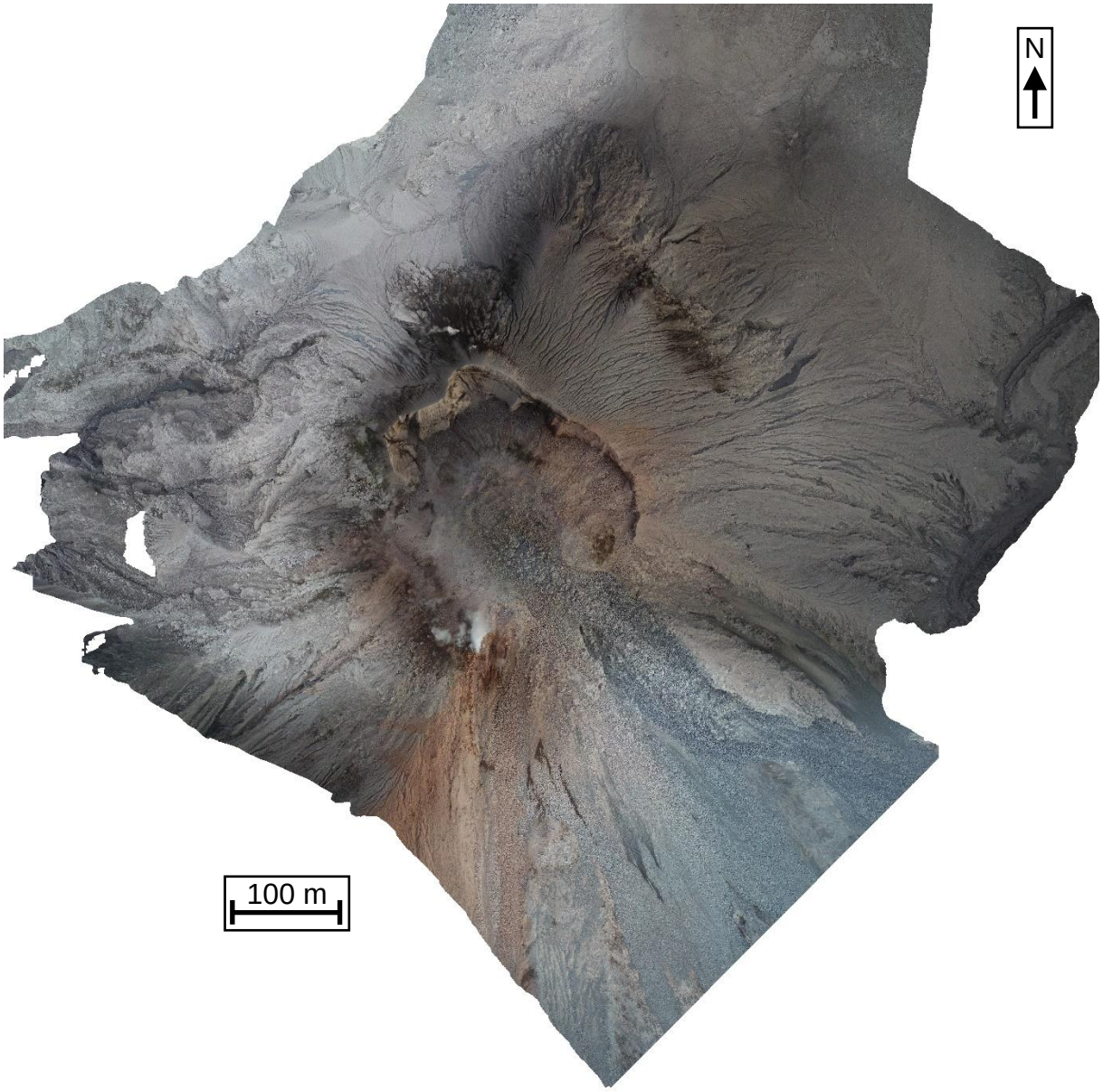

C4:

15.02.2019 at 12:12-12:25 UTC with FLIR TAU 2

SfM spatial Resolution: 40.9 cm

Orthophoto texture resolution: 2977 by 3056 px, 40.9 cm/px

Relative georeferencing RMS: 0.27 m

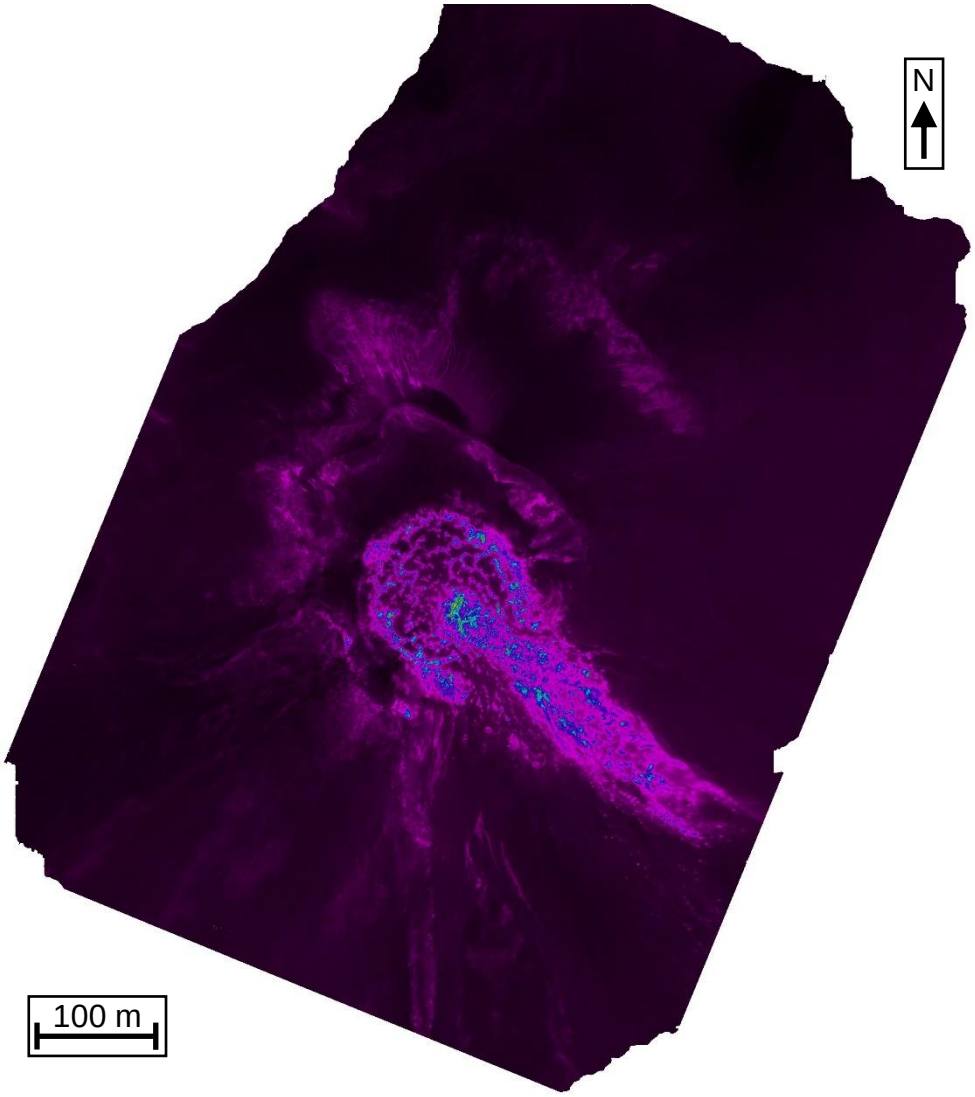

C5 (Survey B):

15.02.2019 at 12:37-12:43 UTC with DJI Phantom 4 Pro

SfM spatial Resolution: 10.6 cm

Orthophoto texture resolution: 22925 by 23534 px, 5.32 cm/px

Relative georeferencing RMS: 0.27 m

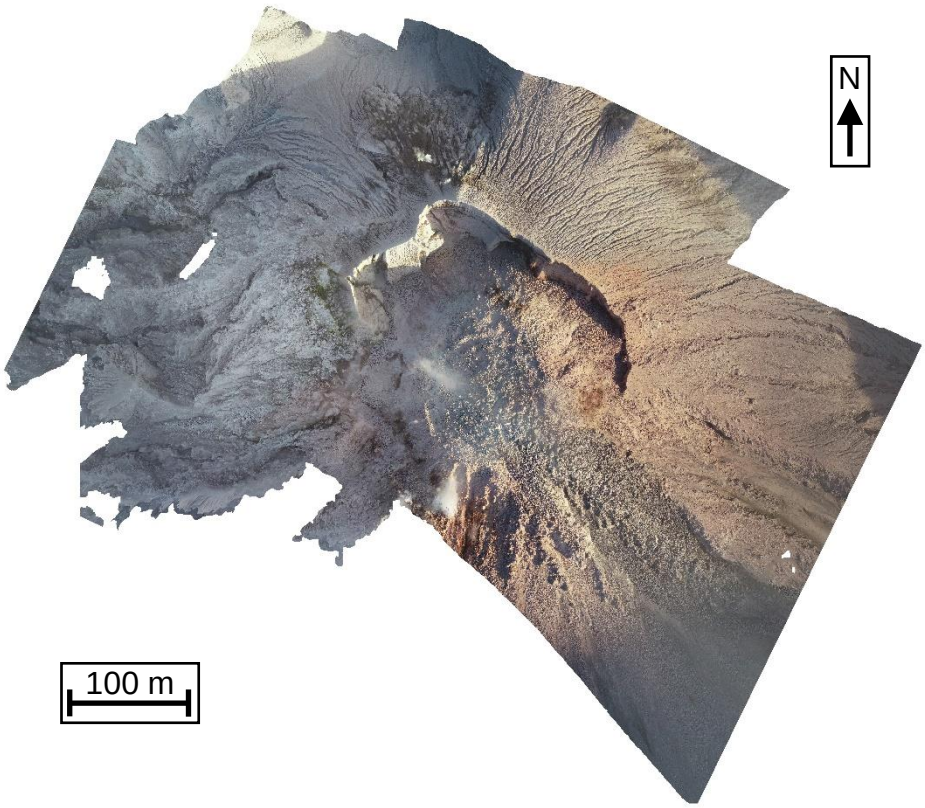

C6 (Survey C):

15.02.2019 at 15:20-15:33 UTC with DJI Phantom 4 Pro

SfM spatial Resolution: 13.3 cm

Orthophoto texture resolution: 18325 by 18811 px, 6.65 cm/px

Relative georeferencing RMS: 0.27 m

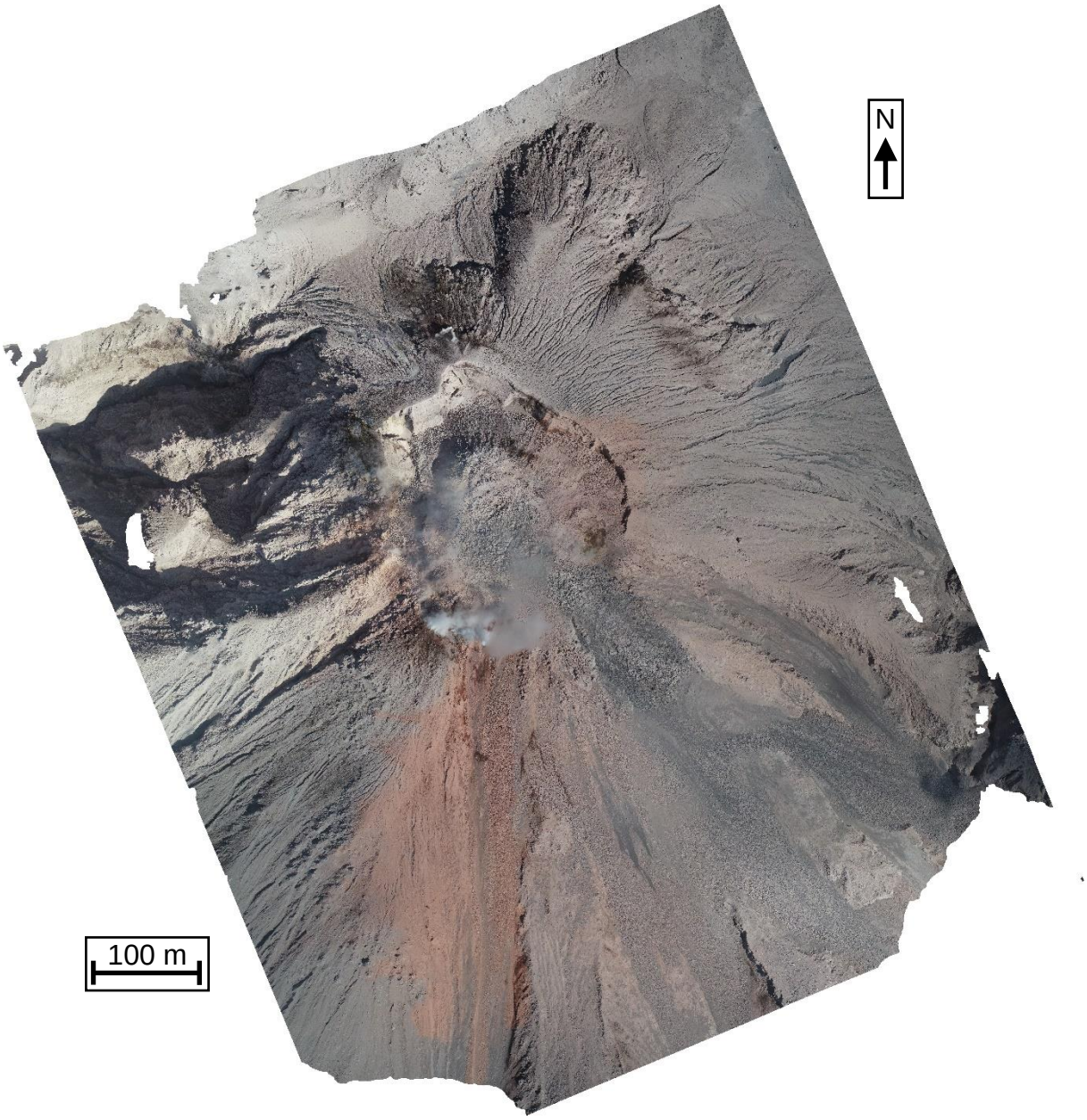

C7:

18.02.2019 at 11:49-12:19 UTC with FLIR TAU 2

SfM spatial Resolution: 27.1 cm

Orthophoto texture resolution: 4496 by 4615 px, 27.1 cm/px

Relative georeferencing RMS: 0.16 m

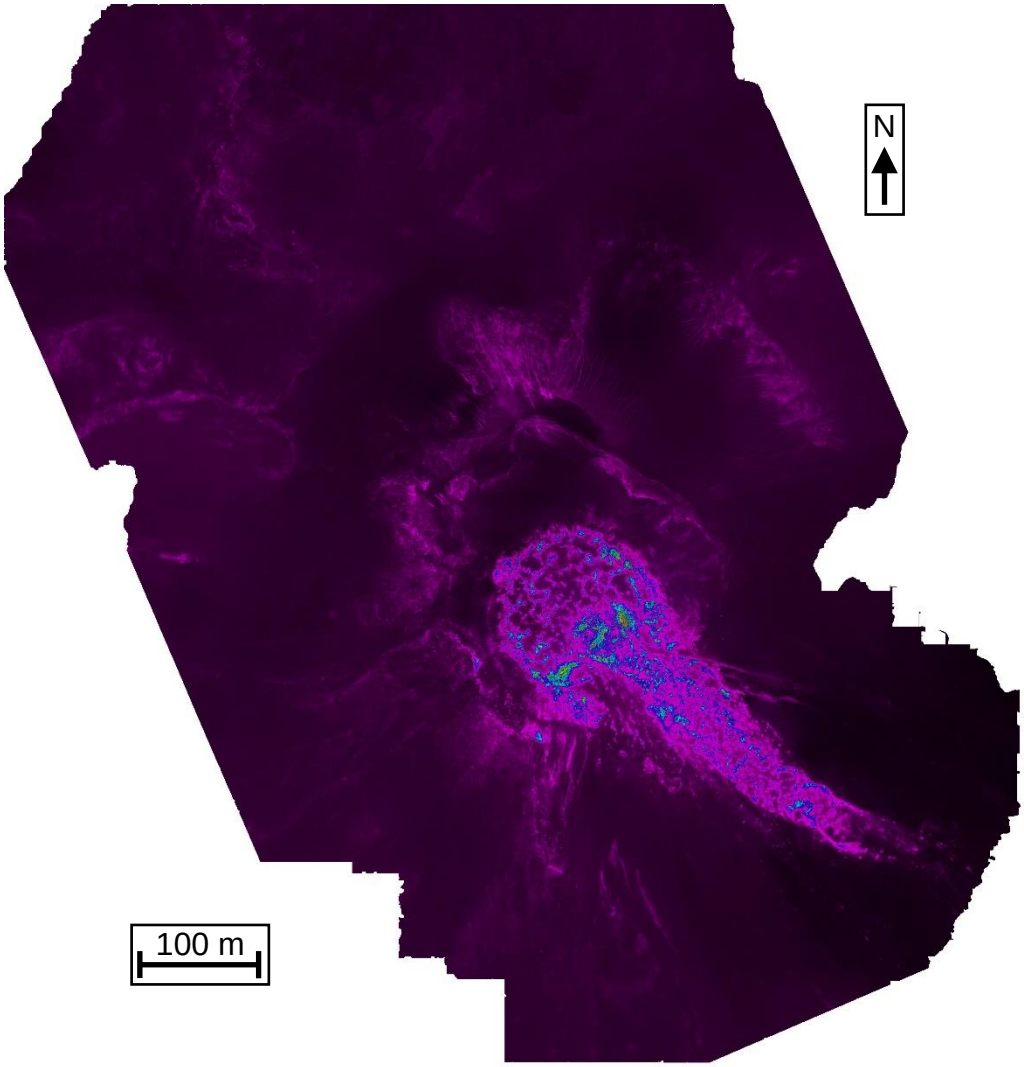

C8 (Survey D):

18.02.2019 at 14:38-14:50 UTC with DJI Phantom 4 Pro

SfM spatial Resolution: 11.3 cm

Orthophoto texture resolution: 19651 by 20173 px, 6.20 cm/px

Relative georeferencing RMS: Not applicable

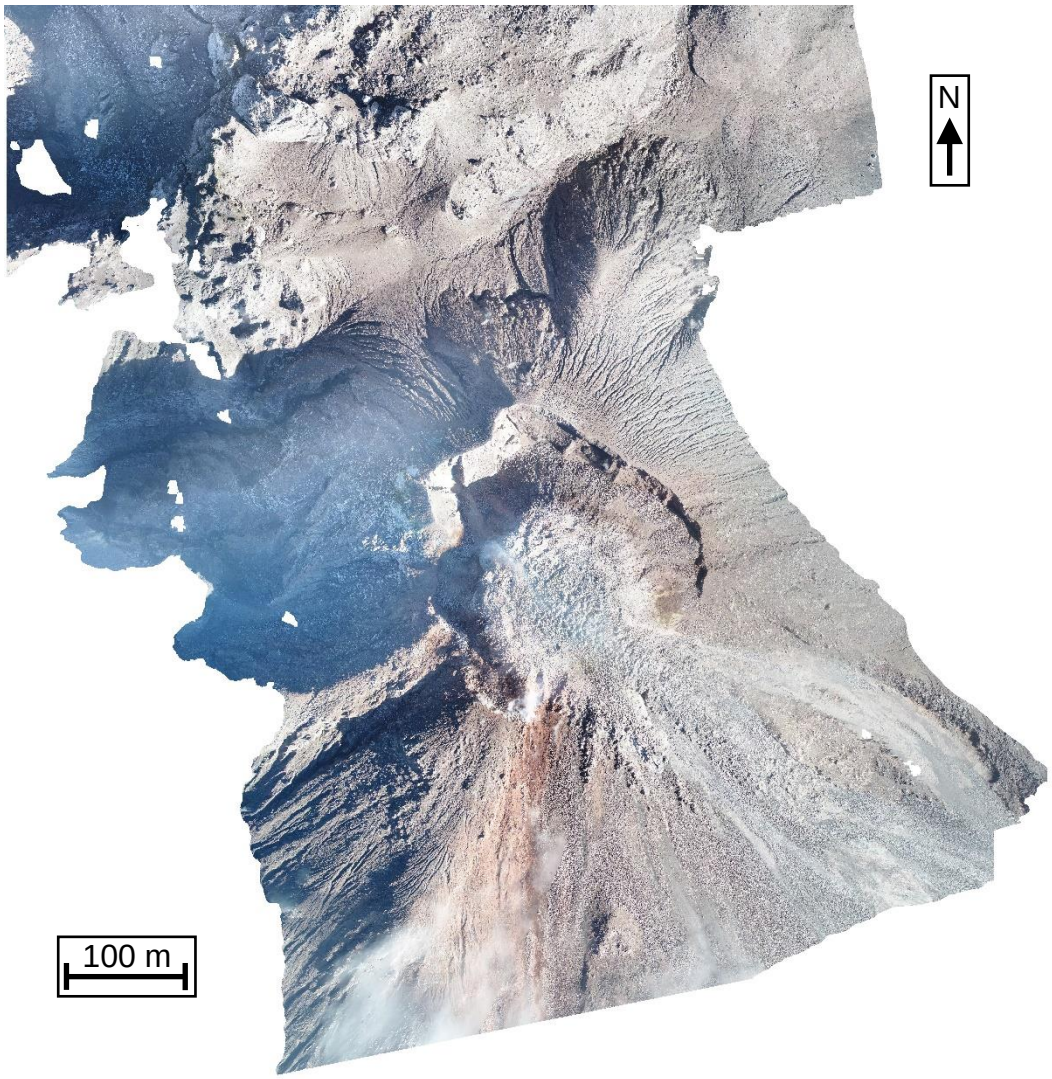

C9-11:

The figures consist of animated GIFs of the used Surveys (A-B, B-C and C-D, respectively). They can be downloaded in the supplementary information sections of the study: https://doi.org/10.1038/s41598-020-65386-2

Appendix D:

Insights into lava dome and spine extrusion using analogue sandbox experiments

Edgar U. Zorn[1], Thomas R. Walter[1], Michael J. Heap[2], Ulrich Kueppers[3]

[1]German Research Centre for Geosciences GFZ, Potsdam, Germany

[2]Géophysique Expérimentale, Institut de Physique de Globe de Strasbourg (Université de Strasbourg/EOST), Strasbourg, France

[3]Department of Earth and Environmental Sciences, Ludwig-Maximilians-Universität München, Munich, Germany

D1:

We measured the spine sizes in our experiments and compiled the results in the tables and figures below. We measured the spine width W (at its base on the dome surface), the spine height H (from the base on the dome surface), and the spine height H_C (total spine height from the conduit). W_C is the width of the conduit (40 mm). We further calculate the height to width ratios, which may characterize the spine growth regardless of their scale. Since we could not vary our conduit size here, we cannot characterize how different conduit widths affect these ratios. By further training these datasets with known spine rock strengths and conduit dimensions, the results could be used to predict unknown conduit depth (under the main dome edifice) or width by measuring the surface spines.

10% Plaster:

H (mm)	W (mm)	H_C (mm)	H/W-Ratio	H_C/W_C-Ratio
5.6	4.1	28.9	1.37	0.72
8.9	7.1	33.4	1.25	0.84
11.2	8.6	35.8	1.30	0.90
10.4	10.7	36.6	0.97	0.92
12.3	13.2	39.3	0.93	0.98
9.3	10.7	40.0	0.87	1.00
11.7	12.2	40.9	0.96	1.02
11.4	10.7	41.4	1.07	1.04
11.0	11.5	41.5	0.96	1.04
6.5	8.5	40.1	0.76	1.00
9.5	10.5	41.2	0.90	1.03
7.4	8.3	40.2	0.89	1.01
8.6	8.4	40.7	1.02	1.02

15% Plaster:

H (mm)	W (mm)	H_C (mm)	H/W-Ratio	H_C/W_C-Ratio
9.3	15.3	31.3	0.61	0.78
17.9	20.7	38.8	0.86	0.97
12.3	18.6	37.0	0.66	0.93
12.3	15.6	38.4	0.79	0.96
17.9	22.6	42.8	0.79	1.07
11.8	20.6	40.1	0.57	1.00
10.8	17.6	41.1	0.61	1.03
11.8	17.1	41.6	0.69	1.04
14.0	21.3	45.0	0.66	1.13
15.2	17.7	45.7	0.86	1.14
12.0	21.3	45.1	0.56	1.13
13.4	18.8	45.2	0.71	1.13
12.0	16.1	46.1	0.75	1.15
12.8	19.8	45.9	0.65	1.15
12.6	19.2	46.4	0.66	1.16
10.0	15.8	44.9	0.63	1.12

20% Plaster:

H (mm)	W (mm)	H_C (mm)	H/W-Ratio	H_C/W_C-Ratio
13.7	22.2	33.2	0.62	0.83
22.3	28.0	44.0	0.80	1.10
23.2	27.7	44.7	0.84	1.12
15.3	21.3	43.8	0.72	1.10
19.8	23.3	44.5	0.85	1.11
19.7	25.6	50.4	0.77	1.26
21.6	21.9	51.4	0.99	1.29
18.1	23	51.8	0.79	1.30
23.5	25.7	56.6	0.91	1.42

30% Plaster:

H (mm)	W (mm)	H_C (mm)	H/W-Ratio	H_C/W_C-Ratio
37.6	37.6	56.5	1.00	1.41
31.2	35.9	55.0	0.87	1.38
31.8	37.2	58.8	0.85	1.47
31.7	35.8	59.2	0.89	1.48
26.9	34.2	61.8	0.79	1.55

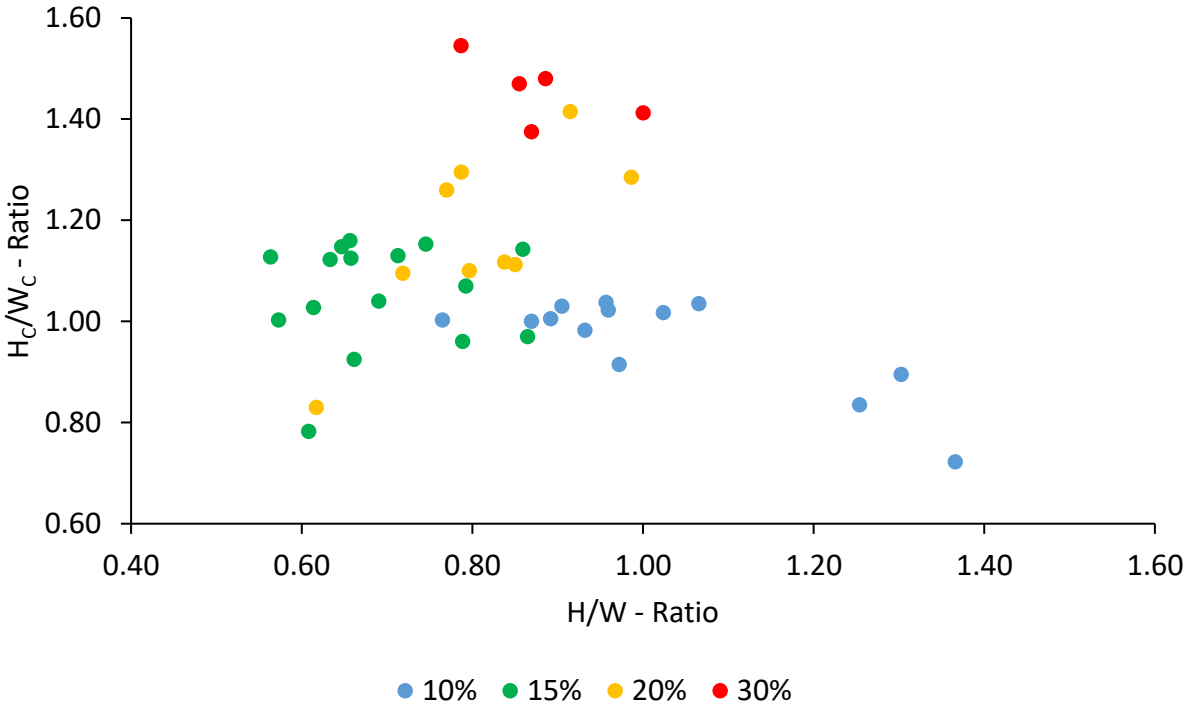
1.60
1.40
1.20
1.00
0.80
0.60
H_C/W_C - Ratio
0.40
0.60
0.80
1.00
1.20
1.40
1.60
H/W - Ratio
10%
15%
20%
30%

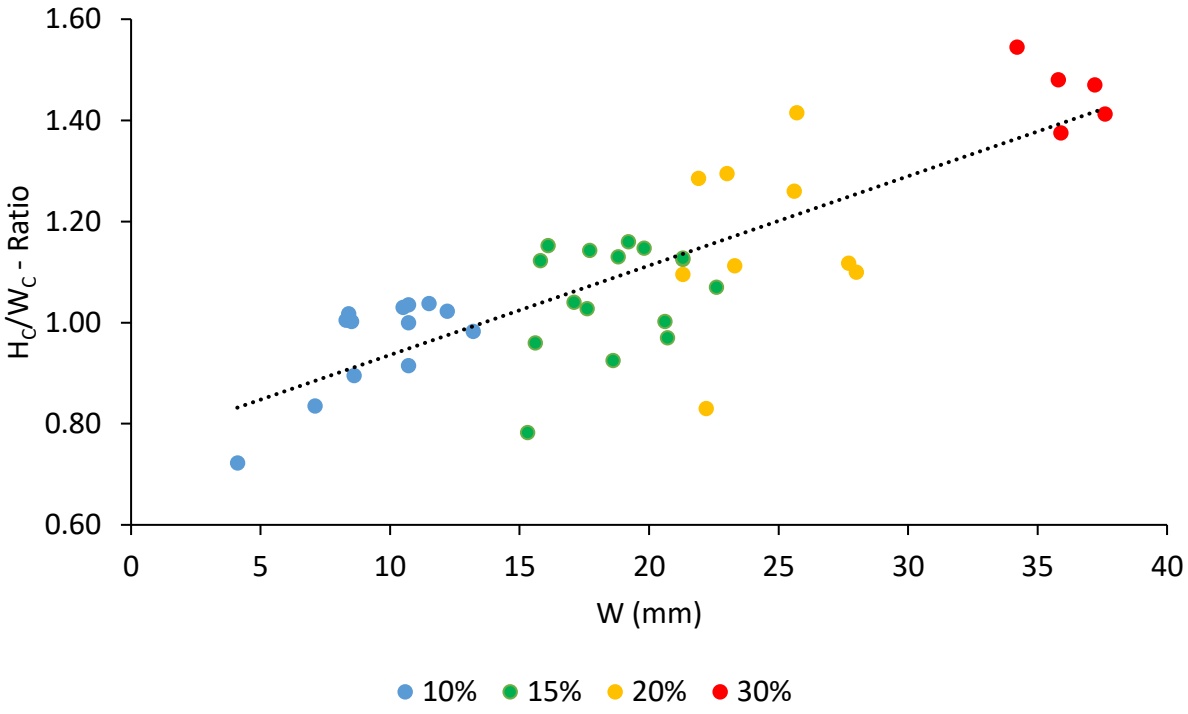
1.60
1.40
1.20
1.00
0.80
0.60
H_C/W_C - Ratio
0
5
10
15
20
25
30
35
40
W (mm)
10%
15%
20%
30%

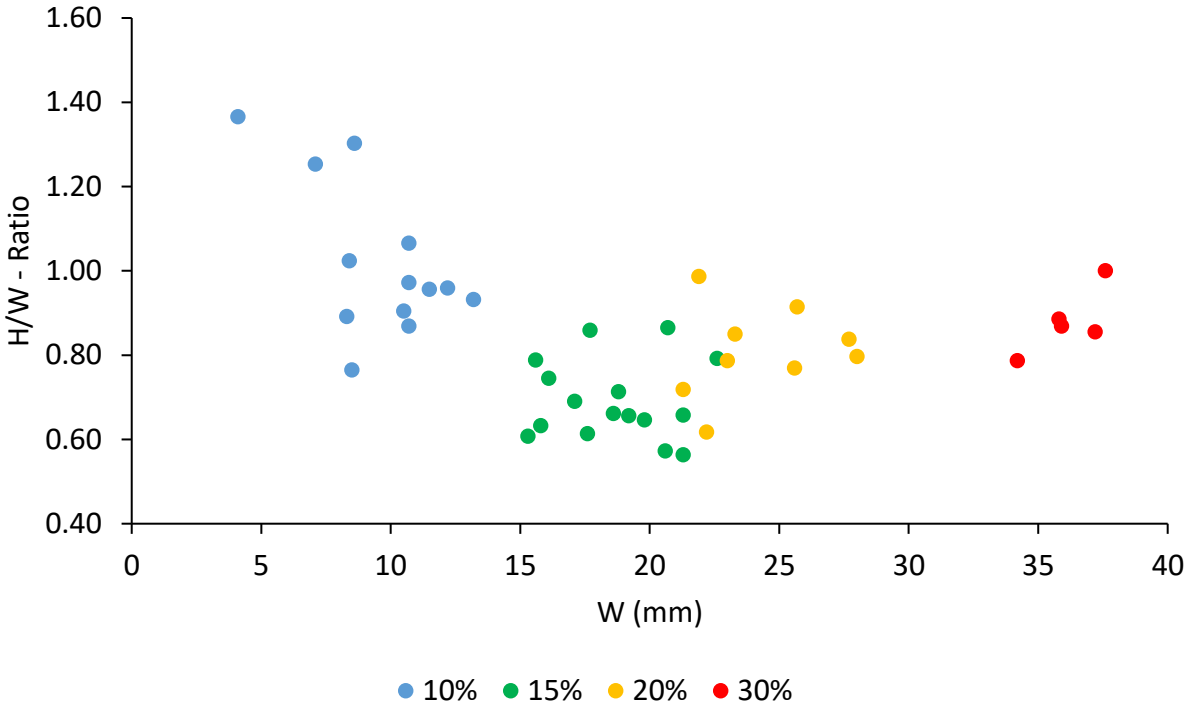

D2:

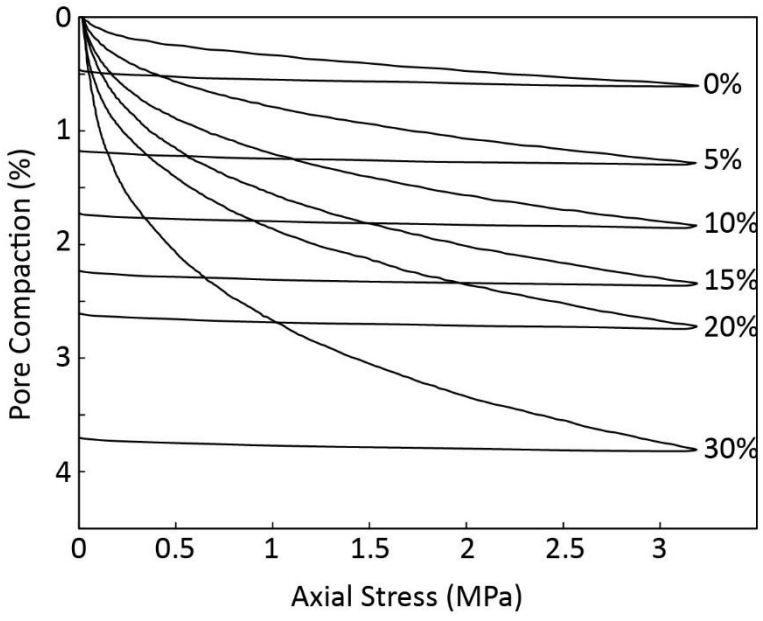

Plot showing the gradual compaction of the sand-plaster mixtures under the increasing compression in the uniaxial experiments. The load was gradually increased on the samples, showing an initially strong compaction that exponentially decays with increasing stresses. After a fixed stress value of ~3.18 MPa was reached, the load was lifted. All samples showed a very low amount of elastic recovery, indicating that nearly all compaction was permanent.

D3:

The following pages contain the results for the peak, dynamic and reactivation cohesion properties of the sand-plaster mixtures as well as the raw ring-shear data. These consist of three measurements per sample and normal stress σ_N (units in Pa). The samples were sheared for three minutes, then briefly reversed and sheared for another three minutes. The mixtures consists of G12 sand (meaning sand grains sieved to ~400 µm) and plaster powder.

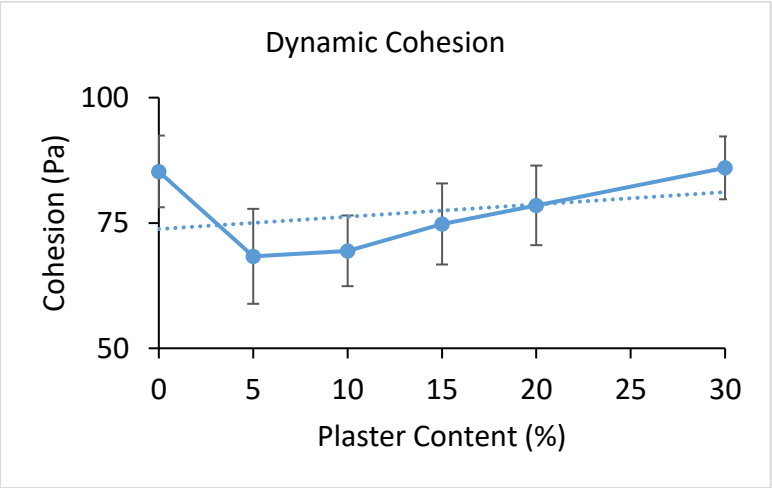

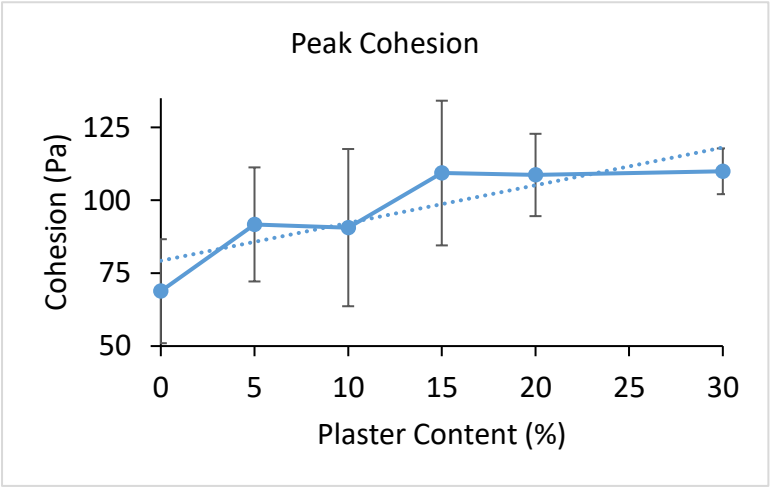

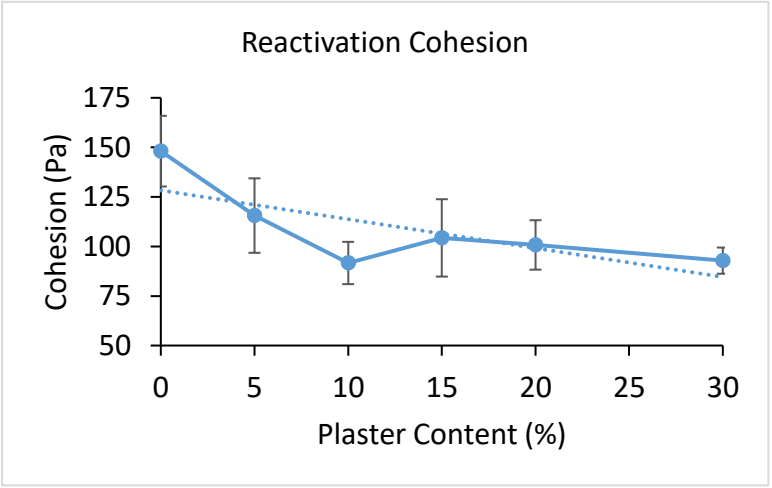

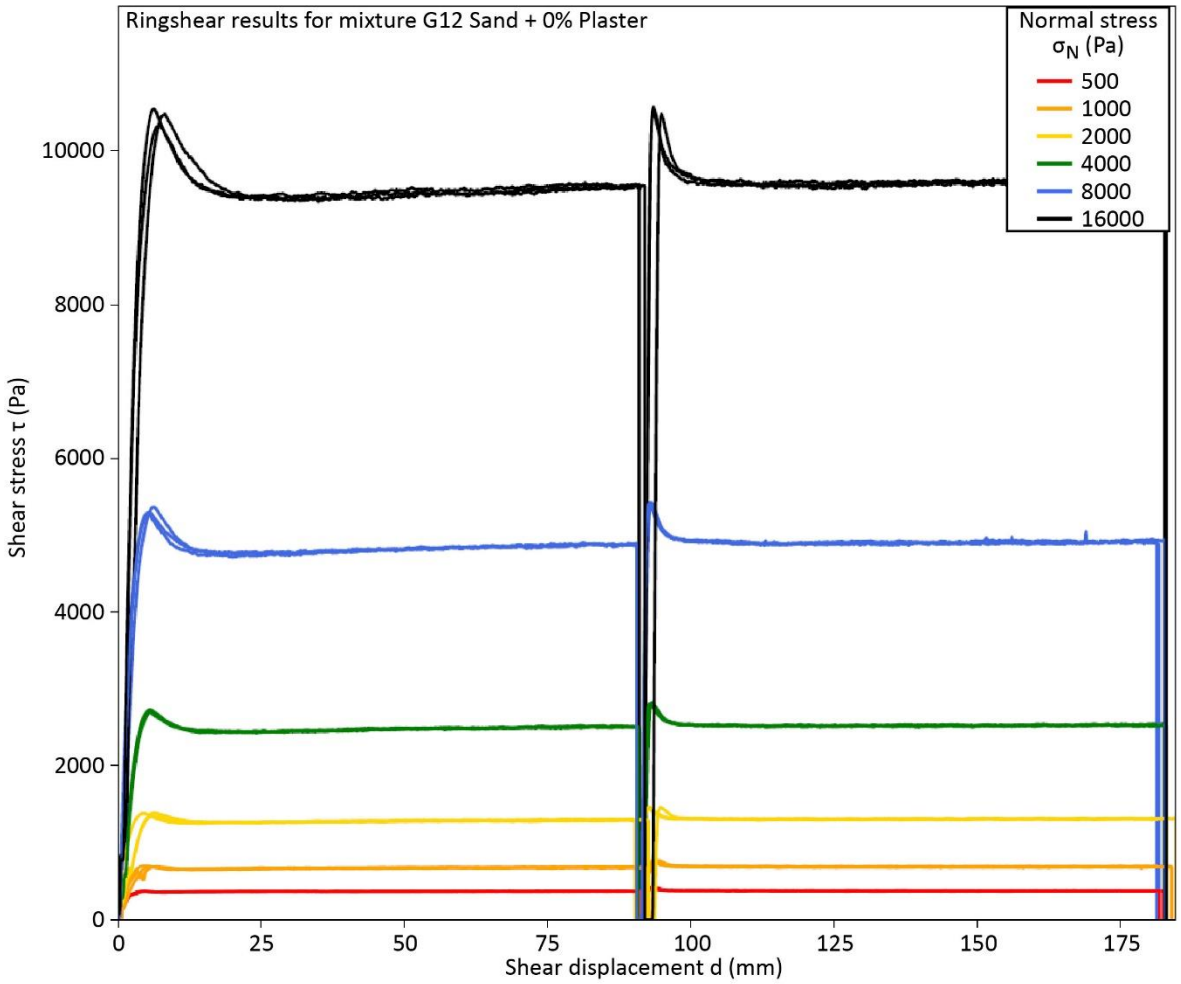
Ringshear results for mixture G12 Sand + 0% Plaster
Normal stress
σN (Pa)
500
1000
2000
4000
8000
16000
Shear stress τ (Pa)
0
2000
4000
6000
8000
10000
0
25
50
75
100
125
150
175
Shear displacement d (mm)

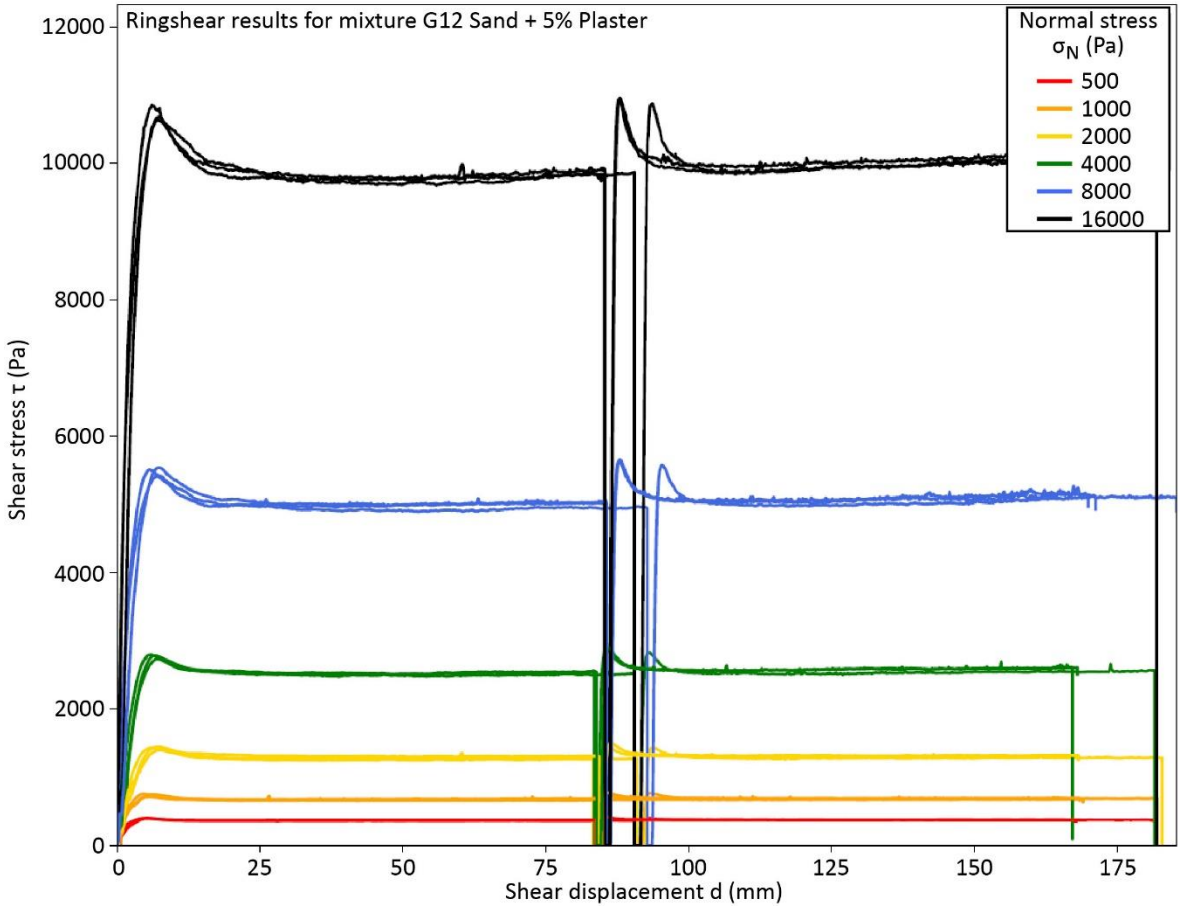
Ringshear results for mixture G12 Sand + 5% Plaster
Normal stress
σN (Pa)
500
1000
2000
4000
8000
16000
Shear stress τ (Pa)
0
2000
4000
6000
8000
10000
12000
0
25
50
75
100
125
150
175
Shear displacement d (mm)

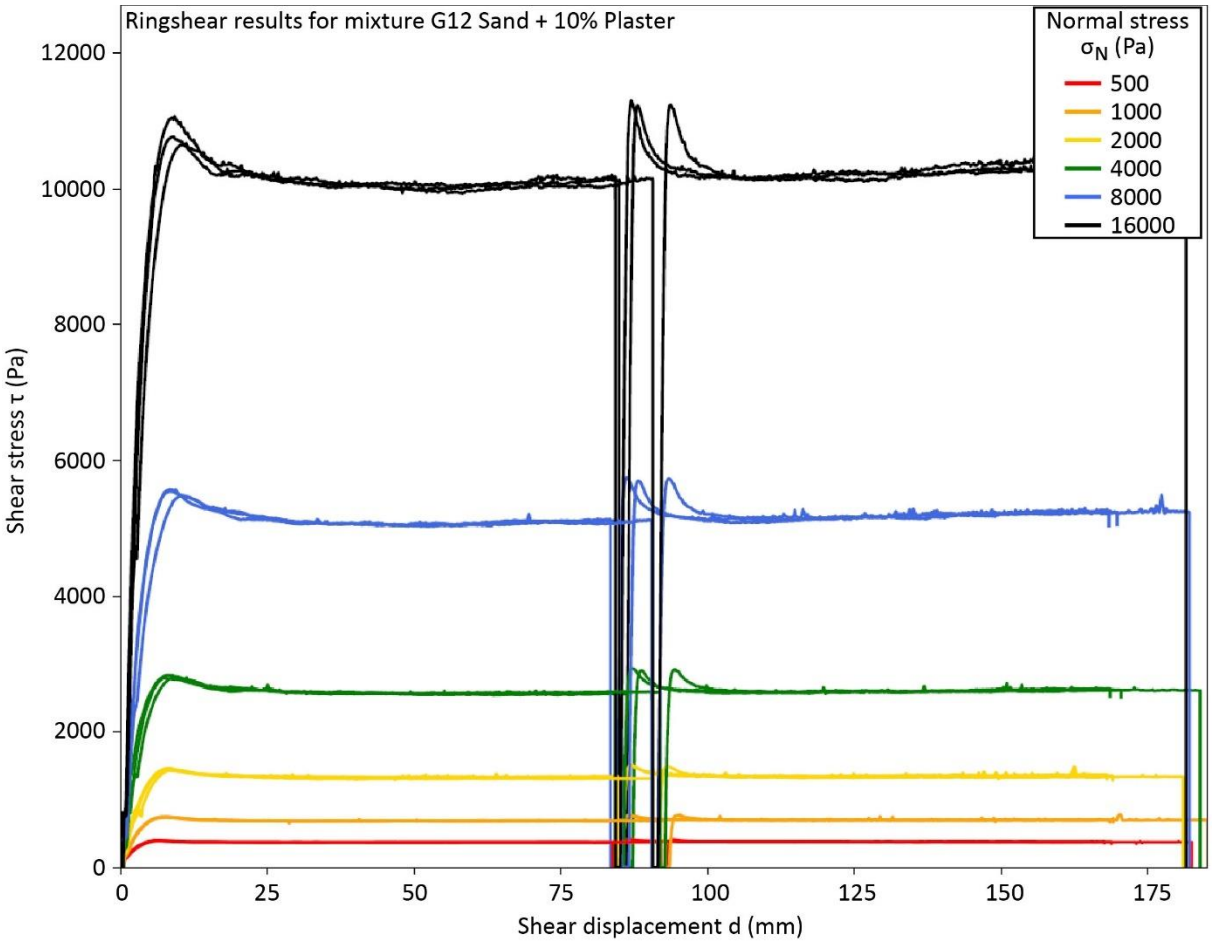
Ringshear results for mixture G12 Sand + 10% Plaster
Normal stress
σN (Pa)
500
1000
2000
4000
8000
16000
Shear stress τ (Pa)
0
2000
4000
6000
8000
10000
12000
0
25
50
75
100
125
150
175
Shear displacement d (mm)

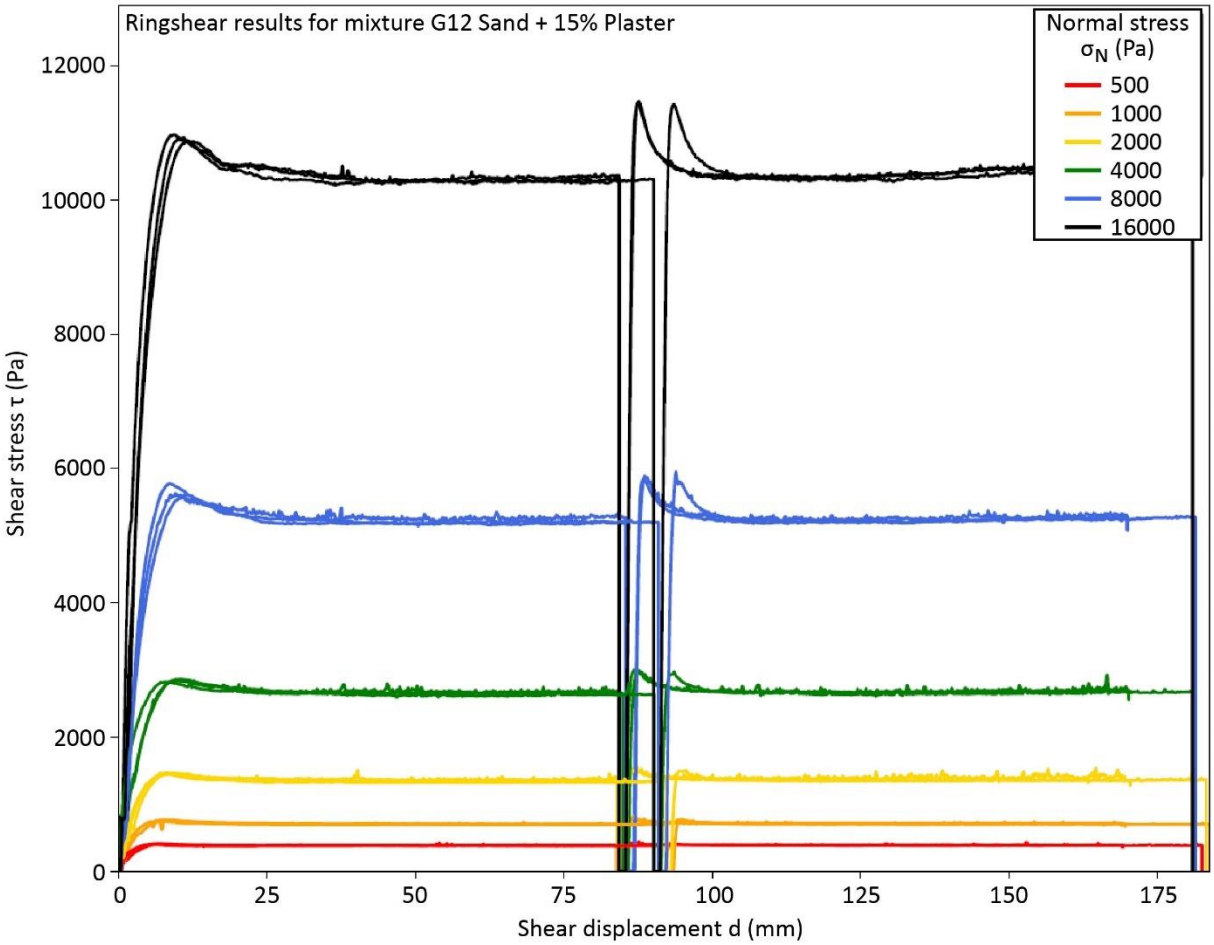
Ringshear results for mixture G12 Sand + 15% Plaster
Normal stress
σN (Pa)
500
1000
2000
4000
8000
16000
Shear stress τ (Pa)
0
2000
4000
6000
8000
10000
12000
0
25
50
75
100
125
150
175
Shear displacement d (mm)

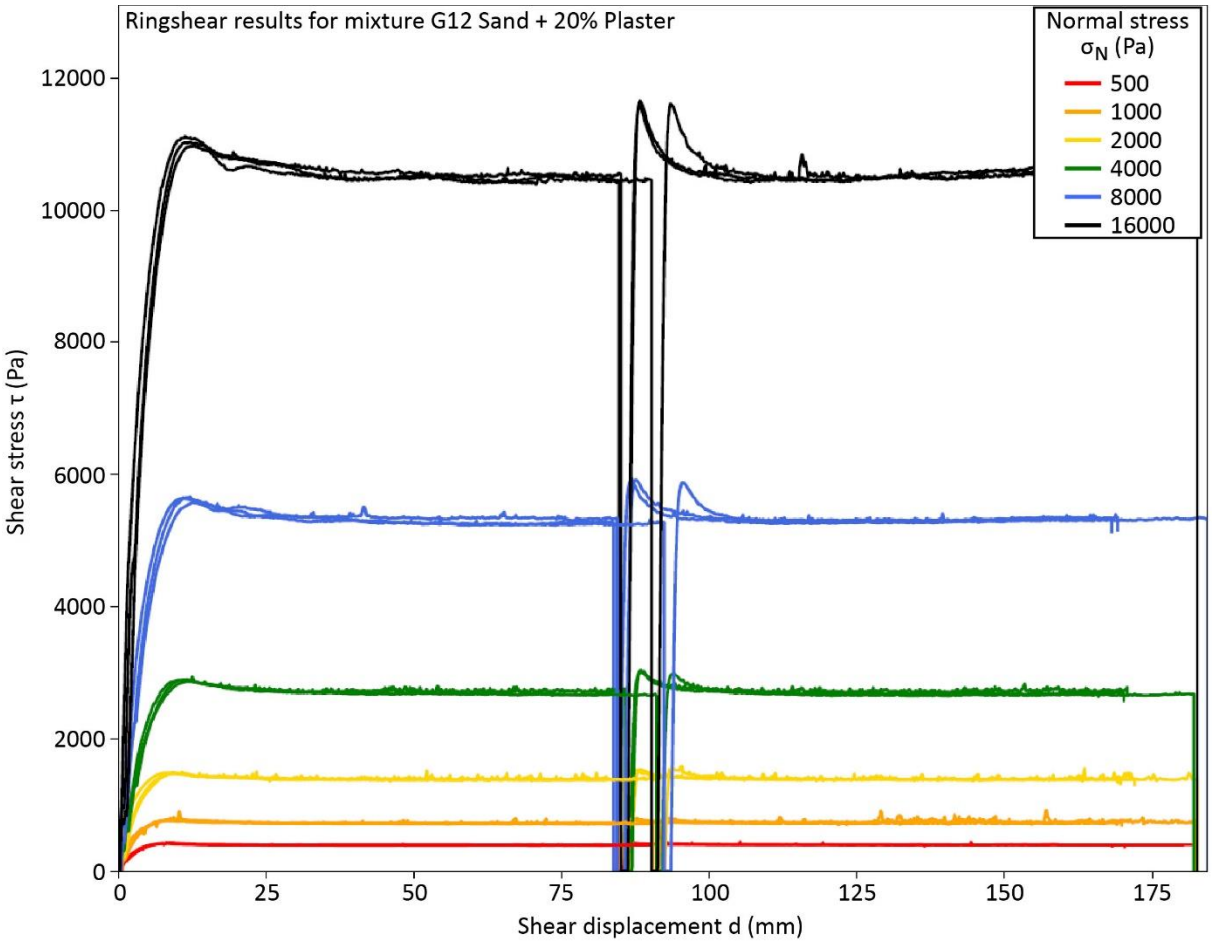
Ringshear results for mixture G12 Sand + 20% Plaster
Normal stress
σN (Pa)
500
1000
2000
4000
8000
16000
Shear stress τ (Pa)
0
2000
4000
6000
8000
10000
12000
0
25
50
75
100
125
150
175
Shear displacement d (mm)

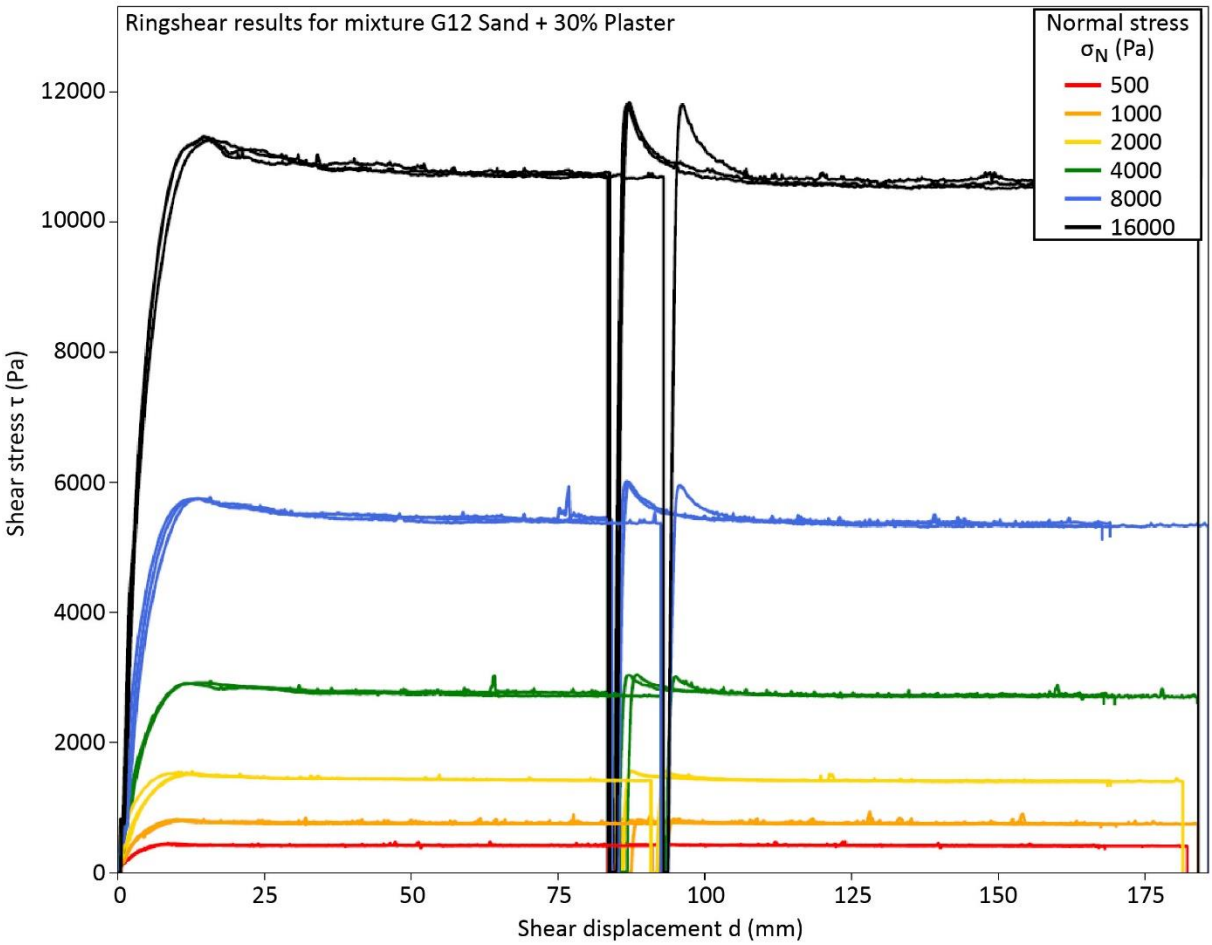
Ringshear results for mixture G12 Sand + 30% Plaster
Normal stress
σN (Pa)
500
1000
2000
4000
8000
16000
Shear stress τ (Pa)
0
2000
4000
6000
8000
10000
12000
0
25
50
75
100
125
150
175
Shear displacement d (mm)